technische universität
dortmund

Universitätsmedizin Essen
Universitätsklinikum
Klinik und Poliklinik für Strahlentherapie

Dissertation for the attainment of the academic degree
Dr. rer. nat.

# Enhancing ocular brachytherapy

## The impact of inhomogeneous $^{106}$Ru dose distributions and the potential of neural network-based dose prediction

Michelle Stroth

January 2026

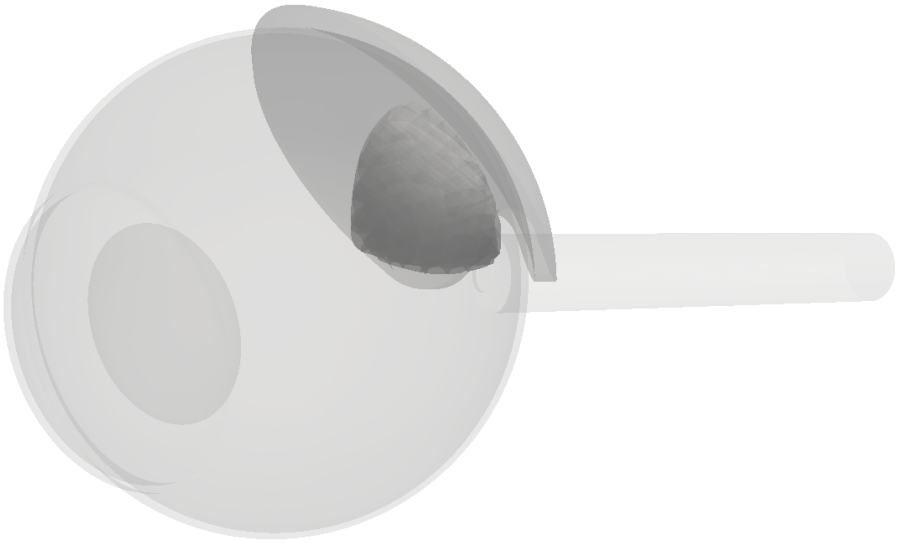

This thesis is submitted by Michelle Stroth, born in Mettingen (Germany) on 19 May 1997, to the Department of Physics of TU Dortmund University on 9 January 2026.

Assessors:
Prof. Dr. Johannes Albrecht
Prof. Dr. Armin Lühr

Chairperson of the examination committee:
Apl. Prof. Dr. Doris Reiter

Representative of the scientific staff:
Dr. Bärbel Siegmann

Date of the oral exam:
27 February 2026

## Abstract

Brachytherapy with ruthenium-106 applicators is an effective treatment for ocular tumours. However, the surface dose profiles of these applicators are not homogeneous, and the effects of hot and cold spots on tumour and organ at risk doses have not yet been fully characterised. Furthermore, there is a lack of dedicated software to support treatment planning and to visualise three-dimensional dose distributions, which are necessary to accurately assess tumour control and the impact on organs at risk. To address these challenges, the efficiency of an existing simulation workflow is improved through the implementation of a particle tracking method combined with a novel external binning approach. This enables flexible, three-dimensional scoring of dose distributions within complex geometries. The impact of inhomogeneous surface dose profiles is evaluated using Monte Carlo simulations for three patient cases and different applicator models. The inhomogeneities are modelled using weighted phase space files. The results indicate that tumour control doses are generally maintained for applicator positions fully covering the target volume. However, hot spot scenarios can increase the dose to adjacent structures, and cold spots may reduce the local dose. To accelerate dose estimation, a 3D U-Net is trained to predict three-dimensional dose distributions from simulation data. The model achieves mean differences of $(4.3 \pm 15.8)\,\%$ for the minimum tumour dose and $(0.6 \pm 0.6)\,\%$ for the maximum scleral dose compared to the simulation results, suggesting that the model provides clinically sufficient accuracy to support treatment decisions. Building on the improved simulation workflow and the neural network-based dose prediction, a prototype web-based treatment planning interface is presented.

## Zusammenfassung

Die Brachytherapie mit Ruthenium-106-Applikatoren gilt als effektive Behandlung okularer Tumoren. Die Oberflächendosisprofile dieser Applikatoren sind jedoch nicht homogen, und die Auswirkungen von Hot- und Cold-Spots auf die Dosis im Tumor sowie in den Risikostrukturen sind noch nicht vollständig charakterisiert. Darüber hinaus fehlt es an Software zur Unterstützung der Therapieplanung und zur Visualisierung dreidimensionaler Dosisverteilungen, um die Auswirkungen der Behandlung auf die Tumorkontrolle und die umliegenden Strukturen präzise beurteilen zu können. Um diesen Herausforderungen zu begegnen, wird die Effizienz eines bestehenden Simulationsworkflows durch die Implementierung einer Methode zur Teilchenverfolgung in Kombination mit einem neuartigen externen Binning-Ansatz gesteigert. Hierdurch wird eine flexible, dreidimensionale Erfassung der Dosisverteilung in komplexen Geometrien ermöglicht. Die Auswirkungen der inhomogenen Oberflächendosisprofile werden mittels Monte Carlo Simulationen für drei Patientenfälle und verschiedene Applikatormodelle untersucht. Die Inhomogenitäten werden mithilfe gewichteter Phase-Space-Dateien modelliert. Die Ergebnisse zeigen, dass die Tumorkontrolldosen im Allgemeinen für Applikatorpositionen beibehalten werden, die das Zielvolumen vollständig abdecken. Allerdings können Hot-Spots die Dosis für benachbarte Strukturen erhöhen, während Cold-Spots die lokale Dosis verringern können. Zur Beschleunigung der Dosisabschätzung wird ein 3D-U-Net darauf trainiert, dreidimensionale Dosisverteilungen aus den Simulationsdaten vorherzusagen. Im Vergleich zu den Simulationsergebnissen liefert das neuronale Netz Vorhersagen für die minimale Tumordosis mit einer mittleren Abweichung von $(4.3 \pm 15.8)\,\%$ sowie von $(0.6 \pm 0.6)\,\%$ für die maximale Skleradosis, was darauf hindeutet, dass das Modell eine klinisch hinreichende Genauigkeit zur Unterstützung von Therapieentscheidungen bietet. Aufbauend auf dem verbesserten Simulationsworkflow und der neuronalen-netz-basierten Dosisvorhersage wird ein Prototyp für eine webbasierte Planungsoberfläche präsentiert.

# Contents

# List of abbreviations

## General

| | |
|---|---|
| **AI** | Artificial Intelligence |
| **CAD** | Computer-Aided Design |
| **CBS** | Command-Based Scorer |
| **CNN** | Convolutional Neural Network |
| **CPU** | Central Processing Unit |
| **CT** | Computed Tomography |
| **DICOM** | Digital Imaging and Communications in Medicine |
| **DL** | Deep Learning |
| **DVH** | Dose-Volume Histogram |
| **GPS** | General Particle Source |
| **GPU** | Graphics Processing Unit |
| **MC** | Monte Carlo |
| **ML** | Machine Learning |
| **MRI** | Magnetic Resonance Imaging |
| **PG** | Particle Gun |
| **QA** | Quality Assurance |
| **SD** | Sensitive Detector |
| **STL** | Standard Triangle Language or Standard Tessellation Language |
| **TPS** | Treatment Planning System |

## Companies and commissions

| | |
|---|---|
| **EZAG** | Eckert & Ziegler Medical, Berlin, Germany |
| **NCS** | Netherlands Commission on Radiation Dosimetry |
| **UME** | University Medicine Essen, Essen, Germany |

## Software

| | |
|---|---|
| `Emscripten` | Emscripten, compiler toolchain to WebAssembly. `https://emscripten.org`. |
| `MeshLib` | MeshLib SDK, open-source 3D geometry library. `https://meshlib.io`. |
| `NumPy` | NumPy, Python library [1]. `https://numpy.org`. |
| `Optuna` | Optuna, a hyperparameter optimization framework. `https://optuna.org`. |
| `Pandas` | Pandas, Python library [2]. `https://pandas.pydata.org`. |
| `PyTorch` | PyTorch, Python library [3]. `https://pytorch.org`. |
| `PyVista` | PyVista, helper library for the Visualization Toolkit (VTK). `https://pyvista.org`. |
| `SDL3` | SDL3, Simple Directmedia Layer, cross-platform development library. `https://www.libsdl.org`. |
| `SciPy` | SciPy, Python library. `https://scipy.org`. |
| `trimesh` | trimesh, library for importing, exporting and doing simple operations on triangular meshes. `https://trimesh.org`. |
| **Fusion** | Autodesk® Fusion®. `https://www.autodesk.com/de/products/fusion-360/`. |
| **Geant4** | Geant4, free software published and maintained by the Geant4 Collaboration. `https://geant4.web.cern.ch`. |
| **MS Excel** | Microsoft® Excel®. |
| **Plaque Simulator** | Eye Physics Plaque Simulator. `https://www.eyephysics.com/PS/Index.html`. |
| **ROOT** | ROOT, data analysis framework, free software published and maintained by the ROOT Team. `https://root.cern`. |
| **VBA** | Microsoft® Visual Basic® for Applications. |
| **VTK** | Visualization Toolkit, open source software for manipulating and displaying scientific data [4]. `https://vtk.org`. |

# 1 Introduction

Ocular tumours, for instance, melanomas of the choroid and ciliary body, pose a serious and potentially life-threatening disease, with approximately half of the affected patients ultimately dying from metastatic spread of the primary tumour. In recent decades, treatment strategies for ocular tumours have evolved from routine enucleation towards eye-preserving modalities. Brachytherapy and proton beam therapy are now established worldwide as standard therapeutic approaches [5]. In Europe, beta-emitting ruthenium-106 ($^{106}$Ru) applicator brachytherapy has become the leading form of ocular brachytherapy [6]. This method is used in most treatments at specialised centres, including the UME[1], where more than 80 % of irradiated ocular tumours were treated using this technique in 2022 [7].

Despite its widespread clinical use and proven effectiveness for tumours with an apex height of up to approximately 6 mm [8], ongoing efforts to improve $^{106}$Ru brachytherapy remain important. These efforts aim to optimise tumour coverage, reduce radiation-induced side effects, and ultimately enhance clinical outcomes. Two key aspects offer particular potential for such enhancement and are investigated in this thesis. The first involves a systematic investigation of the impact of inhomogeneous surface dose profiles of $^{106}$Ru applicators on treatment delivery. The second focuses on improving treatment planning through the incorporation of individual patient-specific geometries and a volumetric dose distribution. This can be achieved through neural network-based predictions of dose distributions within the tumour and adjacent ocular structures, allowing for a more precise and personalised assessment of the delivered dose. The basis for understanding the methods required to address these issues is provided in chapter 2, which presents the relevant physical and medical physics principles.

In treatment planning, a patient-centred approach is essential, as tumour characteristics and ocular anatomy vary between individuals. In Ref. [9], a Monte Carlo (MC) simulation workflow was developed for retrospective analysis of patient cases. However, the methods employed in this workflow present challenges in terms of computational effort, efficiency, and simulation time. To enable the workflow to serve as a basis for the studies on the enhancement of ocular brachytherapy presented in this thesis, it is revised accordingly. The modifications, described in chapter 3, include the implementation of a novel particle tracking method along with a Python-based external binning technique.

Modern protective treatment strategies aim to reduce applicator overlap with adjacent organs at risk, especially when these structures are close to the target volume. This approach takes advantage of the steep dose gradient and helps lower radiation-induced side effects. However, due to the manufacturing process, the surface dose distribution of $^{106}$Ru applicators is inherently inhomogeneous, resulting in hot and cold spots. The presence of surface dose hot spots may compromise the protective concept regarding the structures at risk, whereas cold spots may result in local under-dosing at the tumour margin, potentially jeopardising tumour

[1] University Medicine Essen, Essen, Germany

control. Nevertheless, these variations are neither accounted for in current simulations of applicator dose distributions nor can their impact on the dose delivered to the tumour and surrounding ocular structures be quantified with sufficient accuracy.
To evaluate the impact of hot and cold spots on treatment, a simulation architecture is presented in chapter 4 that takes surface dose inhomogeneities into account. By weighting phase space files that contain the coordinates of $^{106}$Ru primary particles, it is possible to model and simulate inhomogeneous surface dose distributions.
In chapter 5, the effects of hot and cold spots in the surface dose profile on tumour control and the dose to structures at risk are investigated for three different applicator models using specific case studies. Worst- and best-case scenarios are analysed, and their implications for the dose concept employed at UME as well as for a less conservative treatment approach are evaluated.

Historically, ocular brachytherapy treatment planning relied on manual methods. These methods used depth-dose curves with the prescribed dose aimed at the tumour apex. Now, three-dimensional (3D) treatment planning software is recommended. This software combines medical imaging, a volumetric eye model, and full 3D dose calculation [10]. Currently, the Plaque Simulator[2] is the only available treatment planning system for applicator-based brachytherapy. However, its clinical use is limited due to practical constraints, including geometric restrictions. Without standardised software, many centres depend on in-house planning solutions, which generally base treatment decisions on the tumour height and the depth-dose curve of the applicator instead of detailed dose distributions [10]. While MC simulations provide very accurate dose calculations, their high computational demands make them difficult to use in routine clinical practice. New methods that combine machine learning with computer vision and image processing have shown great potential for improving diagnosis, treatment planning, and outcome prediction in radiation oncology [11].
In chapter 6, a neural network approach for predicting dose distributions for $^{106}$Ru applicators is introduced. This method uses MC simulation data generated with the workflow described in chapter 3. A 3D U-Net architecture is trained within a supervised learning framework. To obtain accurate dose predictions, multiple parameter studies are performed, exploring different model configurations, training approaches, and hyperparameter settings.

The methods presented in this thesis for data preparation, 3D visualisation of dose distributions within anatomical structures, and dose prediction for treatments with $^{106}$Ru applicators provide a foundation for a treatment planning system. A concept for a clinical treatment planning interface, building upon this foundation, is presented in chapter 7.

Finally, in chapter 8, the findings of this thesis are summarised with respect to the enhancement of ocular brachytherapy, and directions for further research and future applications are outlined.

All studies presented in this thesis have been conducted by the author. As part of this work, the author supervised three Master's theses, whose developments contributed to the methods and results presented here for the simulation of inhomogeneous $^{106}$Ru surface dose profiles (Refs. [12, 13]) and the neural network-based dose prediction (Ref. [14]).

[2]Eye Physics Plaque Simulator. `https://www.eyephysics.com/PS/Index.html`.

# 2 Theoretical overview

This chapter provides an overview of the physical and medical physics principles that form the foundation for understanding the methods developed in this thesis and their resulting findings. The fundamental anatomy of the eye, outlined in section 2.1, serves as a basis for understanding intraocular tumours as a disease, which are discussed in section 2.2, along with the effects of radiation therapy. The process and challenges of brachytherapy with $^{106}$Ru applicators, the central focus of this work, are examined in detail in section 2.3. Lastly, the interactions of particles involved in this form of radiation therapy with matter, as well as the relevant dose metrics, are presented.

## 2.1 Anatomy of the human eye

This section provides an overview of the anatomy of the human eye, highlighting key aspects essential for interpreting the findings of this thesis within a medical physics and clinical context. Unless otherwise specified, the information presented is based on Ref. [15].

Vision is the primary sensory system in humans, with roughly 70 % of the sensory receptors of the body located in the eyes. Additionally, about 40 % of the cerebral cortex is dedicated to interpreting visual stimuli. Photoreceptor cells detect and encode incoming light patterns, which are then processed by the brain to construct coherent visual representation of the surrounding environment.
A schematic illustration of the anatomical structures of the eye is shown in Figure 2.1. The outermost layer of the eye is composed of dense connective tissue and divided into two main structures: the sclera and the cornea. The **sclera**, the tough, white outer covering, protects the eyeball, maintains its shape, and serves as an anchor for the external eye muscles. In contrast, the **cornea** is a transparent structure that allows light to enter the eye and plays the most significant role in refracting light for clear vision. Beneath the sclera lies the **choroid**, a highly vascularised membrane that supplies nutrients to the other layers of the eye. Together with the ciliary body and the iris, the choroid forms the uvea. The innermost layer consists of the retina and the optic nerve. The **retina** contains a neural layer composed of three types of neurons: photoreceptor cells, bipolar cells, and ganglion cells. When light reaches the photoreceptors, they transmit signals to the bipolar cells, which subsequently activate the ganglion cells. These cells generate nerve impulses, and their axons extend along the inner retinal surface, converging at the back of the eye to form the **optic nerve**, which transmits visual information to the brain. The region where the axons converge and exit the eye is known as the **optic disc**, also called the **papilla**. Since this region lacks photoreceptors, any light falling on it is not detected, which is why it is also known as the blind spot.
Positioned at the posterior pole of the retina is the **macula lutea**, the central region responsible for detailed vision. Within this area lies the **fovea**, the point of maximum visual sharpness due to its high concentration of photoreceptor cells. The transparent, biconvex

structure that dynamically changes shape to adjust focus, ensuring that light is directed accurately onto the retina, is the **lens**. The space between the lens and the retina is filled with **vitreous humor**, a gel-like substance composed of approximately 98 % water. This fluid provides structural stability to the eyeball and plays a crucial role in maintaining intraocular pressure.

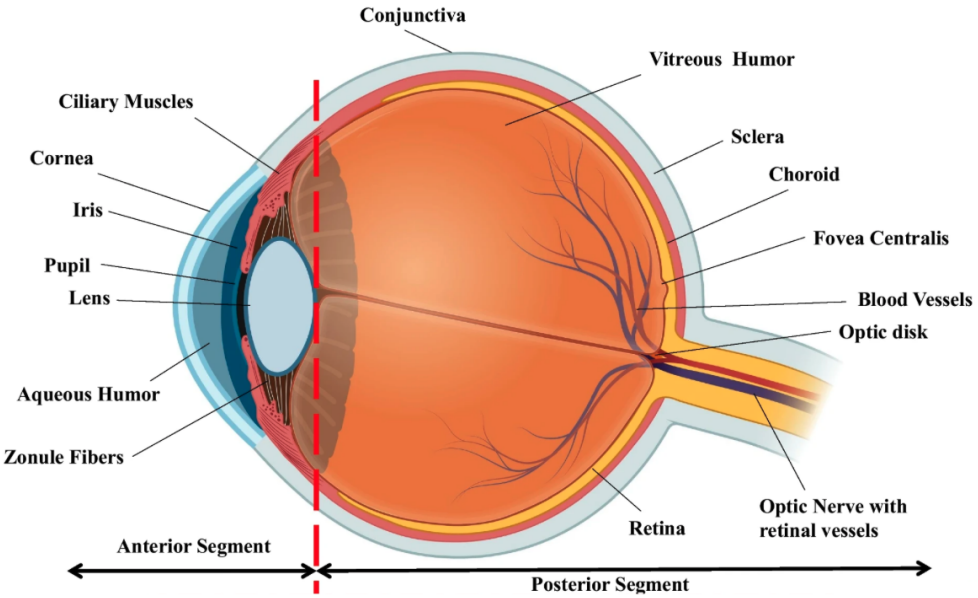


Figure 2.1: Schematic representation of the anatomy of the human eye. The figure is reproduced from Ref. [16] with permission.

## 2.2 Intraocular tumours

Intraocular tumours can be classified based on various factors, including their malignancy, incidence, age of onset, anatomical location within the eye, tissue of origin, association with systemic diseases, and whether they are primary ocular tumours or secondary metastases from other cancers [17].
The clinical presentation of intraocular tumours varies widely. Some patients experience visual disturbances such as reduced visual acuity, visual field loss, or light flashes. However, many remain asymptomatic, with the tumour being incidentally diagnosed during routine ophthalmic examinations or screenings conducted for unrelated medical conditions [17].
With approximately 8,000 new cases diagnosed annually worldwide, retinoblastoma is the most common primary intraocular tumour, typically diagnosed at an average age of 18 months. In adults, the most prevalent primary intraocular tumour is uveal melanoma, with around 7,000 new cases globally each year. Its incidence is approximately 0.6-0.7 cases per 100,000 individuals, occurring ten times more frequently in light-skinned populations than in dark-skinned populations. The typical age of onset is between 50 and 60 years [5].
If the disease progresses to a metastatic stage, the liver is affected in approximately 89 % of cases [18]. Currently, no curative treatment exists for this advanced form of the disease. Due to its clinical significance, uveal melanoma is the tumour type that is of particular relevance to this thesis.

### 2.2.1 Diagnostics

The diagnosis of uveal melanoma primarily relies on clinical evaluation using ophthalmoscopy. This technique allows for detailed visualisation of the posterior segment of the eye, facilitating the identification of intraocular tumours [19]. More than 90 % of intraocular tumours in adults can be diagnosed using this method [20]. Fundus photographs, which document the retinal appearance, are an essential component of the diagnostic process [19, 21]. Examples of such images are shown in Figure 2.2. In most cases, ophthalmoscopy provides sufficient information for diagnosis, with additional confirmatory tests required in fewer than 10 % of the cases [20].

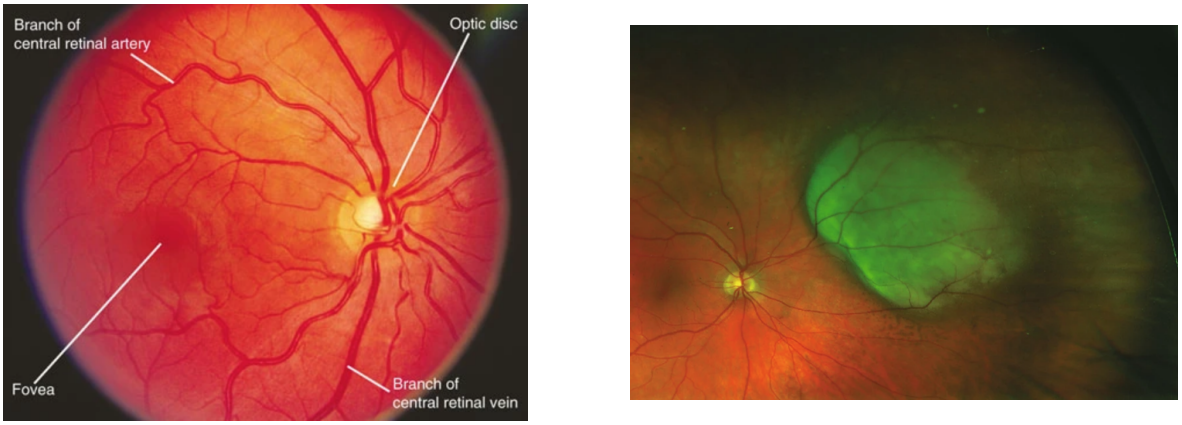


a) b)

Figure 2.2: Example of fundus photographs. In a), a fundus image of a healthy human eye is shown. The figure is reproduced with permission from Ref. [22]. In b), a fundus image showing an uveal melanoma in the choroid is displayed. The photo is used with permission from Ref. [17].

To quantify the size and location of intraocular tumours, ultrasonography is commonly used, specifically through A- and B-mode imaging [8]. An example of these images is shown in Figure 2.3. Ultrasonography is widely employed in clinical practice for diagnosing uveal melanoma due to its availability, lack of radiation exposure, and low cost [23]. While Magnetic Resonance Imaging (MRI) can also be used to measure and locate ocular tumours, it is typically reserved for rare cases where other diagnostic methods cannot provide sufficient localisation information [23, 24].
In A-mode (amplitude mode), echo amplitudes are represented as deviations from the baseline, allowing for the quantification of tissue reflectivity and the delineation of tumour boundaries based on amplitude height. In B-mode (brightness mode), the echo amplitudes are used to modulate the brightness of the screen, generating a cross-sectional echographic image. The basal diameter of the tumour can be measured from the spatial distribution of the echo signals [19, 24].
For very small tumours, repeated fundus photography and ultrasonography are used to document the initial findings and monitor tumour growth over time [19].

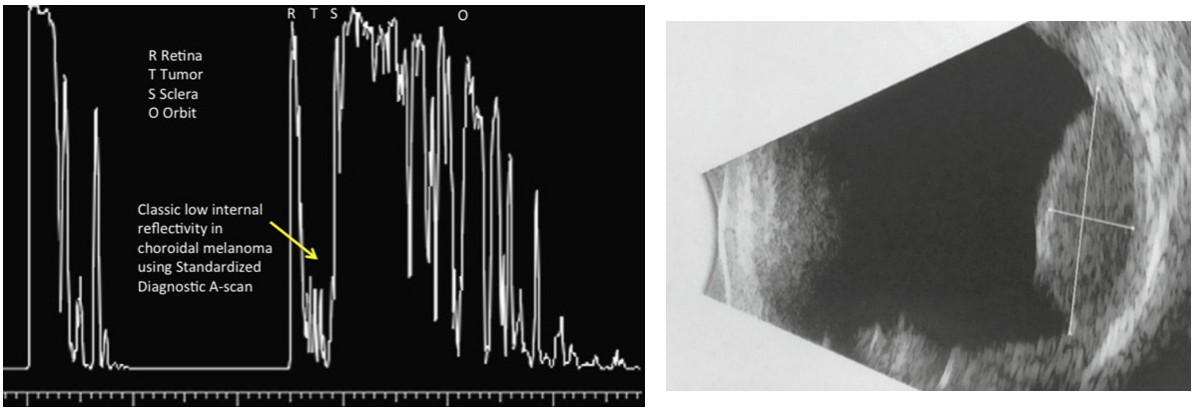


a) b)

Figure 2.3: Example for echography pictures. In a), an A-Scan echography image is shown, used to measure the apex height of the tumour. The figure is used with permission from Ref. [25]. In b), a B-Scan echography image is displayed, used to measure the longitudinal basal tumour. The photo is reproduced with permission from Ref. [26].

### 2.2.2 Treatment options

Historically, the primary treatment for uveal melanoma was enucleation, which involves the complete surgical removal of the eye. While this approach has become less common with the advent of eye-preserving therapies, it remains the preferred option in cases where such treatments are contraindicated or ineffective. This is particularly true for large, extensively growing tumours or those that infiltrate the optic nerve. Enucleation must be performed with great care to prevent the spread of tumour cells into the bloodstream due to surgical pressure [19, 27].
The removal of the eye results in permanent vision loss and can lead to significant social, psychological, and emotional distress [28]. However, advancements in radiation therapy have shifted treatment paradigms, with most centres now favoring radiotherapy, such as proton beam therapy or plaque brachytherapy, when tumour size permits. These approaches achieve high local tumour control rates, with more than 90 % of affected eyes being preserved [27, 29]. Despite treatment, radiation-induced damage to the retina and optic nerve frequently leads to compromised or complete loss of vision [19].
Less commonly, surgical resection techniques, such as transscleral local resection or endoresection, may be employed [27]. Endoresection is particularly considered for large posteriorly located tumors, where radiotherapy alone may lead to significant complications. In such cases, preoperative irradiation is often used to reduce the risk of intraoperative tumor cell dissemination [30].
The choice of treatment depends on various factors, including tumour size, visual acuity of the affected and contralateral eye, patient age and overall health, as well as the presence of metastatic disease [27]. Across all radiation-based treatment modalities, the primary goal is the eradication of tumour tissue. However, despite efforts to minimise collateral damage, healthy tissue and critical ocular structures may still receive high radiation doses, potentially leading to adverse effects.

The following provides an overview of the most commonly used eye-preserving treatment options for uveal melanoma.

**Local resection**

Medium-sized tumours, with a maximum basal diameter of 16 mm, can be surgically resected externally using a specialised procedure, provided they are favorably located within the eye. This approach is particularly considered when the tumour height exceeds the threshold for radiation therapy. Although transretinal resection via vitrectomy is technically feasible, it is not routinely recommended due to unresolved concerns about potential tumour dispersion [19].

**Laser therapy**

Laser therapy is an important treatment modality in ocular oncology, and it is used to manage various intraocular tumours. It can be applied as a primary treatment or as an adjuvant approach, including in the management of uveal melanoma. Different types of laser therapy are available, each with specific clinical indications. These include conventional photocoagulation, thermotherapy, and photodynamic therapy [27].

**Proton therapy**

External proton beam radiation is primarily considered for larger tumours with an apex height greater than 8 mm, where brachytherapy is less suitable due to tumour size or proximity to the optic disc [19, 28]. As protons travel through the medium, they lose energy gradually until they reach a specific point, where the radiation dose they deliver increases sharply over a short distance, reaching the Bragg peak, followed by a steep fall-off as the protons come to rest [28, 31]. This distinct peak in dose deposition, known as the Bragg peak, allows for precise tumour targeting while minimising radiation exposure to surrounding critical structures, as there is no exit dose beyond the target [28, 32].

Proton therapy is available only at a limited number of specialised centres [19]. In 2016, the Particle Therapy Cooperative Oncology Group listed twelve centres in nine countries worldwide that perform ocular proton therapy [33]. This is partly due to the high purchase costs and also because the treatment of uveal melanoma with proton therapy typically requires a dedicated "eyeline" treatment room, where radiation is delivered using a single anterior proton beam through a small aperture while the patient is in a seated position [28, 34]. However, local side effects, such as radiation retinopathy and neovascular glaucoma, can be significant and remain difficult to predict [19].

**CyberKnife**

CyberKnife is an advanced linear accelerator (LINAC) designed to perform stereotactic radiosurgery treatment (SRT) and fractionated SRT [35]. The standard radiation dose typically administered is approximately 20 Gy, which can be delivered in a single session or through multiple fractionated treatments. With a local tumour control rate of 89 % at three years, the effectiveness of CyberKnife is comparable to other radiation therapy techniques, providing additional treatment options based on the needs of the patient [36].

**Brachytherapy**

Brachytherapy is used for the treatment of uveal melanoma by attaching low-dose rate (LDR) radioactive sources or seeds to a brachytherapy plaque, which is temporarily

secured to the globe during surgery [6, 19, 37]. The steep radiation dose fall-off beyond the target area helps minimise adverse effects on adjacent ocular structures [37]. Currently, the two most commonly used isotopes are iodine-125 ($^{125}$I), a low-energy gamma emitter, and $^{106}$Ru, a high-energy beta emitter [6].
$^{125}$I is primarily used in the form of Collaborative Ocular Melanoma Study (COMS) plaques, which consist of a gold backing and a silicone carrier embedded with iodine seeds. This type of brachytherapy source is suitable for tumours with an apical height of up to 10 mm [6].
$^{106}$Ru brachytherapy is the primary focus of this work and will therefore be discussed separately and in greater detail in section 2.3.

## 2.3 Brachytherapy with $^{106}$Ru applicators

$^{106}$Ru applicators are a well-established standard for brachytherapy in the treatment of uveal melanoma worldwide [5]. These applicators are particularly effective for tumours with a thickness of up to 6 mm [8]. They are surgically sutured to the sclera, directly covering the tumour base.
Transillumination is utilised to ensure precise localisation of the tumour margins. In this technique, a fibre optic light is placed 180° opposite the tumour, causing the tumour base to cast a shadow on the underlying sclera, which aids in the accurate positioning of the applicator [38].
A schematic representation of the design of the $^{106}$Ru applicator is provided in Figure 2.4a. The applicators are composed of 99.99 % silver and contain a radioactive core. This core lies on a 0.2 mm thin silver target foil, which is coated on the concave side with a gold foil of thickness $(1.2 \pm 0.6)$µm. A $^{106}$Ru layer thinner than 0.1 µm is deposited on the gold foil. This assembly is positioned between a 0.1 mm thin silver exit window and a 0.7 mm thick silver backing. The backing serves as a radiation shield, absorbing approximately 95 % of beta radiation, thereby minimising exposure to extra-ocular structures in the orbit [39–41].
The manufacturer EZAG[3] offers 13 different $^{106}$Ru applicator models to accommodate various tumour sizes and locations [39]. The different types are illustrated in Figure 2.4c. Except for the COB and COC models, the active surfaces of these applicators are bordered by an inactive edge measuring 0.75 mm in width. For the COB and COC applicators, this inactive margin increases to 1.0 mm [42]. The applicators are curved and equipped with suture holes for fixation to the sclera. Some models feature a notch, allowing closer placement near the optic nerve to ensure optimal irradiation of tumours in this region. This thesis focuses on the CCA, CCB, and COB applicators due to their frequent clinical use, the availability of patient data, and, in the case of the COB, the opportunity it provides to investigate dose distributions in areas near the optic nerve.
$^{106}$Ru is a beta-emitting isotope with a half-life of 371.5 d, decaying into rhodium-106 ($^{106}$Rh) and producing electrons with a maximum energy of 39.4 keV. However, these low-energy electrons are absorbed within the exit window of the applicator and do not contribute to therapy. The clinically relevant radiation originates from the decay of $^{106}$Rh, which emits electrons with a maximum energy of 3.5 MeV and has a half-life of 30.1 s. During this decay, an excited state of palladium-106 ($^{106}$Pd) is produced in approximately 20 % of the decays, leading to the emission of photons, primarily with energies of 512 keV and 622 keV [41, 43].

[3] Eckert & Ziegler Medical, Berlin, Germany

A major advantage of $^{106}$Ru brachytherapy is its steep dose fall-off, which allows for a high radiation dose within the target volume while effectively sparing adjacent healthy tissues [5]. A schematic representation of the typical dose distribution is illustrated in Figure 2.4b.

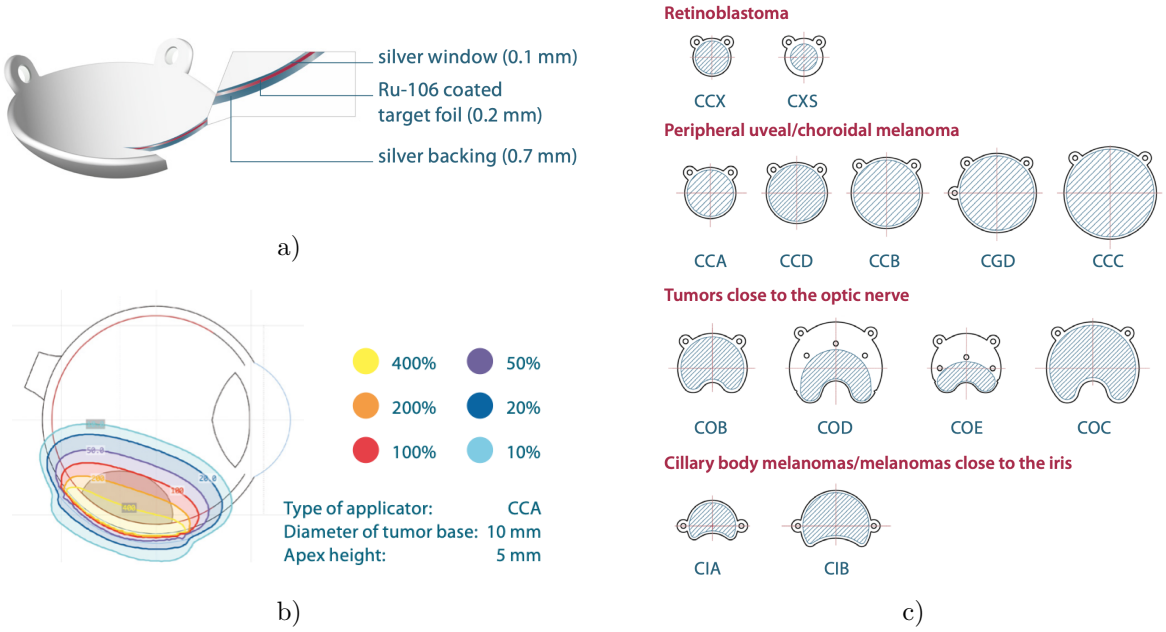


Figure 2.4: The schematic structure of the $^{106}$Ru applicator is shown in a). The typical dose profile of the $^{106}$Ru applicator, using a CCA model for a tumour with an apex height of 5 mm and a base diameter of 10 mm, is illustrated in b). The different applicator models offered by the manufacturer are presented in c). All figures are used with permission from Ref. [39].

### 2.3.1 Inhomogeneous surface dose distribution

The surface dose distribution of $^{106}$Ru eye applicators is not homogeneous due to the manufacturing process. Two main factors can contribute to this effect: the galvanic coating of the active material and the subsequent deep drawing of the applicator.
The active ruthenium is deposited on the target surface by an electroplating process. In order to achieve a uniform coating thickness, a highly homogeneous electric field is required during electrolysis. However, in practice, this field is disturbed by minor surface roughness or edge effects on the target material, despite several cleaning and pre-treatment steps. After coating, the ruthenium-covered target is placed between the silver backing and the silver window (Figure 2.4a), which are soldered together, initially forming a flat applicator. The applicator is then shaped into its final hemispherical form through deep drawing. During this mechanical deformation, all three layers undergo material compression and stretching. Consequently, areas that are subjected to compression may have a slightly increased activity density, while areas that are stretched may have a slightly decreased activity density [44].
As a result, so-called hot and cold spots can occur, where the dose may deviate by up to 20 % from the central dose within a $2\sigma$ confidence interval, according to the manufacturer.

Since April 2019, changes in the measurement process of the manufacturer have led to a reduction in uncertainty to 11 % [9].
Each $^{106}$Ru applicator is supplied with a certificate that includes a measured depth-dose rate profile and surface dose rate distribution. These measurements are conducted in a water phantom using a scintillation detector with a diameter of 1 mm and a height of 0.5 mm [45]. An example of the measurement protocol results is shown in the certificate in Figure 2.5. The depth-dose profile along the central axis, representing the beta radiation component within the first 10 mm, is described by a fit function $y = \exp(P_1 + P_2 \cdot x + P_3 \cdot x^2 + P_4 \cdot x^3)$ with relative data normalised to a reference point located at the central axis at a distance of 2 mm from the surface of the plaque [45].

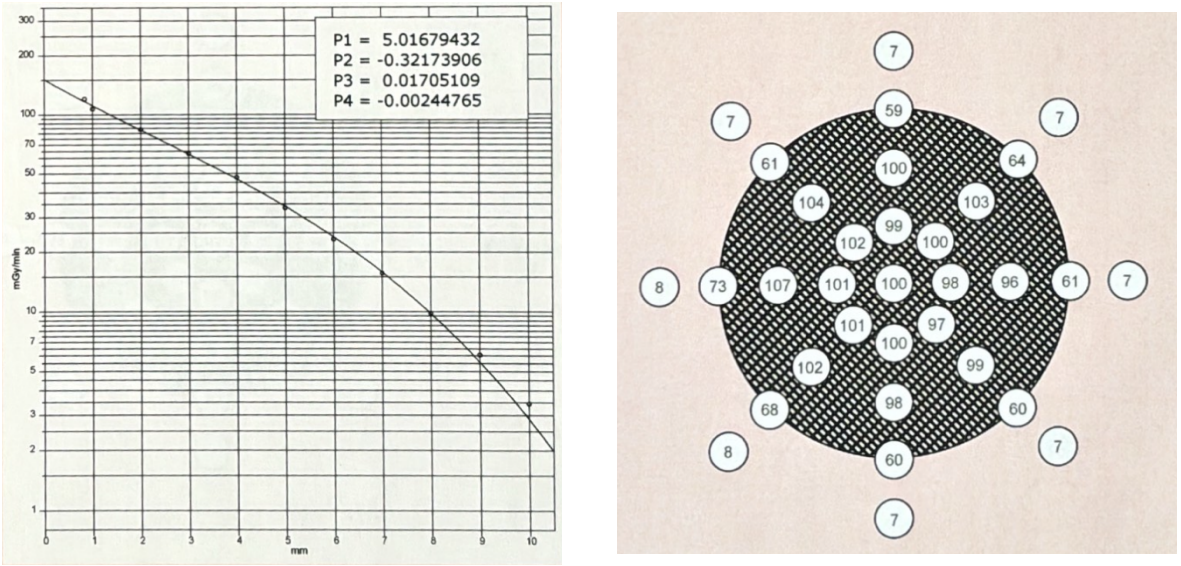


a) b)

Figure 2.5: The results provided with each applicator, obtained from measurements performed in water, are shown. In a), the depth-dose curves reproduced from eleven measurement points are displayed, while b) shows the measured surface dose distribution at a distance of 1 mm from the surface of the applicator. Both figures are reproduced with permission from Ref. [45].

For surface dose measurements, 33 points are evaluated on a concentric sphere located 1.0 mm above the inner surface of the plaque. The relative data, expressed in %, are normalised to the central point at the plaque centre. In Figure 2.5b the normalised relative values are illustrated. The measurement points are distributed across four concentric circles: the two inner circles are positioned at the edge of the active region of the target foil of the plaque, the third circle at the outer boundary of the active region, and the fourth circle outside the plaque surface [45].
Currently, no commercial devices are available for measuring the surface dose rate distribution of $^{106}$Ru applicators. In Refs. [46, 47], a specialised apparatus was developed for this purpose. The results demonstrated that inhomogeneities, particularly at the edges of the eye plaques, can cause lateral shifts in the isodose lines. Additionally, these inhomogeneities can influence the gradient characteristics of the depth-dose curves.

### 2.3.2 Dose concept at University Hospital Essen

The University Hospital Essen (UME[4]) is recognised as one of the largest centres globally for the treatment of ocular tumours. In 2022, the hospital conducted 328 brachytherapy treatments [7].
Unlike many other forms of radiation therapy, there is no universally standardised dose prescription when using $^{106}$Ru applicators. At UME, the treatment protocols are guided by dosage recommendations from the American Brachytherapy Society [48], as well as the clinical experience of the hospital. Additionally, safety margins are incorporated into the plan. The irradiation time for ruthenium plaques is calibrated to ensure that the tumour apex receives a dose of 130 Gy, while the scleral contact dose is set to at least 700 Gy. The scleral contact dose is defined as the radiation dose at a distance of 0.5 mm from the applicator surface, accounting for the thickness of the sclera [49]. The maximum tolerable dose for the sclera is 1500 Gy [40]. For highly prominent tumours exceeding 5 mm in height, the apex dose may be reduced to 100 Gy, in order to remain within the scleral tolerance limits [50]. This dosage strategy accounts for statistical uncertainties in the therapy, ensuring that over 95 % of patients receive a control dose of $(85 \pm 15)$ Gy throughout the entire tumour volume [49].
The choice of $^{106}$Ru applicator type primarily depends on tumour size, with specific applicators being selected for tumours near the optic nerve. However, due to economic constraints, clinics may have access to only a limited selection of applicator models, which can result in using models that exceed the optimal size for the target area. Larger applicators are preferred for tumours with a small base but a large apex height, due to their depth-dose curve. This can result in the irradiation of larger areas of the eye that may not be affected by the tumour [9].
Typically, medical physicists determine the application time based on various factors, such as tumour size, the activity of the selected applicator type, and the relevant depth-dose curve. Many institutions, such as the UME, use custom-developed software that is often built on platforms like MS Excel[5] for treatment planning [9]. The importance of a modern image-guided approach is a frequent topic of discussion in literature [38].

### 2.3.3 Treatment uncertainties

Brachytherapy using $^{106}$Ru applicators is subject to various uncertainties. These uncertainties arise in the treatment process itself and in the areas of dosimetry and therapy planning, and they can lead to localised underdosing of tumour tissue or excessive radiation exposure to structures at risk.
One key source of uncertainty in treatment planning is the determination of tumour height. The axial resolution of ultrasound, which depends on frequency, typically ranges from 0.1 mm to 0.2 mm. However, incorrect assumptions about the speed of sound in tumour tissue can introduce deviations in height measurements of up to 1 mm [51]. Additionally, intraobserver variability contributes to measurement discrepancies, with standard deviations reported at $\pm 0.18$ mm [52] to $\pm 0.24$ mm [53] for tumour height assessed via A-scan ultrasonography.
Beyond the uncertainties inherent to ultrasound imaging, variations in scleral thickness must also be considered. The sclera is not routinely measured by ultrasound, and its thickness can differ significantly even at the same anatomical locations across different individuals [24,

[4] University Medicine Essen, Essen, Germany
[5] Microsoft® Excel®.

54]. Observed scleral thicknesses in the posterior segment of the eye vary from 0.05 mm to 1.52 mm [54]. In regions beneath the extraocular muscles, the sclera may be thinner and subject to mechanical stretching during plaque placement, potentially influencing the effective dose distribution.
Another major source of uncertainty arises from the surgical placement of the applicator, which depends on the expertise of the surgeon and the location of the tumour [9, 24]. No published studies have specifically quantified positional uncertainties for $^{106}$Ru applicators. However, a study with COMS plaques analysed placement accuracy by verifying the position of the plaque through an additional ultrasound scan [55]. The resulting positional deviations followed a normal distribution, with a standard deviation of 1.35 mm used to estimate positional uncertainty [24]. Furthermore, intraoperative bleeding and other physical changes can lead to tilting of the applicator, potentially resulting in suboptimal tumour coverage [56].
As further described in 2.3.1, the manufacturer initially reported an uncertainty of 20 % for a 95 % confidence interval in the calibration certificates of $^{106}$Ru applicators [42]. More recent certificates indicate a significantly reduced uncertainty of 11 % [9].

### 2.3.4 Complications and side effects

In specialised centres with extensive experience, the likelihood of preserving the eye after treatment ranges from 80 % to 95 % [5, 40, 57, 58]. Acute side effects that may arise from therapy include intraocular bleeding, irritation, and retinal detachment. Over time, delayed complications can occur, such as cataract formation, which is generally manageable, as well as radiation-induced damage to the retina or optic nerve, leading to a decline in visual acuity. In particular, if the fovea is affected by radiation damage, the patient's vision in the treated eye can be significantly impaired. Less common long-term complications include secondary glaucoma, dry eye syndrome, and scleral necrosis [57]. These side effects primarily result from radiation doses exceeding the tolerance limits of healthy tissues. Another challenge is inadequate tumour control, often due to unintended underdosing in parts of the tumour. Such underdosing can occur if tumour dimensions are inaccurately determined, the applicator is not correctly positioned relative to the target volume, or the fixation of the applicator on the eye is insufficient, as described in subsection 2.3.3. In cases where tumour control is inadequate, additional treatments or secondary enucleation may be necessary [59, 60].

## 2.4 Particle interactions with matter

In radiation therapy, ionising radiation is classified as either directly ionising or indirectly ionising, depending on its mode of energy deposition. Directly ionising radiation consists of charged particles, such as electrons or protons, that transfer energy to matter through direct Coulomb interactions with atomic electrons. In contrast, indirectly ionising radiation includes neutral particles, such as photons or neutrons, which first release charged particles that subsequently interact with matter.

The following sections elaborate on the interactions of electrons and photons with matter, as they are most relevant to $^{106}$Ru eye applicators. The information presented in this chapter is based on Ref. [61].

### 2.4.1 Electron interactions

As a charged particle, such as an electron, moves through matter, the Coulomb electric field of the particle interacts with the orbital electrons and the nuclei of the surrounding atoms. These interactions lead to two types of energy loss mechanisms. The first type is collisional losses, which occur due to interactions with orbital electrons and are described by the collision stopping power $S_{\text{col}}$. The second type is radiative losses, which arise from interactions with the nuclei that produce bremsstrahlung radiation and are described by the radiation stopping power $S_{\text{rad}}$.
For a charged particle traveling through an absorber, the total stopping power $S_{\text{tot}}$ is described by:

$$S_{\text{tot}} = S_{\text{col}} + S_{\text{rad}}.$$

**Collision stopping power**

Collision stopping power arises from the Coulomb interactions between a charged particle and the orbital electrons of the absorber material. These interactions result in the transfer of energy from the moving particle to the electrons, primarily through impact excitation and ionisation of the absorber atoms. Collisions with orbital electrons can lead to substantial energy transfers, reaching up to 50 % of the incident energy for electrons. In addition, these interactions may cause elastic and inelastic scattering, often resulting in significant angular deviations. The expression for the mass collision stopping power of electrons is given by:

$$S_{\text{col}} = 2\pi r_{\text{e}}^2 \frac{Z}{A} N_{\text{A}} \frac{m_{\text{e}} c^2}{\beta^2} \left\{ \ln\left(\frac{E_{\text{K}}^2}{I^2}\right) + \ln\left(1 + \frac{\tau}{2}\right) + F^-(\tau) - \delta \right\},$$

where $r_{\text{e}}$ is the classical electron radius, $Z$ is the atomic number, $A$ is the mass number, $N_{\text{A}}$ is Avogadro's number, and $m_{\text{e}}$ is the mass of the electron. The speed of light is denoted by $c$, and $\beta$ is the electron velocity normalised to the speed of light. $E_{\text{K}}$ represents the kinetic energy of the electron, and $I$ is the mean excitation potential of the absorbing material. The term $\tau$ is the ratio of the kinetic energy to the rest mass energy of the electron, given by $\tau = E_{\text{K}}/m_e c^2$. The function $F^-(\tau)$ accounts for relativistic effects and is expressed as:

$$F^-(\tau) = (1 - \beta^2)\left(1 + \frac{\tau^2}{8} - (2\tau + 1)\ln(2)\right).$$

**Radiation stopping power**

Radiation stopping power results from the Coulomb interactions between charged particles and the nuclei of an absorber, a process commonly referred to as bremsstrahlung interactions. Whenever a charged particle undergoes acceleration or deceleration, a fraction of its kinetic energy is emitted in the form of bremsstrahlung photons. The cross-section for bremsstrahlung emission $\sigma_{\text{rad}}$ retains the same mathematical form in classical and quantum theories and follows the proportionality:

$$\sigma_{\text{rad}} \propto \alpha r_{\text{e}}^2 Z^2,$$

where $\alpha$ represents the fine structure constant, $r_e$ is the classical electron radius, and $Z$ denotes the atomic number of the absorber material.

The rate of bremsstrahlung production by light charged particles, such as electrons, traveling through an absorber is typically described by the mass radiation stopping power, $S_{\mathrm{rad}}$, and given by:

$$S_{\mathrm{rad}} = \alpha r_{\mathrm{e}}^2 Z^2 N_{\mathrm{a}} E_{\mathrm{i}} B_{\mathrm{rad}},$$

where $N_{\mathrm{a}}$ is the atomic density and $E_{\mathrm{i}}$ is the initial total energy of the charged particle. $B_{\mathrm{rad}}$ is a slowly varying function of $Z$ and $E_{\mathrm{i}}$ and is given by $B_{\mathrm{rad}} = \sigma_{\mathrm{rad}}/(\alpha r_{\mathrm{e}}^2 Z^2)$.

### 2.4.2 Photon interactions

In photon-matter interactions, the behaviour of photons is determined by their energy and the properties of the absorbing material. This subsection provides an overview of the photoelectric effect, Compton scattering, and pair production. These processes occur at distinct energy thresholds and together contribute to the attenuation of photon beams as they pass through matter.

#### Photoelectric effect

The photoelectric effect occurs when a photon transfers its energy to a tightly bound electron within an absorber atom, resulting in the ejection of the electron, referred to as a photoelectron. Since this interaction occurs at the atomic level, the photon must have enough energy to overcome the binding energy $E_{\mathrm{B}}$ of the electron. This process is particularly significant at lower photon energies and is the predominant mode of interaction in water for photon energies below approximately 20 keV.

The probability of photoelectric absorption per unit mass is described by the mass photoelectric attenuation coefficient $\tau_{\mathrm{m}} = \tau/\rho$, where $\tau$ represents the linear photoelectric attenuation coefficient and $\rho$ is the mass density of the absorber material. This coefficient depends on the atomic number $Z$ and the photon energy $E_\gamma$, and follows the relation:

$$\tau_{\mathrm{m}} \propto \frac{Z^n}{E_\gamma^3}$$

where the exponent $n$ depends on the atomic number $Z$, with $n \approx 4$ for low-$Z$ elements and $n \approx 3$ for high-$Z$ elements.

#### Compton scattering

Compton scattering, or the Compton effect, describes the interaction between a photon with energy $E_\gamma$ and a free electron. A free electron is an electron whose binding energy $E_{\mathrm{B}}$ is negligible compared to the incident photon energy. In a Compton interaction, the photon is scattered, transferring part of its energy to the electron, which is referred to as the Compton electron. The sum of the scattered photon energy $E'_\gamma$ and the kinetic energy of the Compton electron $E_{\mathrm{K}}$ is equal to the energy of the incident photon, $E_\gamma$. The energy distribution between the scattered photon and the Compton electron depends on the initial photon energy and the scattering angle $\theta$. The probability of Compton scattering per unit mass is described by the mass Compton attenuation coefficient $\sigma_{\mathrm{C,m}} = \sigma_{\mathrm{c}}/\rho$, where $\sigma_{\mathrm{c}}$ represents the linear Compton attenuation coefficient and $\rho$ is the mass density of the absorber. This coefficient follows the relation:

$$\sigma_{\mathrm{C,m}} \propto E_\gamma^{-1}.$$

In water and biological tissue, Compton scattering is the dominant photon interaction mechanism over a broad photon energy range, from approximately 20 keV to 20 MeV.

**Pair production**

Pair production occurs when a high-energy photon interacts with the Coulomb field of a nucleus or an orbital electron, resulting in the complete annihilation of the photon and the creation of an electron-positron pair. This process exemplifies mass-energy equivalence.

When pair production takes place in the field of a nucleus, it is referred to as nuclear pair production and has a threshold energy of 1.022 MeV, equivalent to twice the electron rest mass energy ($2m_e c^2$). A less probable variant, known as electronic pair production or triplet production, occurs in the Coulomb field of an orbital electron. This process requires a minimum photon energy of 2.044 MeV($4m_e c^2$) and results in the emission of three charged particles: the original electron and the electron-positron pair created in the interaction. In practice, contributions from nuclear and electronic pair production are typically combined and referred to collectively as pair production. The probability of pair production per unit mass is characterised by the mass pair production coefficient $\kappa_m = \kappa/\rho$, where $\kappa$ is the linear pair production coefficient and $\rho$ is the mass density of the material. This coefficient depends on the atomic number $Z$ and the photon energy $E_\gamma$ as follows:

$$\kappa_m \propto Z \cdot \log(E_\gamma), \quad \text{for} \quad E_\gamma > 1.022\,\text{MeV}.$$

## 2.5 Dose metrics

In radiation therapy, accurately assessing and analysing dose distribution is crucial for effective treatment planning and evaluation. This section introduces key dose metrics that play a significant role in the methodologies and analyses presented in this thesis.

### 2.5.1 Absorbed dose

All radiation effects on the human body ultimately result from the absorption of radiation energy within tissue. The fundamental physical quantity describing this process is the absorbed dose $D$, which represents the mean energy $\mathrm{d}\overline{E}_{ab}$ deposited by ionising radiation in a mass element $\mathrm{d}m$ within a volume $\mathrm{d}V$ of density $\rho$:

$$D = \frac{\mathrm{d}\overline{E}_{ab}}{\mathrm{d}m} = \frac{1}{\rho} \cdot \frac{\mathrm{d}\overline{E}_{ab}}{\mathrm{d}V}, \qquad [D] = \frac{\mathrm{J}}{\mathrm{kg}} = \mathrm{Gy}.$$

The energy absorption is primarily induced by secondary electrons produced during interactions with matter. The energy required to free these electrons from atoms varies depending on the atomic composition, meaning that the absorbed dose differs across materials even for the same radiation intensity or number of ionisation events [61, 62].

### 2.5.2 Depth-dose curves

Depth-dose curves are graphical representations that illustrate how the radiation dose varies with depth along the central axis within a medium, typically water or human tissue, which serves as a standard reference. These curves are essential for understanding dose distribution

in radiation therapy and are influenced by several factors, including field size, source-to-surface distance (SSD), radiation type, and energy [63]. An example for a depth-dose curve of a $^{106}$Ru applicator is shown in Figure 2.5a.
As the field size increases, the amount of scattered radiation within the irradiated volume also rises, leading to a higher surface dose and a more gradual decline in dose with depth. Similarly, extending the SSD flattens the depth-dose curve due to the inverse square law, which states that the dose decreases proportionally to the square of the distance from the radiation source. The type and energy of the radiation beam also significantly impact the shape of the depth-dose curve, with higher energy beams penetrating deeper and exhibiting a more gradual dose fall-off [63].
In clinical practice, depth-dose curves are essential for treatment planning and for verifying the accuracy of dose distributions by comparing measured and calculated values as part of regular quality assurance checks for radiation therapy planning systems [63].

### 2.5.3 Dose-volume histograms

A Dose-Volume Histogram (DVH) is an essential tool in radiotherapy treatment planning that provides a summary of the radiation dose distribution within target volumes and surrounding healthy tissues. It displays a cumulative dose-volume frequency distribution, making it easier to interpret the complex 3D dose data generated during treatment planning [64]. By simplifying this information, DVHs allow for a straightforward comparison of different treatment plans and support informed decision-making. An example for a cumulative DVH is shown in Figure 2.6.

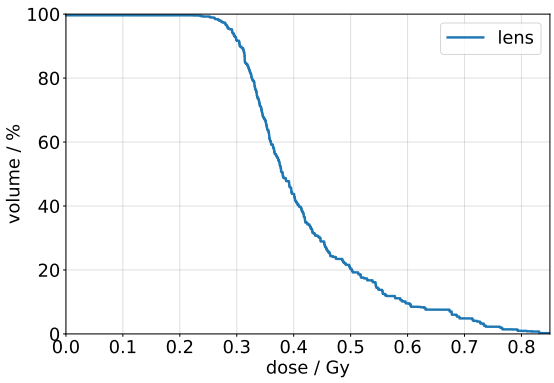


Figure 2.6: Example of a cumulative dose-volume histogram for the lens structure.

One of the key benefits of DVHs is their ability to assess dose uniformity within the planning target volume and to detect hot spots in nearby healthy tissues. This capability helps to ensure that the target receives an adequate and consistent dose while minimising radiation exposure to critical structures [64]. However, a notable limitation of DVHs is the loss of spatial information, which means they should be used alongside other evaluation methods rather than as the sole criterion for assessing treatment plans.

# 3 Simulation workflow for homogenous applicator treatment

In radiation therapy, precise dose calculation is fundamental, especially in cases involving complex anatomical structures and challenging clinical conditions. Monte Carlo (MC) simulations are widely recognised in medical physics for their high accuracy and ability to model particle interactions within diverse settings [65]. A common method for integrating patient-specific geometries into MC simulations involves utilising medical imaging data, typically stored in Digital Imaging and Communications in Medicine (DICOM) format. However, in the context of $^{106}$Ru brachytherapy, conventional imaging techniques such as MRI and Computed Tomography (CT) are rarely used in clinical practice [24, 66].
Consequently, a simulation workflow was developed as part of the work presented in Ref. [9]. This workflow enables retrospective, patient-specific treatment analysis by incorporating patient data derived from fundus photography and ultrasound imaging. By integrating the patient data into a generic Computer-Aided Design (CAD) eye model, this workflow facilitates the simulation of $^{106}$Ru brachytherapy with a homogeneous dose distribution, without accounting for the dose inhomogeneities discussed in subsection 2.3.1. However, the methods employed for simulation pose challenges in terms of computational effort, efficiency, and simulation time. Addressing these limitations is essential, as the generated simulation data serve as the foundation for the development of neural networks for dose prediction, which is a core aspect of this work and is further detailed in chapter 6.

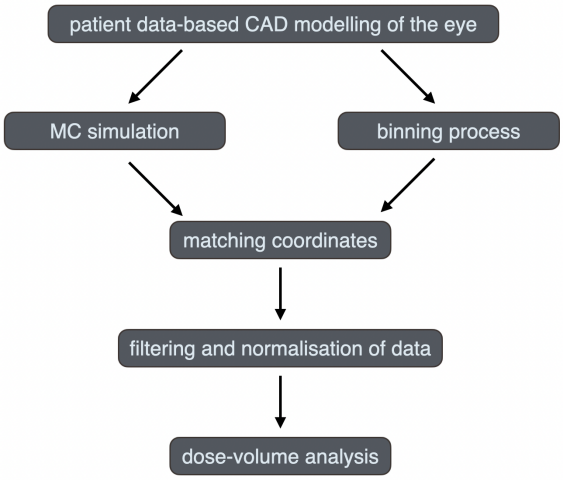


Figure 3.1: Overview of the workflow for generating and processing simulation data for modelling treatment with $^{106}$Ru applicators. The figure is taken from Ref. [67] and has been adapted for the present work.

To overcome these challenges, parts of the existing software workflow have been redesigned and replaced with newly developed methods to enhance efficiency and computational feasibility. The modified workflow introduces particle tracking techniques and a flexible postprocessing framework that decouples simulation from the spatial resolution of the acquired data. Additionally, it enables 3D dose calculation and visualisation within individual anatomical structures. As part of this work, the workflow has been published in Ref. [67].

A schematic overview of the new workflow is presented in Figure 3.1, with each step described in detail in section 3.1 to section 3.6. Subsequently, differences from the previous workflow are discussed in section 3.7, providing context for the presentation of results in section 3.8, where validation and efficiency improvements are analysed. Finally, the findings are evaluated in section 3.9, placing them within the broader scope of this thesis.

## 3.1 Patient data preparation

The patient data required for simulating $^{106}$Ru treatment is obtained using a clinical software tool developed as part of the work presented in Ref. [9]. This software is implemented in MS Excel using VBA[6] and utilises patient data obtained from fundus photographs to model the tumour and surrounding anatomical structures.
The process begins with the contouring of key landmarks, including the papilla, fovea, and tumour, on the fundus images. Following this, the $^{106}$Ru applicator is positioned within the software based on the radiation scar visible in post-treatment fundus photographs, enabling an accurate reconstruction of the original treatment scenario.
To determine the 3D coordinates of the contoured structures, the software employs an azimuthal equidistant projection. This approach allows for the transformation of two-dimensional fundus images into a 3D coordinate system, ensuring precise spatial localisation of the tumour, macula, and papilla relative to the applicator.
The final output of the software, which is essential for the subsequent steps in the workflow, includes the reconstructed tumour contour along with the calculated positions of the papilla and the fovea. Additionally, the coordinates of the center of the convex surface of the $^{106}$Ru applicator are determined.
Further details on the methodology and implementation can be found in Ref. [9].

## 3.2 Model of the human eye

To evaluate dose distributions within individual ocular structures during brachytherapy, a generic eye model was developed in Ref. [68] using Fusion[7], a CAD modelling software that supports automation through scripts and applications written in C++ or Python. The Fusion API enables users to develop custom add-ins, automate repetitive tasks, and extend the functionality of the software [69].
In this work, the eye model comprises ten key anatomical structures: the sclera, choroid, retina, cornea, lens, papilla, fovea, optic nerve, aqueous humour, and vitreous humour. These structures are designed based on anatomical approximations and include their respective

[6] Microsoft® Visual Basic® for Applications.
[7] Autodesk® Fusion®. `https://www.autodesk.com/de/products/fusion-360/`.

chemical compositions. An illustration of the eye model is shown in Figure 3.2.
In Ref. [68], the papilla consists of three distinct structures. Each of these was extracted from one of the three ocular layers, the sclera, choroid, and retina, and approximated using the respective material, as no specific values for its chemical composition are found in the literature. In this work, these three structures are merged into a single papilla structure and approximated using the chemical composition of the optic nerve. Furthermore, in Ref. [68], the posterior pole region comprises the perifovea, parafovea, and fovea. These three structures are also combined into a single fovea structure. Further details regarding the model's dimensions, structure, and composition can be found in Ref. [68].
This model serves as the foundation for integrating patient-specific eye representations within the workflow presented in this thesis.

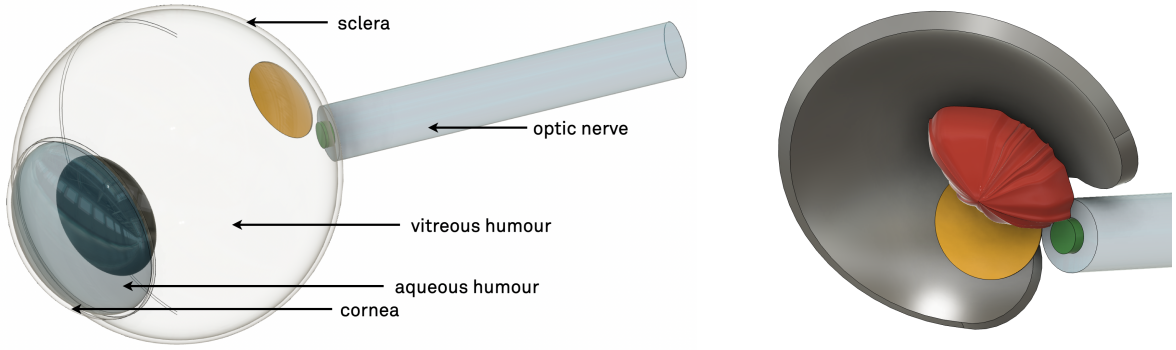


a) b)

Figure 3.2: Illustration of the eye model, with the fovea depicted in yellow, the papilla in green, and the lens in black. In a), the eye model is shown without any patient-specific data implemented. For clarity, the choroid and retina are not depicted. In b), an example of the posterior pole of the eye model with an implemented patient dataset is shown. The tumour is highlighted in red, and a COB applicator is shown in silver.

**Patient data implementation** The output generated by the software described in section 3.1 is integrated into the generic eye model to create a patient-specific eye representation for treatment simulation.
The tumour shape reconstruction relies on fundus photography contours and measured height, as MRI data is rarely available. To refine inconsistencies in delineation, the tumour contour is smoothed, and its centroid is calculated to define the central axis, assuming growth toward the centre of the eye. The apex is positioned along this axis at a distance equal to the tumour height. Within Fusion, an interpolation is performed between the contour and apex to generate the surface. A secondary contour, scaled and projected midway between base and apex, enhances reconstruction accuracy [9]. This secondary contour is projected onto a parallel plane halfway between the base and the apex, with a manually adjusted scaling factor to best match clinically observed tumour growth patterns.
During tumour construction, an issue identified in a previous work [9] is corrected. The tumour contour had been projected onto a spherical rather than an ellipsoidal sclera, resulting in discrepancies between the intended and reconstructed tumour heights. This discrepancy is resolved in the current study to improve model accuracy.

The script automates the placement of the $^{106}$Ru applicator, identifying its model type from the case name. Its dimensions and target volume follow the rotationally symmetrical models in Ref. [42] and the COB model from Ref. [24]. The COB applicator, unlike others, is asymmetrical due to a notch aligning with the optic nerve. Manual rotation within Fusion ensures proper positioning, though minor deviations have negligible effects on the DVH [70]. Further details on the patient data implementation are available in Ref. [9].

## 3.3 Geant4 Monte Carlo simulation

**Monte Carlo method** The MC method is a powerful numerical approach used for solving complex physical problems through statistical sampling. It is widely applied in radiation transport simulations, particularly in radiotherapy, where it provides an accurate representation of particle interactions with matter. Although its adoption in medical physics was initially slow in the late 1970s, the method has since gained widespread recognition due to its precision in modelling radiation dose distributions [71].
The MC method simulates the random behaviour of particles as they traverse a medium, interacting with atomic structures based on predefined probability distributions. These interactions, such as scattering, absorption, or energy loss, are governed by fundamental cross-section data. By tracking a sufficiently large number of particle histories, the method enables the statistical estimation of physical quantities such as absorbed dose, energy deposition, and secondary particle production [72]. Unlike deterministic models, which solve transport equations directly, MC simulations rely on stochastic sampling, meaning that different runs of the same simulation yield slightly varied results due to random number sequences. However, as the number of simulated particles increases, the statistical uncertainty decreases, leading to convergence toward an accurate solution [73].
A key advantage of the MC approach is its ability to model complex geometries and heterogeneous media without requiring simplifications that may compromise accuracy. By simulating individual particle trajectories at the microscopic level, the method inherently accounts for the intricacies of radiation transport in biological tissues. As a result, MC techniques are considered the gold standard for dose calculation in radiotherapy, particularly in cases where precise modelling of energy deposition is critical [71]. However, this accuracy comes at the cost of high computational demands, as achieving statistically acceptable results typically requires simulating millions of primary particle interactions [72].

The simulation of $^{106}$Ru eye applicator treatment is performed using the Geant4[8] software framework (Version 11.0, patch 03), a MC simulation toolkit developed by the CERN collaboration [74]. Geant4 is widely used in particle and medical physics to model particle interactions with matter, providing precise particle tracking within complex geometries while accounting for relevant physical processes.
Following the recommendations in Ref. [41], the `G4EmStandardPhysics_option4` physics list is selected for this work. The simulation setup is based on the methodologies outlined in Refs. [9, 41] and further informed by the official Geant4 example applications No. 2 and No. 3a. To balance computational feasibility with the accurate modelling of charged particle trajectories, the simulation integrates multiple scattering models derived from the theoretical

[8] Geant4, free software published and maintained by the Geant4 Collaboration. `https://geant4.web.cern.ch`.

frameworks presented in Refs. [75–77].
To enhance computational efficiency, a range cut-off is applied. Particles with a remaining range below this threshold are stopped, and their residual energy is deposited at their final position. Based on the recommendations in Ref. [41], a threshold of 0.01 mm is implemented to balance computational cost and simulation accuracy.

### 3.3.1 Geometry import

The geometric complexity of the eye model poses challenges for direct implementation in Geant4. Instead of manually constructing these irregularly shaped volumes directly in C++ within Geant4, they are imported as Standard Triangle Language or Standard Tessellation Language (STL) files using the `CADMesh` library, as outlined in Ref. [78]. This approach allows for seamless integration of 3D models created with CAD software such as Fusion. The STL format describes 3D objects by modelling their surfaces as collections of small triangular elements. In Fusion, several export settings are available that control how finely the surface is tessellated. Users may choose between low, medium, and high mesh resolutions, or define a custom setting in which the number of triangles is set manually. This allows the level of geometric detail to be adjusted while managing file size. The simulation includes ten anatomical eye structures, the patient-specific tumour, the $^{106}$Ru applicator, and a target volume. The target is a cutout from the applicator, allowing particle generation directly at the target surface.
While this method enhances geometric accuracy, it also increases computational complexity. Simulating particle transport through these intricate structures requires additional calculations to track particle trajectories and determine their locations within the model.
Within the Geant4 `G4VUserDetectorConstruction` class the material properties are assigned to each structure, based on predefined chemical compositions. The surrounding medium is set to water, and the specific material compositions of the eye structures are detailed in Ref. [68].

### 3.3.2 Primary particle generation

In this Geant4 simulation workflow, the `G4GeneralParticleSource` (GPS) method is used for particle generation, allowing for precise control over the characteristics of primary particles. This includes defining their spectral, spatial, and angular distributions. To simulate a homogeneous distribution, particles are emitted from random positions across the inner surface of the target. For this purpose, the $^{106}$Ru atoms are first distributed over the surface of a sphere whose radius corresponds to the radius of curvature of the applicator model to be simulated and which is centred at the focal point of the plaque. Particles are only considered in the simulation if they lie within the spherical boundary and the target surface. Geant4 offers a flexible approach to configuring particle sources, either through direct commands within the simulation environment or via macro files, streamlining the setup process for various simulation scenarios [79]. To ensure statistical independence, all simulations are performed with different random seeds, and the results are subsequently averaged.

### 3.3.3 Scoring methods and particle tracking

**Scoring methods** In Geant4, scoring involves the recording of physical quantities, such as energy deposition or dose distribution, within a simulated environment. For the purpose of dose scoring in this study, two main methods are employed: the Command-Based Scorer (CBS) and the Sensitive Detector (SD). Each of these techniques presents unique benefits and limitations, making them suitable for different aspects of the simulation.
The CBS provides a straightforward method for scoring various physical parameters through predefined commands. This approach employs scoring meshes confined to simple geometric shapes, such as cylinders and cuboids, within a parallel virtual world that does not interfere with particle interactions but still allows tracking [79]. In this study, a cylindrical CBS is used to obtain the depth-dose distribution of the $^{106}$Ru applicator. Positioned perpendicular to the central concave surface of the plaque, as illustrated in Figure 3.3a, the binned scorer enables spatially resolved dose measurements along the central axis. This configuration allows for dose normalisation based on depth-dose curves and established therapeutic dose values. However, a key limitation of the CBS is that the binning must be predetermined before the simulation, requiring a full rerun if modifications are needed. Furthermore, the number of CBS is limited, and their shape is restricted to basic geometries and cannot be directly assigned to specific anatomical structures in the eye model, limiting its adaptability to complex shapes.

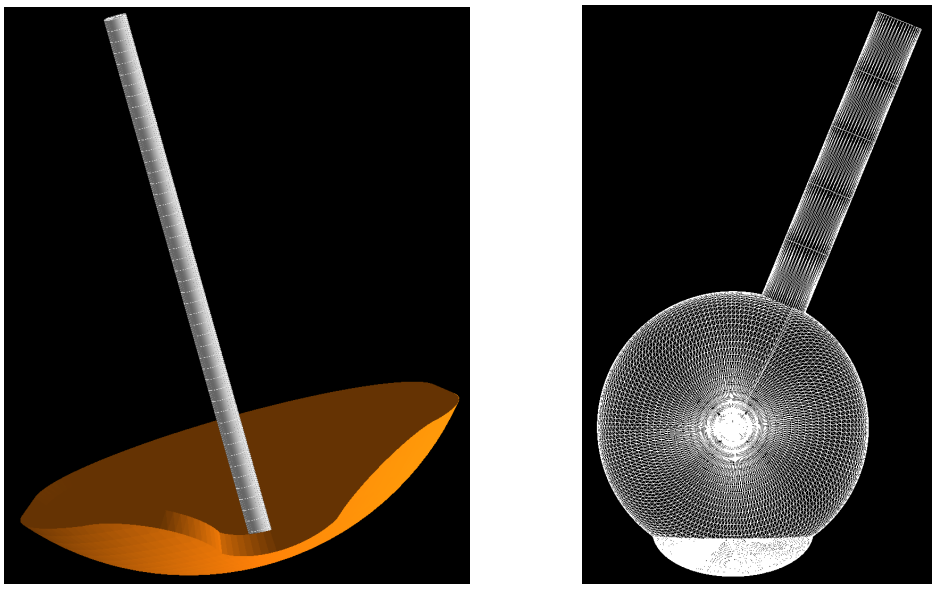

a) b)

Figure 3.3: In a), an example of the COB eye applicator, including the binned CBS, is displayed. In b), the generic eye model, implemented through STL files Geant4, is shown in mesh form.

SDs are used to record dose distributions within the intricate and irregular anatomical structures of the eye model. These detectors allow each anatomical volume in the simulation to be defined as a separate scoring entity, enabling precise tracking of dose within anatomically accurate representations. By importing 3D models of the ocular structures as STL files via

the `CADMesh` library, SDs enable the tracking of physical quantities such as energy deposition or dose in complex geometries. This method eliminates the need for explicitly defining these shapes within the C++ framework of Geant4, enhancing flexibility and accuracy when associating scored variables with specific regions of interest. The imported eye model, shown in Figure 3.3b, is represented as a mesh. Through careful construction, where the eye structures are separated in the CAD software to avoid overlap, it is not necessary to define a complex hierarchy for the imported volumes.

**Particle tracking** In the simulation, particle tracking involves monitoring the charge of each particle as it passes through a SD, recording key parameters at every step within that volume. For each particle, important properties such as position, energy deposition, particle identification, and particle type are logged into specific data vectors. These vectors are then saved into ROOT[9] files for each respective structure, creating a dataset that includes the deposited energy and the corresponding interaction position. The ROOT format, developed by a CERN collaboration for the ROOT data analysis framework [80], is used to efficiently store and manage the datasets generated in Geant4.
This method allows for flexible analysis of dose resolution, enabling the deposited energy and its associated spatial coordinates to be mapped to specific volumes after the simulation. As a result, the dose resolution can be adjusted based on spatial data, offering high precision in tracking energy deposition.

### 3.3.4 Multi-threading in Geant4

To enhance computational efficiency and reduce simulation runtime, the multi-threading capabilities of Geant4 are utilised. By distributing the computational workload across multiple Central Processing Unit (CPU) cores, this approach significantly accelerates the processing of complex physics simulations. The multi-threading framework in Geant4 employs a hybrid model that balances shared and independent data among threads to maximise performance. Within this framework, a distinction is made between the master thread and worker threads. The master thread is responsible for initialising the simulation environment, defining event structures, and managing shared resources. However, it does not actively process simulation events. Instead, worker threads execute independent instances of the simulation, handling event processing with separate data structures for particles, hits, and trajectories. To prevent resource conflicts, each worker thread operates on an independent copy of the simulation geometry and physics processes, while global parameters, such as magnetic field properties, remain shared across threads [81].
For data generation in this study, the Geant4 multi-threading architecture ensures that each thread records its output independently. Specifically, the master and worker threads write to separate ROOT files, preventing concurrent access to the same file and thereby preserving the consistency and integrity of the output data.

[9] ROOT, data analysis framework, free software published and maintained by the ROOT Team. `https://root.cern`.

## 3.4 The binning strategy

In addition to performing MC simulations of the irradiation of the eye model with the $^{106}$Ru applicator in Geant4, it is necessary to define the spatial resolution of the detector volumes. This is achieved through a binning approach implemented in Python, separate from the simulation environment. Since this process runs independently of the MC simulation, it can be executed in parallel, enhancing efficiency and flexibility. The method allows for adjustable resolution and involves the virtual division of the eye structures of interest into a structured grid of spatial units or bins. By calculating the volume overlap between each bin and the corresponding structure, a discretised representation of the volume is obtained. Once this discretisation is complete, the energy deposition coordinates recorded during the MC simulation can be mapped to the respective bins, as detailed in subsection 3.5.1.
In this work, an initial binning strategy has been developed, which is described in subsection 3.4.1. After implementation, the method has been refined and simplified using the Python library `MeshLib`[10]. With the release of version v0.1.0.0 on 29 December 2022 [82], the first compatible version for the MacOS operating system used in this study became available. Throughout 2023, the library underwent further development, enabling the integration of geometric mesh operations into the binning approach presented here. The updated method, incorporating `MeshLib`, is described in detail in subsection 3.4.2. A schematic representation of the binning strategy is shown in Figure 3.4.

### 3.4.1 Binning process with PyVista Boolean operation

The binning process begins with preparing the detector volumes, where individual structures of the eye model are imported as STL files into Python using `PyVista`[11]. This library, built on VTK[12], provides an interface to VTK via `NumPy`[13] and facilitates 3D visualisation, analysis, and manipulation of spatial datasets. It offers efficient mesh data structures and filtering methods for handling complex geometries and enables 3D plotting, even for large datasets [83].
To enable precise geometric operations, the imported meshes undergo triangulation. This step is fundamental for performing geometric calculations, such as Boolean operations, which determine spatial relationships between intersecting geometries by evaluating whether a given point lies within a defined solid [84]. Since the accuracy of these operations depends on the resolution of the mesh, an optional subdivision factor $n$ can be applied, where each triangle in the mesh is further divided into $4^n$ smaller triangles. Increasing the number of triangular elements provides more vertices for computational procedures, enhancing the precision of overlap volume calculations. However, this improvement in accuracy comes at the cost of increased computational effort.

Following the preparation of the mesh, the binning process is carried out in multiple stages:

- **Defining the bounding box and binning grid** The structure is enclosed by a bounding box, which represents the smallest rectangular volume that fully contains

[10]MeshLib SDK, open-source 3D geometry library. `https://meshlib.io`.
[11]PyVista, helper library for the Visualization Toolkit (VTK). `https://pyvista.org`.
[12]Visualization Toolkit, open source software for manipulating and displaying scientific data [4]. `https://vtk.org`.
[13]NumPy, Python library [1]. `https://numpy.org`.

the mesh. To prevent numerical instabilities and edge-related artefacts, an enlargement factor is applied, slightly enlarging the bounding box beyond the mesh boundaries. This precaution minimises computational issues in Boolean operations, which can occur when intersecting surfaces have only minimal overlap. The bounding box is then subdivided into discrete bins, where the chosen bin size directly influences the spatial resolution of the subsequent dose distribution analysis. If the dimensions of the bounding box are not an exact multiple of the bin size, they are adjusted accordingly to ensure complete coverage.

- **Bin Classification** Each bin is categorised based on its spatial relationship with the structure, falling into one of three groups: fully contained within the structure, completely outside, or intersecting its boundaries. This classification is performed using ray-casting techniques, which are implemented via the `trimesh`[14] library. Ray casting involves projecting a virtual ray in a predefined direction and detecting intersections with the mesh surface. By identifying these intersection points, the algorithm determines whether a vertice of a bin intersects the structure, allowing for precise classification.
- **Overlap volume computation** Based on the bin classification, the volume of intersection between the structure and each bin is calculated. For bins entirely contained within the structure, the overlap volume is equivalent to the full volume of the bin. Conversely, bins completely outside the structure have an overlap volume of zero. For intersecting bins, `PolyDataFilters.boolean_intersection`, a `PyVista` Boolean operation, is applied to compute the exact overlap region. The precision of these calculations is influenced by the resolution of the mesh, which is defined by the number of triangular elements representing the object. To enhance accuracy, the subdivision factor is introduced at the beginning of the process, increasing the number of vertices available for geometric computations.

A quality factor $\epsilon$ serves as an indicator for evaluating the accuracy of the binning procedure. It is computed using the following formula:

$$\epsilon = \frac{\sum_{i=0}^{n} V_{\text{bin},i} - V_{\text{total}}}{V_{\text{total}}} \cdot 100\,, \qquad [\epsilon] = \%.$$

This metric compares the total volume derived from the individual bin volumes $V_{\text{bin}}$ to the overall mesh volume $V_{\text{total}}$, which is calculated using `PyVista`. The resulting value of $\epsilon$ provides a measure of how closely the binning process approximates the true volume of the mesh.

The precision and efficiency of the binning process are influenced by several key factors:

- **Bin size** The size of the bins determines the spatial resolution. Finer bin sizes lead to higher resolution but also increase the computational workload. Additionally, smaller bins require more Boolean operations and may result in a higher number of tiny volumes, which can present challenges during these operations. This can affect the accuracy of the overlap volume calculations between the bins and the mesh.

[14] trimesh, library for importing, exporting and doing simple operations on triangular meshes. `https://trimesh.org`.

- **Enlargement factor** This factor is applied to prevent the bin edges from perfectly aligning with the mesh boundaries, minimising potential errors due to edge effects. However, depending on the binning grid setup, this can lead to very small overlap volumes between the bins and the mesh, which may reduce the precision of the Boolean operations.
- **Mesh quality and subdivision factor** The accuracy of overlap volume calculations is greatly influenced by the mesh quality and subdivision level. Meshes of higher quality and more subdivisions enhance the precision of Boolean operations, although these improvements come with a trade-off in terms of increased computational effort.

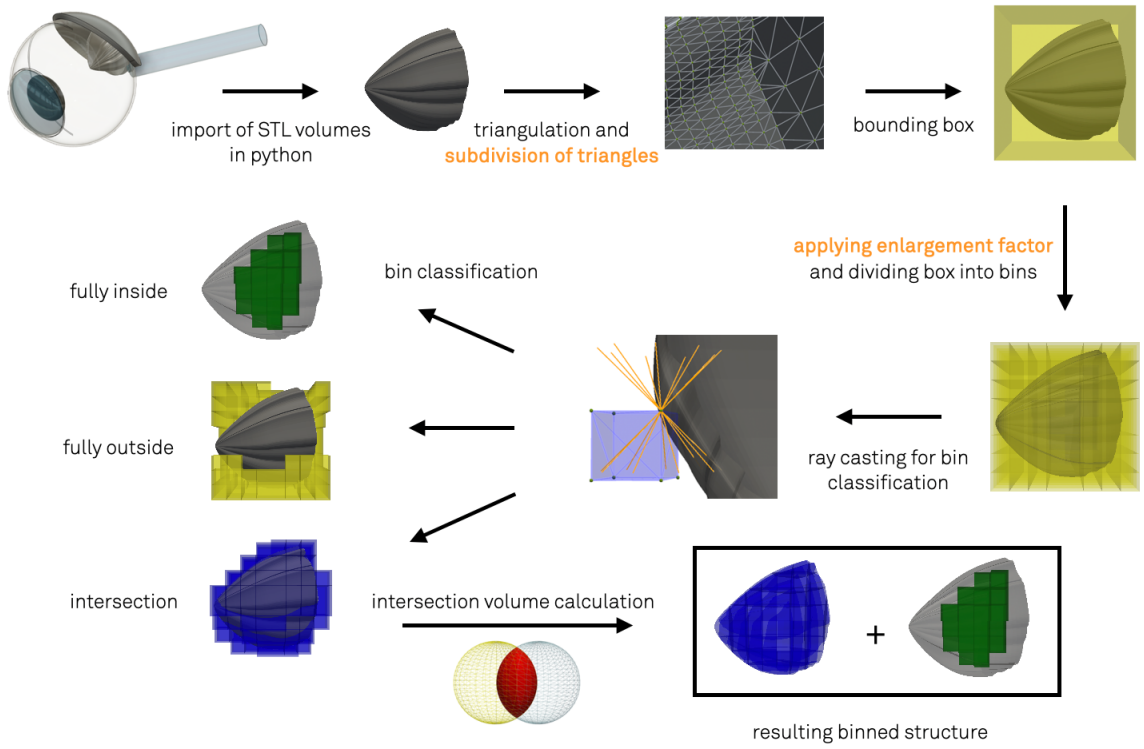


Figure 3.4: Schematic representation of the binning strategy using the example of a tumour volume as the structure of interest. The elements highlighted in orange are specific to the `PyVista`-based approach and are omitted in the version in which `MeshLib` is used for Boolean overlap calculations. The figure has already been published and is therefore taken from Ref. [67].

The effectiveness of the binning process depends on the interaction of the key parameters described. When incorporating new, complex geometries, it is important to identify the settings for these geometries that result in an acceptable volume approximation by the bins. In this work, such an analysis is performed for the structures of the eye model, and the findings are presented in subsection 3.8.3.
To enhance computational efficiency, the binning process is partially parallelised using the Python module `concurrent.futures` [85]. This module allows multiple tasks to be executed simultaneously, thereby reducing processing time and improving overall performance.

### 3.4.2 Binning process with MeshLib Boolean operation

The binning strategy described in subsection 3.4.1 is further optimised with the integration of the `MeshLib` library [86]. In this updated approach, `MeshLib` is specifically employed for calculating the overlap volumes. For bins that intersect with the structure, Boolean operations `meshlib.mrmeshpy.BooleanOperation.Intersection` [87] from the `MeshLib` library, are employed to compute the overlap volume. Compared to `PyVista`, `MeshLib` offers advanced and more accurate algorithms for performing 3D Boolean operations, providing computational efficiency and higher precision [88].
As a result of the improved robustness of the computational algorithms, the previously necessary enlargement factor for the bounding box and the subdivision factor for additional triangulation are no longer required. The quality of the binning process is no longer influenced by these factors or by the bin size. As a result, the need for analysing optimal settings for achieving acceptable volume approximations with the bins has been eliminated. The rest of the binning process remains unchanged, with `PyVista` still being used for mesh handling and `trimesh` for ray casting. Only the overlap volume calculation, which previously relied on `PyVista`, has been replaced with `MeshLib` for enhanced performance and accuracy.

## 3.5 Data postprocessing

After completing the binning process for the structures of interest within the eye model and conducting the MC simulation of treatment with the $^{106}$Ru applicator, the results from both steps are integrated. The coordinates of the deposited energy from the MC simulation are assigned to the corresponding bins of each structure. To ensure the robustness of the workflow, statistical outliers are filtered out, followed by normalisation of the dose values for clinical application.

### 3.5.1 Matching deposited energy coordinates

Following the MC simulation and binning process, which can be executed in parallel, the next step involves assigning the deposited energy to the corresponding spatial bins to generate a 3D dose distribution within the structures of interest. The coordinates of each energy deposition point are recorded during the simulation, allowing the associated energy to be assigned to the appropriate bin within the detector volume. The energy deposited in each bin is accumulated and then converted into dose values using the formula in subsection 2.5.1. The conversion is based on the overlap volume between the mesh representing the structure and the bins. The uncertainty in the simulated dose values is evaluated using the standard error of the mean.

### 3.5.2 Truncated mean filtering

Upon analysing the dataset, it has been found that the binning process could lead to small overlapping volumes, on the order of $10^{-5}$ to $10^{-6}$ of the bin volume, particularly in regions with complex geometries. These overlaps, occurring between the bins and the mesh, can cause statistical fluctuations that distort the maximum and minimum dose values within the detector. Even minute portions of the total volume may disproportionately affect the dose

distribution. A potential contributing factor to this issue is the statistical scattering of dose values assigned to these small volumes, resulting in outliers that do not accurately represent the true dose distribution within the structure.
To address this challenge and provide a more reliable estimate of the central tendency of the dose values, the truncated mean method is applied. This technique removes a specified proportion of the highest and lowest dose values, minimising the impact of outliers and yielding a more robust representation of the average dose.
Selecting the appropriate cut-off points for the truncated mean is essential. The proportion of discarded values must be carefully determined based on the characteristics of the specific structure and the simulation parameters. This threshold is established through a detailed analysis tailored to the simulation context, ensuring that the postprocessing method provides accurate and meaningful results that are not unduly influenced by extreme dose values.

### 3.5.3 Dose normalisation

In subsection 3.3.3, the application of the CBS to record the depth-dose curve of the $^{106}$Ru applicator is described. The CBS measures the dose up to a depth of 24 mm using 48 bins, resulting in a curve consisting of 48 data points. As $^{106}$Ru brachytherapy is primarily used for uveal melanomas with tumour heights of up to 6 mm [8], the depth-dose curve in this study is additionally used to estimate the necessary number of simulated particles, ensuring statistically significant values within this range. The number of required particles is chosen such that the standard error of the mean for the depth-dose curve points remains below 1 % within the first 10 mm.
However, the primary purpose of the depth-dose curve in this study is dose normalisation. The dose concept at the UME prescribes a minimum dose of 130 Gy at the tumour apex [49]. Using the depth-dose curve, the dose values generated through simulations are normalised to this value at the tumour apex for the evaluation of clinical scenarios. Within the first 10 mm, a fit function of the form

$$D(x) = \exp(a \cdot x^2 + b \cdot x + c)$$

is applied to the curve, where $D(x)$ denotes the dose at a distance $x$ from the applicator surface. This function is used to determine the normalisation value for the desired tumour height. The distance $x$ is composed of the tumour height, which is the distance from the tumour base to the tumour apex, as well as the thickness of the sclera. An example of a depth-dose curve with the fitted function is shown in Figure 3.5a.

## 3.6 Dose-volume analysis

After processing the dataset, the computed dose values are used to generate DVHs, as described in subsection 2.5.3, and to visualise the dose distribution within the volumes of interest. In Figure 3.5b, an example of a 3D visualisation of the dose distribution within a tumour treated with a COB applicator is presented. These results play a fundamental role in assessing the effectiveness of the treatment plan by providing a detailed representation of radiation exposure across different anatomical structures. Additionally, the processed data help refine treatment strategies, contributing to improved therapeutic outcomes.
Beyond the generation of DVHs and 3D dose visualisations, key dose metrics, including the

minimum, mean, and maximum applied dose, are calculated for each structure of interest. Compliance with the tumour control dose of $(85 \pm 15)$ Gy across the entire tumour volume, as well as the scleral contact dose limit of 1500 Gy, is evaluated, as these parameters provide critical insights into the likelihood of treatment-related side effects, as described in subsection 2.3.2. Furthermore, conventional radiotherapy dose constraints are also considered. According to Ref. [89], the maximum dose to the optic nerve should not exceed 55 Gy to maintain a probability of less than 3 % for radiation-induced optic neuropathy, a condition associated with insufficient blood supply to the optic nerve head. In $^{125}$I COMS brachytherapy, a macular dose of $\geq 52$ Gy is associated with a significantly higher risk of retinopathy, visual acuity loss, and blindness [90]. More recent data specific to $^{106}$Ru brachytherapy report that a maximum dose of approximately $(46.9 \pm 4.1)$ Gy to the optic nerve is associated with a 50 % probability of developing grade $\geq 1$ optic nerve neuropathy, based on individualized dose-response modeling [91]. Additionally, to prevent lens opacification, the dose deposited in the lens should remain below 5 Gy [92], although this is not considered as severe side effect.

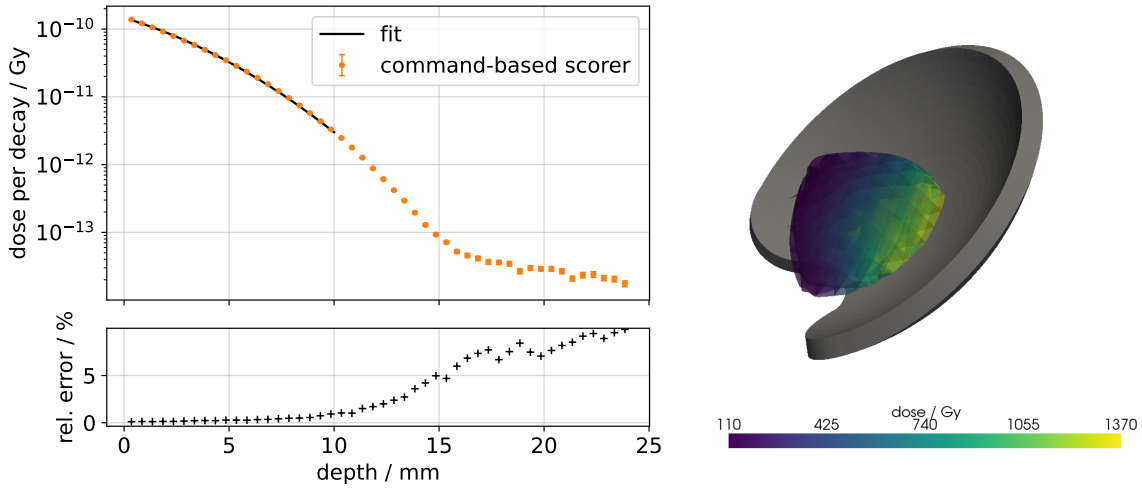


a) b)

Figure 3.5: In a), an example of a depth-dose curve obtained from the simulation of treatment with a $^{106}$Ru COB applicator is shown. The fit is described by the function $D(x) = \exp(a \cdot x^2 + b \cdot x + c)$ and is used to normalise the entire dose profile to the desired dose at the tumour apex. In b), an example of the 3D visualisation of the dose distribution within the tumour is presented, with the COB applicator shown in silver. Figure b) has already been published and is therefore taken from Ref. [67].

## 3.7 CAD volume cutting approach

In the following, the software workflow developed in this study is referred to as $\mathrm{wf}_{\mathrm{trac}}$. While it is based on the workflow introduced in Ref. [9], designated here as $\mathrm{wf}_{\mathrm{cut}}$, it employs a different approach for scoring and postprocessing. Unlike $\mathrm{wf}_{\mathrm{cut}}$, $\mathrm{wf}_{\mathrm{trac}}$ integrates the particle tracking method described in subsection 3.3.3, the binning strategy outlined in section 3.4,

and the postprocessing steps detailed in subsection 3.5.1 and subsection 3.5.2, none of which are included in $wf_{cut}$. In $wf_{cut}$, dose resolution is predetermined before the simulation by dividing the anatomical structures in the eye model into smaller sub-volumes using a cubic cutting approach. This involves calculating the overlap volume between the cube and the structure and subsequently isolating the intersecting region. Unlike conventional voxelisation, this method ensures that boundary regions are not approximated by voxels but instead retain their original shape. The resolution is determined by the edge length of the cube, which is constrained to a minimum of 1 mm due to software limitations [9]. Attempts to use smaller cube sizes result in crashes of the Fusion software. Overall, the process is computationally intensive and time-consuming. The program exhibits instability and requires extensive manual intervention. The outcome of this cutting process in Fusion is illustrated in Figure 3.6.

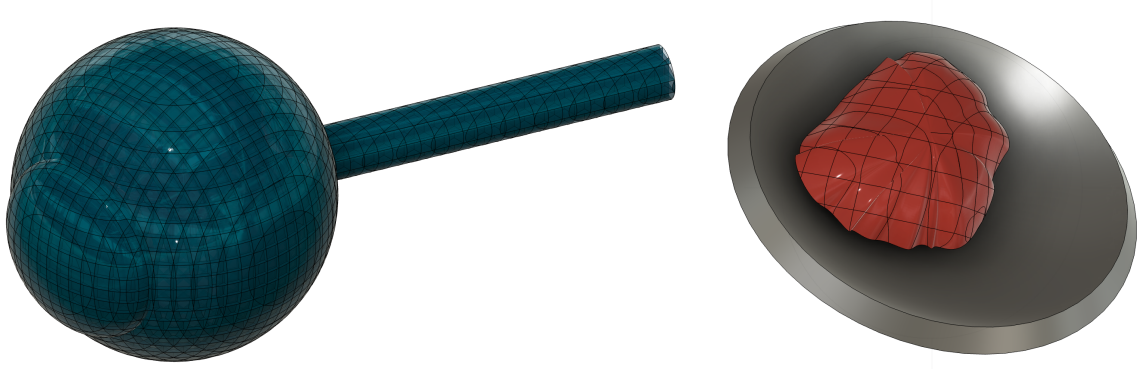

a) b)

Figure 3.6: Examples of Fusion output produced with the CAD volume cutting approach in $wf_{cut}$. In a), the generic eye model divided using the cubic cutting technique is shown. In b), an example of a cut tumour (red) along with a CCA applicator (grey) is presented.

Following the cutting of the structures, the resulting volumes are imported as STL files into Geant4, similar to the implementation in $wf_{trac}$. However, this approach generates approximately 9,000 individual STL volumes per simulation, resulting in significant computational demands in terms of runtime and memory usage. Each volume functions as a SD, as described in subsection 3.3.3, and records the deposited dose. Unlike $wf_{trac}$, $wf_{cut}$ does not employ particle tracking, and the dose resolution remains fixed after the simulation, requiring a full rerun if adjustments are needed.

## 3.8 Results

This section presents the results of the validation and efficiency enhancement of the developed workflow, $wf_{trac}$, in comparison to the workflow $wf_{cut}$, as introduced in Ref. [9]. Additionally, the results of the binning analysis, based on the method described in subsection 3.4.1, are shown. The updated binning approach using `MeshLib` Boolean operations, outlined in subsection 3.4.2, is then compared and validated against the binning method using `PyVista` Boolean operations. Furthermore, the effectiveness of the truncated mean method in filter-

ing datasets, as described in subsection 3.5.2, is analysed. Finally, the overall output of the workflow is examined. The following studies are based on the eye model with implemented patient data. The treatment with a $^{106}$Ru applicator of the model COB, of a tumour measuring 6.3 mm in height is simulated. Except for the studies in subsection 3.8.3, the binning process for the analyses is performed using the method described in subsection 3.4.2, which involves `MeshLib` Boolean operations. In all analyses involving the eye model, the resolution for dose calculation within the ocular structures as detector volumes is defined by a bin size of 0.01 mm$^3$.

**Workflow automation** The execution of both workflows, $\mathrm{wf}_{\mathrm{trac}}$ and $\mathrm{wf}_{\mathrm{cut}}$, is automated using Snakemake [93], with the exception of the detector geometry creation, which is carried out in Fusion. Snakemake is a Python-based workflow automation system designed to facilitate scalable and reproducible data analysis. To evaluate the computational efficiency of individual workflow steps, the `benchmark` function in Snakemake is used. This function records the time taken and memory consumption for each process, where memory usage is defined as the Resident Set Size (RSS).

### 3.8.1 Validation of the simulation workflow

To validate the new methods in $\mathrm{wf}_{\mathrm{trac}}$, which include the implementation of particle tracking and simulation-independent binning for dose resolution, the results are compared with those of $\mathrm{wf}_{\mathrm{cut}}$. For this purpose, 1000 simulations, each consisting of 300,000 particles, are performed using both workflows. This ensures statistically significant results, which are fundamental for clinical relevance, particularly as it meets the requirement that the uncertainty in the depth-dose curve within the first 10 mm is below 1 %.

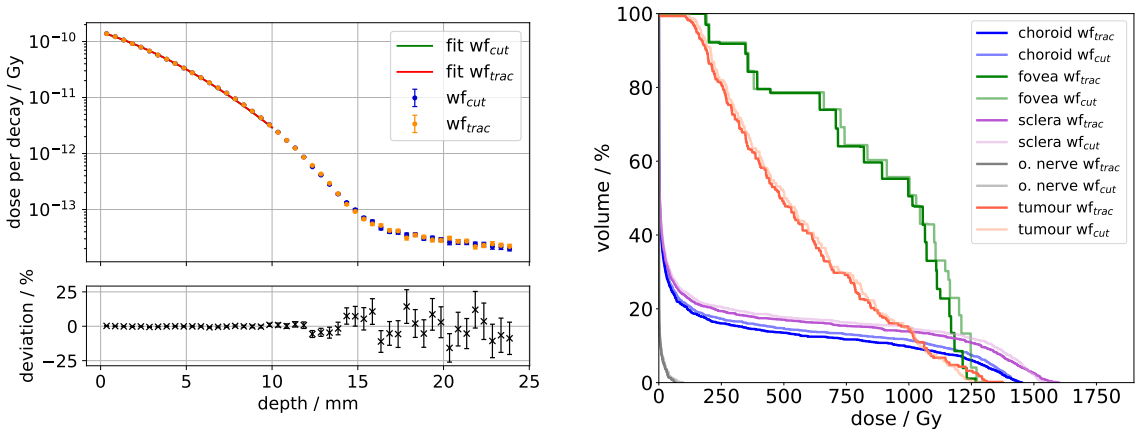


a) b)

Figure 3.7: Comparison of the simulation workflows $\mathrm{wf}_{\mathrm{trac}}$, as presented in this thesis, and $\mathrm{wf}_{\mathrm{cut}}$, as described in Ref. [9]. In a), the comparison of the depth-dose curves is shown, including the fit functions of the form $D(x) = \exp(a \cdot x^2 + b \cdot x + c)$. In b), the comparison of the minimum, maximum, and mean doses in the respective structures is shown.

Within the first 10 mm in the depth-dose curves, the deviation of the recorded data points with $\mathrm{wf_{trac}}$ and $\mathrm{wf_{cut}}$ is below 1 % (Figure 3.7a). The deviation of the fit function parameters between the two workflows is also below 1 %. These variations are attributed to statistical fluctuations, thereby ruling out any significant influence from the different methods.
Regarding the DVHs, for all structures considered, the curve shapes for both workflows are very similar (Figure 3.7b). A slight shift between the curves can be observed, indicating that $\mathrm{wf_{cut}}$ irradiates a marginally greater volume with the respective dose. This trend is further confirmed in Figure 3.8 when examining the mean dose values. For all structures, the mean dose in $\mathrm{wf_{cut}}$ is higher than in $\mathrm{wf_{trac}}$, except for the lens, where the mean dose values are equal. With the exception of a $(33 \pm 33)$ % deviation for the cornea and a $(15 \pm 359)$ % deviation for the optic nerve, the deviation of the mean dose values for all other structures is below 10 %. Due to the high uncertainties in the mean dose values within the structures, these values have limited interpretative significance.

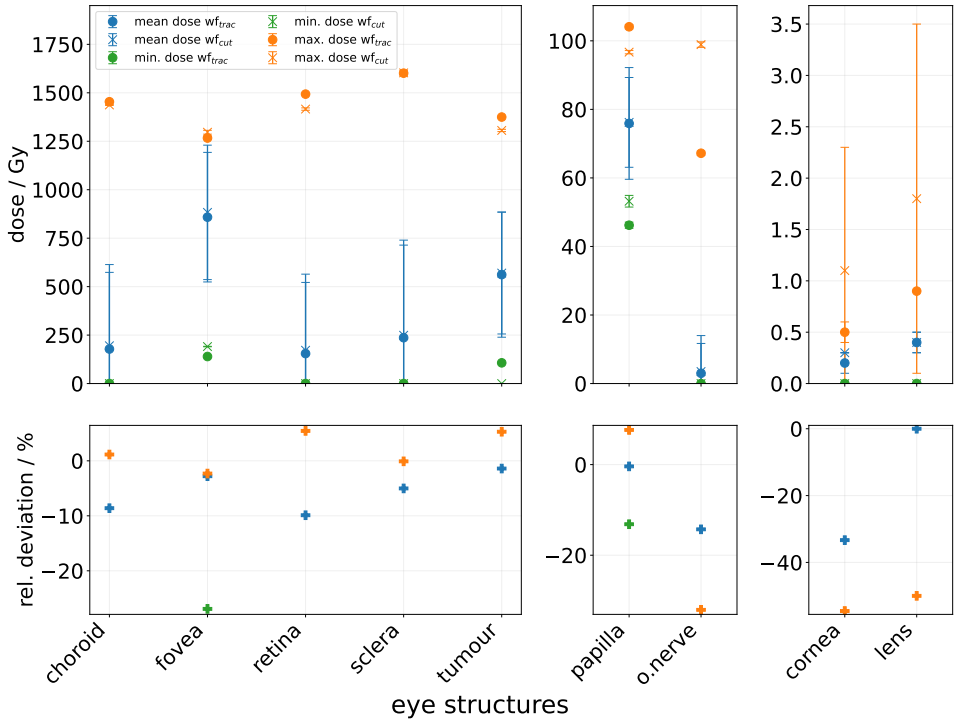


Figure 3.8: Comparison of the minimum, maximum, and mean doses in the respective structures for the simulation results of $\mathrm{wf_{trac}}$ and $\mathrm{wf_{cut}}$. The relative deviation $R$ of the dose values is calculated with the formula $R = 100 \cdot (x_{\mathrm{trac}} - x_{\mathrm{cut}})/x_{\mathrm{cut}}$, where $x$ represents the particular dose value for the respective structure. The associated uncertainties are calculated using Gaussian error propagation. For clarity, the uncertainties of the relative deviations are not shown. The exact values can be found in Table A.1, Table A.2, and Table A.3.

No clear trend is observed regarding the deviations in the maximum and minimum dose values between the two workflows. The deviations in the maximum dose values for all structures are below 10 %, except for the optic nerve, which shows a $(32 \pm 1)$ % lower maximum dose in $\mathrm{wf_{trac}}$,

the cornea with $(55 \pm 51)\,\%$, and the lens with $(50 \pm 47)\,\%$. Due to the high uncertainties in the maximum dose values for cornea and lens and the overlap of these values including their uncertainties between the two workflows, these data do not give a clear indication of whether the workflows lead to different results. Regarding the minimum dose values, the largest deviation is observed in the tumour. In $\mathrm{wf_{trac}}$ the minimum dose in the tumour is $(107 \pm 1)\,\mathrm{Gy}$, while in $\mathrm{wf_{cut}}$ the minimum dose is $0\,\mathrm{Gy}$. Furthermore another large deviation, $(27 \pm 3)\,\%$, is observed in the fovea, where the minimum dose is lower in $\mathrm{wf_{trac}}$ and in the papilla, with $(13 \pm 3)\,\%$. The precise dose values, including their uncertainties and their deviations, are listed in Table A.1, Table A.2, and Table A.3.
One possible explanation for the deviations of more than $10\,\%$ in the dose values between the workflows is the absence of a method like the truncated mean calculation in $\mathrm{wf_{cut}}$. While both workflows exhibit outliers due to the small statistical significance in sections of structures with very low volume, these outliers are less pronounced in $\mathrm{wf_{cut}}$ than in $\mathrm{wf_{trac}}$. Applying truncated mean filtering to $\mathrm{wf_{cut}}$ would not be beneficial, as it has been shown to discard valuable data, particularly in larger structures. For this reason, truncated mean filtering is only applied in $\mathrm{wf_{trac}}$ in this study. This may also explain the high statistical uncertainties in the maximum dose values for the cornea and lens in $\mathrm{wf_{cut}}$. These structures are farthest from the radiation source, receive the lowest doses, and their small volume sections have limited statistical significance, which can lead to distortions.

### 3.8.2 Monte Carlo simulation

To compare the computational efficiencies of the MC simulations for the two workflows, $\mathrm{wf_{trac}}$ and $\mathrm{wf_{cut}}$, ten simulations, each with 300,000 particles, are performed. In order to minimise external influences, all computations are performed on a dedicated machine isolated from other processes within a computer cluster. This machine has 64 CPUs and 264 GB of memory.

#### Influence of STL mesh quality

To investigate the impact of mesh quality of the STL files implemented from Fusion on simulation time and memory usage, this study is conducted without the use of multi-threading, employing a single core for each simulation.
Overall, the simulation time and memory usage in $\mathrm{wf_{trac}}$ are lower for each mesh quality than in $\mathrm{wf_{cut}}$ (Figure 3.9). Simulation time is reduced by over $70\,\%$ for the low and medium mesh qualities in $\mathrm{wf_{trac}}$ compared to $\mathrm{wf_{cut}}$, and by $62\,\%$ for the high mesh quality (Figure 3.9a). Memory usage in $\mathrm{wf_{trac}}$ is reduced by $61\,\%$ for the low mesh quality, $44\,\%$ for the medium mesh quality, and $24.5\,\%$ for the high mesh quality, compared to $\mathrm{wf_{cut}}$ (Figure 3.9b). The higher efficiency of $\mathrm{wf_{trac}}$ in terms of computing, compared to $\mathrm{wf_{cut}}$, for all mesh qualities can be attributed to the fewer STL volumes imported. While $\mathrm{wf_{cut}}$ simulates with approximately 9,000 STL files, $\mathrm{wf_{trac}}$ works with only 13 STL files.
For $\mathrm{wf_{trac}}$, increasing the mesh quality from low to medium resulted in a $52\,\%$ increase in simulation time and a $48\,\%$ increase in memory usage. Further increasing the mesh quality from medium to high led to a $58\,\%$ rise in simulation time and a $114\,\%$ increase in memory usage. These trends are attributed to the higher number of triangular facets in the mesh, which increases the computational load due to additional collision, intersection, and navigational checks required for each triangle during particle tracking in Geant4.

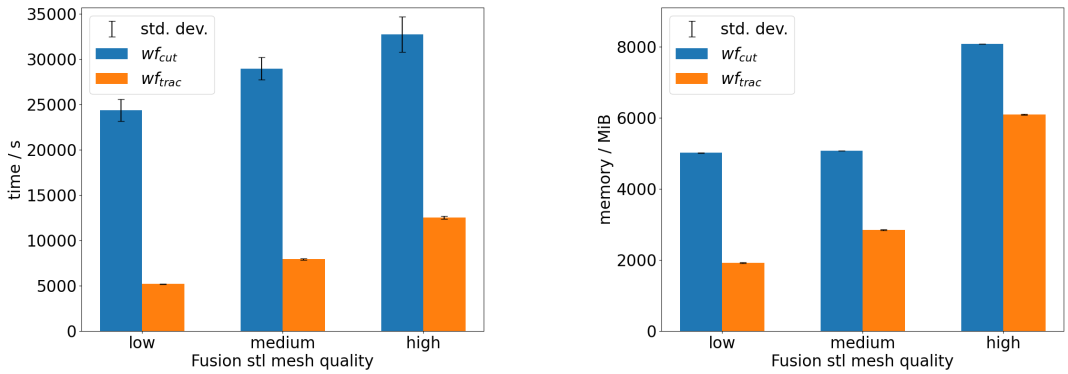


a) b)

Figure 3.9: Benchmark results for influence of the mesh quality of the STL files on runtime and memory usage. In a), the comparison of simulation time between $wf_{cut}$ and $wf_{trac}$ for different STL export qualities from Fusion is shown. In b), the comparison of memory usage between $wf_{cut}$ and $wf_{trac}$ for different STL export qualities from Fusion is presented.

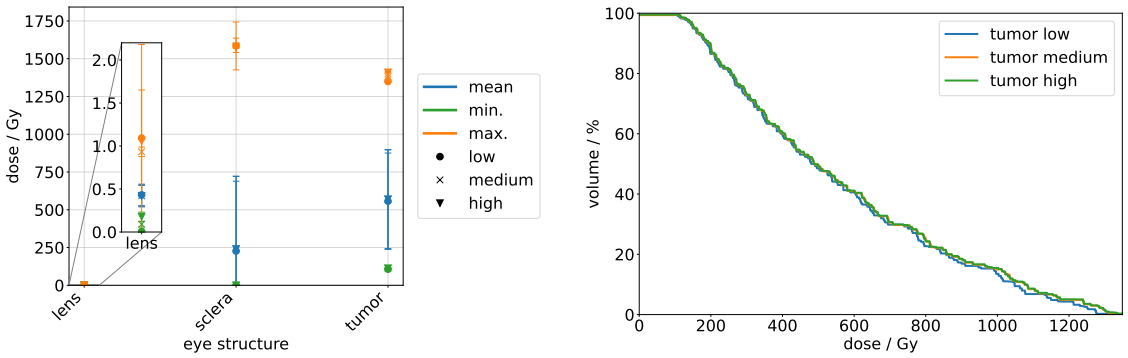


a) b)

Figure 3.10: Simulation results for the eye model using various STL export qualities from Fusion. In a), minimum, maximum, and mean dose values for the lens, sclera, and tumour structures are shown for each mesh quality. In b), the DVH of the tumour is presented for the different mesh qualities. Both figures have already been published and are therefore taken from Ref. [67].

In theory, this trend should also be reflected in $wf_{cut}$. While the trend in simulation time is consistent, the same cannot be said for memory usage. Increasing memory usage from low to medium quality in $wf_{cut}$ only results in a 1 % increase. Even when the STL files are recreated and the simulation is repeated, the same pattern is observed. A mistake in the creation of the STL files in Fusion is unlikely, as the trend in simulation time for $wf_{trac}$ with these files aligns with expectations. The data presented in Figure 3.9 are listed with their

exact numerical values, in the appendix in Table A.4.
For the workflow $wf_{trac}$ developed and utilised in this thesis, the influence of STL export mesh quality on simulation accuracy is evaluated. This is done by comparing the results for several ocular structures, including the lens, sclera, and tumour. The analysis focused on the maximum, minimum, and mean dose values for these structures across the various mesh qualities (Figure 3.10a). However, the deviations observed in the dose values did not follow a consistent pattern that could correlate with the mesh quality. This conclusion is further supported by the DVH of the tumour, which serves as a representative example (Figure 3.10b). As a result, all subsequent analyses are carried out using the low mesh quality.

### Impact of multi-threading

One of the main objectives of $wf_{trac}$ is to improve efficiency in terms of simulation time and memory consumption compared to $wf_{cut}$. In this context, the effect of using multiple threads for the simulation is also investigated. For the analysis, simulations are conducted using one, two, and four threads. Increasing the number of threads beyond four is not considered beneficial in the long term in the context of this work, as the computing resources of the cluster used are limited and should therefore be utilised as efficiently as possible.
In this study, the simulation time and memory usage in $wf_{trac}$ are lower for the number of threads used (Figure 3.11). For both workflows, the simulation time decreased substantially with the addition of used threads (Figure 3.11a). When using a single thread, the simulation time in $wf_{trac}$ is reduced by 78 % compared to $wf_{cut}$. For two threads, the simulation time in $wf_{trac}$ decreased by 83 %, and for four threads, it is reduced by 84 % compared to $wf_{cut}$. Specifically for $wf_{trac}$, the use of two threads results in a 52.0 % reduction in simulation time relative to single-threaded execution, and a further 37.7 % reduction is achieved with four threads.

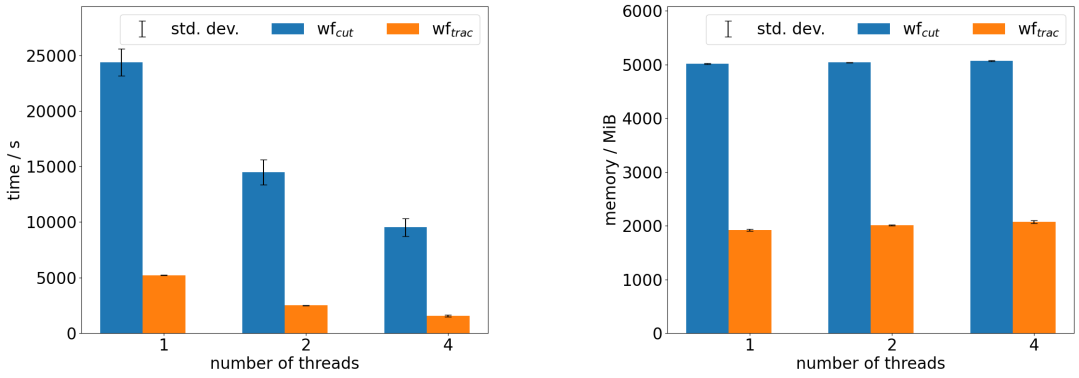


a) b)

Figure 3.11: Benchmark results for influence of multi-threading of the STL files on runtime and memory usage. In a), the comparison of simulation time between $wf_{cut}$ and $wf_{trac}$ for different number of threads is presented. In b), the comparison of memory usage between $wf_{cut}$ and $wf_{trac}$ for different number of threads is shown.

In terms of memory usage, both workflows exhibit relatively stable behaviour. However, the memory usage in $wf_{trac}$ is approximately 60 % lower than in $wf_{cut}$ (Figure 3.11b).
The data presented in Figure 3.11 is also available in the appendix in Table A.5, with the exact numerical values listed.

### 3.8.3 The binning process

In section 3.4, the binning strategy is outlined, and two distinct methods are introduced. The first approach, which uses `PyVista` Boolean operations, involves an analysis to determine optimal parameters for binning each anatomical structure of the eye, to achieve an accurate volumetric representation. This analysis is performed on a single patient case as an example, and the corresponding results are presented in this subsection. Additionally, the alternative binning method based on `MeshLib` Boolean operations is compared with the initial approach, in order to validate the new technique. This study is conducted using data from 1000 simulations, with 300,000 particles each.

#### Volume analysis of the method with PyVista Boolean operation

In subsection 3.4.1, $\epsilon$ is introduced as a metric for evaluating the success of the binning process. To achieve an accurate approximation of the total volume of the structure using the `PyVista` Boolean operation method, derived from the sum of the bin volumes, a parameter analysis is conducted for each complex detector volume. This analysis aims to determine the combination of Fusion STL export quality, enlargement factor, and subdivision factor that minimises the deviation $\epsilon$ between the total bin volume and the actual mesh volume. For the eye model, the deviation is set to remain under 5 %, as higher deviations could lead to significant errors in dose calculation. Figure 3.12 illustrates the various parameter combinations for the sclera structure, while Figure A.1 to Figure A.8 depict the corresponding results for the remaining ocular structures. The analysis is carried out for all structures, and the optimal parameter combinations are selected for this study (Table 3.1).

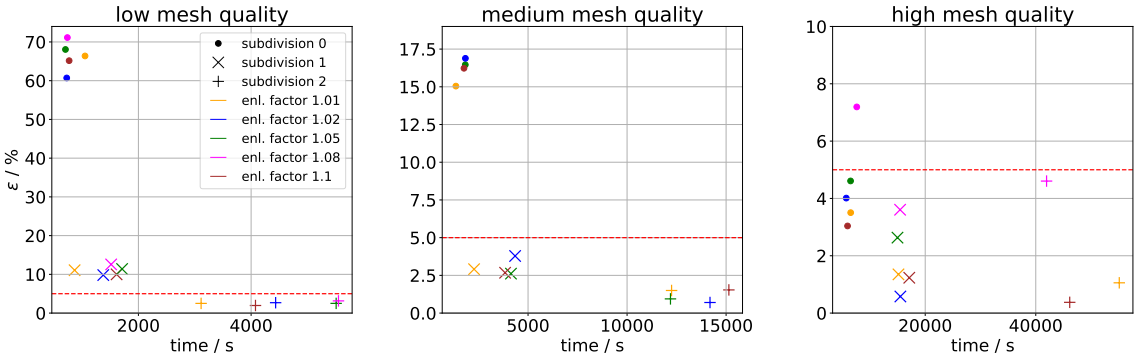


Figure 3.12: Volume analysis for the example structure sclera using the binning process with `PyVista` Boolean operation. Volume deviation $\epsilon$ in percentage represents the relative deviation between the volume obtained from the sum of the bin volumes and the calculated volume of the unbinned mesh. The mesh qualities correspond to the STL export qualities in Fusion.

When considering only the computational performance of the MC simulation, as discussed in subsubsection 3.8.2, low mesh quality would be preferable. However, based on the results from this volume analysis, medium mesh quality represents a compromise between binning accuracy and simulation efficiency, and is thus selected in most cases. Contrary to expectations, the papilla and tumour structures show better results with low STL mesh quality. In contrast, for the cornea structure, it is not possible to achieve a deviation of less than 5 % in volume with any mesh quality other than high. Ultimately, a subdivision factor of 2 is applied in all cases. No regular pattern is observed for the enlargement factors, which vary on a case-by-case basis.

Table 3.1: Parameters resulting from the volume analysis for the structures to be binned in the eye model with a bin size of $1\,\mathrm{mm}^3$ with the binning method using `PyVista` Boolean operation.

| structure | mesh quality | subdivision factor | enlargement factor | $\epsilon$ / % |
|---|---|---|---|---|
| choroid | medium | 2 | 1.01 | 1.55 |
| cornea | high | 2 | 1.05 | 2.97 |
| fovea | medium | 2 | 1.01 | 0.1 |
| lens | medium | 2 | 1.1 | 0.001 |
| retina | medium | 2 | 1.1 | 3.21 |
| papilla | low | 2 | 1.08 | 0.02 |
| sclera | medium | 2 | 1.02 | 0.7 |
| optic nerve | medium | 2 | 1.08 | 0.97 |
| tumour | low | 2 | 1.01 | 0.5 |

#### Validation of the method with MeshLib Boolean operation

To validate the binning method using the `MeshLib` Boolean operation, the simulation results processed with this approach are compared to those generated using the `PyVista` Boolean operation (Figure 3.13). For all structures handled with the `MeshLib` Boolean operation at low, medium, and high STL export quality, the deviation $\epsilon$ remains below 5 %. Except for the retina, which shows a deviation of $\epsilon = 2.4\,\%$ at medium mesh quality, and the sclera at low mesh quality with $\epsilon = 0.2\,\%$, the volume deviation for all other structures ranges from $10^{-6}$ to $10^{-8}$ %. The volume deviation $\epsilon$ for the structures processed using the `PyVista` Boolean operation is detailed in Table 3.1.
To compare the two methods, the maximum, minimum, and mean dose values for the individual structures of the eye model are examined (Figure 3.13). With a few exceptions, the relative deviations between the values are under 5 %. Notably, the minimum dose value in the fovea is 24 % higher when calculated with the `MeshLib` method, while the maximum dose value for the optic nerve is 20 % lower compared to the `PyVista` method. Overall, no consistent trend is observed that would suggest one method generally produces higher or lower dose values.

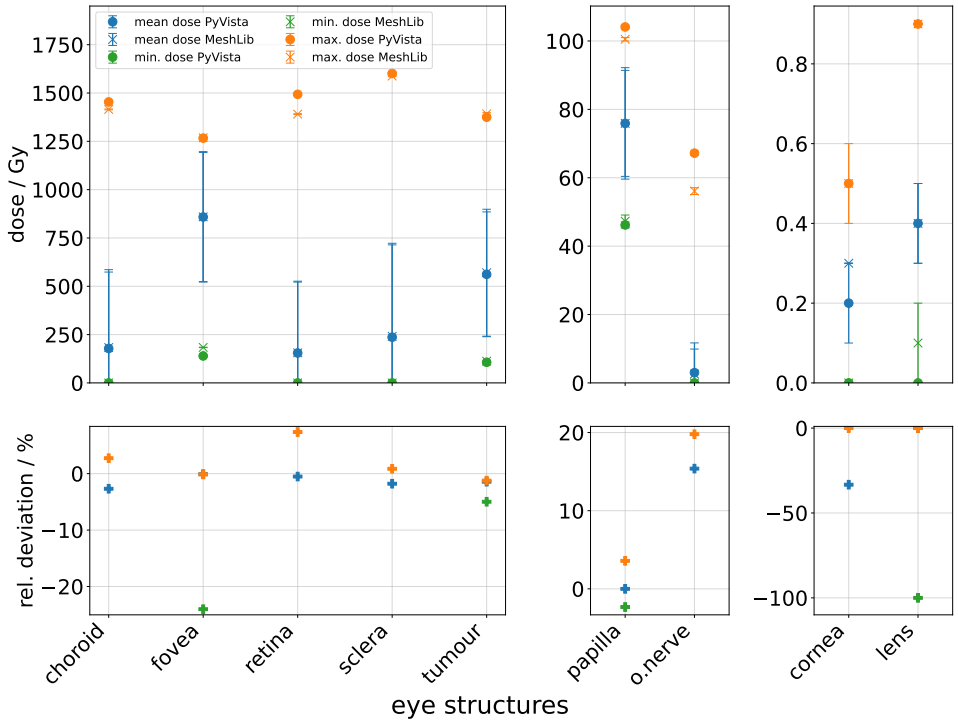


Figure 3.13: Comparison of the minimum, maximum, and mean doses obtained using `PyVista` (PV) and `MeshLib` (MH) in the binning process. The relative deviation $R$ of the dose values is calculated with the formula $R = 100 \cdot (x_{\mathrm{PV}} - x_{\mathrm{MH}})/x_{\mathrm{MH}}$, where $x$ represents the particular dose value for the respective structure. The associated uncertainties are calculated using Gaussian error propagation. For clarity, the uncertainties of the relative deviations are not shown. The exact values can be found in Table A.6, Table A.7, and Table A.8.

### Computing analysis of the method with MeshLib Boolean operation

The performance evaluation of the binning process using the `MeshLib` Boolean operation is carried out using the sclera, as it represents the largest detector structure by surface area, offering a useful reference for calculations involving relatively large volumes and numerous bins. The tumour structure, on the other hand, serves as a representation of smaller, highly detailed volumes (Figure 3.14). Across all STL export qualities, simulation time and memory usage are consistently lower for the tumour structure compared to the sclera. For the sclera, the simulation time decreases exponentially with the increase in the number of threads used for binning, particularly for the medium and high mesh qualities (Figure 3.14a). However, in other scenarios, the reduction in simulation time is less significant, as binning times are already below 5000 s. Additionally, the memory consumption for both structures in high STL quality is more than double that of low quality and nearly twice the amount seen in medium quality (Figure 3.14b).

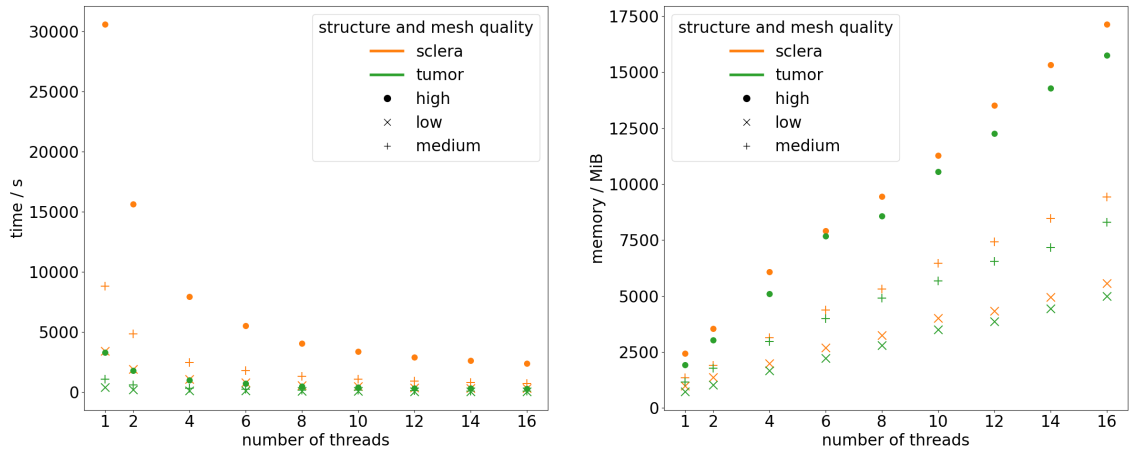


a) b)

Figure 3.14: Runtime and memory consumption as a function of the number of threads used during the binning process with `MeshLib` Boolean operation for two example structures of different sizes, evaluated across three STL export qualities in Fusion. In a), the simulation time is plotted against the number of threads, while in b), the corresponding memory usage is shown. Both figures have already been published and are therefore taken from Ref. [67].

### 3.8.4 Truncated mean filtering

The truncated mean method and its implementation into the software workflow are detailed in subsection 3.5.2. The maximum, minimum, and average dose values for the retina, used here as an example structure, are presented as a function of the proportion of values discarded from the upper and lower extremes of the dose distribution (Figure 3.15a). Additionally, the volume of discarded elements is shown as a percentage of the total structure relative to the discarded dose values. Without applying the truncated mean, the maximum dose for the retina is approximately $(161\,100 \pm 22\,600)$ Gy, which is more than one hundred times greater than the value obtained when the truncated mean is utilised (Table A.9). The data from the truncated mean filtering for all structures is listed in Table A.9 to Table A.17.
For the eye model, with a cut-off value set at 2 %, the relation between the number of bins and the discarded volume is illustrated (Figure 3.15b). In most cases, except for minor statistical variations, the discarded volumes are relatively small, typically less than 0.01 $mm^3$. These tiny volumes, although minimal, can introduce significant distortion into the resulting dose distribution. As a result of these observations, all subsequent results presented in this thesis, generated using the developed $wf_{trac}$ workflow, adopt a 2 % cut-off value. For all structures, this threshold results in an excluded volume of less than 1.5 % of the total structure volume.

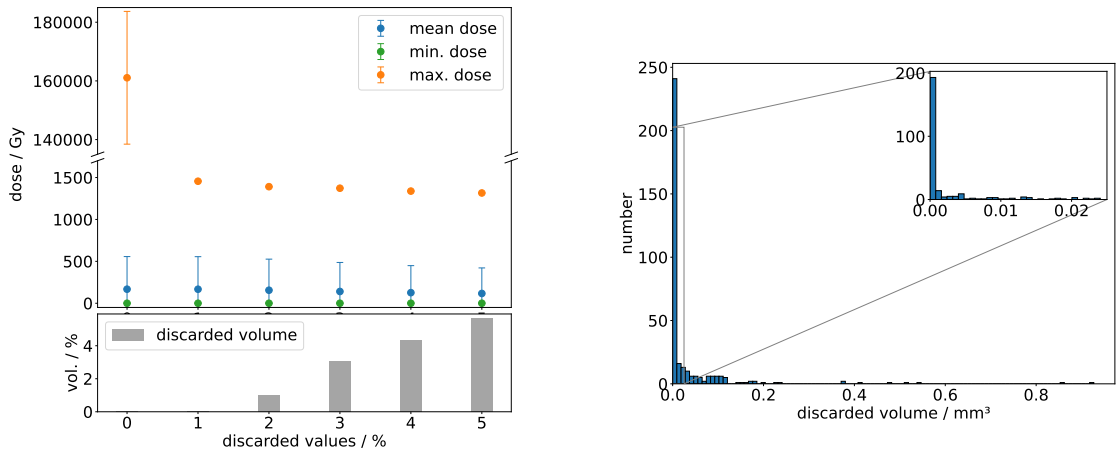


a) b)

Figure 3.15: Analysis of the truncated mean filtering. In a), the minimum, maximum, and mean dose values for the retina structure are plotted against the proportion of discarded dose values at the upper and lower extremes of the distribution. The lower plot shows the percentage of the discarded volume relative to the total volume of the structure. In b), the number of discarded volumes is shown as a function of their size in cubic millimeters for the entire eye model, based on a scenario where 2 % of the dose values at the upper and lower ends are excluded. Both figures have already been published and are therefore taken from Ref. [67].

## 3.9 Discussion

This chapter introduces an enhanced software workflow for simulating $^{106}$Ru brachytherapy. A particle tracking method has been implemented in Geant4, allowing the coordinates of deposited energy within the structures of the eye model to be recorded. Additionally, a complementary Python-based external binning technique has been developed to virtually divide the eye structures into smaller spatial units. By associating the stored energy coordinates with these bins, the workflow enables variable 3D scoring of physical quantities within the complex detector geometries of the eye model using Monte Carlo simulations. This approach allows for flexible resolution adjustments after simulation, eliminating the need to rerun simulations to change spatial resolution.

The newly developed workflow, $\mathrm{wf}_{\mathrm{trac}}$, presented in this thesis, has been validated through comparison with the existing software workflow, $\mathrm{wf}_{\mathrm{cut}}$, from Ref. [9] (Figure 3.7, Figure 3.8). The depth-dose curves show deviations of less than 1 % within the first 10 mm, confirming that the integration of particle tracking into the simulation framework do not introduce unintended changes to the results (Figure 3.7a).
A comparison of the DVHs (Figure 3.7b) and the corresponding dose values (Figure 3.8) reveal no consistent trends in the deviations. However, a slight tendency towards higher mean dose values in $\mathrm{wf}_{\mathrm{cut}}$ suggests a marginally increased dose deposition. Since these deviations remain below 10 % for all structures, except for the optic nerve, where they reach up to 15 %, the results indicate that the newly implemented methods in $\mathrm{wf}_{\mathrm{trac}}$ work as expected.

One possible explanation for these discrepancies is that $wf_{cut}$ lacks a mechanism to account for statistical outliers caused by small volume effects. The truncated mean method implemented in $wf_{trac}$ has not been suitable for $wf_{cut}$, as outliers occur less frequently in the latter. Applying this method to $wf_{cut}$ would have resulted in the exclusion of significant values.

A key objective in the development of $wf_{trac}$ is the improvement of the computational efficiency over $wf_{cut}$, as the MC simulations serve as the basis for generating training and validation data for the neural networks discussed in chapter 6. This goal has been successfully achieved across all tested STL mesh qualities and thread configurations in multi-threading mode (Figure 3.9, Figure 3.11). In every scenario examined, the simulation time is reduced by at least 62 %. The most significant improvement is observed in simulations using four threads with the eye model at low mesh quality, where $wf_{trac}$ achieves a 84 % reduction in simulation time compared to $wf_{cut}$. Additionally, in this case, memory consumption is reduced by approximately 60 %.

The newly developed binning method has been initially implemented using the `PyVista` Boolean operation. This approach involves analysing each structure to determine the optimal binning parameters, ensuring that the volume represented by the bin divisions closely matches the actual structure volume with minimal deviation $\epsilon$ (Figure 3.12). From a computational efficiency perspective, low mesh quality results in shorter simulation times. However, a balance between simulation efficiency and binning accuracy is found with medium mesh quality, which is used for the eye model in this study. This analysis is a one-time effort specific to a given simulation environment, such as the eye model used in this study, and enables efficient reuse of the parameters across multiple simulations and patient cases. However, it should be noted that when adapting the workflow to simulate other patient scenarios, adjustments to the binning parameters may be required for structures affected by variations in tumour morphology, such as the retina, from which the tumour is excised, and the tumour itself.
Throughout this thesis, the binning process has been further optimised using the `MeshLib` Boolean operation. This eliminates the need for individual structure-specific analyses to determine optimal binning parameters for accurate volume representation. Validation is carried out by comparing the two methods using different Boolean operations (Figure 3.13). The binning process with the `MeshLib` Boolean operation results in a lower deviation $\epsilon$, allowing all structures to be processed effectively using low mesh quality. This led to faster computation times and reduced memory consumption.

The eye structure volumes have been exported as STL meshes using Fusion, and the influence of mesh quality on simulation and binning performance has been analysed. In terms of computational efficiency, low mesh quality results in reduced simulation and binning times, as well as lower memory usage (Figure 3.9, Figure 3.14). While variations in simulation outcomes are noted across different mesh qualities, no statistically significant trends are observed (Figure 3.10). For the simulations of the eye model in this study, low mesh quality is considered sufficient to maintain the accuracy of the results while reducing the computational effort.

The use of multi-threading significantly reduces simulation and binning times, particularly when there are sufficient computational resources available (Figure 3.11, Figure 3.14). While the memory consumption for the simulation remains relatively constant regardless of the number of threads, the binning process shows a linear increase in memory requirements as

additional threads are employed. This can be attributed to the `concurrent.futures` Python module, where each worker process is given a copy of the necessary data. Consequently, this can result in duplicated memory usage. Even with parallel execution, each process retains its own independent memory space, meaning large datasets may need to be replicated across the address space of each worker. These results emphasise the need to balance computational efficiency, memory usage, and simulation accuracy, highlighting the importance of optimising the system according to the available hardware resources.

The analysis of the dose distribution reveals significant distortions caused by very small volumes, often below 0.01 $mm^3$, which disproportionately affect the results. These distortions are due to statistical variations and the allocation of sparse dose values (Figure 3.15b). To address these issues, an additional analysis has been conducted to identify suitable cut-off values for the dose distributions, aiming for a more robust and accurate representation (Figure 3.15a). The findings indicate a 2 % cut-off value for the software workflow $wf_{cut}$ used to simulate the $^{106}$Ru treatment of the eye model.

The software workflow developed in this work offers a significant improvement in computational efficiency compared to the workflow presented in Ref. [9]. The error-prone process of dividing structures into approximately 9,000 individual STL files, as well as its integration into Geant4, has been eliminated in the new workflow. The enhanced computational efficiency is essential for the ongoing simulations conducted in this study, particularly in the generation of training data for neural networks, as described in chapter 6, which requires a large number of simulations.
For more targeted analyses involving spatial information, the binning method facilitates the visualisation of 3D dose distributions within specific structures, such as the tumour (Figure 3.5b).
Another major advantage of this workflow is the ability to adjust the dose resolution according to the needs of the analysis. By optimising the bin size, a balance between computational efficiency and precision can be achieved. This flexibility is especially valuable for medical applications, allowing for higher resolution in clinically significant areas, such as the tumour region, while maintaining lower resolution in less critical regions to reduce computational costs.

# 4 Simulation architecture for inhomogeneous surface dose profiles

The simulation of a homogeneous surface dose profile for $^{106}$Ru applicators constitutes an approximation of the actual inhomogeneous dose distribution, which contains potential hot and cold spots. These are not included in the simulation workflow presented in chapter 3. To assess their impact on treatment, a simulation architecture that accounts for surface dose inhomogeneities is required. Such a framework enables the estimation of the probability of insufficient tumour coverage due to local underdosage and, conversely, the likelihood of overdosing in healthy tissue. The basic principles of this simulation framework are developed in Ref. [12] and have been refined and extended in this work.
A schematic overview of the simulation workflow for inhomogeneous applicator treatment is presented in Figure 4.1. The modifications required for the simulation of inhomogeneous dose distributions are fully implemented within the MC simulation step of the workflow introduced in chapter 3 and are described in detail in this chapter.

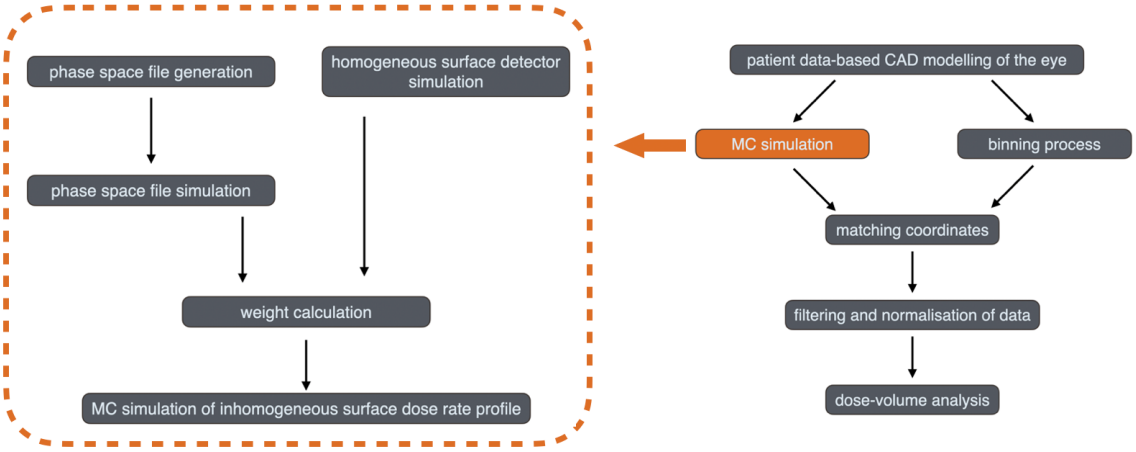


Figure 4.1: Overview of the workflow used to generate and process simulation data for modelling inhomogeneous treatment with $^{106}$Ru applicators. The left-hand side illustrates the implemented modifications for simulating inhomogeneous surface dose profiles, while the right-hand side shows the simulation workflow described in chapter 3.

In section 4.1, an overview of the quality assurance criteria for $^{106}$Ru applicators is provided, defining the permissible limits for inhomogeneities in the surface dose profile. The detectors modelled for the simulations, as well as for the generation of phase space files, are subsequently described in section 4.2. The challenges associated with the MC simulation of inhomogeneous surface dose profiles are outlined in section 4.3, establishing the context

for sections 4.4 and 4.5, which detail the creation and use of phase space files as the basis for simulating hot and cold spots. The corresponding simulation strategies for modelling inhomogeneous surface dose profiles are then presented in section 4.6, with the results summarised in section 4.7 and further discussed in section 4.8.

## 4.1 Quality assurance criteria for $^{106}$Ru applicators

Before a $^{106}$Ru eye applicator is supplied to clinics, it must undergo a comprehensive Quality Assurance (QA) assessment performed by the manufacturer, EZAG, to verify conformity with the safety and performance requirements specified under the Medical Device Regulation (MDR).
The surface dose profiles provided in the measurement certificates (Figure 2.5b) are evaluated against two quality assurance criteria to confirm the suitability of the applicator for treatment. These criteria are the source non-uniformity and the source asymmetry, both of which must not exceed 20 % [42]. Both quantities are defined in accordance with Report 14 of the NCS[15], which provides detailed recommendations for the quality control of beta-emitting radiation sources [94].
In the coordinate system described by the NCS, the z-axis corresponds to the longitudinal source axis, while the r-axis extends perpendicularly to it, with the coordinate origin located at the source surface. For ophthalmic applicators, all reference points are situated along the central axis, and the source strength is expressed as the absorbed dose rate to water at the reference position.
According to the NCS recommendations, the assessment of spatial dose variations is restricted to the clinically relevant region surrounding the central axis, typically within a radius corresponding to 80 % of $R_{50}$. Here, $R_{50}$ represents the radial distance at which the mean absorbed dose rate decreases to 50 % of its maximum value [94]. In the context of QA for $^{106}$Ru eye applicators, this implies that only the two innermost measurement rings provided in the calibration certificate are taken into account in the calculations. The third ring, located furthest from the applicator centre and representing the dose distribution at its edge, is excluded from the evaluation of the two quality criteria. In the case of applicator models featuring a notch for the optic nerve, such as the COB model, the manufacturer considers only the measurement points on the first two rings of the semicircle opposite the cut-out [95].
The NCS recommends treating the concepts of source strength and source non-uniformity in relation to one another, with the source strength characterising the dose rate at the reference point and the source non-uniformity describing the largest expected deviation from this value within the clinically relevant region.The source non-uniformity $U_{\mathrm{NU}}$ is quantified using the expression

$$U_{\mathrm{NU}} = \frac{\max\left(\left|\dot{D}_{\min} - \dot{D}_{r=0}\right|, \left|\dot{D}_{\max} - \dot{D}_{r=0}\right|\right)}{\dot{D}_{r=0}} \cdot 100\%, \tag{4.1}$$

where $\dot{D}_{r=0}$ is the dose rate at the reference point, and $\dot{D}_{\min}$ and $\dot{D}_{\max}$ denote the minimum and maximum dose rates, respectively, within the region of interest.

[15] Netherlands Commission on Radiation Dosimetry

To characterise deviations in the dose distribution parallel to the source surface, the source asymmetry $U_{\mathrm{AS}}$ is defined as

$$U_{\mathrm{AS}} = \max \left( \frac{\dot{D}_{\max}(r) - \dot{D}_{\min}(r)}{\dot{D}_{\mathrm{avg}}(r)} \right) \cdot 100\%. \tag{4.2}$$

Here, the variation in dose rate is evaluated along a circular path at radius r, and the maximum deviation observed within the range from r = 0 to $0.8 \cdot R_{50}$ determines the asymmetry. $\dot{D}_{\mathrm{avg}}$ denotes the average dose rate [94].

## 4.2 Detector geometries

The simulation and analysis of inhomogeneous dose profiles involve two distinct detector architectures. The fundamental concepts of these detectors were developed in Refs. [12, 13] and have been adapted in the present work to address the specific requirements of this study. To record the surface dose profile, the surface detector is employed, while for the generation of phase space files, an arrangement of cylindrical detectors is used, as discussed in section 4.4. This cylindrical configuration is based on the detector setup described in the measurement protocol of the manufacturer and used in the certificates presented in subsection 2.3.1. Both detector architectures are constructed in the Fusion software for the CCA, CCB, and COB applicator models and are described in detail in the following subsections.

### 4.2.1 Surface detector

To record the surface dose profile of the $^{106}$Ru eye applicator, a surface detector is designed for each applicator model. The detector features a spherical calotte geometry corresponding to the shape of the applicator, ensuring a uniform and symmetrical gap between the inner surface of the plaque and the outer surface of the detector. This configuration provides consistent and reproducible conditions for surface dose profile measurements, in accordance with the source-to-detector distance specified in the measurement certificates of the manufacturer. The opening angle of the detector is defined such that its edge extends to the position of the third measurement ring listed in the certificates. To minimise potential edge effects caused by binning, the opening angle is chosen to be one degree larger than that of the third measurement ring.
According to the manufacturer, the effective measurement distance between the detector and the applicator is 1 mm [45]. In order to maintain comparability, the same spacing is adopted for the surface detector in this study. The detector has a thickness of 0.1 mm, and is positioned such that its inner surface lies 1.05 mm from the applicator, ensuring that the effective measurement volume is at the intended distance. In the simulation, the detector material is modelled as water.
In Figure 4.2, the surface detector created for the COB applicator model is shown. The specific dimensions employed for constructing surface detectors for the various applicator models are summarised in Table A.18.

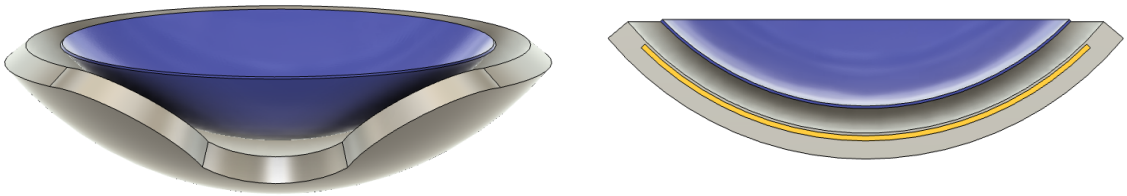

Figure 4.2: Surface detector illustrated for the COB applicator model. The applicator is shown in grey, the surface detector in blue, and the target region appears in yellow in the cross-section on the right.

### 4.2.2 Cylindrical detectors

To replicate the measurement setup used by the manufacturer, a series of cylindrical detectors is constructed for each applicator model considered in the simulations. In Figure 4.3, the arrangement of the cylindrical detectors for the COB applicator model is presented. Each measurement position is represented in the simulations by a single cylindrical detector. The positions correspond to the first three rings specified in the measurement certificates of the manufacturer. This configuration enables a direct comparison between the simulated results and the corresponding reference values provided in the certificates.
In addition, the cylindrical detectors form the basis for the generation of phase space files, which are described in detail in section 4.4.

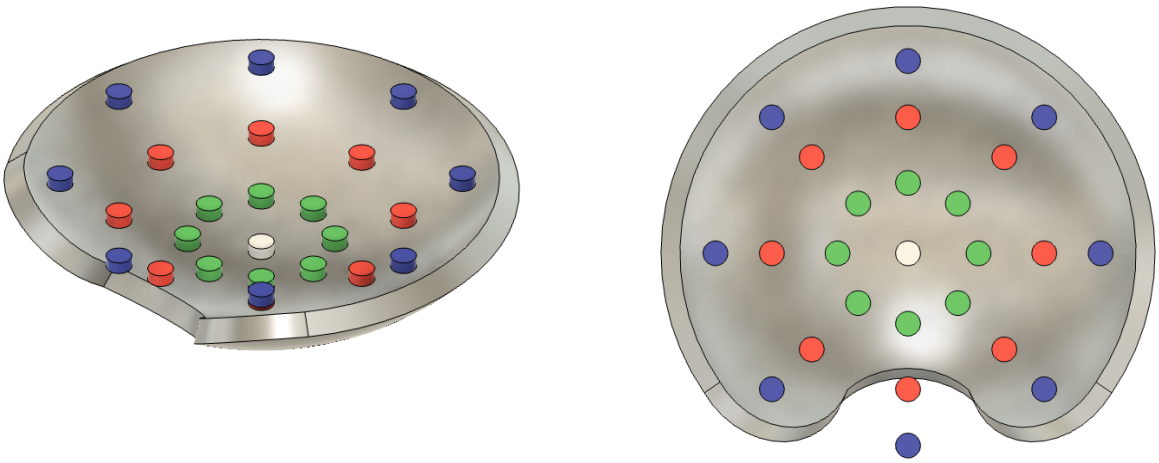

Figure 4.3: Arrangement of the cylindrical detectors for the COB applicator model, corresponding to the measurement configuration described in the certificates of the manufacturer. The central detector is shown in white, while the first, second, and third measurement rings are displayed in green, red, and blue, respectively.

The spatial arrangement of the individual measurement rings for each applicator model follows the specifications of the manufacturer and is summarised in Table A.18. Each ring comprises eight cylindrical detectors representing the scintillation detector positions. The 25 cylindrical scoring volumes have a diameter of 1 mm and a height of 0.5 mm [45]. The symmetry axis of the plaque is oriented parallel to the central axes of the cylindrical detectors. Within the MC simulations, the detectors are modelled with the material properties of water.

## 4.3 Inverse Monte Carlo problem

The simulation architecture presented in this chapter is designed to model inhomogeneous surface dose profiles of $^{106}$Ru applicators. The characterisation and quantification of these inhomogeneities are carried out in accordance with the measurement procedure of the manufacturer and as outlined in subsection 2.3.1, by evaluating the surface dose profile at a distance of 1 mm from the applicator surface. For this purpose, the surface detector described in subsection 4.2.1 is employed.
The underlying problem can be formulated as an inverse MC problem, the geometry of which is shown in Figure 4.4. In this context, the desired inhomogeneous surface dose profile, recorded by the surface detector, represents the known outcome of the simulation and is expressed as the output function $g(\varphi, \vartheta)$, with the azimuthal angle $\varphi$ and the polar angle $\vartheta$. The corresponding distribution of primary particles required to produce this outcome constitutes the unknown input $v(\varphi, \vartheta)$. The challenge lies in the fact that the physical systematics of the simulation, denoted by the operator $S$, must also be taken into account, leading to the following general formulation of the inverse MC problem:

$$v(\varphi, \vartheta) = S^{-1}(g(\varphi, \vartheta)). \tag{4.3}$$

The relationship between the input particle distribution and the resulting surface dose is highly complex due to the geometry of the system and is not directly accessible. The region where the primary particles are generated, corresponding to the input distribution $v(\varphi, \vartheta)$, is spatially separated from the scoring surface, where the surface dose $g(\varphi, \vartheta)$ is recorded, by approximately 1.1 mm. This separation is not planar but follows a concave curvature and comprises the two distinct materials, water and silver.
The combined effects of this curved geometry, the material interfaces, and the physical interaction processes render an analytical description of particle trajectories impractical. Consequently, alternative numerical strategies must be employed to approximate the inverse relationship.
A conventional method for addressing inverse problems through simulation involves optimising a set of parameters that define the target function by minimising a chosen objective function. This process necessitates performing multiple forward simulations while iteratively varying the parameter set, which can rapidly lead to excessive computational demands [96]. In Refs. [12, 13], an approach was investigated in which the data provided in the measurement certificates of the manufacturer are used directly as input. In this method, the spatial distribution of $^{106}$Ru atoms within the target is mapped according to the information specified in the certificates. However, attempts to combine this approach with various iterative procedures to determine a suitable scaling operator, $S$ or $S^{-1}$, do not yield a successful solution to the inverse MC problem.

Building upon this strategy, Ref. [12] explored the decomposition of the overall scaling factor $S$ into its systematic components, which are subsequently approximated using fit functions. Nevertheless, this method also results in considerable discrepancies between the simulated and desired dose profiles.
A revised strategy adopting an inverse approach was therefore introduced in Ref. [12], leading to the development of a simulation technique capable of reproducing inhomogeneous surface dose profiles. Within this framework, the inverse problem is spatially decomposed, allowing for a systematic incremental solution. This concept, along with the simulation architecture for modelling inhomogeneous surface dose distributions, is described in detail in sections 4.4 to 4.6.

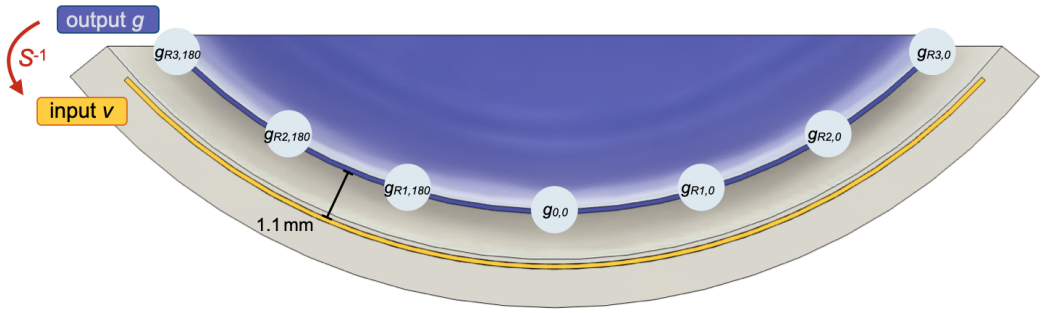


Figure 4.4: Scheme of the cross-section illustrating the geometry of the inverse MC problem. The blue surface represents the scoring region, where the relative dose rate values from the centre and certificate measurement rings $R_1$, $R_2$, and $R_3$, correspond to the desired simulation output $g$. The input to the simulations consists of a distribution of $^{106}$Ru primary particles generated within the yellow target model. Due to the 0.1 mm silver exit window and a 1 mm gap filled with water, the two calottes are separated. The transformation from the output $g$ to the input $v$ requires the consideration of the systematics operator $S^{-1}$, which is not directly accessible. This figure is adapted from Ref. [12].

## 4.4 Phase space file generation

In Figure 4.1, it is shown that the process of phase space file generation forms the foundation for the subsequent steps in the MC simulation of inhomogeneous surface dose profiles.
A phase space file consists of a dataset recording the position, direction, energy, particle type, and additional parameters for each particle crossing a defined scoring geometry. Such files are widely used in radiotherapy, where precise treatment planning relies on a well-characterised radiation source. As commercial therapy units are limited and key components are often reused in simulations, pre-validated phase space files are employed to reduce computational time. These files serve as primary particle sources, removing the need for detailed machine geometry, which is often proprietary [97].
To address the inverse problem described in section 4.3, phase space files are generated for each applicator model included in this work. These files contain the data required for particle generation, including the spatial coordinates at which primary $^{106}$Ru atoms are emitted. The generation of the phase space files is based on the cylindrical detectors, whose geometry

follows the measurement configuration of the manufacturer, as outlined in subsection 4.2.2. In this setup, the cylindrical detectors act as scorers, and the primary vertices of particles reaching these detectors are recorded using the backtracking method described below.
Since the CCB and COB applicator models have larger diameters than the CCA model (Table A.18), three additional rings of cylindrical detectors are introduced for these models to ensure sufficient phase space coverage of the entire surface. For the CCB model, the additional detector rings are placed at polar angles of $\vartheta = 8°$, 24°, and 40°, while for the COB model, they are positioned at $\vartheta = 7°$, 23°, and 38°. Each measurement ring comprises eight cylindrical detectors arranged equidistantly around the central axis, except for the rings at the polar angles $\vartheta = 7°$ and 8°, which contain seven detectors due to their smaller radius. To solve the inverse problem formulated in Equation 4.3, the problem is divided spatially into $i$ subproblems, where $i$ corresponds to the number of cylindrical detectors. Consequently, the global operator $S^{-1}$, described in section 4.3, is divided into a set of local operators $S_i^{-1}$, allowing the inverse relationship to be expressed as

$$v_i(\varphi, \vartheta) = S_i^{-1}(g_i(\varphi_i, \vartheta_i)). \tag{4.4}$$

For each cylindrical detector, a target dose value $g_i(\varphi_i, \vartheta_i)$ is defined, to replicate the inhomogeneous surface dose profile of the applicator. The objective for each detector is to determine the $^{106}$Ru primary distribution $v_i(\varphi, \vartheta)$ that reproduces the specified dose value $g_i(\varphi_i, \vartheta_i)$.

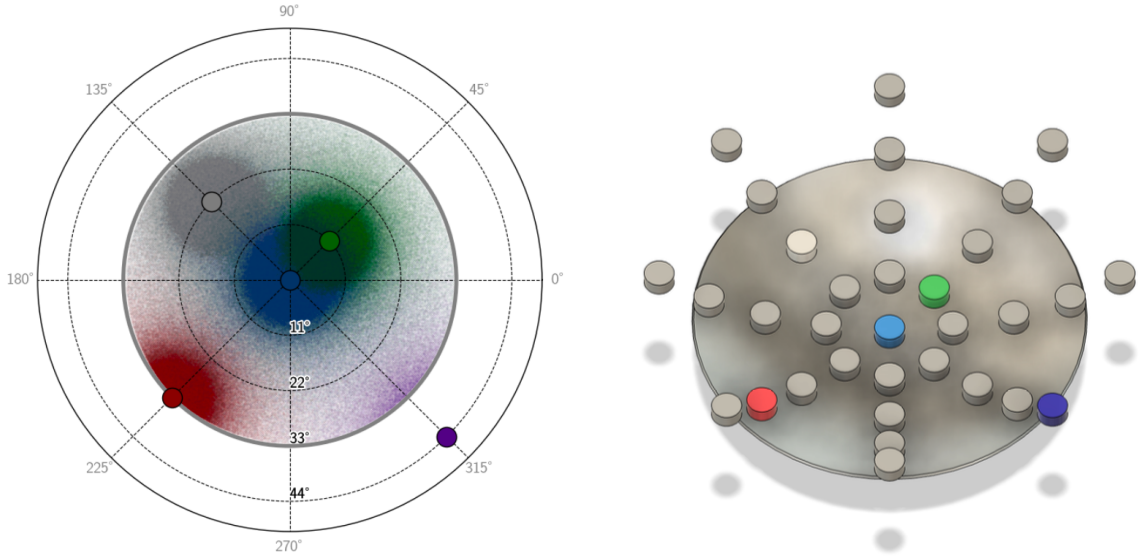


a) b)

Figure 4.5: In a), particle coordinates sampled from five phase space files for the CCA applicator model are shown as scatter points, with colours indicating the association between each detector and its backtracked particle origins. In b), the spatial positions of the cylindrical detectors above the target model are illustrated using the same colour scheme to highlight their arrangement. The figures are acquired from Ref. [12].

This inversion is realised using a backtracking method, which links dose deposition events to the corresponding $^{106}$Ru primary vertices. When a particle deposits energy within a detector, its trajectory is traced back to the originating vertex, representing the emission point of the primary atom. The resulting spatial coordinates of these vertices are stored in separate phase space files for each detector, ensuring that each vertex is counted once per file. The backtracking process thus provides $i$ distributions $v_i(\varphi, \vartheta)$, each associated with a measured dose $g_i(\varphi_i, \vartheta_i)$, effectively serving as the local inverse operators $S_i^{-1}$ [12, 98].
The spatial correlation between the phase space distributions $v_i(\varphi, \vartheta)$ and the corresponding cylindrical detector positions is demonstrated in Figure 4.5, where selected phase space coordinates are visualised to highlight their geometric association with the detector locations.
To simulate inhomogeneous surface dose distributions, it is necessary to quantify the individual contribution of primary particles from each phase space file to the recorded dose at the surface detector, enabling an appropriate weighting of particle sources.
In this work, 100 simulations with $3 \times 10^6$ particle histories are performed per applicator model to generate the phase space files. Consistent with the certificate measurements carried out by the manufacturer, water is selected as the surrounding medium.

## 4.5 Phase space file simulation

After the phase space files have been generated, the next essential step in modelling inhomogeneous $^{106}$Ru surface dose distributions is their simulation. The phase space data serve as the source for primary particle generation in the MC simulations. To randomly select emission coordinates from each phase space file, the `DataFrame.sample` function from the `Pandas`[16] library is used, which returns a stochastic subset of stored entries. These sampled coordinates are then passed to the particle generator within Geant4, where, at each sampled point, four $^{106}$Ru primaries are generated using the `G4ParticleGun` (PG), which emits particles with specified spatial and momentum characteristics [79].
Due to the rotational symmetry of the CCA and CCB applicator models, only one phase space file per measurement ring and one for the centre needs to be simulated, significantly reducing the computational workload. Accordingly, for the CCA model, simulations are performed for phase space files located at $\varphi = 0°$ and $\vartheta = 0°$, 11°, 22°, and 33°, while for the CCB model phase space files at $\varphi = 0°$ and $\vartheta = 0°$, 7°, 15°, 23°, 30°, 38°, and 45° are evaluated, ensuring adequate angular coverage. Unlike the CCA and CCB models, the COB model is not rotationally symmetric, so phase space files for all detectors on the mirror-symmetric axis must be simulated individually. The positions and numbers of the cylindrical detectors serving as the basis for the simulated phase space files for the CCA, CCB and COB applicator models are listed in Table A.19. The surface detector described in subsection 4.2.1 is employed to record the dose, and the surrounding medium is set to water.
Since phase space sampling restricts particle production to a subset of the target area rather than the full source, each phase space file is simulated using 100 runs with $3 \times 10^5$ particle histories per run, which provides sufficient statistical precision for determining weighting factors. In Figure 4.6 an example of a resulting surface dose distribution from the simulation of a single phase space file for the COB applicator is presented, which is measured using the surface detector.

[16] Pandas, Python library [2]. `https://pandas.pydata.org`.

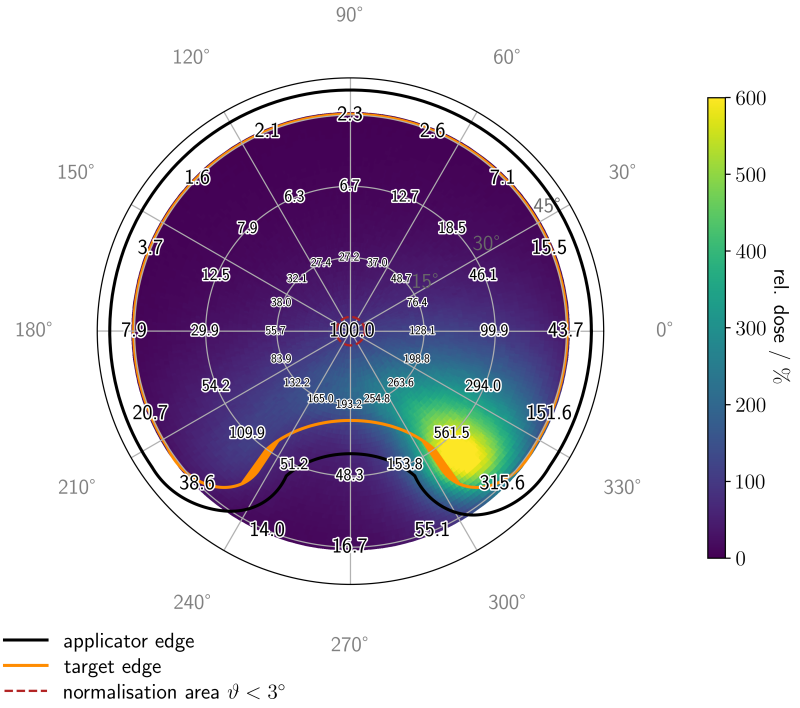


Figure 4.6: Surface dose distribution recorded with the surface detector at a distance of 1 mm from the COB applicator, obtained from the simulation of the phase space file associated with the cylindrical detector positioned at $\vartheta = 45°$ and $\varphi = 285°$. The dose values are normalised to 100 % in the central region ($\vartheta < 3°$), corresponding to the spherical base area of the reference detector of the manufacturer and consistent with the certificate normalisation procedure. The normalisation factor is determined by averaging the dose in the azimuthal direction and applying a constant fit $d(\vartheta) = a, \vartheta \in [0°, 3°]$ to the central region (Figure A.9). To maintain a clear visual representation, the statistical uncertainties ($< 8.2\,\%$) for the dose values are not shown.

The aim of employing phase space files in this work is to approximate the full surface dose distribution of the applicator. In principle, an infinite number of phase space files would be required to fully resolve the surface dose, and their use therefore constitutes an approximation. To achieve a sufficiently high spatial resolution of the dose distribution, the phase space files and the corresponding simulation results are rotated azimuthally for the rotationally symmetric applicators using 3D matrix operations. For the COB model, which exhibits mirror symmetry rather than rotational symmetry, the data are reflected accordingly. This procedure ensures a better coverage of the entire applicator surface.

## 4.6 Simulation of inhomogeneous surface dose profiles

Once phase space files have been generated for each applicator model and their individual contributions to the surface dose distribution have been established through dedicated simulations using the surface detector, the basis for modelling inhomogeneous surface dose profiles

is complete. Building upon this foundation, inhomogeneities in the dose distribution can now be introduced and simulated.
Two complementary approaches are employed. For the simulation of hot spots, described in subsection 4.6.1, particle generation is performed using the GPS in combination with the PG. In contrast, the method detailed in subsection 4.6.2 for simulating cold spots, as well as combined hot- and cold-spot configurations, relies exclusively on the phase space coordinates as input to the PG.
As illustrated in Figure 4.1, the modelling of inhomogeneous surface dose profiles builds upon the reference surface dose distribution recorded with the surface detector in the homogeneous simulation presented in chapter 3. Furthermore, both simulation strategies incorporate calculations of weighting factors to account for the individual contributions of particles originating from the phase space files to the resulting surface dose distribution.

### 4.6.1 Hot spot simulation

The simulation of hot spots is achieved by combining the homogeneous particle generation method presented in chapter 3, utilising the GPS, with the phase-space-based particle generation method described in section 4.5, which employs the PG. This combined approach allows for the controlled introduction of localised inhomogeneities and was developed in Refs. [12, 13].
To generate a surface dose profile containing one or more hot spots, the baseline distribution recorded by the surface detector in a homogeneous simulation with the GPS is used as a reference. This baseline is subsequently augmented with additional particle distributions derived from the coordinates stored in the phase space files. The overlay of the homogeneous dose profile with these selected phase-space-derived distributions ensures a smoother and more representative surface dose profile than would be achieved using phase space files alone, which only provide an approximate representation of the full surface dose distribution of the applicator.
As described in section 4.5, the simulation of each individual phase space file provides the corresponding surface dose distribution for the coordinates derived from that file. The contribution of each phase-space-derived distribution to the overall surface dose is then determined by the energy per particle relative to the homogeneous baseline. This ratio defines a weighting factor, which scales the number of primaries sampled from each phase space file, enabling precise control over the intensity and spatial placement of hot spots. By combining contributions from multiple phase space files, complex inhomogeneities can be generated at different locations.
The dose contributions from the homogeneous baseline and each phase space distribution are assessed independently using the surface detector. These contributions are then combined using weighting factors, allowing the optimisation of hot spot configurations entirely in Python and providing preview dose profiles without the need for repeated Geant4 simulations. In Figure 4.7, an example of the weighted superposition of these distributions is visualised.
After determining the appropriate weights, a verification simulation is carried out in Geant4. For this, the particle generation by the GPS and PG is adjusted according to these weights. The resulting surface dose distribution is recorded by the surface detector.

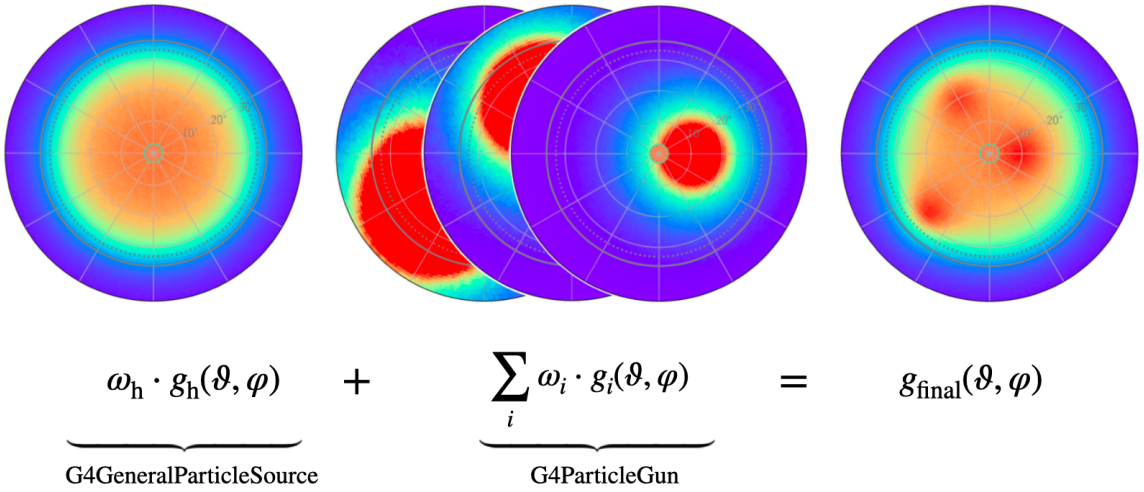


Figure 4.7: Example of the combination of the homogeneous dose distribution $g_h(\vartheta, \varphi)$, weighted with $\omega_h$, and three phase-space-derived components $g_i(\vartheta, \varphi)$, weighted with $\omega_i$, yielding the final profile $g_{final}(\vartheta, \varphi)$. The figure is taken from Ref. [12] and has been adapted for the present work.

### 4.6.2 Simulation of cold spots and combined inhomogeneities

The approach described in subsection 4.6.1 for modelling and simulating hot spots, which combines the homogeneous particle generation method using the GPS (chapter 3) with the phase-space-based particle generation method using the PG (section 4.5), is not suitable for simulating cold spots in the surface dose profile.

During particle generation in Geant4, the PG method can only generate particles at specified input locations. Using the GPS to create a baseline particle distribution is not suitable for simulating cold spots, because there is no mechanism within the Geant4 framework to locally reduce the number of particles once generated. Consequently, the simulation of cold spots, as well as combined hot and cold spots, relies entirely on the PG, with the coordinates of the $^{106}$Ru primaries taken from the phase space files as the basis for particle generation.

When the GPS is not used, sufficient coverage of the target geometry by the phase space files must be ensured in order to accurately approximate the full surface dose distribution. To achieve this, as described in section 4.5, the number of phase space files is increased by applying 3D rotations for the CCB and CCA applicators, and reflection transformations for the COB applicator (Table A.19).

To model cold spots and combined inhomogeneities, the homogeneous surface dose distribution, originally generated with uniformly distributed primary particles using the GPS as described in chapter 3, is first approximated using the phase space distributions. The dose values at the cylindrical detector positions within each measurement ring are extracted from the homogeneous surface dose profile and serve as target values for a subsequent optimisation procedure.

In this work, a numerical optimisation approach is developed to determine phase space weights that reproduce the specified target dose values at the cylindrical detector positions. The optimisation is performed using `scipy.optimize.minimize` from the `SciPy`[17] frame-

[17]SciPy, Python library. `https://scipy.org`.

work [99]. For a given set of candidate weights, the surface dose distribution is reconstructed by summing the contributions of the individual phase space components scaled by the candidate weights, and the resulting dose values are compared to the target values.
For the COB model, the optimiser minimises the objective function $E(\mathbf{w})$,

$$E(\mathbf{w}) = \sum_{i=1}^{n} \sum_{j=1}^{c} \left( D_{i,j}^{\mathrm{phsp}}(\mathbf{w}) - D_{i,j}^{\mathrm{tar}} \right)^2 ,$$

where $D_{i,j}^{\mathrm{phsp}}(\mathbf{w})$ is the surface dose calculated from the phase space distributions in ring $i$ and cylindrical detector position $j$ for a given weight vector $\mathbf{w}$, $D_{i,j}^{\mathrm{tar}}$ is the reference dose from the homogeneous simulation, $n$ is the number of measurement rings, and $c$ is the number of cylindrical detectors per ring (Table A.19). The vector $\mathbf{w} = (w_1, w_2, \dots, w_m)$ collects all weights applied to the $m$ phase space datasets. For the COB applicator, 117 weights are optimised.
Due to the rotational symmetry, the optimisation for the CCA and CCB applicators is simplified. For the CCA applicator, three independent weights are optimised for its three measurement rings, while the CCB applicator required six weights for its six rings because of its bigger size. Within each ring, all azimuthal phase space distributions share the same weight.
For a given set of candidate weights $\mathbf{w}$, the surface dose distribution is reconstructed by superposing the individual phase space contributions scaled by $\mathbf{w}$. The mean dose values in the $n$ measurement rings, $\bar{D} = (\bar{D}_1, \bar{D}_2, \dots, \bar{D}_n)$, are then calculated and compared with the corresponding target values $\bar{D}^{\mathrm{tar}} = (\bar{D}_1^{\mathrm{tar}}, \bar{D}_2^{\mathrm{tar}}, \dots, \bar{D}_n^{\mathrm{tar}})$, which are likewise averaged over each ring.
The optimiser minimises a weighted least-squares objective function $\chi^2(\mathbf{w})$, where $\sigma_i$ are tolerance parameters assigned to each ring:

$$\chi^2(\mathbf{w}) = \sum_{i=1}^{n} \left( \frac{\bar{D}_i - \bar{D}_i^{\mathrm{tar}}}{\sigma_i} \right)^2 .$$

The Powell algorithm, a derivative-free optimisation method based on sequential one-dimensional minimisations along conjugate directions, is used for all applicator models [99]. The optimisation starts from an initial guess and iteratively evaluates candidate weight vectors until convergence. The resulting weights are then used to reconstruct the final surface dose distribution and are validated through dedicated Geant4 simulations.
The optimised phase space weights are used to model surface dose inhomogeneities such as cold spots and combined hot- and cold-spot configurations. To establish a homogeneous reference, the weights are first normalised such that a total of 3,000,000 particles is generated. This value is chosen to enable statistically robust results across 100 simulations of equal size, which is detailed in section 3.8. The corresponding particle numbers per phase space file are then obtained directly from the normalised weights.
By manually adjusting the particle numbers for selected phase space files and automatically recalculating the associated weights, cold spots and combined inhomogeneities are created. The modified weights are subsequently imported into Geant4, where the PG generates the specified number of primaries per phase space file to simulate the resulting surface dose distribution.

## 4.7 Results

This section presents the results of a set of studies evaluating the methodology introduced in this chapter for simulating inhomogeneous surface dose profiles. In subsection 4.7.1, the surface dose profiles obtained using the surface detector are compared with those measured using the cylindrical detectors. Subsequently, subsection 4.7.2 provides a comparison between the surface dose profiles recorded by the cylindrical detectors and those reported in the measurement certificates of the manufacturer. This is followed by the validation of the phase-space-based $^{106}$Ru applicator simulation in subsection 4.7.3. Finally, in subsection 4.7.4, the surface dose distributions predicted by the Python-based method are compared with those obtained from MC simulations to assess the performance of the developed methodology.

Throughout the studies, reference is made to measurement rings R1, R2, and R3. These correspond to the convention for measurement point positions established based on the certificates of the manufacturer and illustrated in Figure 4.3.
All simulations performed in this chapter are conducted using a total of 300,000,000 particles, split across 100 simulations. The only exception concerns the hot spot simulations used in subsection 4.7.4, which automatically have a higher particle count achieved through superposition.

### 4.7.1 Detector comparison

In this study, both detector architectures introduced in section 4.2 are utilised. To investigate the extent of the differences in the surface dose profiles measured with the two detector types, homogeneous MC simulations are performed for all three applicator models using the simulation architecture presented in chapter 3, which relies solely on the GPS for primary particle generation. For each model, one simulation is carried out with the surface detector and one with the cylindrical detectors.

Table 4.1: Absolute minimum, $|\Delta D|_{\text{min}}$, and maximum differences, $|\Delta D|_{\text{max}}$, as well as the mean difference, $\Delta D_{\text{mean}}$, of the surface dose values measured with the surface detector relative to those of the cylindrical detectors for measurement rings R1, R2, and R3. All surface dose values are normalised to 100 % at the centre, consistent with the certificates of the manufacturer. The differences are calculated by subtracting the cylindrical detector values from those of the surface detector. The unit pp denotes percentage points.

| $\Delta D$ / pp | CCA | CCB | COB |
|---|---|---|---|
| $\lvert\Delta D\rvert_{\text{min, R1}}$ | 0.1 ± 1.0 | 0.1 ± 1.2 | 0.1 ± 1.1 |
| $\lvert\Delta D\rvert_{\text{max, R1}}$ | 1.4 ± 0.9 | 2.2 ± 1.2 | 3.5 ± 0.9 |
| $\Delta D_{\text{mean, R1}}$ | 0.0 ± 0.3 | −0.2 ± 0.4 | 1.2 ± 0.4 |
| $\lvert\Delta D\rvert_{\text{min, R2}}$ | 0.0 ± 0.7 | 0.1 ± 1.0 | 0.4 ± 0.9 |
| $\lvert\Delta D\rvert_{\text{max, R2}}$ | 1.9 ± 0.9 | 1.5 ± 1.0 | 1.7 ± 0.7 |
| $\Delta D_{\text{mean, R2}}$ | 0.9 ± 0.3 | −0.2 ± 0.3 | 0.4 ± 0.3 |
| $\lvert\Delta D\rvert_{\text{min, R3}}$ | 2.8 ± 0.4 | 3.0 ± 0.6 | 0.1 ± 0.2 |
| $\lvert\Delta D\rvert_{\text{max, R3}}$ | 4.3 ± 0.5 | 5.2 ± 0.6 | 4.4 ± 0.5 |
| $\Delta D_{\text{mean, R3}}$ | 3.7 ± 0.2 | 4.0 ± 0.2 | 3.4 ± 0.2 |

Since the surface detector covers the entire surface dose profile rather than measuring the dose at selected positions, as it is the case with the cylindrical detector setup, the positions of the scored dose values from the cylindrical detectors are correspondingly identified on the surface detector for the comparison. The differences are calculated by subtracting the cylindrical detector values from those of the surface detector.
For all applicator models, the maximum difference for each of the three measurement rings, $|\Delta D|_{\text{max}}$, remains below 6 pp[18], with the highest value observed in the third measurement ring, R3. While the mean difference, $\Delta D_{\text{mean}}$, is below 1.6 pp in the first two rings, R1 and R2, it exceeds 3 pp in R3 (Table 4.1).
The tendency towards higher doses in the surface detector measurements, particularly in R3, can be attributed to the positioning of the detector relative to the applicator. Whereas the cylindrical detectors are oriented parallel to the centre of the applicator, each measurement point of the surface detector is positioned at the same distance parallel to the inner surface of applicator. This uniform distance results in greater dose deposition in the surface detector, especially at the edges where the dose gradient is steep.

### 4.7.2 Comparison of simulated surface dose profiles with manufacturer certificates

The QA process described in section 4.1 is performed for every applicator, and the corresponding surface dose rate values measured by the manufacturer are documented in individual measurement certificates provided for each applicator. To assess the agreement between the certificate measurements and the simulations carried out in this work, the surface dose profile recorded by the cylindrical detectors, which replicate the measurement setup of the manufacturer, is compared with the values reported in the certificates for each applicator model. For each applicator, the measurement data are averaged over five certificate sets, whose certificate numbers and dates of issue are listed in Table A.20. The MC simulations used for this comparison are homogeneous simulations performed using the simulation architecture presented in chapter 3.
In Figure 4.8, the averaged surface dose profile obtained from the measurement certificates is shown alongside the simulated surface dose profile for the COB applicator. The corresponding dose values for the other two applicator models are provided in section A.6.
The averaged surface dose profile from the certificates is compared with the homogeneous surface dose profile obtained from the MC simulation for each applicator model. The differences are calculated by subtracting the cylindrical detector values from those of the measurement certificates. For all three applicator models, clear deviations between the surface dose profile values can be observed, with the dose rate values reported in the certificates being significantly higher, particularly in the third measurement ring, R3 (Table 4.2, Figure 4.8). For each applicator model, the absolute maximum deviation $|\Delta D|_{\text{max, R3}}$ in the third measurement ring exceeds 30 pp, and the mean deviation $\Delta D_{\text{mean, R3}}$ is greater than 25 pp. While the deviations for the two rotationally symmetric applicator models are similar across the three measurement rings, those for the COB applicator are substantially larger. For the COB model, $\Delta D_{\text{mean, R1}}$ is $(15.4 \pm 4.5)$ pp, and the maximum absolute deviations on R2 and R3 exceed 70 pp. The mean deviation on R2 for the COB applicator is $(16.9 \pm 0.7)$ pp, whereas

[18] The unit pp denotes percentage points.

for the other two models it remains below 6.6 pp. In the third measurement ring, R3, the mean deviation for the COB applicator is $(58.5 \pm 0.7)$ pp.

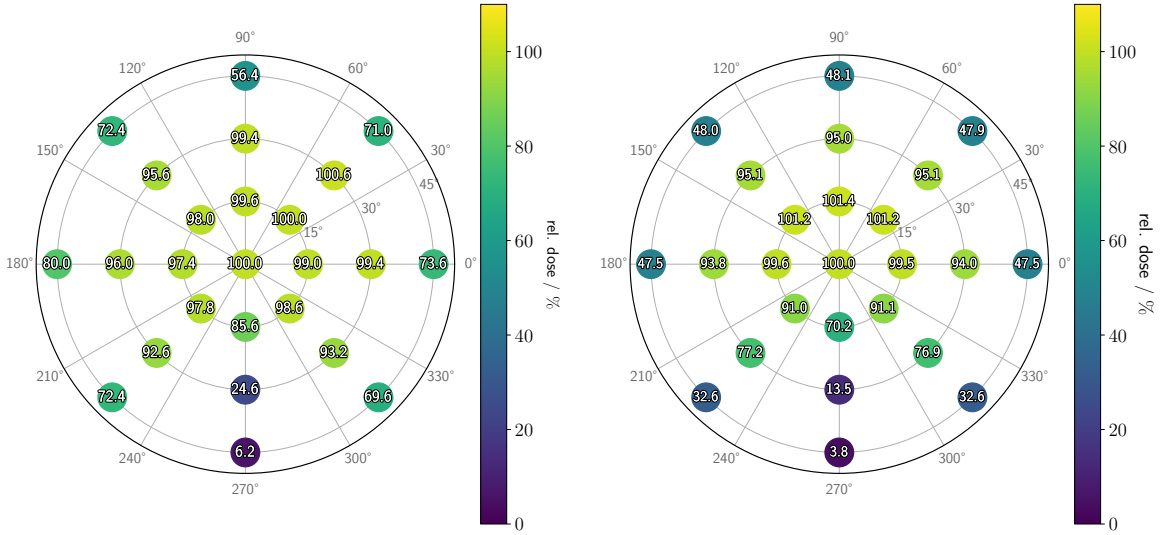


a) b)

Figure 4.8: Surface dose profiles for the COB applicator model. In a), the surface dose rate values averaged from five manufacturer certificates are depicted. In b), the homogeneous surface dose values from the MC simulation, recorded with the cylindrical detectors, are shown. The surface dose values of the simulation are normalised to 100 % at the centre, consistent with the certificates of the manufacturer.

Table 4.2: Absolute minimum, $|\Delta D|_{\text{min}}$, and maximum differences, $|\Delta D|_{\text{max}}$, as well as the mean difference, $\Delta D_{\text{mean}}$, of the mean surface dose rate values of five measurement certificates from the manufacturer relative to the dose values of the cylindrical detectors for measurement rings R1, R2, and R3. The surface dose values of the simulation are normalised to 100 % at the centre, consistent with the certificates of the manufacturer. The differences are calculated by subtracting the cylindrical detector values from those of the measurement certificates. The unit pp denotes percentage points.

| $\Delta D$ / pp | CCA | CCB | COB |
|---|---|---|---|
| $\lvert\Delta D\rvert_{\text{min, R1}}$ | 0.6 ± 1.4 | 0.3 ± 0.9 | 0.5 ± 1.3 |
| $\lvert\Delta D\rvert_{\text{max, R1}}$ | 3.2 ± 1.5 | 1.2 ± 1.5 | 15.4 ± 4.5 |
| $\Delta D_{\text{mean, R1}}$ | 0.1 ± 0.5 | −0.3 ± 0.5 | 2.6 ± 0.7 |
| $\lvert\Delta D\rvert_{\text{min, R2}}$ | 1.5 ± 1.2 | 3.4 ± 2.1 | 2.9 ± 1.1 |
| $\lvert\Delta D\rvert_{\text{max, R2}}$ | 8.7 ± 1.7 | 6.9 ± 3.2 | 72.1 ± 4.5 |
| $\Delta D_{\text{mean, R2}}$ | 5.7 ± 0.7 | 5.3 ± 0.9 | 16.9 ± 0.7 |
| $\lvert\Delta D\rvert_{\text{min, R3}}$ | 24.8 ± 3.9 | 18.6 ± 4.4 | 49.9 ± 1.3 |
| $\lvert\Delta D\rvert_{\text{max, R3}}$ | 34.7 ± 1.6 | 35.0 ± 6.6 | 81.8 ± 4.5 |
| $\Delta D_{\text{mean, R3}}$ | 30.9 ± 1.2 | 25.7 ± 1.5 | 58.5 ± 0.7 |

### 4.7.3 Validation of phase-space-based $^{106}$Ru applicator simulation

To validate the phase-space-based simulation methodology described in subsection 4.6.2, it is compared with the previously employed approach presented in chapter 3. For each applicator model, a homogeneous simulation is performed using primary particles generated by the GPS. In addition, a homogeneous surface dose distribution is modelled based on phase space files, which is then simulated using the PG together with the phase space files.
In Figure 4.9, the transverse dose profiles for both simulations for the three applicator models is shown. The profiles represent the mean dose in the azimuthal direction, plotted as a function of the polar angle $\vartheta$.

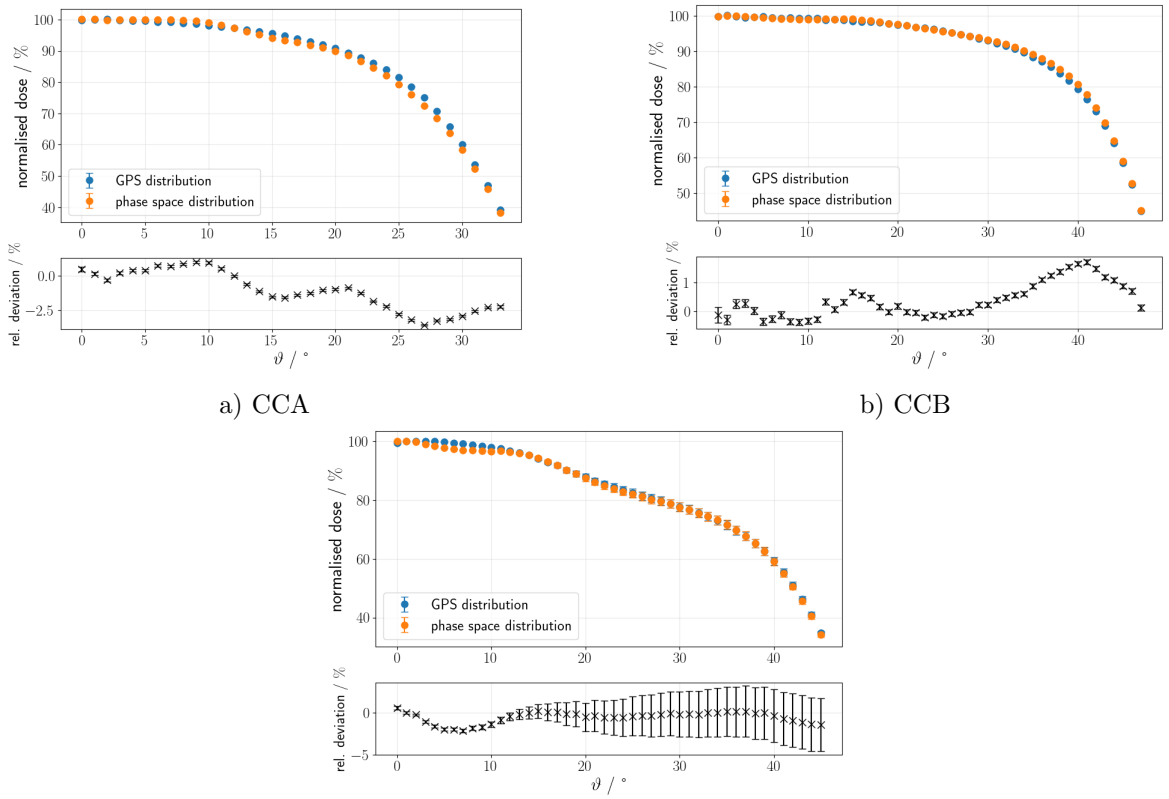


a) CCA

b) CCB

c) COB

Figure 4.9: Comparison of the transverse dose profiles corresponding to the surface dose distributions of the phase-space-based simulation and the GPS-based simulation for the three applicator models. The surface dose distributions are recorded with the surface detector at a distance of 1 mm from the applicator and are shown in section A.7. The profiles represent the mean dose in the azimuthal direction, plotted as a function of the polar angle $\vartheta$. The dose values are normalised to 100 % in the central region.

The results show that the transverse dose profiles from both simulations agree for all applicator models, with relative deviations of up to 5 %. The uncertainty in the data for the COB applicator is higher than for the rotationally symmetric models, due to the greater

statistical uncertainty in the region corresponding to the optic nerve, which arises from the lower particle count.
The pattern of the relative deviation curves indicates the regions in the polar direction where the coverage provided by the phase space files is insufficient for a perfect modelling of the surface dose. However, it should be noted that the number of phase space files does not necessarily need to be too low to achieve the desired dose, as the curves also show that the phase-space-based simulation can sometimes yield higher dose values. Nevertheless, the number of phase space files does influence the optimisation algorithms used to determine the weights for modelling the distribution, where a higher number of phase space files can improve fine-tuning.
In Figure 4.10, the deviations between the GPS-based simulation and the phase-space-based simulation are shown, where the deviation is defined as the segment-wise difference between the respective surface dose values for the CCB and COB applicators. The corresponding surface dose profiles obtained using the two simulation methods, together with those for the CCA model and their respective difference distributions, are shown in section A.7.

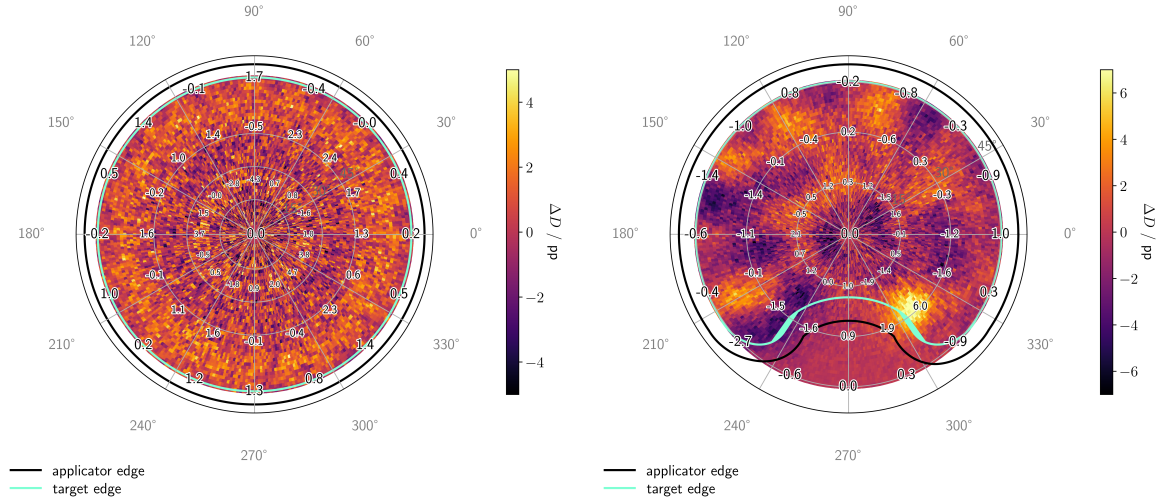


a) CCB b) COB

Figure 4.10: Deviation between the GPS-based homogeneous surface dose profile and the phase-space-based surface dose profile for the two applicator models. The deviation is calculated as the segment-wise difference by subtracting the phase-space-based values obtained using the PG from those of the GPS-based simulation. The corresponding surface dose profiles, as well as the results for the CCA applicator, are shown in section A.7.

For the rotationally symmetric applicators, the deviation across the entire surface dose profile between the two methods remains below 5 pp. For the COB applicator, the deviations remain below 7 pp, although in contrast to the rotationally symmetric models, the COB applicator exhibits a more inhomogeneous distribution of differences. The surface dose profile of the COB applicator generated using the phase space files shows clusters of positive and negative deviations when compared with the corresponding GPS-based profile. This arises from the considerably more complex optimisation required for this applicator. While the algorithm for

the CCB and CCA models determines a single weight for each cylindrical detector ring plus the central detector, the absence of rotational symmetry in the COB applicator necessitates determining an individual weight for every cylindrical detector (Table A.19). This results in a total of 117 variables and consequently leads to a more inhomogeneous distribution.
When comparing the absolute minimum and maximum differences, as well as the mean difference, for the three measurement rings of the surface dose profiles, the overall trend is confirmed that the surface dose profiles obtained from the two simulations conducted using different methods are in good agreement (Table 4.3). For the rotationally symmetric models, CCA and CCB, the largest maximum absolute deviation occurs on the first measurement ring of the CCB applicator and amounts to $(4.7 \pm 1.9)$ pp. For the COB applicator, the highest maximum deviation of $(6.0 \pm 1.1)$ pp is observed on the second measurement ring. The mean deviation for all measurement rings and all models remains below 1.5 pp.

Table 4.3: Absolute minimum, $|\Delta D|_{\text{min}}$, and maximum differences, $|\Delta D|_{\text{max}}$, as well as the mean difference, $\Delta D_{\text{mean}}$, of the surface dose values measured with the surface detector for the GPS-based simulation relative to the phase-space-based simulated values are presented for measurement rings R1, R2, and R3. All surface dose values are normalised to 100 % at the centre, in accordance with the certificates of the manufacturer. The differences are calculated by subtracting the phase-space-based values obtained using the PG from those of the GPS-based simulation. The unit pp denotes percentage points.

| $\Delta D$ / pp | CCA | CCB | COB |
|---|---|---|---|
| $\lvert\Delta D\rvert_{\text{min, R1}}$ | 0.0 ± 1.2 | 0.0 ± 1.6 | 0.0 ± 1.4 |
| $\lvert\Delta D\rvert_{\text{max, R1}}$ | 3.6 ± 1.4 | 4.7 ± 1.9 | 2.1 ± 1.6 |
| $\Delta D_{\text{mean, R1}}$ | 0.9 ± 0.3 | 0.5 ± 0.4 | 0.3 ± 0.4 |
| $\lvert\Delta D\rvert_{\text{min, R2}}$ | 0.0 ± 1.0 | 0.1 ± 1.2 | 0.1 ± 1.3 |
| $\lvert\Delta D\rvert_{\text{max, R2}}$ | 2.6 ± 1.1 | 2.4 ± 1.4 | 6.0 ± 1.1 |
| $\Delta D_{\text{mean, R2}}$ | −0.6 ± 0.3 | 1.0 ± 0.3 | 0.0 ± 0.3 |
| $\lvert\Delta D\rvert_{\text{min, R3}}$ | 0.2 ± 0.6 | 0.0 ± 0.8 | 0.0 ± 0.2 |
| $\lvert\Delta D\rvert_{\text{max, R3}}$ | 1.8 ± 0.7 | 1.7 ± 1.0 | 2.7 ± 0.6 |
| $\Delta D_{\text{mean, R3}}$ | 0.9 ± 0.2 | 0.6 ± 0.2 | 0.5 ± 0.2 |

### 4.7.4 Comparison of Python-predicted and simulated surface dose distributions

Before an inhomogeneous surface dose distribution is simulated, it is first modelled in Python, as described in section 4.6. To validate this approach, a scenario-specific comparison is made between the Python-predicted and simulated surface dose distributions. For each of the three applicator models, a hot spot, a cold spot, and a combined scenario, situated near the limits defined by the QA criteria described in section 4.1, are modelled and simulated. The details of these scenarios are provided in chapter 5.
The inhomogeneous primary particle distributions modelled in Python based on phase space files are simulated using the workflow illustrated in Figure 4.1 and detailed in this chapter. The resulting surface dose profiles are recorded with the surface detector and subsequently compared with the Python-predicted profiles. The deviation is calculated as the segment-wise difference by subtracting the predicted values from the simulated values.

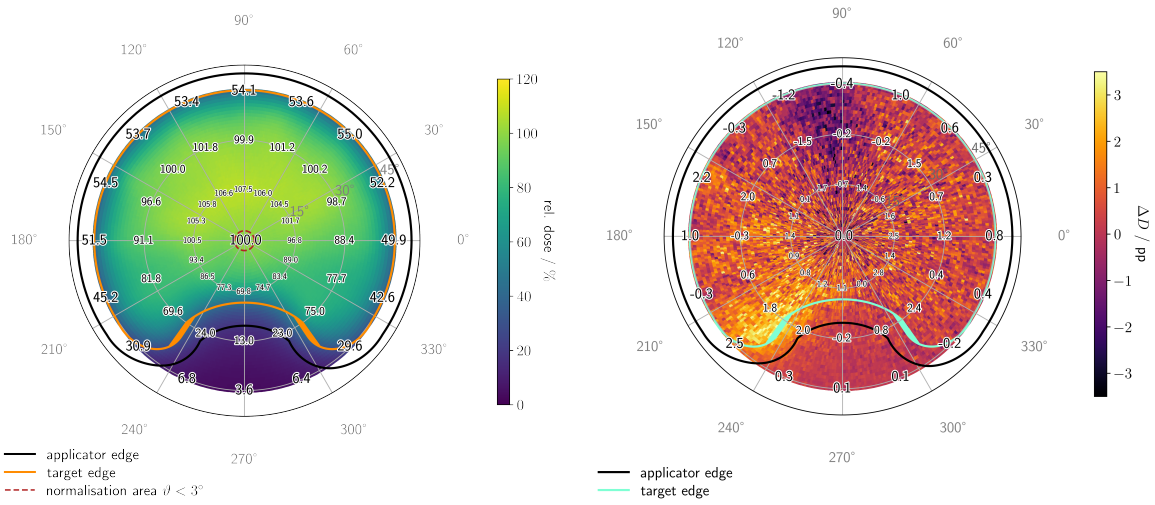


a) b)

Figure 4.11: Surface dose profiles for the cold spot scenario of the COB applicator. In a), the Python-predicted surface dose distribution is shown, and in b), the deviation from the corresponding MC-simulated distribution. The deviation is calculated as the segment-wise difference by subtracting the predicted values from the simulated values.

Table 4.4: Absolute minimum, $|\Delta D|_{\text{min}}$, and maximum differences, $|\Delta D|_{\text{max}}$, as well as the mean difference, $\Delta D_{\text{mean}}$, of the Python-predicted surface dose values relative to those of the MC simulation, recorded with the surface detector, for measurement rings R1, R2, and R3. For all three applicator models, a hot spot scenario (HS), a cold spot scenario (CS), and a combined scenario (HC) are considered. All surface dose values are normalised to 100 % at the centre, in accordance with the certificates of the manufacturer. Differences are calculated by subtracting the Python-predicted values from those of the simulation. The unit pp denotes percentage points.

| | CCA | | | CCB | | | COB | | |
|---|---|---|---|---|---|---|---|---|---|
| $\Delta D$ / pp | HS | CS | HC | HS | CS | HC | HS | CS | HC |
| $\lvert\Delta D\rvert_{\text{min, R1}}$ | 0.0 | 0.1 | 0.1 | 0.0 | 0.0 | 0.0 | 0.1 | 0.0 | 0.0 |
| $\lvert\Delta D\rvert_{\text{max, R1}}$ | 0.3 | 2.1 | 2.2 | 0.5 | 2.7 | 4.2 | 1.3 | 2.8 | 3.0 |
| $\Delta D_{\text{mean, R1}}$ | 0.1 | 0.2 | 0.4 | -0.1 | 0.4 | 0.9 | 0.3 | 1.0 | -0.2 |
| $\lvert\Delta D\rvert_{\text{min, R2}}$ | 0.1 | 0.1 | 0.0 | 0.0 | 0.1 | 0.0 | 0.0 | 0.2 | 0.3 |
| $\lvert\Delta D\rvert_{\text{max, R2}}$ | 0.5 | 1.8 | 1.4 | 0.2 | 1.7 | 3.3 | 1.5 | 2.4 | 2.5 |
| $\Delta D_{\text{mean, R2}}$ | 0.1 | -0.8 | -0.3 | 0.1 | -0.1 | 1.4 | 0.1 | 0.7 | -0.5 |
| $\lvert\Delta D\rvert_{\text{min, R3}}$ | 0.0 | 0.0 | 0.1 | 0.0 | 0.1 | 0.2 | 0.0 | 0.1 | 0.0 |
| $\lvert\Delta D\rvert_{\text{max, R3}}$ | 0.2 | 1.2 | 1.0 | 0.6 | 1.1 | 2.5 | 0.7 | 2.5 | 1.9 |
| $\Delta D_{\text{mean, R3}}$ | 0.1 | -0.2 | -0.1 | 0.1 | 0.2 | 1.3 | 0.1 | 0.4 | -0.1 |

In Figure 4.11, an example of a Python-predicted surface dose distribution is shown together with the deviation from the corresponding MC-simulated distribution.

With a highest absolute maximum deviation, $|\Delta D|_{\text{max}}$, of 4.2 pp in the first measurement ring of the COB applicator for the hot spot scenario, it is evident that the Python-predicted distributions agree well with the simulated distributions (Table 4.4). This is further supported by the mean deviations, $\Delta D_{\text{mean}}$, which are all below 1.5 pp.

## 4.8 Discussion

In this chapter, a simulation architecture for inhomogeneous surface dose profiles of the $^{106}$Ru applicators has been presented. The underlying inverse MC problem, which concerns the determination of the primary particle distribution required for the simulation, is spatially decomposed into smaller subproblems. Using the backtracking method, dose deposition events in a homogeneous simulation recorded by a set of cylindrical detectors, which measure the surface dose profile, are linked to their corresponding $^{106}$Ru primary vertices. These coordinates, together with additional physical quantities, are stored in phase space files. The generation and subsequent simulation of phase space files form the basis for approximating the solution to the inverse Monte Carlo problem. The simulated particle distributions contained in the phase space files serve as the foundation for weighting the dose contributions of the primary particles generated by each file, thereby allowing the reconstruction of the desired inhomogeneous surface dose profile.
For the simulation of hot spot scenarios, a homogeneous particle distribution generated via the GPS is superimposed with primary particles from the phase space files, simulated using the PG, to reproduce the required hot spots. The simulation of cold spot and combined inhomogeneity scenarios, on the other hand, is performed solely using the primary particles generated by the PG from the phase space files. For this purpose, a numerical optimisation approach is developed to determine the phase space weights that yield the desired target distribution.

For the inhomogeneous simulations, both detector geometries introduced in section 4.2 are employed. The cylindrical detectors replicate the setup used in the measurement certificates of the manufacturer, where the surface dose profile is represented by 25 measurement points distributed across the first three measurement rings. In contrast, the surface detector enables the recording of the surface dose profile with higher spatial resolution. It is positioned such that it lies parallel to the applicator surface, rather than parallel to the central axis of the applicator as in the case of the cylindrical detectors.
For all applicator models, a homogeneous simulation comparing both geometries shows that the maximum difference across the three measurement rings, $|\Delta D|_{\text{max}}$, remains below 6 pp, and the mean difference, $|\Delta D|_{\text{mean}}$, below 4.5 pp (Table 4.1). The largest deviations occur in the third ring, corresponding to the applicator edge, likely because the constant parallel distance of the surface detector leads to greater dose deposition near steep dose gradients.

The quantification of the inhomogeneity of the surface dose profile for a $^{106}$Ru applicator is provided by the measurement certificates of the manufacturer. A comparison of the mean values from five certificates per model with the surface dose values recorded by the cylindrical detectors in homogeneous simulations reveals significant deviations. In particular, the dose values reported in the certificates are substantially higher in the third measurement ring, with mean deviations, $\Delta D_{\text{mean, R3}}$, of $(30.9 \pm 1.2)$ pp for the CCA model, $(25.7 \pm 1.5)$ pp for the CCB model, and $(58.5 \pm 0.7)$ pp for the COB model (Table 4.2).

The discrepancy between the certificate values and the simulation results may arise from several factors. Firstly, the values listed in the certificates represent experimentally measured dose rate values of an inhomogeneous surface dose profile, whereas the dose values obtained with the cylindrical detectors correspond to a simulated homogeneous surface dose profile. Although averaging five certificates per applicator model reduces the influence of local inhomogeneities, this alone does not account for the large deviations observed, particularly at the edges of the applicators. A larger number of certificates would allow for a more robust comparison.
Additional differences between experiment and simulation must therefore be considered. In the measurements of the manufacturer, slight deviations in detector positioning relative to the idealised cylindrical detector setup used in the simulation may occur. Differences arising from CAD modelling of the applicators may also contribute to discrepancies between the real and simulated applicators. Moreover, the cylindrical detectors employed in the simulation do not replicate the actual scintillation volumes used by the manufacturer. In Geant4, the detector is modelled with the material properties of water. Therefore, geometric and material differences may contribute to the discrepancy.
Furthermore, the Cherenkov effect may influence the comparison. In measurements using scintillators, Cherenkov radiation can contribute to the detected signal, whereas in the Geant4 simulations, the Cherenkov photons do not distort the quantity of interest. This difference may have a significant impact, particularly in regions with steep dose gradients, such as at the edge of the applicator.
To further evaluate the certificate measurements and analyse the reasons for the observed discrepancies between experimental and simulated values, a measurement setup that accounts for the Cherenkov effect and avoids potential geometric differences arising from the simulation could be employed. The development of such a setup is the subject of a parallel PhD thesis [100].

The newly developed methodology of phase-space-based simulation, including the numerical optimisation approach for calculating the phase space weights required to reproduce the target surface dose profile in the PG simulation, is validated by comparison with a distribution generated using the GPS.
The transverse dose profiles from both simulations show good agreement for all applicator models, with relative deviations of up to 5 % (Figure 4.9), and the mean deviation across all measurement rings and models remains below 1.5 pp (Table 4.3). The results further demonstrate that the number of phase space files generated for the three applicator models is sufficient to approximate the solution of the inverse problem using the numerical optimisation approach. This allows the generation of the required primary particle distributions and the simulation of the desired surface dose profiles.
In the case of the COB applicator, the homogeneous GPS-based distribution could be reproduced using the phase space files with maximum deviations of $|\Delta D|_{\text{max, R1}} = (2.1 \pm 1.6)\,\text{pp}$, $|\Delta D|_{\text{max, R2}} = (6.0 \pm 1.1)\,\text{pp}$ and $|\Delta D|_{\text{max, R3}} = (2.7 \pm 0.6)\,\text{pp}$. However, cluster-like deviations occur in the resulting surface dose profile (Figure 4.10b). These inhomogeneities arise from the optimisation procedure described in subsection 4.6.2, which requires determining 117 weights for the COB applicator. Future work could investigate whether improvements to the optimisation algorithm or the use of alternative approaches, such as neural networks, might yield more accurate results.

To validate the modelling of inhomogeneous surface dose distributions using Python, the Python-predicted and simulated surface dose distributions are compared for several inhomogeneity scenarios. For all scenarios, the mean deviations, $\Delta D_{\mathrm{mean}}$, remain below 1.5 pp across all measurement rings. This confirms that the Python-based modelling provides a reliable basis for simulating inhomogeneous surface dose distributions across different scenarios. However, it should be noted that only three scenarios are examined for each applicator model, so larger deviations cannot be completely disregarded in specific cases. Therefore, for all inhomogeneity scenarios considered in this work, a simulation using the surface detector is performed to ensure that the simulated distributions meet the expected behaviour.

Overall, the new simulation approach allows for the reliable modelling of inhomogeneous $^{106}$Ru surface dose profiles.
It is important to emphasise that the generation and simulation of individual phase space files, which form the basis for calculating the weights of the respective distributions, require computational effort. However, this process needs to be performed only once for each applicator model to be simulated. Moreover, the Python-based predictive modelling reduces computational resource requirements, as no simulations are required for the modelling itself. The simulation architecture described in this chapter is employed in chapter 5 to investigate the impact of inhomogeneous surface dose profiles on the treatment of intraocular tumours.

# 5 Clinical impact of inhomogeneous surface dose distributions

In clinical practice, the inhomogeneities of the surface dose profile of the $^{106}$Ru applicators can only be considered in an approximate manner. In most cases, they are neither accounted for in the simulation of the applicator dose distributions nor can their effects on the tumour dose and on organs at risk be accurately quantified. This may lead to undesirable effects in therapy. For instance, a cold spot could compromise the prescribed tumour control dose, particularly at the tumour margin, as the steep dose gradient in this region increases the risk of underdosage. Conversely, hot spots may result in the scleral tolerance dose being exceeded or may generally increase the risk of damage to nearby organs at risk.
This chapter investigates the influence of inhomogeneous surface dose distributions on the treatment of intraocular tumours with $^{106}$Ru eye applicators. For this, the software workflow introduced in chapter 3 is combined with the MC simulation methodology presented in chapter 4.

In section 5.1, various inhomogeneity scenarios are modelled and the corresponding surface dose profiles are simulated in combination with a patient-specific eye model. This includes worst-case scenarios, which approach or exceed the limits defined in the QA for the applicators. In addition, best-case scenarios are examined to investigate the potential beneficial effects of inhomogeneous surface dose profiles on treatment outcomes. The parameters required for the treatment evaluation are presented in section 5.2. Subsequently, the results of the simulations are analysed in section 5.3 through three case studies, each representing one of the three applicator models, CCA, CCB and COB, and are discussed in section 5.4 with regard to their clinical relevance.

## 5.1 Modelling of inhomogeneity scenarios

As a basis for the simulations investigating the influence of inhomogeneous $^{106}$Ru surface dose profiles on treatment, representative patient cases are modelled, which is described in subsection 5.1.1. In addition, a homogeneous simulation is performed for each case, which is detailed in subsection 5.1.2, to provide a reference for the analysis of the inhomogeneity scenarios presented in subsection 5.1.3.

### 5.1.1 Patient cases

For the studies in this chapter, three patient cases are created in Fusion using the methods described in section 3.2. The patient cases are fictitious but are modelled based on real clinical data. One case is created for each of the three applicator models. The tumour heights, measured from the tumour base to the apex, are 4.2 mm for the CCA case, 5.0 mm

for the CCB case, and 4.7 mm for the COB case. An overview of the geometries of the three patient cases is shown in Figure 5.1.

**Phase space file shift:** The integration of patient-specific data into the generic eye model results in a displacement of the applicator to ensure full coverage of the tumour base. Consequently, the particle coordinates contained in the phase space files used for the MC simulations, whose generation is described in section 4.4, must also be shifted accordingly. The rotational and translational operations applied to perform this shift from the original position are stored as a rotation matrix and a translation vector, allowing the coordinates within the phase space files to be adjusted consistently with the displacement of the applicator. Furthermore, any rotation of the applicator around its own axis is represented by an additional rotation matrix and applied analogously to the phase spaces.

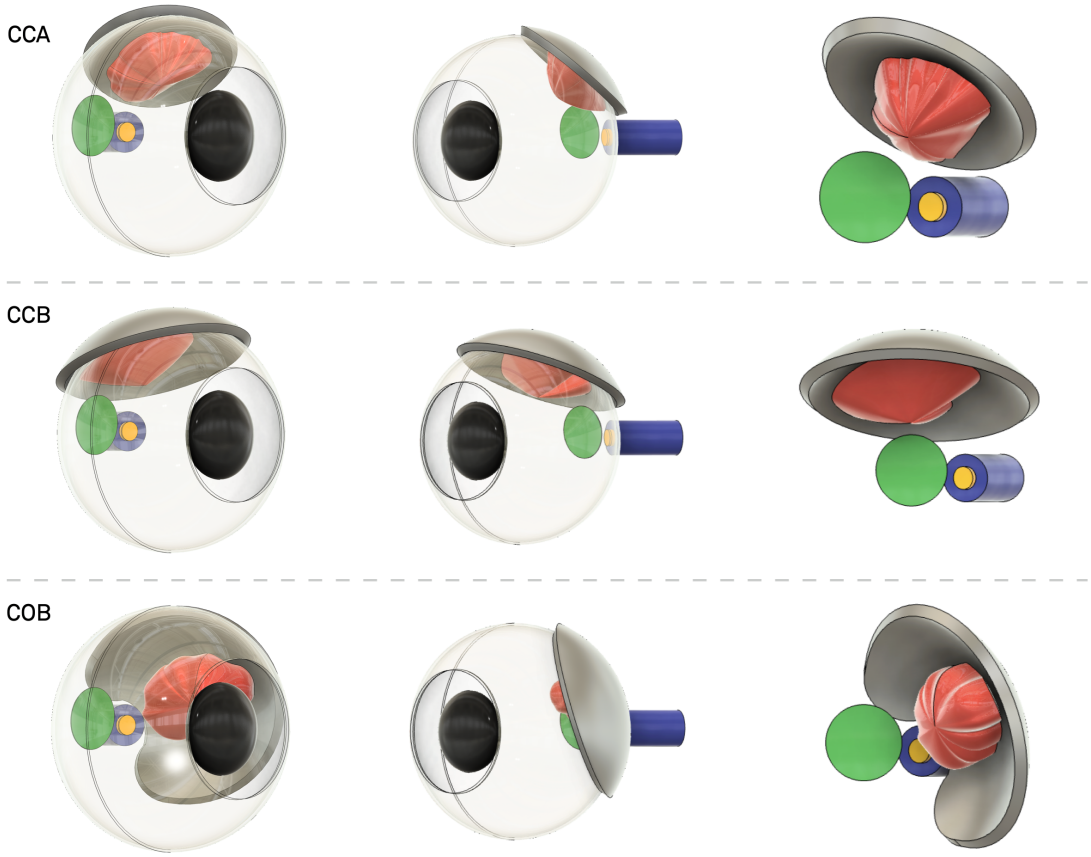


Figure 5.1: Overview of the modelled patient cases shown from three perspectives. The top, middle, and bottom rows present the cases with the CCA, CCB, and COB applicators, respectively. In all cases, the applicator is illustrated in grey, the fovea in green, the papilla in yellow, the tumour in red, the sclera in white, the optic nerve in blue, and the lens in black.

### 5.1.2 Homogeneous reference scenario

To assess the impact of inhomogeneous surface dose profiles on the dose distributions within the individual ocular structures, a homogeneous reference simulation is performed for each

of the three patient models. This simulation is conducted using the workflow introduced in chapter 3, employing 300,000,000 particles distributed across 100 runs.
In addition to the simulations performed with the eye model, simulations using the surface detector are carried out for each applicator model to determine the surface dose profile. The resulting characteristic parameters of the surface dose profiles for the three applicator models are listed in Table 5.1 and the corresponding homogeneous surface dose profiles are presented as part of the figures shown in section A.7.

Table 5.1: Values characterising the homogeneous surface dose profiles for the three applicator models, with the source non-uniformity $U_{\mathrm{NU}}$ and and source asymmetry $U_{\mathrm{AS}}$. All surface dose values $D$ are normalised to 100 % at the centre, in accordance with the certificates of the manufacturer. $D_{\mathrm{max,\,R}i}$ and $D_{\mathrm{min,\,R}i}$ represent the maximum and minimum normalised dose values on measurement ring R$i$ ($i$ = 1,2,3), corresponding to the measurement certificates. For the COB applicator, values between 240° and 300° for the second and third measurement rings are excluded from the determination of the minimum, as these lie outside the target and do not meaningfully contribute to the characterisation of the surface dose profile. The uncertainty of all listed values is below 2.3 %.

| | CCA | CCB | COB |
|---|---|---|---|
| $U_{\mathrm{AS,R1}}$ / % | 4.0 | 5.4 | 4.8 |
| $U_{\mathrm{AS,R2}}$ / % | 2.6 | 3.4 | 3.9 |
| $U_{\mathrm{NU}}$ / % | 12.0 | 9.4 | 7.2 |
| $D_{\mathrm{max,\,R1}}$ / % | 100.0 | 101.0 | 104.0 |
| $D_{\mathrm{max,\,R2}}$ / % | 90.3 | 93.2 | 96.5 |
| $D_{\mathrm{max,\,R3}}$ / % | 47.6 | 53.9 | 51.6 |
| $D_{\mathrm{min,\,R1}}$ / % | 96.1 | 95.7 | 73.7 |
| $D_{\mathrm{min,\,R2}}$ / % | 88.0 | 90.6 | 78.4 |
| $D_{\mathrm{min,\,R3}}$ / % | 45.9 | 51.6 | 36.2 |

### 5.1.3 Inhomogeneous scenarios

The inhomogeneous surface dose profiles are modelled using the method described in section 4.6. In this work, the influence of hot spot (HS), cold spot (CS), and combined (HC) distributions is studied for each of the three applicator models. For each type of inhomogeneity and patient case, two worst-case (WC) scenarios are examined. In the case of cold spots, the worst-case corresponds to a cold spot located at the tumour margin, where the steep lateral dose fall-off may reduce the delivered dose in a region that is critical for local tumour control. For hot spots, the worst-case scenario occurs when the hot spot is located at the edge, close to the organs at risk.
One of the worst-case scenarios lies at one or both of the limits (QA) defined in section 4.1, meaning that the source non-uniformity $U_{\mathrm{NU}}$ and source asymmetry $U_{\mathrm{AS}}$ must not exceed 20 %. The other worst-case scenario exceeds one or both of those limits (QA+) to assess the potential impact of inadequate or incorrect QA on treatment and to evaluate the appropriateness of the limits. The values characterising the surface dose profiles for the hot spot scenarios are presented in Table 5.2, while those for the cold spot scenarios are listed in Table 5.3.

Table 5.2: Values characterising the modelled hot spot surface dose profiles for the three applicator models. All surface dose values $D$ are normalised to 100 % at the centre, in accordance with the certificates of the manufacturer. $D_{\text{max, R}i}$ represents the maximum normalised dose values on measurement ring R$i$ ($i = 1,2,3$), corresponding to the measurement certificates. The uncertainty of all listed values is below 2.5 %.

| | CCA | | CCB | | COB | |
|---|---|---|---|---|---|---|
| | $\text{HS}_{\text{QA}}$ | $\text{HS}_{\text{QA+}}$ | $\text{HS}_{\text{QA}}$ | $\text{HS}_{\text{QA+}}$ | $\text{HS}_{\text{QA}}$ | $\text{HS}_{\text{QA+}}$ |
| $U_{\text{AS,R1}}$ / % | 7.5 | 9.8 | 8.0 | 9.9 | 9.9 | 15.2 |
| $U_{\text{AS,R2}}$ / % | 20.2 | 29.6 | 20.2 | 30.8 | 4.8 | 29.6 |
| $U_{\text{NU}}$ / % | 13.9 | 14.7 | 10.3 | 19.1 | 20.3 | 21.6 |
| $D_{\text{max, R1}}$ / % | 102.6 | 104.3 | 103.4 | 105.1 | 113.3 | 113.6 |
| $D_{\text{max, R2}}$ / % | 104.7 | 113.0 | 109.0 | 119.1 | 101.6 | 112.7 |
| $D_{\text{max, R3}}$ / % | 68.4 | 79.3 | 81.2 | 99.1 | 57.1 | 83.3 |

Table 5.3: Values characterising the modelled cold spot surface dose profiles for the three applicator models. All surface dose values $D$ are normalised to 100 % at the centre, in accordance with the certificates of the manufacturer. $D_{\text{min, R}i}$ represents the minimum normalised dose values on measurement ring R$i$ ($i = 1,2,3$), corresponding to the measurement certificates. For the COB applicator, values between 240° and 300° for the second and third measurement rings are excluded from the determination of the minimum, as these lie outside the target and do not meaningfully contribute to the characterisation of the surface dose profile. The uncertainty of all listed values is below 2.5 %.

| | CCA | | CCB | | COB | |
|---|---|---|---|---|---|---|
| | $\text{CS}_{\text{QA}}$ | $\text{CS}_{\text{QA+}}$ | $\text{CS}_{\text{QA}}$ | $\text{CS}_{\text{QA+}}$ | $\text{CS}_{\text{QA}}$ | $\text{CS}_{\text{QA+}}$ |
| $U_{\text{AS,R1}}$ / % | 6.3 | 10.0 | 6.9 | 8.7 | 13.6 | 14.7 |
| $U_{\text{AS,R2}}$ / % | 11.5 | 27.6 | 14.6 | 27.3 | 16.5 | 24.9 |
| $U_{\text{NU}}$ / % | 19.8 | 32.0 | 20.1 | 29.2 | 12.8 | 21.8 |
| $D_{\text{min, R1}}$ / % | 95.6 | 92.5 | 95.5 | 92.9 | 68.7 | 66.6 |
| $D_{\text{min, R2}}$ / % | 80.2 | 68.0 | 79.9 | 70.8 | 67.8 | 59.5 |
| $D_{\text{min, R3}}$ / % | 34.7 | 27.1 | 41.8 | 34.6 | 28.3 | 26.0 |

For the combined inhomogeneity distributions, a best-case scenario (BC) is also modelled in addition to the two worst-case scenarios. In this case, the cold spot is located at the organs at risk, potentially reducing their dose, while the hot spot is positioned centrally beneath the tumour. The plaque is placed slightly off-centre relative to the tumour to ensure that the cold spot at the margin does not lead to underdosing of the tumour. This scenario also lies at one or both of the QA limits.
All distributions are additionally simulated using the surface detector instead of the eye model to cross-check whether the Python-modelled surface dose profile meets expectations. The simulated surface dose distributions for all inhomogeneity scenarios modelled in this

chapter are provided in section A.8. Each scenario simulated in this chapter employs 300,000,000 particles, divided over 100 simulations per inhomogeneous distribution.

Table 5.4: Values characterising the modelled combined hot and cold spot surface dose profiles for the three applicator models. Since the CCA and CCB applicators are rotationally symmetric, the values of the worst-case (WC) scenario also describe those of the best-case (BC) scenario for these models, as the applicator is rotated to meet the BC requirements described above. All surface dose values $D$ are normalised to 100 % at the centre, in accordance with the certificates of the manufacturer. $D_{\text{max, R}i}$ and $D_{\text{min, R}i}$ represent the maximum and minimum normalised dose values on measurement ring R$i$ ($i$ = 1,2,3), corresponding to the measurement certificates. For the COB applicator, values between 240° and 300° for the second and third measurement rings are excluded from the determination of the minimum, as these lie outside the target and do not meaningfully contribute to the characterisation of the surface dose profile. The uncertainty of all listed values is below 2.5 %.

| | CCA | | CCB | | COB | | |
|---|---|---|---|---|---|---|---|
| | $\text{HC}_{\text{QA}}^{\text{WC}}$ | $\text{HC}_{\text{QA+}}^{\text{WC}}$ | $\text{HC}_{\text{QA}}^{\text{WC}}$ | $\text{HC}_{\text{QA+}}^{\text{WC}}$ | $\text{HC}_{\text{QA}}^{\text{WC}}$ | $\text{HC}_{\text{QA+}}^{\text{WC}}$ | $\text{HC}_{\text{QA}}^{\text{BC}}$ |
| $U_{\text{AS,R1}}$ / % | 5.2 | 9.9 | 5.0 | 8.0 | 7.0 | 13.0 | 12.2 |
| $U_{\text{AS,R2}}$ / % | 20.9 | 31.3 | 19.7 | 28.8 | 14.8 | 28.5 | 21.2 |
| $U_{\text{NU}}$ / % | 19.5 | 27.0 | 18.0 | 20.6 | 16.5 | 27.5 | 11.2 |
| $D_{\text{max, R1}}$ / % | 102.5 | 103.3 | 101.2 | 103.3 | 103.9 | 103.4 | 111.2 |
| $D_{\text{max, R2}}$ / % | 99.0 | 100.4 | 100.0 | 106.0 | 99.1 | 103.0 | 109.9 |
| $D_{\text{max, R3}}$ / % | 57.7 | 56.6 | 65.6 | 74.5 | 54.8 | 57.1 | 58.7 |
| $D_{\text{min, R1}}$ / % | 97.3 | 93.5 | 97.1 | 95.4 | 75.6 | 76.9 | 72.0 |
| $D_{\text{min, R2}}$ / % | 80.5 | 73.0 | 82.0 | 79.4 | 83.5 | 72.5 | 63.0 |
| $D_{\text{min, R3}}$ / % | 34.7 | 29.3 | 44.0 | 41.8 | 36.1 | 34.4 | 27.1 |

## 5.2 Parameters for treatment evaluation

To assess the effects of the inhomogeneous $^{106}$Ru surface dose profiles on the treatment of intraocular tumours, specific parameters are considered for treatment evaluation.
According to the dose concept of the UME, as described in subsection 2.3.2, a tumour control dose of $(85 \pm 15)$ Gy within the tumour volume is aimed for. Taking into account the uncertainties, detailed in subsection 2.3.3, and the inclusion of safety margins, the dose is normalised to 130 Gy at the tumour apex, provided that the scleral contact dose is at least 700 Gy. Otherwise, the scleral contact dose is normalised to this target value. The following parameters are considered to evaluate the irradiation of the tumour:

- $V_{100\,\text{Gy}}^{\text{tumour}}$: The relative volume of the tumour receiving at least 100 Gy. To ensure sufficient destruction of tumour tissue, and accounting for systematic treatment uncertainties, $V_{100\,\text{Gy}}^{\text{tumour}} \geq 99\,\%$ is required.
- $D_{\text{min}}^{\text{tumour}}$: The minimum dose received by the tumour allows categorisation of tumour control. At least 99 % of the tumour volume should receive $\geq$ 100 Gy to ensure adequate destruction while accounting for systematic treatment uncertainties. If 99% of the tumour volume receives 85 to 100 Gy, the treatment is considered acceptable.

Irradiation of 99% of the tumour volume within 70 to 85 Gy is regarded as suboptimal, posing a risk of insufficient tumour control, while irradiation $\leq 70$ Gy is unacceptable.

In section 3.6, dose constraints for conventional radiotherapy and ophthalmic brachytherapy are outlined. In relation to the evaluation of inhomogeneous dose distributions to the structures at risk, the following parameters are employed for treatment assessment:

- $D_{\text{max}}^{\text{sclera}}$: To avoid structural damage such as scleral perforation, the maximum dose to the sclera should not exceed 1500 Gy.
- $D_{\text{max}}^{\text{papilla}}$: To avoid the development of radiation-induced optic neuropathy, the maximum dose to the papilla and the optic nerve should remain below 50 Gy, as higher doses are associated with an approximately 50 % probability of neuropathy of grade $\geq 1$.
- $D_{\text{max}}^{\text{fovea}}$: To minimise the associated risk of radiation retinopathy, visual acuity loss, and blindness, the maximum dose to the fovea should remain below 52 Gy.

## 5.3 Case study analysis

In this section, the MC simulation results for the various inhomogeneity scenarios are presented. For each patient case, which differs in geometry and the applicator model used, the effects of the inhomogeneous surface dose profile on the treatment evaluation parameters are analysed separately.
For this purpose, the dose at the tumour apex is normalised to 130 Gy for every case and each scenario considered, following the dose concept of the UME. To investigate whether reducing the apex dose, and thus decreasing the dose to the structures at risk, compromises the required tumour control dose, an additional normalisation to an apex dose of 100 Gy is performed for each scenario. The normalisation is performed using the depth-dose curve, as described in subsection 3.5.3.
Since the destruction of the tumour volume is the highest priority in treatment, the two cold spot scenarios are further examined for the CCB case at different tumour heights to assess the influence of cold spots on tumour control under varying tumour dimensions. For this analysis, the apex height of the modelled tumour in Fusion is reduced from 5 mm to 2.5 mm and 3.5 mm, and increased to 6.5 mm. These cases, along with the homogeneous reference case, are simulated accordingly.

### 5.3.1 Case study 1: CCA applicator

For this patient case, the tumour does not infiltrate the fovea or the papilla, and the distance to these structures is sufficiently large such that the CCA applicator does not overlap them (Figure 5.1). The inhomogeneous surface dose profiles are generated such that the inhomogeneity is positioned on the side of the target facing the fovea. In the combined worst-case scenario, the hot spot is directed towards the fovea and the cold spot towards the opposite side. In the best-case scenario, this configuration is reversed. The treatment evaluation parameters for the various CCA applicator treatment scenarios, for both apex dose normalisations, are listed in Table 5.5.

Table 5.5: Evaluation parameters for the various CCA applicator treatment scenarios for a tumour with a height of 4.2 mm. The volume $V_{100\,\mathrm{Gy}}^{\mathrm{tumour}}$ is calculated as the relative percentage of the total structure, and all dose values are normalised to the tumour apex dose $D_{\mathrm{A}}$.

| study | $D_{\mathrm{A}}$/ Gy | $V_{100\,\mathrm{Gy}}^{\mathrm{tumour}}$ / % | $D_{\mathrm{min}}^{\mathrm{tumour}}$ / Gy | $D_{\mathrm{max}}^{\mathrm{sclera}}$ / Gy | $D_{\mathrm{max}}^{\mathrm{papilla}}$ / Gy | $D_{\mathrm{max}}^{\mathrm{fovea}}$ / Gy |
|---|---|---|---|---|---|---|
| homogeneous | 130 | 99.7 | 131.9 ± 0.5 | 666.9 ± 0.6 | 27.2 ± 0.2 | 75.1 ± 0.4 |
| | 100 | 99.7 | 101.4 ± 0.4 | 513.0 ± 0.5 | 20.9 ± 0.1 | 57.8 ± 0.3 |
| $\mathrm{HS_{QA}}$ | 130 | 99.7 | 135.1 ± 0.5 | 665.7 ± 1.1 | 31.7 ± 0.2 | 90.8 ± 0.5 |
| | 100 | 99.7 | 103.9 ± 0.4 | 512.1 ± 0.8 | 24.4 ± 0.1 | 69.9 ± 0.4 |
| $\mathrm{HS_{QA+}}$ | 130 | 99.7 | 136.8 ± 0.5 | 667.9 ± 0.6 | 33.9 ± 0.1 | 98.6 ± 0.4 |
| | 100 | 99.7 | 105.2 ± 0.4 | 512.9 ± 0.5 | 26.1 ± 0.1 | 75.8 ± 0.3 |
| $\mathrm{CS_{QA}}$ | 130 | 99.8 | 124.3 ± 0.4 | 644.6 ± 2.3 | 19.9 ± 0.1 | 54.8 ± 0.4 |
| | 100 | 99.5 | 95.6 ± 0.3 | 495.9 ± 1.8 | 15.3 ± 0.1 | 42.2 ± 0.3 |
| $\mathrm{CS_{QA+}}$ | 130 | 99.8 | 118.7 ± 1.2 | 655.1 ± 0.8 | 17.2 ± 0.1 | 46.2 ± 0.4 |
| | 100 | 98.5 | 91.3 ± 0.9 | 503.9 ± 0.6 | 13.3 ± 0.1 | 35.5 ± 0.3 |
| $\mathrm{HC_{QA}^{WC}}$ | 130 | 99.7 | 136.8 ± 0.5 | 646.0 ± 0.9 | 28.3 ± 0.2 | 84.1 ± 0.5 |
| | 100 | 99.6 | 105.2 ± 0.4 | 498.9 ± 0.5 | 21.8 ± 0.1 | 64.7 ± 0.4 |
| $\mathrm{HC_{QA+}^{WC}}$ | 130 | 99.7 | 136.1 ± 0.6 | 651.2 ± 6.0 | 28.9 ± 0.2 | 84.5 ± 0.5 |
| | 100 | 99.7 | 104.7 ± 0.4 | 501.3 ± 0.8 | 22.2 ± 0.1 | 65.0 ± 0.4 |
| $\mathrm{HC_{QA}^{BC}}$ | 130 | 99.8 | 126.8 ± 2.1 | 651.7 ± 0.9 | 19.7 ± 0.2 | 54.5 ± 0.5 |
| | 100 | 99.5 | 97.5 ± 1.6 | 501.3 ± 0.7 | 15.2 ± 0.1 | 41.9 ± 0.4 |

For the apex normalisation to 130 Gy, more than 99 % of the tumour volume receives at least 100 Gy in all scenarios, and the minimum tumour dose exceeds 115 Gy in all cases. The lowest minimum dose occurs in the $\mathrm{CS_{QA+}}$ scenario, with $(118.7 \pm 1.2)$ Gy, which is $(10.0 \pm 0.9)$ % lower than the minimum dose in the homogeneous simulation.
The discrepancy between the minimum dose being $\geq 100$ Gy and the fact that not 100 % of the tumour volume receives this dose arises from the truncated mean filtering procedure described in subsection 3.5.2. In this method, the upper and lower 2 % of dose values are removed to obtain a robust estimate of the central tendency of the dose values.
For the apex normalisation to 100 Gy, more than 99 % of the tumour volume receives at least 100 Gy in all scenarios except $\mathrm{CS_{QA+}}$. In this scenario, the value is 98.5 %, and the minimum tumour dose is $(91.3 \pm 0.9)$ Gy, which remains acceptable given the tumour control dose of $(85 \pm 15)$ Gy. In all scenarios except the two cold spot configurations and $\mathrm{HC_{QA}^{BC}}$, the minimum tumour dose remains above 100 Gy.

For both normalisation levels and across all scenarios, the maximum scleral dose remains below 700 Gy. Consequently, the maximum tolerable dose of 1500 Gy is not exceeded in any scenario. However, the scleral contact dose of 700 Gy required by the dose concept is likewise not achieved. In clinical practice, the treatment would therefore typically be normalised to a scleral contact dose of 700 Gy rather than to 130 Gy at the tumour apex, in order to account for therapeutic uncertainties and to ensure delivery of the required tumour control dose of $(85 \pm 15)$ Gy. As the minimum tumour dose exceeds the required tumour control dose in every scenario, such an adjustment would not be necessary for this particular patient geometry.
For the apex normalisation to 130 Gy, the maximum dose to the papilla remains below 34 Gy for all considered surface dose profiles, ensuring that the threshold of 50 Gy is not exceeded in any scenario. The highest dose deposition occurs in the $\mathrm{HS_{QA+}}$ scenario, with $(33.9 \pm 0.1)$ Gy,

which is $(24.6 \pm 1.0)$ % higher than the corresponding value in the homogeneous case. In the cold spot scenario $CS_{QA+}$, the dose to the papilla is lowest at $(17.2 \pm 0.1)$ Gy, though this scenario also yields the lowest minimum tumour dose.
For the apex normalisation to 100 Gy, the maximum dose to the papilla remains below 27 Gy for all scenarios, with the lowest value of $(13.3 \pm 0.1)$ Gy observed in the $CS_{QA+}$ scenario.
The recommended maximum dose to the fovea, defined as 52 Gy, is exceeded for the apex normalisation to 130 Gy in all scenarios except $CS_{QA+}$, in which the fovea receives a maximum of $(46.2 \pm 0.4)$ Gy. For the apex normalisation to 100 Gy, the threshold is exceeded in all scenarios except the two cold spot configurations and the $HC_{QA}^{BC}$ scenario. The lowest foveal dose is observed in the $CS_{QA+}$ scenario, with $(35.5 \pm 0.3)$ Gy.

In the best-case combined scenario, the doses to the papilla and fovea are reduced by at least 26 % compared with the homogeneous scenario, with a corresponding reduction in the minimum tumour dose of $(3.9 \pm 1.6)$ %. The modelled hot spot at the $U_{AS,R2}$ QA limit increases the maximum dose to the papilla by $(16.5 \pm 1.1)$ % and to the fovea by $(20.9 \pm 0.9)$ %. The hot spot exceeding the $U_{AS,R2}$ QA limit by 29.6 % leads to an increase in the maximum dose to the papilla by $(24.6 \pm 1.0)$ % and to the fovea by $(31.3 \pm 0.9)$ % relative to the homogeneous scenario.

### 5.3.2 Case study 2: CCB applicator

In the patient geometry irradiated with the CCB applicator, the tumour does not infiltrate the fovea or the papilla. However, a small part of the applicator lies directly above the fovea (Figure 5.1). The inhomogeneous surface dose profiles are generated such that the hot or cold spot is positioned on the part of the target facing the fovea. In the combined worst-case scenario, the hot spot faces the fovea and the cold spot the opposite side, whereas in the best-case scenario, this arrangement is reversed. The treatment evaluation parameters for the various CCB applicator treatment scenarios are listed in Table 5.6 for both apex dose normalisations.

In all scenarios and for both apex normalisations, the minimum tumour dose is $\geq 117$ Gy, and at least 98.8 % of the tumour volume receives 100 Gy or more. As described in subsection 5.3.1, the discrepancy arises from the truncated mean filtering procedure. For this patient case, this procedure results in the reported minimum tumour dose being at least 20 Gy higher than the 130 Gy apex dose used for normalisation, or at least 17 Gy higher than the 100 Gy apex dose, depending on the normalisation. The doses below the reported minimum would affect at most 1.2 % of the tumour volume in all cases. None of the inhomogeneous scenarios exhibit a deviation of the minimum tumour dose exceeding $(2.7 \pm 0.5)$ % relative to the homogeneous case. This deviation is observed in the reduction of the minimum tumour dose in the $CS_{QA}$ scenario for an apex normalisation of 130 Gy.

For an apex normalisation to 130 Gy, the scleral contact dose of 700 Gy required by the UME dose concept is exceeded in all scenarios, while the maximum dose of 1500 Gy is not reached. For an apex normalisation to 100 Gy, the maximum dose in the sclera remains below 615 Gy in all scenarios, and thus below the required scleral contact dose. As in the CCA case, this has no adverse effect on the achievement of the tumour control dose.
For an apex normalisation to 130 Gy, the maximum dose in the papilla remains below 32 Gy for all considered surface dose profiles, ensuring that the dose limit of 50 Gy is not exceeded in

any scenario. For an apex normalisation to 100 Gy, the maximum dose in the papilla remains below 24 Gy, representing a reduction of approximately 25 %. In both normalisations, the highest dose is observed in the $HS_{QA+}$ scenario, with an increase of over 32 % compared with the homogeneous case. Conversely, the $CS_{QA+}$ scenario leads to a reduction in dose of more than 26 % relative to the homogeneous case.
Regarding the maximum dose in the fovea, the dose limit of 52 Gy is clearly exceeded for both normalisations, by at least 81 Gy in the case of an apex normalisation to 130 Gy and by 52 Gy for an apex normalisation to 100 Gy.

Table 5.6: Evaluation parameters for the various CCB applicator treatment scenarios for a tumour with a height of 5.0 mm. The volume $V_{100\,\mathrm{Gy}}^{\mathrm{tumour}}$ is calculated as the relative percentage of the total structure, and all dose values are normalised to the tumour apex dose $D_{\mathrm{A}}$.

| study | $D_{\mathrm{A}}$ / Gy | $V_{100\,\mathrm{Gy}}^{\mathrm{tumour}}$ / % | $D_{\mathrm{min}}^{\mathrm{tumour}}$ / Gy | $D_{\mathrm{max}}^{\mathrm{sclera}}$ / Gy | $D_{\mathrm{max}}^{\mathrm{papilla}}$ / Gy | $D_{\mathrm{max}}^{\mathrm{fovea}}$ / Gy |
|---|---|---|---|---|---|---|
| homogeneous | 130 | 98.8 | 156.5 ± 0.5 | 770.5 ± 2.3 | 23.3 ± 0.2 | 196.9 ± 0.7 |
| | 100 | 98.8 | 120.4 ± 0.4 | 592.7 ± 1.8 | 18.0 ± 0.1 | 151.4 ± 0.6 |
| $HS_{QA}$ | 130 | 98.9 | 159.1 ± 0.5 | 782.9 ± 2.5 | 28.0 ± 0.2 | 261.7 ± 0.8 |
| | 100 | 98.8 | 122.4 ± 0.4 | 602.3 ± 1.9 | 21.5 ± 0.2 | 201.3 ± 0.6 |
| $HS_{QA+}$ | 130 | 98.9 | 157.5 ± 0.5 | 793.4 ± 1.0 | 31.1 ± 0.2 | 303.4 ± 0.9 |
| | 100 | 98.9 | 121.2 ± 0.4 | 610.3 ± 0.7 | 24.0 ± 0.2 | 233.4 ± 0.7 |
| $CS_{QA}$ | 130 | 99.0 | 152.2 ± 0.6 | 767.3 ± 2.0 | 19.6 ± 0.2 | 165.6 ± 0.8 |
| | 100 | 99.0 | 117.4 ± 0.4 | 590.2 ± 1.5 | 15.1 ± 0.2 | 127.4 ± 0.6 |
| $CS_{QA+}$ | 130 | 98.9 | 154.2 ± 1.2 | 777.3 ± 2.9 | 17.1 ± 0.2 | 134.5 ± 0.8 |
| | 100 | 98.9 | 118.6 ± 1.0 | 597.9 ± 2.2 | 13.1 ± 0.1 | 103.4 ± 0.6 |
| $HC_{QA}^{WC}$ | 130 | 98.8 | 162.7 ± 0.6 | 773.7 ± 16.7 | 25.1 ± 0.2 | 243.2 ± 1.0 |
| | 100 | 98.8 | 125.2 ± 0.5 | 595.2 ± 12.8 | 19.3 ± 0.2 | 187.1 ± 0.7 |
| $HC_{QA+}^{WC}$ | 130 | 98.9 | 162.8 ± 1.5 | 781.3 ± 3.0 | 27.8 ± 0.3 | 270.4 ± 1.1 |
| | 100 | 98.9 | 125.2 ± 1.2 | 601.0 ± 2.3 | 21.4 ± 0.2 | 208.0 ± 0.9 |
| $HC_{QA}^{BC}$ | 130 | 98.9 | 155.6 ± 1.6 | 786.3 ± 2.8 | 20.0 ± 0.2 | 169.7 ± 0.9 |
| | 100 | 98.9 | 119.7 ± 1.2 | 604.9 ± 2.2 | 15.4 ± 0.2 | 130.6 ± 0.7 |

For the present patient geometry, neither the cold spot nor the hot spot scenarios results in a significant deviation in the percentage of the tumour volume receiving 100 Gy, nor in the minimum tumour dose, compared with the homogeneous case.
The modelled hot spot at the $U_{\mathrm{AS,R2}}$ QA limit increases the maximum dose to the papilla by $(20.2 \pm 1.3)$ % and to the fovea by $(32.9 \pm 0.6)$ %. The hot spot exceeding the $U_{\mathrm{AS,R2}}$ QA limit by 30.8 % leads to an increase in the maximum dose to the papilla by $(33.5 \pm 1.4)$ % and to the fovea by $(54.1 \pm 0.7)$ % relative to the homogeneous scenario.
For both normalisations, the best-case combined scenario reduces the doses in the papilla and fovea by at least 13 %, while the minimum tumour dose decreases by less than 1 % relative to the homogeneous scenario.

### Cold spot scenarios for varying tumour heights

To evaluate how cold spots affect tumour control across different tumour dimensions, the two cold spot scenarios, $CS_{QA}$ and $CS_{QA+}$, are further analysed for tumour heights of 2.5 mm, 3.5 mm, and 6.5 mm, in addition to the apex height of 5 mm already modelled in the present CCB case.

The relative tumour volume receiving at least 100 Gy exceeds 96.5 % for both normalisation methods and all scenarios (Figure 5.2a). For tumours with apex heights of 5 mm and 6.5 mm, no differences between the two normalisation cases are observed. For the 5 mm tumour, $V_{100\,\mathrm{Gy}}^{\mathrm{tumour}}$ is 99 % in $\mathrm{CS_{QA}}$ and 98.9 % in $\mathrm{CS_{QA+}}$, which is 0.2 pp and 0.1 pp, respectively, higher than in the homogeneous scenario. This increase is attributed to the truncated mean filtering, as the minimum dose remains above 100 Gy (Figure 5.2b). For the 3.5 mm tumour, $V_{100\,\mathrm{Gy}}^{\mathrm{tumour}}$ is reduced by 0.7 pp in the $\mathrm{CS_{QA+}}$ scenario compared to the homogeneous case, and for the 2.5 mm tumour the reduction is 1 pp.

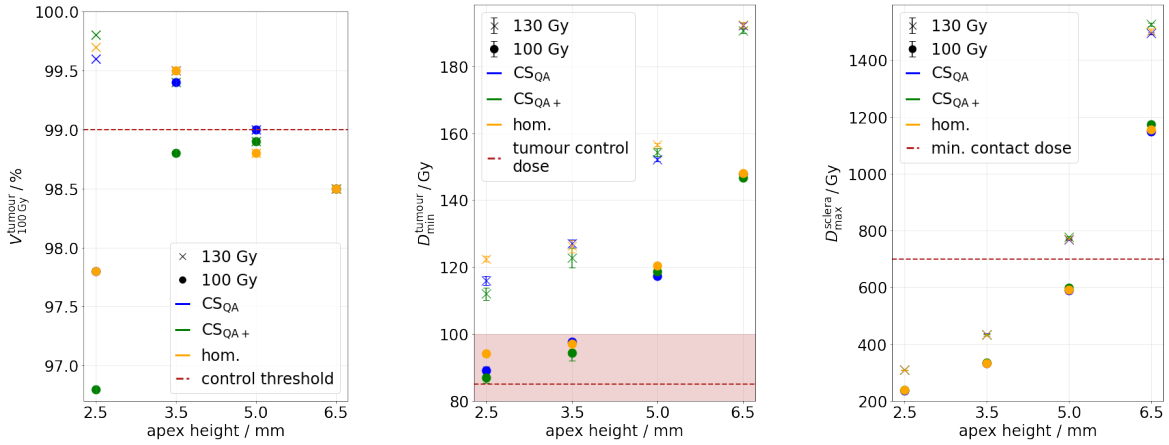


Figure 5.2: Treatment evaluation parameters with respect to tumour height for the CCB applicator case, for homogeneous and inhomogeneous surface dose distributions. The inhomogeneous distribution includes, in one scenario, a cold spot $\mathrm{CS_{QA}}$ at the edge of the $U_{\mathrm{NU}}$ QA limit, and in another scenario, a cold spot $\mathrm{CS_{QA+}}$ extending beyond the $U_{\mathrm{NU}}$ and the $U_{\mathrm{AS,R2}}$ QA limits. Each scenario is normalised to 130 Gy at the tumour apex, as well as to 100 Gy. In a), the relative tumour volume receiving at least 100 Gy is shown for the various tumour heights, in b), the minimum tumour dose is presented, and in c), the maximum scleral dose is shown.

With increasing tumour apex height, the minimum dose within the tumour and the maximum dose in the sclera rise across both normalisation approaches and all scenarios considered (Figure 5.2b, Figure 5.2c). This occurs because normalisation to the tumour apex requires a larger scaling factor when the apex is located further from the applicator, which in clinical practice corresponds to a longer treatment duration and therefore results in a higher dose delivered to the tumour volume.
For a normalisation to 130 Gy at the tumour apex, the minimum tumour dose exceeds 110 Gy in all scenarios, with the lowest value obtained in the $\mathrm{CS_{QA+}}$ scenario at $(112.0 \pm 1.9)$ Gy (Figure 5.2b). For this normalisation and for the tumours with apex heights of 5 mm and 6.5 mm, the maximum scleral dose is higher than the prescribed scleral contact dose of 700 Gy specified in the UME dose concept. For the 3.5 mm tumour, the maximum scleral dose is just above 430 Gy in all scenarios, and for the 2.5 mm tumour it is slightly above 305 Gy. Across all tumour heights, none of the cold spot scenarios deviates by more than 2 % from the maximum scleral dose obtained under homogeneous conditions. However, for the 6.5 mm

tumour, the upper limit of 1500 Gy is marginally exceeded, with a maximum scleral dose of $(1502.7 \pm 8.9)$ Gy in the homogeneous scenario and $(1526.0 \pm 5.9)$ Gy in the $CS_{QA+}$ scenario. For a normalisation to 100 Gy at the tumour apex, only the tumours with apex heights of 5 mm and 6.5 mm receive a minimum tumour dose above 100 Gy in all scenarios (Figure 5.2b). For the tumour with an apex height of 3.5 mm, the lowest minimum tumour dose occurs in the $CS_{QA+}$ scenario at $(94.3 \pm 2.2)$ Gy, which is $(2.9 \pm 2.7)$ % lower than in the homogeneous scenario. For the tumour with an apex height of 2.5 mm, the smallest minimum tumour dose is also observed in the $CS_{QA+}$ scenario at $(86.9 \pm 1.5)$ Gy, corresponding to a reduction of $(8.5 \pm 1.7)$ % compared with the homogeneous scenario. The scleral contact dose exceeds the threshold of 700 Gy, as defined in the dose concept, only for the tumour with an apex height of 6.5 mm (Figure 5.2c). The minimum required tumour dose of 85 Gy is not undershot in any scenario across all tumour heights and normalisation conditions.

### 5.3.3 Case study 3: COB applicator

In the COB patient geometry, a small part of the applicator lies directly above the fovea (Figure 5.1). The surface dose profiles are generated such that the inhomogeneity is positioned on the part of the target adjacent to the optic nerve. In the $CS_{QA+}$ scenario, the cold spot is primarily located on the side facing the fovea. In the combined worst-case scenario, the cold spot is placed on the side of the tumour opposite the optic nerve, while the hot spot lies above the fovea. The arrangement is reversed in the best-case scenario. The treatment evaluation parameters for the various COB applicator scenarios, for both apex dose normalisations, are listed in Table 5.7.

Table 5.7: Evaluation parameters for the various COB applicator treatment scenarios for a tumour with a height of 4.7 mm. The volume $V_{100\,\mathrm{Gy}}^{\mathrm{tumour}}$ is calculated as the relative percentage of the total structure, and all dose values are normalised to the tumour apex dose $D_{\mathrm{A}}$.

| study | $D_{\mathrm{A}}$/ Gy | $V_{100\,\mathrm{Gy}}^{\mathrm{tumour}}$ / % | $D_{\mathrm{min}}^{\mathrm{tumour}}$ / Gy | $D_{\mathrm{max}}^{\mathrm{sclera}}$ / Gy | $D_{\mathrm{max}}^{\mathrm{papilla}}$ / Gy | $D_{\mathrm{max}}^{\mathrm{fovea}}$ / Gy |
|---|---|---|---|---|---|---|
| homogeneous | 130 | 99.6 | 123.6 ± 0.4 | 788.9 ± 2.2 | 56.0 ± 0.3 | 110.1 ± 0.7 |
| | 100 | 99.5 | 95.1 ± 0.3 | 606.8 ± 1.7 | 43.1 ± 0.2 | 84.7 ± 0.5 |
| $HS_{QA}$ | 130 | 99.1 | 122.0 ± 0.6 | 769.0 ± 1.7 | 75.7 ± 0.3 | 188.1 ± 0.8 |
| | 100 | 98.8 | 93.9 ± 0.5 | 591.6 ± 1.3 | 58.2 ± 0.2 | 144.8 ± 0.6 |
| $HS_{QA+}$ | 130 | 99.2 | 120.4 ± 0.6 | 785.5 ± 6.8 | 79.1 ± 0.3 | 265.9 ± 0.9 |
| | 100 | 98.3 | 92.7 ± 0.5 | 604.3 ± 5.2 | 60.8 ± 0.2 | 204.5 ± 0.7 |
| $CS_{QA}$ | 130 | 99.5 | 135.4 ± 0.8 | 860.2 ± 2.6 | 116.9 ± 0.6 | 233.9 ± 1.4 |
| | 100 | 99.5 | 104.2 ± 0.6 | 661.7 ± 2.0 | 90.0 ± 0.5 | 180.0 ± 1.1 |
| $CS_{QA+}$ | 130 | 99.8 | 133.9 ± 2.1 | 886.3 ± 1.8 | 127.5 ± 0.7 | 289.7 ± 1.6 |
| | 100 | 99.8 | 103.0 ± 1.6 | 681.4 ± 1.3 | 98.1 ± 0.5 | 222.9 ± 1.2 |
| $HC_{QA}^{WC}$ | 130 | 99.6 | 131.0 ± 1.3 | 844.9 ± 1.7 | 127.3 ± 0.7 | 275.3 ± 1.4 |
| | 100 | 99.6 | 100.8 ± 1.0 | 649.9 ± 1.3 | 97.9 ± 0.5 | 211.8 ± 1.1 |
| $HC_{QA+}^{WC}$ | 130 | 99.2 | 124.6 ± 0.6 | 859.4 ± 23.5 | 129.3 ± 0.7 | 283.4 ± 1.5 |
| | 100 | 99.1 | 95.9 ± 0.5 | 661.1 ± 18.1 | 99.4 ± 0.5 | 218.0 ± 1.2 |
| $HC_{QA}^{BC}$ | 130 | 99.6 | 137.7 ± 1.0 | 866.1 ± 2.2 | 121.8 ± 0.6 | 272.5 ± 1.5 |
| | 100 | 99.6 | 105.9 ± 0.7 | 666.2 ± 1.7 | 93.7 ± 0.4 | 209.6 ± 1.1 |

For an apex normalisation to 130 Gy, more than 99 % of the tumour volume receives at least 100 Gy in all scenarios, and the minimum tumour dose exceeds 120 Gy in all cases. The

lowest minimum tumour dose occurs in the $HS_{QA+}$ scenario, with $(120.4 \pm 0.6)$ Gy.
Notably, all scenarios simulated solely using the PG and phase space files exhibit a higher minimum tumour dose than scenarios generated using the GPS-based simulation or the combination of PG and GPS. This systematic shift likely originates from limitations in how the phase-space-based surface dose profile is modelled and how the corresponding weighting factors are determined. For the COB applicator, 117 weights must be optimised, which leads to a less accurate optimisation and a more inhomogeneous surface dose profile (Figure 4.10b). In contrast, the rotationally symmetric CCA and CCB applicators require far fewer weights, so this tendency is not observed in those cases.
For an apex normalisation to 100 Gy, more than 99 % of the tumour volume is irradiated with at least 100 Gy in all scenarios except the hot spot scenarios. In the $HS_{QA}$ scenario, the volume of the tumour receiving at least 100 Gy is 98.8 %, and in the $HS_{QA+}$ scenario, it is 98.3 %. In both cases, the minimum tumour dose exceeds 90 Gy, which is acceptable given a tumour control dose of $(85 \pm 15)$ Gy.

When the dose at the tumour apex is normalised to 130 Gy, the scleral contact dose of 700 Gy prescribed by the UME dose concept is exceeded in all scenarios, though the absolute maximum dose of 1500 Gy is not reached. For an apex normalisation to 100 Gy, the maximum dose in the sclera remains below 683 Gy in all scenarios, and thus below the required contact dose. As observed for the CCA and CCB applicator cases, this has no adverse impact on achieving the tumour control dose.
For an apex normalisation to 130 Gy at the tumour apex, the maximum dose in the papilla exceeds 50 Gy in all scenarios. The lowest maximum dose in the papilla is deposited in the homogeneous scenario, with $(56.0 \pm 0.3)$ Gy. However, in the scenarios simulated solely using phase space files, a higher dose is deposited in the papilla, with an increase of at least $(108.0 \pm 1.5)$ % relative to the homogeneous scenario. Consequently, a direct comparison between the phase-space-based scenarios and those incorporating the GPS cannot be reliably made. The same applies for the apex normalisation to 100 Gy, although in this case the maximum dose in the homogeneous scenario remains below the limit of 50 Gy, with $(43.1 \pm 0.2)$ Gy deposited in the papilla.
For both apex normalisations and all dose profile scenarios, the dose limit of 52 Gy in the fovea is exceeded, likely due to the proximity of the applicator to the fovea. As observed for the papilla, the lowest maximum dose is deposited in the homogeneous scenario. In this scenario, the limit is exceeded by $(111.0 \pm 1.3)$ % for an apex dose of 130 Gy and by $(62.9 \pm 1.3)$ % for an apex dose of 100 Gy.

For the investigated patient case with the COB applicator, neither an apex normalisation to 130 Gy nor to 100 Gy shows any effect of inhomogeneous surface dose profiles that would compromise the primary objective of achieving a tumour control dose of $(85 \pm 15)$ Gy.
The modelled hot spot at the $U_{NU}$ QA limit increases the maximum dose in the papilla by $(35.2 \pm 0.9)$ % and in the fovea by $(70.8 \pm 1.3)$ %. The hot spot exceeding the $U_{AS,R2}$ QA limit by 29.6 % leads to an increase in the maximum dose in the papilla of $(41.2 \pm 0.9)$ % and in the fovea of $(141.5 \pm 1.7)$ % compared with the homogeneous scenario.

## 5.4 Clinical and treatment implications

The influence of inhomogeneous surface dose distributions on the treatment of intraocular tumours with $^{106}$Ru eye applicators has been investigated in this chapter. Three representative patient cases are modelled, one for each of the applicator types CCA, CCB, and COB. For every applicator model, a homogeneous reference scenario is simulated alongside several worst-case inhomogeneous scenarios at or above the QA limits, as well as one best-case scenario per model. Each scenario is assessed using a range of treatment evaluation parameters. The dose values are normalised to an apex dose of 130 Gy in accordance with the UME dose concept, and additionally to 100 Gy to investigate whether a less conservative treatment approach could still achieve the therapeutic objectives in the presence of inhomogeneous surface dose profiles.

For all three patient cases investigated, no effects of inhomogeneous surface dose profiles that would compromise the primary objective of achieving a tumour control dose of $(85 \pm 15)$ Gy are observed, neither when normalised to 130 Gy at the tumour apex nor to 100 Gy. The lowest minimum tumour dose, $(91.3 \pm 0.9)$ Gy, is recorded in the CCA case in the $\mathrm{CS}_{\mathrm{QA+}}$ scenario when normalised to 100 Gy at the tumour apex, which is still considered acceptable treatment.
The safety margins in the UME dose concept cover all eventualities related to the inhomogeneous surface dose profile in all three cases, ensuring the goal of sufficient tumour volume irradiation is achieved. Normalisation to a scleral contact dose of 700 Gy is not necessary in any case, as tumour control can be maintained without it. This applies to both normalisation schemes, although normalisation to 100 Gy at the tumour apex can result in the minimum dose lying between 85 Gy and 100 Gy, rather than being $\geq 100$ Gy. While this still constitutes an acceptable treatment, it may not fully account for all treatment uncertainties. In the case of normalisation to 100 Gy at the apex, the dose to the structures at risk is significantly reduced in all scenarios compared with normalisation to 130 Gy, while still maintaining tumour control.

In all three patient cases, the hot spot scenarios result in a significant increase in dose to the structures at risk. The smallest increase is observed in the CCA applicator case in the $\mathrm{HS}_{\mathrm{QA}}$ scenario. Compared with the homogeneous scenario, the dose increases by $(20.9 \pm 0.9)$ % in the fovea and by $(16.5 \pm 1.1)$ % in the papilla. The largest increases occur in the COB case. In the $\mathrm{HS}_{\mathrm{QA}}$ scenario, the dose increases by $(70.8 \pm 1.3)$ % in the fovea and by $(35.2 \pm 0.9)$ % in the papilla compared with the homogeneous scenario. In the $\mathrm{HS}_{\mathrm{QA+}}$ scenario, the dose increases by $(41.2 \pm 0.9)$ % in the fovea and by $(41.2 \pm 0.9)$ % in the papilla relative to the homogeneous scenario.
Neither in the CCA case nor in the CCB case do the cold spot scenarios compromise the achievement of the tumour control dose for either normalisation. However, the $\mathrm{HC}_{\mathrm{QA}}^{\mathrm{BC}}$ scenario demonstrates that inhomogeneous surface dose profiles can have a beneficial effect in reducing the dose to the structures at risk when the applicators are positioned advantageously. In the CCA case, the maximum dose in the fovea and papilla is reduced by at least 26 %, while the minimum tumour dose is only marginally affected, with a reduction of $(3.9 \pm 1.6)$ %. In the CCB case, the maximum dose in the fovea and papilla is reduced by at least 13 %, whereas the minimum tumour dose is minimally affected, with a reduction of less than 1 %.

In the case of the COB applicator, no definitive statement can be made, as the modelling of inhomogeneities using phase space files shows deviations for all structures compared with the scenarios generated using GPS. These deviations are not only caused by the intended hot and cold spots, but also by a general inhomogeneity in the surface dose profile, which arises from the approximation of the surface dose profile using the phase space files and the associated determination of 117 weights. For further modelling of inhomogeneities in the COB case and their comparison with a homogeneous profile, the procedure for determining the weights should be optimised, either through modification of the minimisation algorithm of the objective function or potentially through the use of neural networks.

To examine the influence of tumour height, three additional tumour heights are modelled for the CCB case, and irradiation has been simulated using both cold spot surface dose distributions, as well as a homogeneous reference. With respect to the relative tumour volume receiving at least 100 Gy, no deviations greater than 1 pp due to cold spots in the surface dose profile are observed.
The minimum tumour dose and the maximum dose in the sclera correlate with the tumour apex height due to the normalisation procedure. A higher tumour apex leads to a larger normalisation factor, which in practice corresponds to a longer irradiation time, and consequently, to a higher dose in the tumour volume and the sclera.
For the given tumour heights, all scenarios and normalisations achieve a tumour control dose of $> 85$ Gy. In the case of normalisation to 130 Gy at the tumour apex, the minimum tumour dose for a tumour height of 2.5 mm in the $\mathrm{CS}^{\mathrm{BC}}_{\mathrm{QA+}}$ scenario is $(112.0 \pm 1.9)$ Gy. Only for this tumour, a deviation in the minimum dose of more than 5 % from the homogeneous scenario is recorded, caused by a cold spot beyond the QA limits.
The trend of the data points in the correlation between tumour height and minimum tumour dose suggests that for tumours with an apex height $< 2.5$ mm, normalisation to 100 Gy at the tumour apex may not achieve the tumour control dose of $(85 \pm 15)$ Gy, particularly in the presence of a pronounced cold spot in the surface dose profile. In such cases, normalisation to the scleral contact dose would be required to ensure sufficient tumour irradiation. For a tumour height of 2.5 mm, the scleral contact dose corresponds to just above 237 Gy for all scenarios when normalised to an apex dose of 100 Gy. To achieve the tumour control dose for smaller tumours and other geometries, the prescribed scleral contact dose of 700 Gy is likely higher than necessary and should therefore be re-evaluated, to minimise the dose to structures at risk.
With normalisation to 130 Gy apex dose, there is no indication that tumours $\leq 2.5$ mm would fail to achieve the required tumour control dose, even in the presence of pronounced cold spots. Normalisation to the scleral contact dose of 700 Gy is therefore not necessary for these tumour heights.

Overall, within the framework of the UME dose concept, a compromise of the required tumour control dose due to inhomogeneous surface dose profiles can be excluded for the cases investigated here. It is reasonable to assume that this will also be valid for other patient geometries, as the uncertainties and safety margins incorporated in the concept are sufficiently large to account for even the worst-case scenarios modelled here, not only with respect to the extent of the inhomogeneities but also their positioning. Even surface dose profiles that fail to meet the QA criteria and exhibit substantial deviations from the required symmetry and uniformity values do not jeopardise tumour control.

This conclusion, however, relies on the assumption that the applicator is positioned such that the target volume is fully covered. In clinical practice, this may not always be guaranteed. Unintentional geometric miss, a displacement of the applicator due to a hematoma during the therapy period, or intentionally placing the applicator very close to the tumour boundary, for example, to avoid resecting additional muscle tissue or to spare major blood vessels, can reduce the effective safety margin. In such situations, a cold spot located near the tumour margin becomes critical, as it may overlap with the steep lateral dose fall-off. If the tumour edge extends into this fall-off region, the delivered dose may be insufficient for reliable tumour control, and the risk of recurrence increases. Therefore, while the investigated scenarios demonstrate robustness against surface dose inhomogeneities, future studies could examine special cases in which the applicator only partially covers the tumour.
Regarding the dose to structures at risk, a pronounced increase due to hot spots in the surface dose profiles is observed. In cases where doses are already near the threshold limits, this could lead to exceedances and thus an increased risk of side effects. However, the magnitude of this effect is highly dependent on patient geometry and applicator positioning.
To spare the structures at risk, thereby reducing the likelihood of side effects and potentially preserving patient vision, a reduction of the apex dose to 100 Gy within the UME dose concept could be beneficial. In combination with treatment planning software that more comprehensively accounts for patient geometry through 3D modelling and, in particular, considers hot spots in the surface dose distribution, the sparing of structures at risk could be significantly improved. For smaller tumours, the software could also take cold spots into account, together with an appropriate scleral contact dose, which in many cases may be below 700 Gy. This approach would prioritise the protection of structures at risk more effectively than current practice.

# 6 Neural networks for dose prediction

Radiotherapy is a central modality in cancer management, with over half of all patients receiving irradiation either with curative or palliative intent. While image-guided techniques have advanced treatment precision, the process remains highly complex and data-intensive. The large volumes of heterogeneous clinical information generated during radiotherapy highlight the need for computational approaches capable of supporting clinical decision-making and reducing the risk of error. Machine learning, in combination with computer vision and image processing, has shown significant potential in radiation oncology and radiology, particularly for diagnosis, treatment planning, and outcome prediction [11].
In treatment planning, predictive planning has become an active research area, as plan generation is especially resource-intensive, requiring specialist expertise and extensive iteration to achieve clinically acceptable outcomes. Recent developments in deep learning have further enabled the prediction of 3D dose distributions by integrating diverse imaging and planning data [101, 102].

As outlined in subsection 2.3.2, there is currently no commercially available Treatment Planning System (TPS) for brachytherapy with $^{106}$Ru applicators that fulfils the stringent quality assurance requirements of the UME. Consequently, the UME, along with many other institutes, relies on in-house software solutions for treatment planning. Without a dedicated TPS, the treatment is usually based on the tumour height and the depth-dose curve of the applicator rather than detailed dose distributions [10]. While MC simulations can provide more accurate dose calculations, they are computationally intensive and therefore unsuitable for routine clinical scenario evaluation.
The development of a neural network for dose prediction with $^{106}$Ru applicators, based on the methodology introduced in chapter 3, could address these limitations. Such a model would allow for rapid evaluation of different therapeutic scenarios, thereby supporting efficient treatment planning without the need for repeated MC simulations.
A proof of concept demonstrating the feasibility of dose prediction with $^{106}$Ru applicators using neural networks has been presented in Ref. [14], where the eye was approximated by a water sphere. This approach was subsequently extended by employing the MC workflow described in chapter 3 on the anatomically approximated eye model presented in section 3.2. Building upon these findings, the present study conducts further investigations and expands the training of the proposed neural network using a substantially larger dataset.

In section 6.1, the theoretical foundations of neural networks are introduced, providing the basis for understanding the network architecture applied in this work. The generation of the underlying data and their preprocessing are then described in section 6.2, followed by a presentation of the 3D U-Net in section 6.3. The parameter tuning and its results are outlined in section 6.4. Subsequently, in section 6.5, the overall findings of the chapter are discussed in relation to clinical application.

## 6.1 Foundations of neural networks

This section introduces the fundamental concepts underlying neural networks. It situates them within the broader field of artificial intelligence and machine learning, outlines their core components, and presents convolutional neural networks as a central concept used in this work.

### 6.1.1 Neural networks in the context of AI and machine learning

Artificial Intelligence (AI) represents a broad field within computer science concerned with designing systems that replicate aspects of human intelligence [103, 104]. Within AI, Machine Learning (ML) focuses on algorithms that enable systems to improve their performance by learning from data rather than relying on explicit programming [11, 105]. ML approaches can generally be categorised into supervised, unsupervised, and reinforcement learning, each providing different strategies for handling diverse problem types [105]. In the present work, supervised learning is employed, where models are trained on labelled datasets in order to infer relationships between inputs and outputs and make accurate predictions on previously unseen data [105].
Deep Learning (DL) is a specialised area of ML that employs multi-layered artificial neural networks to extract meaningful representations directly from raw data [11, 104]. Unlike earlier ML methods, which often required hand-crafted feature design, deep learning allows the model to automatically identify relevant patterns, substantially advancing performance across a wide range of tasks [104]. The term 'deep' reflects the hierarchical structure of these networks, where successive layers progressively capture higher-level abstractions [104].
Artificial neural networks themselves can be understood as adaptive computational models inspired by the human brain. They consist of interconnected units, called neurons, which are arranged in layers. Information passes from an input layer that receives raw data, through one or more hidden layers that progressively transform the information, to an output layer that produces the final result [105, 106].
The process of learning, referred to as training, involves repeatedly presenting the network with input data and the desired outputs so that it can adapt its internal parameters, ultimately enabling it to generalise from training samples to unseen data [11].
By combining the adaptive learning capabilities of neural networks with the representational power of deep architectures, modern DL methods have become central to contemporary AI, supporting a wide spectrum of applications from image analysis to clinical decision-making [11, 103].

### 6.1.2 Core components

A neural network can be expressed mathematically as a nonlinear mapping from an input vector $\vec{x}$ to an output value $y$ [107]. For the $k$-th neuron, this can be written as

$$\mathcal{N}_k(\vec{x}) = f\left[\sum_{i=0}^{N-1} \omega_{ik} x_i + b\right],$$

where $\omega_{ik}$ are the weights applied to each input $x_i$, $b$ is a bias term influencing the activation function, and $f$ is the activation function itself. The $N$ weighted inputs $x_i$ are aggregated

and transformed by $f$, producing the state value $\mathcal{N}_k(\vec{x})$ of the neuron, which is then passed to subsequent neurons [107].
When neurons are arranged in multiple layers, with each layer connected to the preceding and following layer, the architecture is referred to as a multi-layer perceptron. In such a network with $k$ layers, starting from the input $\vec{x}_0$, the weight matrices $W_k$, and the bias vectors $\vec{b}_k$, the outputs of the subsequent layers $k > 0$ are obtained through

$$\vec{x}_k = f_k(W_{k-1}\vec{x}_{k-1} + \vec{b}_k),$$

where $f_k$ denotes the activation function of the $k$-th layer [107].
Activation functions are essential, as they introduce nonlinearity. Without them, networks would be limited to modelling only linear relationships. A widely used activation function is the Rectified Linear Unit (ReLU)

$$\mathrm{ReLU}(x) = \max(0, x),$$

which outputs $x$ when positive and zero otherwise. ReLU is computationally efficient, supports gradient propagation during training, and encourages sparsity in hidden layers [105, 107].
The training of neural networks is based on comparing the predicted output with a reference value. Using the current weights and biases, the network produces an output $\vec{x}_k$, which is then evaluated against the desired target $\vec{d}$. This discrepancy is quantified by means of a loss function $\mathcal{L}$. A common example of such a function is the squared error

$$\mathcal{L} = (\vec{x}_k - \vec{d})^2.$$

The weights are iteratively adjusted to minimise $\mathcal{L}$, typically using gradient descent. In this process, the gradient of the loss with respect to each weight indicates the direction of steepest increase. Updating weights in the opposite direction reduces the error. This procedure, performed from output to input across the layers, is known as backpropagation [105, 107].
The training process is also influenced by hyperparameters, which are not learned directly by the network but are defined beforehand. Important examples include the learning rate, which controls the size of the weight updates [108], the batch size, which specifies how many training samples are processed before each update, and the number of epochs, each corresponding to a complete pass through the dataset [109]. Hyperparameters are usually optimised through experimental methods. A common approach is grid search, where the algorithm is tested across a predefined range of values. Another strategy is random search, in which values are sampled from a user-specified distribution. Both methods aim to identify settings that yield the best model performance [104].

### 6.1.3 Convolutional neural networks

The network architecture employed in this study, as described in section 6.3, is a type of Convolutional Neural Network (CNN).
CNNs are a class of deep learning architectures specifically designed for processing data with a grid-like structure, such as images, time series, or volumetric scans [105, 110]. By exploiting the spatial organisation of data and using weight sharing, CNNs reduce the number of trainable parameters and achieve greater computational efficiency [110]. They are capable

of automatically learning relevant features directly from the data, avoiding the need for manual feature engineering [105].
The fundamental operation of a CNN is the convolution, where a small kernel or filter slides across the input to extract local features [105]. Mathematically, the convolution between two discrete and finite two-dimensional signals $I[i, j]$ and $K[i, j]$ with $i, j \in \mathbb{Z}$ is given by

$$H[i, j] = \sum_m \sum_n I[i - m, j - n]K[m, n].$$

This operation is generally followed by a non-linear activation function, such as ReLU, which introduces nonlinearity and enables the network to learn complex patterns [110].
Pooling layers are frequently applied to reduce the spatial dimensions of feature maps, summarise local information, and decrease computational cost. Common pooling methods include max pooling, average pooling, and global average pooling, which select the maximum, average, or spatially averaged value within a predefined region, respectively. Pooling also helps to prevent overfitting by reducing the capacity of the network to memorise training data.

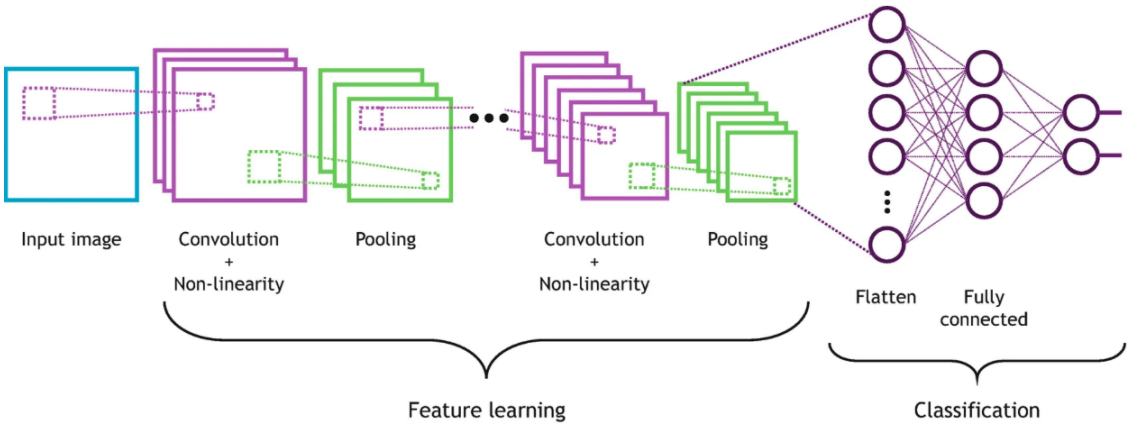


Figure 6.1: Example of a basic CNN architecture, where the feature extraction component uses convolutional blocks to learn hierarchical representations, which are then flattened and passed through fully connected layers for classification or regression [110].

A typical CNN is shown in Figure 6.1. It is generally composed of two main parts. The first part, often referred to as the feature extraction component, consists of a series of convolutional blocks, each including a convolution, a non-linear activation function, and a pooling operation. This part is responsible for learning hierarchical features from the input data. The second part, known as the classification or regression component, flattens the extracted features and passes them through fully connected layers to produce the final output. The network is trained end-to-end, with all layers optimised simultaneously to learn the mapping from input to output [105, 110].

## 6.2 Dataset generation

For training the neural networks in this work, MC simulation data are used, generated with the software workflow presented in chapter 3. The required 3D eye models, which contain patient-specific data, are created in Fusion on the basis of eleven representative baseline patient cases. Of these baseline cases, five are derived from actual patients, while the remaining six were generated artificially to represent additional clinically observed scenarios.
For each baseline case, further variations are produced by modifying the tumour height, width, and the contour of the tumour base. In addition, the tumour and applicator positions are altered. In total, the dataset used in this work comprises 72 configurations derived from the eleven baseline cases, each irradiated with either the CCA, CCB, or COB applicator.
The optic nerve of the generic eye model is shortened from 26 mm to 8 mm, as this modification reduces computational resources associated with the tensor size, whose creation is described below.

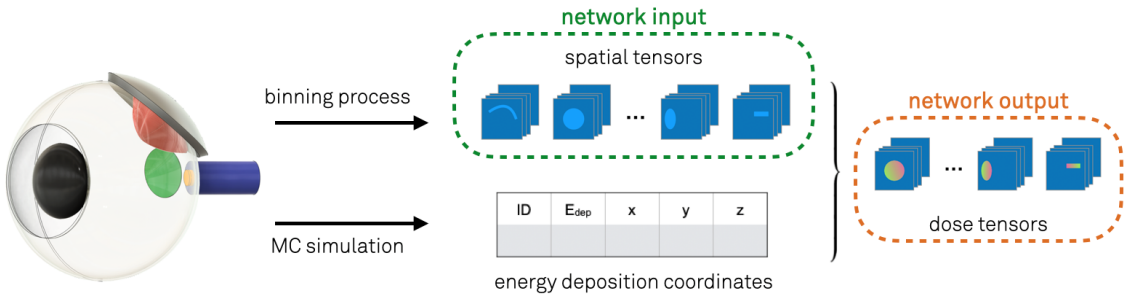


Figure 6.2: Illustration of the data generation and preprocessing workflow underlying the neural network training. The dataset is generated through 3D modelling of patient cases, after which the eye structures are binned in Python and converted into spatial tensors. MC simulations result in deposited energy values, which are combined with the spatial tensors to generate dose tensors for each structure. The spatial tensors serve as network inputs, while the dose tensors constitute the network outputs. The figure is taken from Ref. [14] and has been adapted for the present work.

The individual eye structures of the generated patient cases are then virtually divided into bins in Python using the method described in section 3.4. The binned data are subsequently converted into spatial tensors following the methodology described in Ref. [14], which encode the spatial relationships of the eye structures. Each tensor has dimensions of $32 \times 32 \times 32$, corresponding to the binning grid resolution, with each bin measuring 1 mm. The tensor size also motivates the shortening of the optic nerve in the eye model, as described above. This adjustment substantially reduces the tensor size while retaining only the anterior portion of the optic nerve, which is the region of interest for dose analysis in the present studies.
Because each ocular structure is binned independently but within a shared coordinate system, some bins may contain multiple structures. To address this, the eye structures and the target of the applicator are encoded in separate binary tensors, which serve as the input tensors for the neural networks for each configuration.

Each of the 72 configurations in the dataset is MC simulated, with 100 simulations per case, each comprising 3,000,000 particles. Of these configurations, 39 derived from five baseline patient cases were simulated in Ref. [14]. The resulting energy values are combined with the binned data, and the dose values are normalised to 130 Gy at the tumour apex, following the dose concept of the UME. This combination results in dose tensors, in which each element represents the normalised dose at its corresponding spatial location. These tensors serve as labels for training, allowing the network to learn the mapping from spatial information to dose distributions. The data generation and preprocessing workflow is illustrated in Figure 6.2.

## 6.3 Network architecture

The neural network architecture employed in this work is a 3D U-Net, based on the design originally proposed in Ref. [111]. For the specific application investigated here, dose prediction for $^{106}$Ru eye applicators, the architecture was adapted and implemented in Ref. [14] using `PyTorch`[19]. As a Python library for deep learning, `PyTorch` offers Graphics Processing Unit (GPU)-based tensor computations and a set of tools for neural network development [112].

The U-Net is a CNN architecture characterised by a symmetric encoder-decoder structure, in which feature maps are progressively down-sampled and subsequently up-sampled. A defining feature of this design is the use of skip connections that link each stage of the encoding pathway to its corresponding stage in the decoding pathway, allowing high-resolution spatial information from the encoder to be concatenated with the up-sampled feature maps in the decoder [11, 109]. This mechanism enables the network to preserve fine structural detail while reconstructing dense output representations. Introduced originally for 2D medical image segmentation [113], the U-Net demonstrated that accurate, end-to-end learning could be achieved without pre-training and with relatively limited amounts of annotated data. The architecture was later extended to volumetric data through the development of the 3D U-Net, which applies the same principles of multiscale feature extraction and spatially informed decoding to 3D medical images [111].
In radiotherapy, U-Net architectures, especially their 3D variants, have shown strong performance in dose prediction for treatment planning. The goal of dose prediction with neural networks is to generate realistic dose distributions that closely approximate those produced by expert planners, providing valuable support for plan evaluation and optimisation. Their relatively simple design and effective retention of low-level spatial features make 3D U-Nets well suited for voxel-wise prediction problems encountered in radiotherapy planning [114, 115].

The 3D U-Net used in this work is illustrated in Figure 6.3. The network input is a tensor with 10 channels, each representing a $32\times32\times32$ binary tensor that encodes the spatial arrangement of the particular eye structure and the target of the applicator, as described in section 6.2. In the encoder path, each stage consists of two consecutive 3D convolutional layers, each followed by batch normalisation and a ReLU activation.
Batch normalisation is employed to address internal covariate shift, a phenomenon in which the input distribution of a layer changes due to updates in the parameters of preceding layers. This is achieved by normalising the activations of each unit across a batch to have approximately zero mean and unit variance, while learnable scaling and offset parameters

[19] PyTorch, Python library [3]. `https://pytorch.org`.

preserve the representational capacity of the network. As a result, training becomes more stable, less sensitive to weight updates, and converges faster [11, 109].
The convolutional layers use a kernel size of 3×3×3 with padding of 1, and the number of feature channels is doubled at each subsequent encoder stage. Following the convolutional block, spatial resolution is reduced by a factor of two via max pooling with a 2×2×2 kernel and a stride of 2. At the bottleneck of the network, convolutional operations are applied without reducing spatial resolution.
Each stage of the decoder begins with an up-sampling operation that doubles the spatial resolution using a 2×2×2 kernel and a stride of 2. Up-sampling reverses the spatial reduction performed during down-sampling, either by replicating values across the expanded volume or through unpooling operations that restore the positions of maximal values recorded during pooling. This allows the network to reconstruct high-resolution, voxel-wise predictions from the compressed feature representations [109].
The up-sampled features are merged with the corresponding encoder maps via skip connections to preserve spatial detail. The resulting tensor passes through two convolutional layers with batch normalisation and ReLU activation, with the number of channels being reduced by a factor of two at each decoder stage. A final 1×1×1 convolution produces the predicted dose distribution tensor, which contains a total of nine individual dose tensors, one for each eye structure. Since the dose within the target of the applicator does not need to be predicted, there is consequently one tensor less in the output than in the input. The predicted dose tensors are subsequently normalised to 130 Gy at the tumour apex, in accordance with the dose concept of the UME.

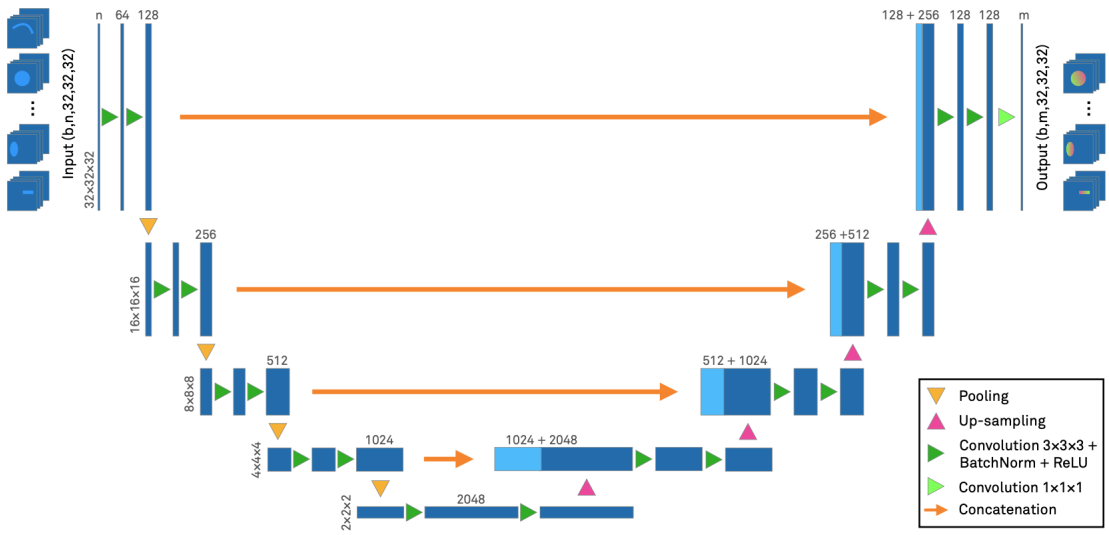


Figure 6.3: 3D U-Net architecture employed in this work. As input, the network receives a 10-channel tensor encoding the spatial arrangement of the eye structures and the applicator target. The output is a dose distribution tensor comprising nine individual dose tensors, one for each of the eye structures. The figure is acquired from Ref. [14].

## 6.4 Parameter tuning

In this study, the 3D U-Net architecture described in section 6.3 is investigated with respect to systematic variations in model configurations, training strategies, and hyperparameters to achieve the most accurate dose predictions within the tumour and ocular structures.
The training objective is to accurately predict dose distributions by minimising deviations from the simulated reference values, while maintaining generalisation across the applicator models, spatial orientations, and tumour geometries.
The dataset consists of 72 configurations, of which 14 are allocated exclusively for testing, resulting in an 80/20 split between training and test data. The remaining 58 configurations are further divided into training and validation subsets using a four-fold cross-validation procedure. In this approach, the training data is split into four non-overlapping subsets, with three subsets used for training and the remaining subset used for validation in each fold. This process is repeated four times so that every subset serves as validation once, allowing the performance of the model to be evaluated robustly across the available data. For each fold, 75 % of the data is employed for training, and the remaining 25 % serves as validation to monitor model performance and prevent overfitting, thereby maximising the utility of the limited dataset [11].

After the network has been trained, the following evaluation parameters are employed on the normalised data to assess the performance of the network and the effects of each optimisation strategy:

- **Mean Absolute Error (MAE):** The MAE is used as a bin-wise error metric. It quantifies the mean absolute deviation between the predicted dose $\hat{d}_i$ and the corresponding simulated reference dose $d_i$ within the tumour and ocular structures. It is defined as

$$\mathrm{MAE} = \frac{1}{n}\sum_{i=1}^{n}\left|\hat{d}_i - d_i\right|, \qquad [\mathrm{MAE}] = \mathrm{Gy},$$

  where $n$ denotes the number of bins belonging to the particular anatomical structures. All MAE values presented correspond to the mean MAE calculated over the full test dataset.

- **MAE of Dose-Volume Histograms ($\mathbf{MAE_{DVH}}$):** DVHs are routinely used in radiotherapy for treatment planning and analysis. Accordingly, the performance of the neural network is assessed by calculating the mean absolute error of the cumulative DVH curves. For each anatomical structure, the error at a given dose level $j$ is defined as the difference between the predicted cumulative volume percentage $\hat{V}_j$ and the corresponding simulated reference value $V_j$. This metric is given by

$$\mathrm{MAE}_{\mathrm{DVH}} = \frac{1}{m}\sum_{j=1}^{m}\left|\hat{V}_j - V_j\right|, \qquad [\mathrm{MAE}_{\mathrm{DVH}}] = \mathrm{pp}, \tag{6.1}$$

  where $m$ corresponds to the number of sampled dose levels. All $\mathrm{MAE}_{\mathrm{DVH}}$ values presented correspond to the mean $\mathrm{MAE}_{\mathrm{DVH}}$ calculated over the full test dataset.

- **Treatment parameters:** For clinical evaluation of the treatment with $^{106}$Ru eye applicators, several dosimetric parameters are assessed, as described in section 5.2. Consequently, the performance of the network is also evaluated by comparing the

predicted and simulated treatment-related dose metrics. These include the deviations

$$\Delta D_{\text{min}}^{\text{tumour}}, \quad \Delta D_{\text{max}}^{\text{sclera}}, \quad \Delta D_{\text{max}}^{\text{papilla}}, \quad \Delta D_{\text{max}}^{\text{fovea}},$$

which represent the differences $\Delta D_i = D_i - \hat{D}_i$ between simulated reference values $D_i$ and predicted values $\hat{D}_i$ for minimum tumour dose and maximum doses in the sclera, papilla, and fovea, respectively. All treatment parameters presented correspond to the respective mean values calculated across the entire test dataset.

### 6.4.1 Initial network configuration

The initial configuration of the 3D U-Net in this work is based on the network parameters that yielded the best performance in Ref. [14]. In that study, the same 3D U-Net architecture was implemented and optimised using a smaller dataset comprising 39 configurations derived from five baseline patient cases.
Building on these results, the network employed in the present work is initially configured with four layers and 64 feature maps per layer. The learning rate is set to 0.01, and the model is trained for 500 epochs with a batch size of 2. The output tensors are scaled by a factor of $1 \cdot 10^{13}$ before training. Following prediction, the network outputs are rescaled back to their original units and then normalised to 130 Gy at the tumour apex for DVH computation and performance evaluation, allowing direct comparison with the simulated data.
To optimise the training, the `Adam` [116] optimiser is used, complemented by a learning rate scheduler. The scheduler reduces the learning rate by a factor of 0.5 if the validation loss does not improve over a period of 10 epochs, thereby allowing the model to converge more effectively.
The loss function used during training is the masked mean absolute error ($\text{MAE}_{\text{masked}}$). It was demonstrated in Ref. [14] that this loss function significantly improves prediction performance compared with the standard, unmasked MAE loss function, achieving an improvement of more than 65 % in terms of the mean MAE and the mean $\text{MAE}_{\text{DVH}}$ over all structures. The masked approach ensures that only bins corresponding to the anatomical structures contribute to the loss, while background regions are ignored, thereby preventing them from distorting the optimisation.

In Figure 6.4, an example of the predicted and simulated DVHs is shown for one of the test cases. For the structures receiving higher dose values, namely the choroid, retina, sclera, and tumour, the maximum absolute difference between the predicted and simulated cumulative volume percentages is below 16 pp, with the largest deviations occurring in the tumour.
For the structures receiving lower doses, the cornea, fovea, lens, papilla, and optic nerve, the maximum absolute difference between the predicted and simulated cumulative volume percentages is below 49 pp, with the largest deviations appearing in the papilla. When excluding the papilla from this assessment, the maximum absolute of the difference between the predicted and simulated cumulative volume percentages remains below 30 pp.
Overall, it can be observed that the predicted values generated by the model tend to be lower than the simulated values for this case.

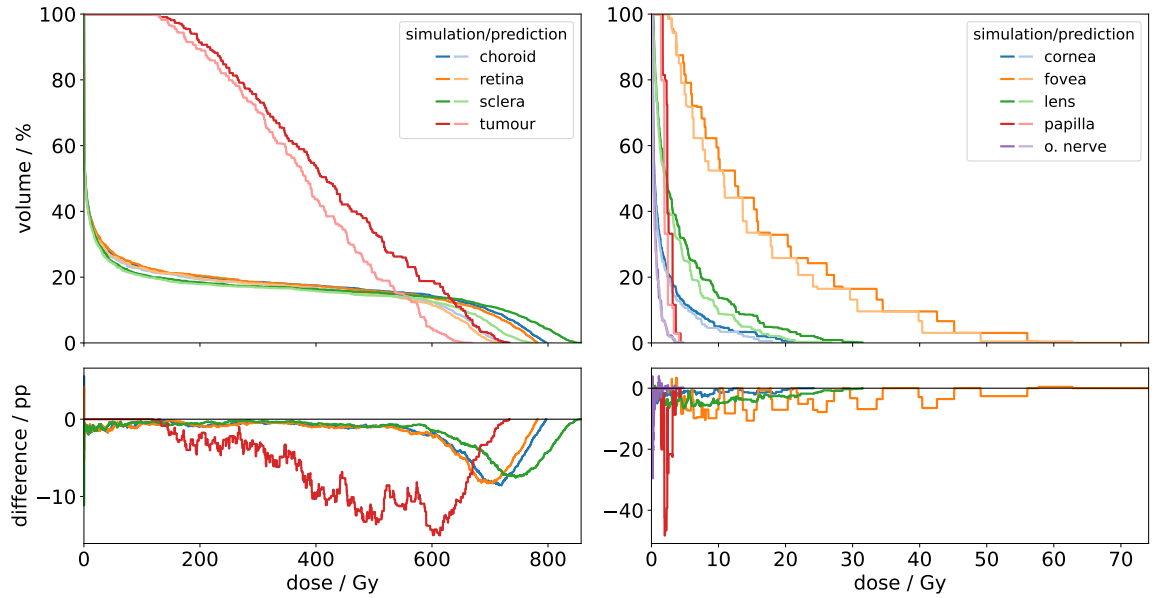


Figure 6.4: Comparison of predicted and simulated DVH curves for the anatomical structures in a representative CCB applicator test case, illustrating the performance of the initial network configuration. The lower row shows the absolute deviations of the cumulative volume percentages, calculated as the difference between the predicted and simulated values.

Tables 6.1 and 6.2: Evaluation parameters used to assess the performance of the initial network configuration, including their standard deviations, averaged across all test cases.

| structures | MAE / Gy | $\text{MAE}_{\text{DVH}}$ / pp |
|---|---|---|
| tumour | 74.7 ± 61.5 | 4.0 ± 2.8 |
| sclera | 52.8 ± 62.7 | 0.9 ± 0.6 |
| choroid | 51.7 ± 62.2 | 0.9 ± 0.5 |
| retina | 50.6 ± 61.9 | 0.8 ± 0.5 |
| papilla | 4.0 ± 3.7 | 8.5 ± 7.2 |
| o. nerve | 2.7 ± 3.1 | 2.6 ± 3.6 |
| fovea | 24.5 ± 52.8 | 3.0 ± 1.9 |
| lens | 0.8 ± 1.8 | 3.3 ± 2.8 |
| cornea | 0.4 ± 1.0 | 3.4 ± 4.2 |
| $\overline{x}_{\text{all}}$ | 29.1 ± 15.0 | 3.0 ± 1.1 |

| | $\Delta D$ / Gy |
|---|---|
| $D_{\text{min}}^{\text{tumour}}$ | 5.8 ± 14.7 |
| $D_{\text{max}}^{\text{sclera}}$ | 2.6 ± 3.0 |
| $D_{\text{max}}^{\text{papilla}}$ | −0.2 ± 1.4 |
| $D_{\text{max}}^{\text{fovea}}$ | −2.9 ± 7.5 |
| $\overline{x}_{\text{all}}$ | 1.3 ± 4.2 |

The structures that receive higher doses also exhibit larger MAE values compared with other structures (Table 6.1). The highest MAE occurs in the tumour, with a value of $(74.7 \pm 61.5)$ Gy. The fovea also shows a relatively high MAE of $(24.5 \pm 52.8)$ Gy, which is a result of averaging across the entire dataset. In some cases, the fovea is located very close to the applicator and therefore receives a correspondingly high dose.
The highest $\text{MAE}_{\text{DVH}}$ occurs in the papilla, reaching $(8.5 \pm 7.2)$ pp, likely due to its small

size. With fewer bins contributing to the metric, individual deviations have a proportionally greater effect, causing the average error to appear relatively large.
The mean difference in treatment parameters $\Delta D$ across all test cases is $(1.3 \pm 4.2)$ Gy, with the largest deviation arising from the tumour at $(5.8 \pm 14.7)$ Gy, as shown in Table 6.2.

### 6.4.2 Dose tensor scaling

For most machine-learning methods, model performance improves when the input data are standardised, ensuring that features lie on comparable scales [117]. In Ref. [14], different scaling methods for the dose tensors were tested. These included leaving the simulated dose values unscaled, normalising the input tensors within the ranges $[0, 1]$ and $[0, 100]$, and multiplying all values by a constant scaling factor, which increases their numerical magnitude.
The initial scaling factor of $1 \cdot 10^{13}$, which approximately normalises the simulation dose values to the order of 130 Gy at the tumour apex, yielded the best results. This is likely because the network performs more efficiently when input values are of moderate magnitude, avoiding extremely small or large numbers that can destabilise training or slow convergence.
In the present work, additional scaling factors and methods are investigated. In addition to the initial factor of $1 \cdot 10^{13}$, factors of $2 \cdot 10^{13}$ and $9 \cdot 10^{12}$ are tested to evaluate the sensitivity of network performance to the choice of the scaling factor.
Moreover, alternative scaling strategies are considered, including logarithmic scaling and mixed linear-logarithmic scaling. Given the small magnitude of the dose values, a scaling factor of $10^{13}$ is first applied to bring them into a numerically stable range, which is also oriented on the magnitude of the factor with which the dose values are normalised to 130 Gy at the tumour apex. Logarithmic scaling compresses higher dose values while preserving relative differences in lower doses. Mixed linear-logarithmic scaling applies linear scaling to doses below a threshold of 10 after scaling, and logarithmic scaling to doses above this threshold. This approach allows small doses to retain their linear relationships, while higher doses are compressed to prevent them from dominating the network training.
With respect to the mean MAE across all anatomical structures in the normalised test dataset ($\overline{\text{MAE}}$), the mixed linear-logarithmic scaling achieves the best performance, yielding a value of $(27.7 \pm 14.8)$ Gy (Table 6.3). In comparison, the logarithmic scaling results in the highest $\overline{\text{MAE}}$, exhibiting a relative deviation of $(5.4 \pm 79.9)$ % from the mixed scaling approach.
In contrast, the model using logarithmic scaling performs best with regard to the mean $\text{MAE}_{\text{DVH}}$ ($\overline{\text{MAE}_{\text{DVH}}}$), resulting in the lowest value of $(2.2 \pm 0.6)$ pp. The largest value is observed for the model employing the scaling factor $9 \cdot 10^{12}$, for which $\overline{\text{MAE}_{\text{DVH}}} = (4.3 \pm 2.1)$ pp, corresponding to an increase of $(95.5 \pm 109.3)$ % relative to the logarithmic scaling. The values of MAE and $\text{MAE}_{\text{DVH}}$ for the individual structures of the different models are listed in Tables A.21 and A.22.
When considering the mean difference $\overline{x}_{\text{all}}$ between the simulated and predicted values of all treatment parameters $\Delta D$, the model employing the scaling factor $1 \cdot 10^{13}$ yields the smallest deviation, with $\overline{x}_{\text{all}} = (1.3 \pm 4.2)$ Gy (Figure 6.5). The largest value of $\overline{x}_{\text{all}}$, amounting to $(2.6 \pm 3.4)$ Gy, is the result of the mixed linear-logarithmic scaling. For the parameters $D_{\text{min}}^{\text{tumour}}$ and $D_{\text{max}}^{\text{sclera}}$, the simulated values are higher than the predicted values for all models, whereas for $D_{\text{max}}^{\text{fovea}}$ the simulated values are consistently lower than the corresponding predictions.

| scaling | $\overline{\text{MAE}}$ / Gy | $\overline{\text{MAE}_{\text{DVH}}}$ / pp |
|---|---|---|
| factor: $1 \cdot 10^{13}$ | 29.1 ± 15.0 | 3.0 ± 3.1 |
| factor: $2 \cdot 10^{13}$ | 27.9 ± 14.9 | 2.8 ± 0.9 |
| factor: $9 \cdot 10^{12}$ | 28.5 ± 15.2 | 4.3 ± 2.1 |
| log | 29.2 ± 15.7 | 2.2 ± 0.6 |
| mixed linear-log | 27.7 ± 14.8 | 2.7 ± 1.0 |

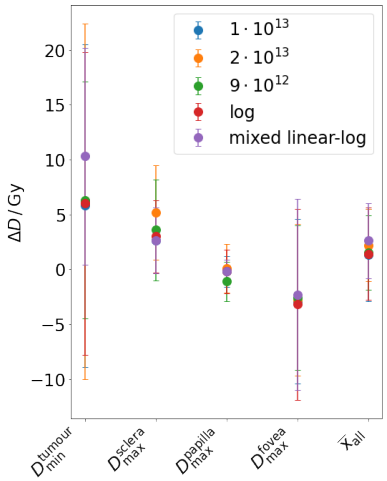


Table 6.3 and Figure 6.5: The table presents the mean MAE and mean $\text{MAE}_{\text{DVH}}$, including their standard deviations, averaged over all anatomical structures and across the full test dataset, for the models trained on the dose tensors scaled using the respective approaches. The figure shows the corresponding mean treatment parameters across the entire test dataset for the different models, along with the overall mean calculated across all treatment parameters.

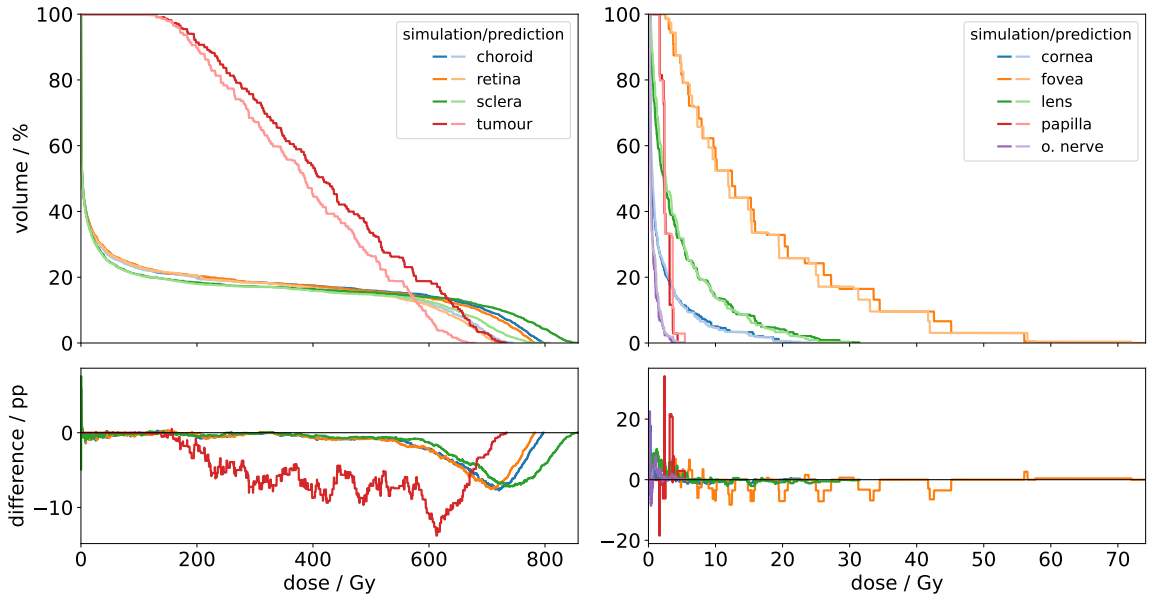


Figure 6.6: Comparison of predicted and simulated DVH curves for the anatomical structures in a representative CCB applicator test case, illustrating the performance of the model trained on the dose tensors scaled with a factor of $2 \cdot 10^{13}$. The lower row shows the absolute deviations of the cumulative volume percentages, calculated as the difference between the predicted and simulated values.

Overall, no scaling method demonstrates a clear advantage across all evaluation parameters. Although the model using mixed linear-logarithmic scaling achieves the lowest $\overline{\text{MAE}}$, it also exhibits the largest mean difference $\overline{x}_{\text{all}}$ between simulated and predicted treatment parameters, and is therefore not considered further. The logarithmic scaling is likewise excluded from subsequent investigations due to its comparatively high $\overline{\text{MAE}}$. Among the three scaling factors, the factor $2 \cdot 10^{13}$ provides the best performance with respect to $\overline{\text{MAE}}$ and $\overline{\text{MAE}_{\text{DVH}}}$, and is consequently used for the following studies. In Figure 6.6, the predicted and simulated DVHs are shown for the same test case as in Figure 6.4, but this time for the model trained on the dose tensors scaled with a factor of $2 \cdot 10^{13}$. For all structures except for the lens, the maximum absolute difference between the predicted and simulated cumulative volume percentages is lower than in the initial network configuration.

### 6.4.3 Loss function

In addition to the $\text{MAE}_{\text{masked}}$ loss function, other masked loss functions are also evaluated, including the masked mean squared error ($\text{MSE}_{\text{masked}}$) and the masked Huber loss ($\text{Huber loss}_{\text{masked}}$), to determine whether they can improve the network performance. The Huber loss combines the advantages of MAE and MSE. It applies a squared term for errors smaller than a specified threshold $\delta$, and a linear term proportional to the absolute error for larger deviations [118]. In this work, $\delta$ is set to 5.0.

| loss function | $\overline{\text{MAE}}$ / Gy | $\overline{\text{MAE}_{\text{DVH}}}$ / pp |
|---|---|---|
| $\text{MAE}_{\text{masked}}$ | 27.9 ± 14.9 | 2.8 ± 0.9 |
| $\text{MSE}_{\text{masked}}$ | 28.8 ± 14.4 | 3.9 ± 1.1 |
| $\text{Huber loss}_{\text{masked}}$ | 28.0 ± 14.8 | 3.4 ± 1.5 |

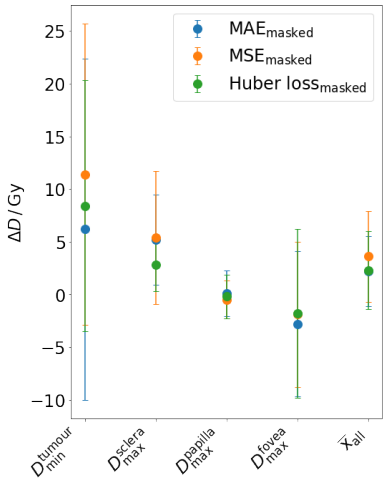


Table 6.4 and Figure 6.7: The table presents the mean MAE and mean $\text{MAE}_{\text{DVH}}$, including their standard deviations, averaged over all anatomical structures and across the full test dataset, for the models trained with the different loss functions. The figure shows the corresponding mean treatment parameters across the entire test dataset for the various models, along with the overall mean calculated across all treatment parameters.

With a $\overline{\text{MAE}}$ of $(27.9 \pm 14.9)$ Gy and a $\overline{\text{MAE}_{\text{DVH}}}$ of $(2.8 \pm 0.9)$ Gy, the model using the $\text{MAE}_{\text{masked}}$ loss function demonstrates the best performance with respect to these two evaluation parameters (Table 6.4). Relative to this model, the models trained with the $\text{MSE}_{\text{masked}}$ function and the $\text{Huber loss}_{\text{masked}}$ show deviations in $\overline{\text{MAE}}$ of $(3.2 \pm 75.5)$ % and $(0.4 \pm 75.4)$ %,

respectively. Regarding $\overline{\text{MAE}_{\text{DVH}}}$, the largest deviation of $(39.3 \pm 59.6)\,\%$ is observed for the model trained with the $\text{MSE}_{\text{masked}}$ loss function. The values of MAE and $\text{MAE}_{\text{DVH}}$ for the individual structures of the different models are listed in Table A.23.
In terms of the mean difference $\overline{x}_{\text{all}}$ between the simulated and predicted values of all treatment parameters, this is smallest for the model using the $\text{MAE}_{\text{masked}}$ loss function at $(2.2 \pm 3.3)\,\text{Gy}$, with the model trained with the Huber $\text{loss}_{\text{masked}}$ only slightly higher at $(2.3 \pm 3.7)\,\text{Gy}$ (Figure 6.7). For the parameters $D_{\text{max}}^{\text{sclera}}$, $D_{\text{max}}^{\text{papilla}}$, and $D_{\text{max}}^{\text{fovea}}$, the absolute differences are smaller for the model using the Huber $\text{loss}_{\text{masked}}$ than for the model using the $\text{MAE}_{\text{masked}}$ loss function, whereas for $D_{\text{min}}^{\text{tumour}}$ it is higher, at $(2.2 \pm 20.1)\,\text{Gy}$. The model trained with the $\text{MSE}_{\text{masked}}$ loss function exhibits the largest mean difference, with $\overline{x}_{\text{all}} = (3.6 \pm 4.3)\,\text{Gy}$.

Across all evaluation parameters examined, the model trained with the $\text{MAE}_{\text{masked}}$ loss function achieves the best overall performance. However, the differences compared with the models trained with the $\text{MSE}_{\text{masked}}$ function and Huber $\text{loss}_{\text{masked}}$ are small, and no clear preference for any particular loss function can be identified in this study. For the subsequent investigations, the neural network is trained using the $\text{MAE}_{\text{masked}}$ loss function.

### 6.4.4 Optimiser

The initial network configuration employs the `Adam` optimiser, which is widely used due to its adaptive learning-rate mechanism [116]. However, `Adam` is known to couple weight decay with the gradient update, which can lead to suboptimal regularisation. For this reason, the `AdamW` optimiser is additionally investigated, as it decouples weight decay from the gradient update [119]. In this work, `AdamW` is tested with weight-decay values of $10^{-2}$, $10^{-3}$, and $10^{-4}$ to assess its impact on the performance of the model.

| optimiser | $\overline{\text{MAE}}$ / Gy | $\overline{\text{MAE}_{\text{DVH}}}$ / pp |
|---|---|---|
| `Adam` | 27.9 ± 14.9 | 2.8 ± 0.9 |
| $\texttt{AdamW}_{10^{-2}}$ | 28.6 ± 14.2 | 3.0 ± 0.8 |
| $\texttt{AdamW}_{10^{-3}}$ | 28.3 ± 14.5 | 4.7 ± 2.3 |
| $\texttt{AdamW}_{10^{-4}}$ | 28.6 ± 14.4 | 2.7 ± 0.9 |

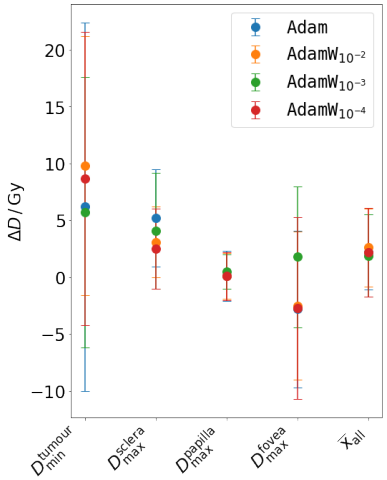


Table 6.5 and Figure 6.8: The table presents the mean MAE and mean $\text{MAE}_{\text{DVH}}$, including their standard deviations, averaged over all anatomical structures and across the full test dataset, for the models trained with the different optimiser. The figure shows the corresponding mean treatment parameters across the entire test dataset for the various models, along with the overall mean calculated across all treatment parameters.

The influence of the optimiser selection on network performance with respect to $\overline{\text{MAE}}$ is small, with a maximum deviation of only $(2.5 \pm 76.2)\,\%$ between `Adam` and $\texttt{AdamW}_{10^{-4}}$ (Table 6.5). The lowest $\overline{\text{MAE}}$, at $(27.9 \pm 14.9)\,\text{Gy}$, is obtained with the model trained using the `Adam` optimiser. In contrast, the $\overline{\text{MAE}_{\text{DVH}}}$ is smallest for the model trained with $\texttt{AdamW}_{10^{-4}}$, with a value of $(2.7 \pm 0.9)\,\text{Gy}$, which is $(3.6 \pm 44.7)\,\%$ lower than that of the model using `Adam`, and $(42.6 \pm 34.1)\,\%$ lower than that of the model trained with $\texttt{AdamW}_{10^{-3}}$, which has the highest value at $(4.7 \pm 2.3)\,\text{Gy}$. The MAE and $\text{MAE}_{\text{DVH}}$ values for the individual structures of the different models are reported in Tables A.24 and A.25.
When examining the mean difference $\overline{x}_{\text{all}}$ between the simulated and predicted values of all treatment parameters, the model employing $\texttt{AdamW}10^{-3}$ exhibits the smallest deviation, with $(1.9 \pm 3.6)\,\text{Gy}$ (Figure 6.8). For this model, all differences $\Delta D$ are positive, indicating that the predicted values consistently lie below the simulated values. For the models using the other optimisers, this behaviour is observed for all parameters except for $D_{\text{max}}^{\text{fovea}}$.

The `Adam` optimiser is used in the subsequent investigations, as training the network with the `AdamW` optimiser does not provide any notable performance advantages based on the evaluation parameters.

### 6.4.5 Data augmentation

In Ref. [14], data augmentation was applied to investigate whether increasing the dataset size could improve network performance, leading to reductions in the evaluation metrics $\overline{\text{MAE}}$ and $\overline{\text{MAE}_{\text{DVH}}}$.
In this work, the dataset already contains 72 configurations, which is 85 % larger than the 39-configuration dataset used in Ref. [14]. The dataset is expanded by a factor of three by incorporating rotated and mirrored versions of the original dose tensors. Specifically, rotations around the $y$-axis of $\pm5°$, $\pm10°$, and $\pm90°$ are applied, and each original tensor is mirrored across the $yz$ plane. This results in three separate augmented datasets, each consisting of the original dataset, the mirrored dataset, and the two datasets rotated by the corresponding positive and negative angles. For the small-angle rotations, the dose values are calculated using trilinear interpolation, which estimates the dose at new bin positions that do not align exactly with the original grid.

With respect to the $\overline{\text{MAE}}$ evaluation parameter, no data augmentation method results in a reduction of the value compared with the model trained on the dataset without augmentation (Table 6.6). In terms of $\overline{\text{MAE}_{\text{DVH}}}$, the augmentations with a $\pm5°$ rotation and with a $\pm10°$ rotation lead to a reduction in the metric. The smallest value, $\overline{\text{MAE}_{\text{DVH}}} = (2.4 \pm 0.9)\,\text{Gy}$, corresponds to a decrease of $(14.3 \pm 38.6)\,\%$ relative to the model trained without augmentation. The MAE and $\text{MAE}_{\text{DVH}}$ values for the individual structures of the different models are reported in Tables A.26 and A.27.
In terms of the mean difference $\overline{x}_{\text{all}}$ between the simulated and predicted values of all treatment parameters, the model trained with the augmentation with a $\pm90°$ rotation exhibits the smallest deviation, with $(1.8 \pm 3.0)\,\text{Gy}$ (Figure 6.9). With the exception of the prediction for $\Delta D^{\text{fovea}}\text{max}$, all predicted values are lower than the corresponding simulated values.

| rotation | $\overline{\text{MAE}}$ / Gy | $\overline{\text{MAE}_{\text{DVH}}}$ / pp |
|---|---|---|
| ±5° | 28.4 ± 15.2 | 2.6 ± 1.1 |
| ±10° | 28.4 ± 15.4 | 2.4 ± 0.9 |
| ±90° | 29.0 ± 14.7 | 5.8 ± 3.2 |
| no augmentation | 27.9 ± 14.9 | 2.8 ± 0.9 |

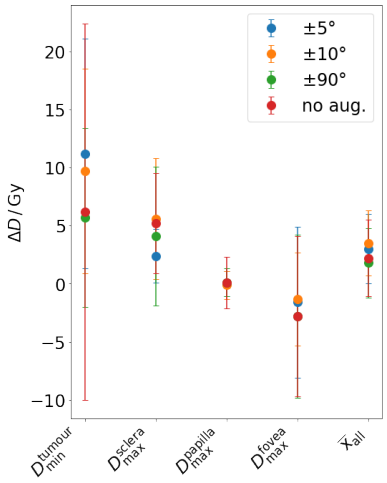


Table 6.6 and Figure 6.9: The table presents the mean MAE and mean $\text{MAE}_{\text{DVH}}$, including their standard deviations, averaged over all anatomical structures and across the full test dataset, for the models trained on the augmented dataset and the model trained on the original dataset. The figure shows the corresponding mean treatment parameters across the entire test dataset for the various models, along with the overall mean calculated across all treatment parameters.

Overall, none of the models trained on datasets expanded through data augmentation consistently yield improved evaluation parameters. The use of data augmentation to expand the dataset does not provide significant benefits to network performance that would justify the training time being increased by approximately a factor of three. For this reason, the subsequent hyperparameter optimisation is conducted using the non-augmented dataset.

### 6.4.6 Hyperparameter optimisation

To investigate potential improvements through hyperparameter tuning, the open-source software `Optuna`[20] was employed, which automates the search for optimal hyperparameters [120]. In this study, the optimisation is defined as the minimisation of an objective function, corresponding to the average validation loss obtained during cross-validation. The hyperparameter search is conducted as a grid search over the following intervals, with each configuration trained for 200 epochs:

- learning rate: $\{0.001, 0.005, 0.01, 0.05\}$
- batch size: $\{2, 4\}$
- number of network layers: $\{3, 4\}$
- number of initial feature maps: $\{32, 64\}$

The optimisation results in a best learning rate of 0.005, an optimal number of 4 layers, 64 initial feature maps, and a batch size of 4. Compared to the initial network configuration described in subsection 6.4.1, this corresponds to a different learning rate and batch size.

[20]Optuna, a hyperparameter optimization framework. `https://optuna.org`.

In Table 6.7, the evaluation parameters for the model trained for 500 epochs using the best hyperparameter configuration determined by `Optuna` are presented, along with a comparison with the previously best-performing model, referred to as the baseline model. The baseline model is trained using the parameters described in subsection 6.4.1, except for the scaling of the dose tensors, which, as described in subsection 6.4.2, is changed to a scaling factor of $2 \cdot 10^{13}$. The `Optuna` model and the baseline model differ only in the learning rate and batch size used for training.
The comparison shows no clear improvement in the evaluation parameters for the model trained with the optimised hyperparameter configuration over the baseline model. Only the value of $\overline{\mathrm{MAE}_{\mathrm{DVH}}}$ improved by $(10.7 \pm 45.9)\,\%$, and the value of $\Delta D_{\mathrm{max}}^{\mathrm{sclera}}$ by $(17.3 \pm 104.3)\,\%$. For all other evaluation parameters, the baseline model performs better. In particular, the value of $\Delta D_{\mathrm{min}}^{\mathrm{tumour}}$ is lower for the baseline model by $(72.6 \pm 485.2)\,\%$.

Table 6.7: Evaluation parameters, including their standard deviations, for the entire test dataset, comparing the model trained with the optimised hyperparameter configuration (`Optuna` model) to the model trained with the initial hyperparameter configuration (baseline model). Both models were trained on dose tensors scaled by a factor of $2 \cdot 10^{13}$. Absolute deviation is calculated as the difference between the baseline model value and the corresponding `Optuna` model value.

| evaluation parameters | `Optuna` model | baseline model | abs. deviation |
|---|---|---|---|
| $\overline{\mathrm{MAE}}$ / Gy | 28.4 ± 15.0 | 27.9 ± 14.9 | 0.5 ± 21.2 |
| $\overline{\mathrm{MAE}_{\mathrm{DVH}}}$ / pp | 2.5 ± 1.0 | 2.8 ± 0.9 | −0.3 ± 1.3 |
| $\Delta D_{\mathrm{min}}^{\mathrm{tumour}}$ / Gy | 10.7 ± 11.1 | 6.2 ± 16.2 | 4.5 ± 19.6 |
| $\Delta D_{\mathrm{max}}^{\mathrm{sclera}}$ / Gy | 4.3 ± 4.1 | 5.2 ± 4.3 | −0.9 ± 5.9 |
| $\Delta D_{\mathrm{max}}^{\mathrm{papilla}}$ / Gy | 0.3 ± 2.3 | 0.1 ± 2.2 | 0.2 ± 3.2 |
| $\Delta D_{\mathrm{max}}^{\mathrm{fovea}}$ / Gy | −2.5 ± 8.0 | −2.8 ± 6.9 | 0.3 ± 10.6 |
| $\overline{x}_{\mathrm{all}}$ | 3.2 ± 3.6 | 2.2 ± 3.3 | 1.0 ± 4.9 |

## 6.5 Evaluation of network optimisation and clinical relevance

In this chapter, a neural network-based approach for dose prediction with $^{106}$Ru applicators for intraocular tumours is presented. Building on [14], a 3D U-Net architecture is trained on an extended dataset, increased from 39 to 72 MC-simulated treatment configurations generated using the framework described in chapter 3. Binary spatial tensors encode the positions of the ocular structures and the applicator target as network input, while the corresponding dose tensors serve as the output, enabling supervised learning.
To achieve accurate dose predictions, several parameter tuning studies are conducted, systematically varying model configurations, training strategies, and hyperparameters. The network performance and the effects of each optimisation strategy are evaluated using multiple error metrics, including the bin-wise mean absolute error, the mean absolute error of dose-volume histograms, and essential treatment parameters, providing a more clinically specific assessment.

The initial network configuration shows a mean absolute error of $\overline{\mathrm{MAE}} = (29.1 \pm 15.9)\,\mathrm{Gy}$ and a mean DVH error of $\overline{\mathrm{MAE}_{\mathrm{DVH}}} = (3.0 \pm 1.1)\,\mathrm{pp}$ across all structures in the test data-

set. The average difference between simulated reference values and the predicted treatment parameters is $(1.3 \pm 4.2)$ Gy. Clinically, this corresponds to a performance level suitable for treatment planning, as mean deviations in the two most essential factors for dose conformity, the minimum tumour dose and maximum scleral dose, remain within acceptable ranges with $\Delta D_{\text{min}}^{\text{tumour}} = (5.8 \pm 14.7)$ Gy $((4.3 \pm 15.8)\,\%)$ and $\Delta D_{\text{max}}^{\text{sclera}} = (2.6 \pm 3.0)$ Gy $((0.6 \pm 0.6)\,\%)$. Overall, these results suggest that the model provides sufficiently reliable estimates to support treatment decisions and anticipate potential side effects.
Varying the scaling of the dose tensors has shown no consistent advantages across the evaluation metrics. With respect to the $\overline{\text{MAE}}$, mixed linear-logarithmic scaling performs best $((27.7 \pm 14.8)$ Gy), but it shows the worst results for the mean of the four treatment parameters $((2.6 \pm 3.4)$ Gy). Logarithmic scaling yields the lowest $\overline{\text{MAE}_{\text{DVH}}}$ $((2.2 \pm 0.6)$ pp), yet performed worst in terms of $\overline{\text{MAE}}$. Among the three scaling factors tested, $2 \cdot 10^{13}$ provides the best overall performance and is therefore used in further studies. For both logarithmic and mixed linear-logarithmic scaling, an initial factor of $10^{13}$ ensures numerical stability. Future work could explore alternative scaling factors and adjust the threshold in the mixed scaling to further optimise performance.
Neither the exploration of alternative loss functions, including masked MSE and masked Huber loss, nor changing the optimiser from `Adam` to `AdamW` with various weight decay values, have improved performance compared with the model trained with the initial parameters, apart from the modified scaling factor. These findings indicate that the initial training configuration was already appropriate to the task and that network performance is robust to reasonable variations in the loss function and optimiser settings.
Increasing the dataset with data augmentation methods, such as mirroring and rotations, has yielded only minor improvements in $\overline{\text{MAE}_{\text{DVH}}}$ and, in part, the treatment parameters. Overall, models trained with augmented data do not outperform the original model across all metrics, likely because these transformations do not alter the fundamental shapes of the structures. Including additional patient cases, diverse tumour geometries and positions, and further applicator models could enhance the robustness and predictive accuracy of the network.
To investigate potential improvements through hyperparameter tuning, a grid search has been performed using the `Optuna` software, exploring variations in learning rate and batch size. The model trained with these modified parameters has not demonstrated any clear performance improvement compared with the initial model using the other scaling factor. It is possible that a broader search space could reveal configurations that enhance performance. Overall, the parameter tuning studies conducted in this work do not result in a significant improvement in the performance of the initial network configuration. Additional investigations into alternative scaling factors, including an analysis of the threshold in the mixed linear-logarithmic scaling, could reveal whether further variations in the dose tensor scaling lead to noticeable improvements in performance. Also, improvements through alternative loss functions or optimisers cannot be excluded. However, given that neither dataset expansion through augmentation nor hyperparameter tuning has resulted in significant changes in the evaluation metrics, it is reasonable to conclude that the performance of the existing network is unlikely to be substantially enhanced through parameter tuning.

From a clinical perspective, the performance of the network, particularly with respect to the treatment parameters, is sufficiently accurate to serve as an initial indicator in treatment planning. Potential underdosing of the tumour, exceeding the tolerable dose of the sclera,

and trends indicating possible side effects from high doses in structures at risk can be estimated using the predicted dose values. However, this currently applies only to cases that are geometrically similar to the configurations modelled here. Whether the network performs equally well for entirely different tumour and applicator geometries must be evaluated in subsequent studies. For clinical application, the network should ideally be trained on a dataset that includes greater variability in clinical scenarios, covering tumour position within the eye and tumour geometry, to improve the robustness of the model. Furthermore, clinical studies are required to determine the extent to which neural network-assisted planning enhances the quality of existing treatment plans before such methods can be adopted in routine clinical practice.
The development of a planning interface that appropriately visualises the predicted dose distributions for medical physicists and clinicians would also facilitate the integration of the network into everyday planning. A first approach to this is presented in chapter 7.

# 7 Concept for a clinical treatment planning interface

In external beam radiotherapy, TPSs are used to determine radiation beam configurations and dose distributions, to achieve effective tumour control while minimising damage to surrounding organs at risk. These systems commonly employ 3D representations of the patient anatomy and tumour volumes to facilitate precise treatment delivery [121]. With regard to brachytherapy using $^{106}$Ru applicators, there is currently no commercially available TPS that meets the quality assurance standards of the UME. Therefore, treatment planning is based on internally developed software tools. However, these tools are limited in terms of 3D visualisation and calculation of dose distributions. In addition, imaging modalities are often restricted to ultrasound and fundus photography due to financial limitations. This creates significant challenges in adapting commercial TPSs, which are typically designed to work with CT- or MRI-based imaging, for ocular brachytherapy.
The methodologies presented in chapter 3 for the simulation of homogeneous applicator treatments, together with the neural network architecture introduced in chapter 6, provide a fundamental basis for the development of a clinical treatment planning interface. A concept for such an interface is presented in this chapter.[21]

The architectural basis of the treatment planning interface is `Emscripten`[22], which enables the compilation of C++ code to WebAssembly for platform-independent, web-based deployment [122]. Building on this foundation, the application is implemented using `SDL3`[23] as the underlying cross-platform framework for window creation, rendering, and event handling.
An example of the graphical user interface is shown in Figure 7.1, illustrating a patient case treated with a CCA applicator. The interface is designed to integrate multiple data modalities relevant to clinical treatment planning in ocular brachytherapy.

In the treatment of uveal melanoma, fundus photographs are essential for planning. They allow the measurement of the tumour base and the visualisation of its position relative to the fovea and the papilla. In combination with the 3D representation of the scenario generated in Fusion, these images provide an overview of the location of the tumour within the eye and facilitate assessment of potential challenges related to applicator placement during surgery, for instance in relation to the optic nerve. The images generated in Fusion can be automatically created and saved using the existing Python scripts for patient-specific modelling, allowing them to be loaded into the interface alongside the fundus photographs for integrated visualisation.
The STL files exported from Fusion are loaded by the `Emscripten`-compiled application and used to generate an interactive 3D visualisation of the patient case within the web environment. This allows the inspection of the geometric configuration of the eye and tumour.

[21] The development of the interface was carried out with contributions from Nicholas Oldman and Annika Bennemann, two student research assistants, who assisted with data processing and software implementation.
[22] Emscripten, compiler toolchain to WebAssembly. `https://emscripten.org`.
[23] SDL3, Simple Directmedia Layer, cross-platform development library. `https://www.libsdl.org`.

Individual anatomical structures can be displayed selectively and assigned distinct colours, thereby improving visual differentiation and spatial understanding.

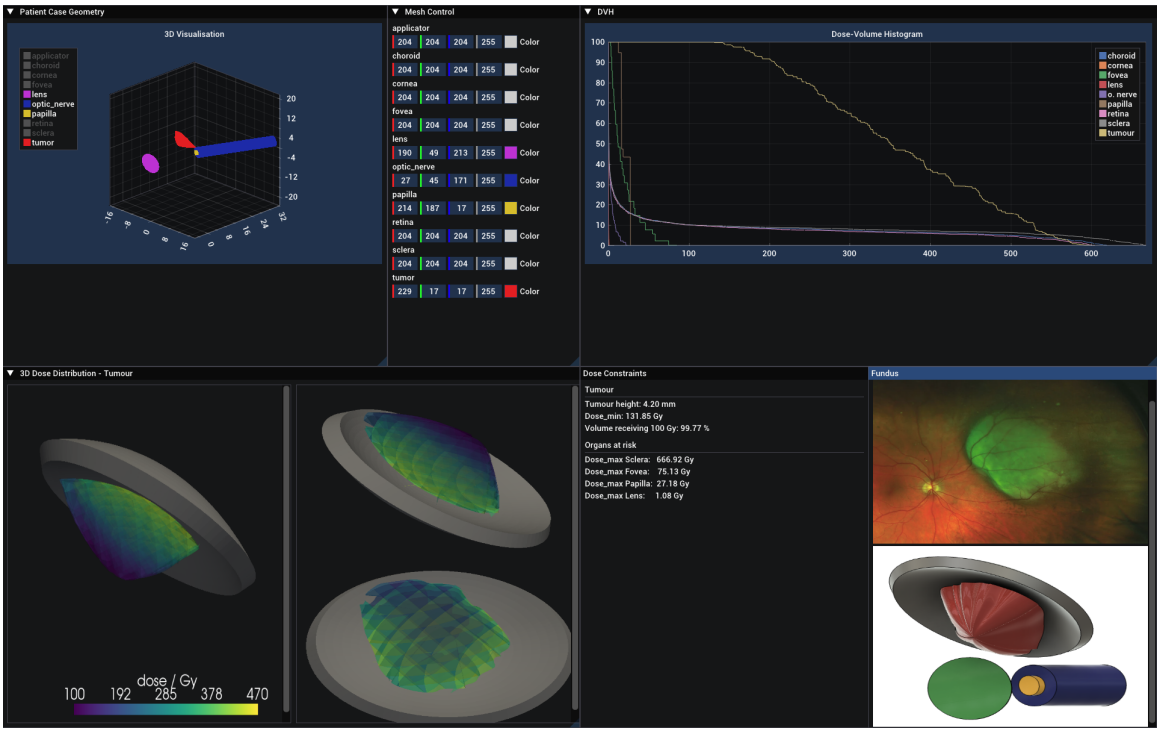


Figure 7.1: Treatment planning interface for a patient case treated with a CCA applicator. The upper-left quadrant displays the interface for visualising the patient geometry using STL files. The upper-right quadrant shows the corresponding DVH. The lower-left quadrant presents the 3D dose distribution within the tumour, together with the applicator, from multiple spatial perspectives. The lower-right quadrant is divided into a panel displaying the critical treatment parameters for the tumour and surrounding structures at risk, and a panel presenting the fundus photograph alongside a view from Fusion showing the tumour and applicator positions relative to these structures. The fundus photograph is not from the displayed patient case and is used with permission from Ref. [17] as an illustrative example.

The binning strategy developed in this work and described in section 3.4 enables the 3D representation of dose distributions within the tumour and surrounding ocular structures. Deposited energy values obtained from MC simulations are assigned to spatial bins based on their coordinates, allowing reconstruction of the dose distribution. In particular for the tumour, this representation supports assessment of whether modifications to the applicator model or its positioning are required to achieve adequate tumour coverage. Using the `PyVista` library, 3D dose distributions can be visualised for selected structures from multiple viewing angles and exported in various file formats. These visualisations are automatically generated within the workflow and can be subsequently loaded by the interface.
As part of the software workflow for the simulation of homogeneous applicator treatments, DVHs are generated in the analysis pipeline, constituting a fundamental component of radiotherapy treatment planning. Based on the simulation data, relevant treatment parameters

are derived, including maximum doses to the tumour and organs at risk, as well as the tumour volume receiving at least 100 Gy. The data required for treatment analysis and DVH visualisation are provided to the interface via JSON files.

The integration of the neural network described in chapter 6 into the software workflow enables prediction of dose distributions without the need for time-consuming and resource-intensive MC simulations. Using the predicted dose values, the data required for 3D dose visualisation, DVH generation, and treatment analysis can be produced analogously. These predicted dose data are processed identically to the MC-based results and are likewise loaded by the `Emscripten`-compiled application for visualisation within the interface.

Overall, the presented interface provides an extensible framework for interactive, multimodal visualisation in ocular brachytherapy treatment planning, with the relevant treatment planning data accessible within the interface. Its web-based implementation allows platform-independent access via standard web browsers, offering advantages for clinical usability. While neural network–based dose prediction represents a promising direction for prospective treatment planning, its use in clinical practice will require careful validation through dedicated clinical studies.

# 8 Conclusion and outlook

Intraocular tumours represent a serious clinical condition, with the potential for vision loss and life-threatening metastatic disease [5]. Among eye-preserving treatment options, brachytherapy with $^{106}$Ru applicators has become a well-established and widely used modality [6]. This thesis aims to enhance $^{106}$Ru ocular brachytherapy by investigating the impact of inhomogeneous surface dose profiles on treatment and by developing an efficient MC simulation workflow together with a neural network-based dose prediction model that enables the incorporation of patient-specific, 3D information into treatment planning.

An improved software workflow for simulating $^{106}$Ru ocular brachytherapy was developed by extending the original workflow presented in Ref. [9]. In this work, a particle tracking method is integrated in Geant4, and an external Python-based binning approach is implemented in the workflow. This combination allows for flexible, 3D scoring of dose distributions within complex geometries. The workflow was validated against the previous implementation from Ref. [9], demonstrating agreement in depth-dose curves and dose-volume histograms.

A key achievement of this workflow is its enhancement of computational efficiency compared to the workflow presented in Ref. [9]. The simulation times were reduced by 62 to 84 %, and the memory usage decreased by up to 60 %, depending on mesh quality and multi-threading configuration. The binning method enables patient-specific visualisation of dose distributions and allows adjustments of spatial resolution after simulation to balance precision and computational cost. The analysis of the simulated dose distributions showed distortions in very small bin volumes, usually below 0.01 mm$^3$. These distortions were caused by statistical variations and sparse dose allocations. To address these issues, a 2 % cut-off was applied to the highest and lowest dose values. This helped to remove extreme outliers and provided a more robust representation of the dose distribution.

Implemented in this workflow, a simulation architecture for modelling inhomogeneous surface dose profiles of $^{106}$Ru applicators was presented, based on a phase space approach to approximate the solution of the underlying inverse MC problem. Dose deposition events from homogeneous simulations are linked to primary particle vertices and stored in phase space files, which are then weighted and combined to reproduce desired inhomogeneous surface dose profiles, including hot and cold spots, as well as combined scenarios.
For the inhomogeneous simulations, two detector geometries were employed. The cylindrical detectors replicate the measurement setup of the manufacturer, while the surface detector provides higher spatial resolution as it lies parallel to the applicator surface. The comparison of homogeneous simulations with the two geometries showed good agreement, with maximum differences below 6 pp and mean differences below 4.5 pp. The largest deviations occurred near the applicator edge, due to the steep dose gradient.
The comparison of the cylindrical detector results with the measurement certificates of the manufacturer revealed substantial deviations, particularly in the third measurement ring, where the mean differences reached up to $(58.5 \pm 0.7)$ pp for the COB model. These dis-

crepancies likely arise from differences between simulated homogeneous and experimentally measured inhomogeneous profiles, geometric and material approximations in the simulation, slight variations in detector positioning, and contributions from Cherenkov radiation in the experimental measurements. A dedicated measurement setup is required to investigate these effects and is currently being developed in a parallel PhD thesis [100].
The phase-space-based simulation was further validated against GPS-generated distributions, demonstrating good agreement across all applicator models with mean deviations below 1.5 pp. For the COB applicator, cluster-like deviations arise from the optimisation approach used to determine the large number of phase space weights. The improvement of the optimisation algorithm, or a potential replacement with a neural network-based approach, could improve the accuracy and should be investigated in future work, particularly for studying the surface-dose profiles of applicator geometries that are not rotationally symmetric.

The impact of inhomogeneous surface dose distributions on $^{106}$Ru brachytherapy was investigated using three representative patient cases, one for each applicator model (CCA, CCB, COB). Each case included a homogeneous reference and multiple inhomogeneous scenarios, including hot spots, cold spots, and combinations of both. In all cases, the tumour control doses ($(85 \pm 15)$ Gy) were achieved, regardless of normalisation to 130 Gy or 100 Gy at the tumour apex. This indicates that the safety margins of the UME dose concept are sufficient to compensate for surface dose inhomogeneities.
In the simulated scenarios of the COB applicator, a systematic shift towards higher dose values can be observed in those cases modelled using solely phase space files, compared with scenarios that also employ the GPS. This shift is a consequence of deviations introduced by the optimisation approach used to determine the large number of phase space weights. This finding highlights that, for the COB applicator, the current method should be further optimised in future work to achieve greater accuracy.
The hot spot scenarios generally increased doses to structures at risk, whereas cold spots could reduce these doses without compromising tumour coverage, particularly when applicators were positioned appropriately. The tumour height affected the minimum tumour dose and the maximum scleral dose, indicating that for very small tumours or pronounced cold spots, normalisation to the scleral contact dose may be required to ensure adequate irradiation. Overall, even surface dose profiles exceeding quality assurance limits did not compromise the tumour control. However, the cases in this thesis represent full coverage of the target volume. In clinical practice, geometric uncertainties or intentional positioning near the tumour margins may reduce the effective safety margin, making cold spots at the tumour edge potentially critical.
The results highlight the potential benefit of reducing the apex dose to 100 Gy to spare structures at risk. Especially the combination with 3D treatment planning that accounts for patient geometry and dose inhomogeneities, could improve safety and support vision preservation.

Within the broader framework of improving treatment planning for $^{106}$Ru brachytherapy, it was demonstrated that neural networks can approximate MC dose distributions with high accuracy, providing fast decision support. A 3D U-Net trained on simulated patient case configurations was able to reproduce 3D dose distributions with clinically acceptable deviations in key treatment parameters, with mean differences of $(5.8 \pm 14.7)$ Gy ($(4.3 \pm 15.8)$ %) for the minimum tumour dose and $(2.6 \pm 3.0)$ Gy ($(0.6 \pm 0.6)$ %) for the maximum scleral dose between MC-simulated and predicted doses for the initial configuration.

A series of parameter-tuning studies examined scaling strategies, loss functions, optimisers, hyperparameters, and data augmentation. While minor improvements were observed in selected metrics, no consistent enhancement across all evaluation criteria was achieved. These results suggest that the network architecture and training strategy are generally suitable. Further advancements are more likely to come from increasing and diversifying the training dataset rather than from more parameter adjustments. In particular, a broader range of tumour geometries, positions, and applicator configurations would be required before robust generalisation to the full clinical spectrum can be expected.
Overall, the network performs effectively for geometries similar to those represented in the dataset and provides a foundation for future developments, such as integration into planning tools.

The software workflow for simulating homogeneous $^{106}$Ru applicator treatment and the integration of a neural network for the prediction of 3D dose distributions in patient-specific eye models can serve as a basis for a prototype treatment planning interface. The presented web-based interface combines multiple data modalities, including fundus photographs, 3D anatomical models, dose distributions, and dose-volume histograms, to support visualisation and analysis of the tumour control and organ-at-risk exposure. The system demonstrates a flexible framework for interactive ocular brachytherapy planning and highlights the potential of neural network-based dose prediction. Before such a tool can be used clinically, it must be integrated into the treatment workflow and validated against established treatment planning methods through clinical studies.

Altogether, the results of this work support the enhancement of $^{106}$Ru ocular brachytherapy by investigating the effects of inhomogeneous surface dose distributions and introducing a neural network-based approach for patient-specific, 3D treatment planning. Further studies are required to evaluate the impact of inhomogeneous surface dose profiles in cases of incomplete tumour coverage or more complex tumour geometries. Furthermore, the feasibility and safety of incorporating neural network-based dose prediction into routine planning should be investigated.
In parallel, the presented planning interface provides a prototype framework for a future treatment planning system, but it will need further technical development and prospective validation in clinical workflows before it can be considered for clinical implementation.

# A Attachments

## A.1 Benchmarking and validation data for the simulation workflow of homogeneous applicator treatment

The following tables and figures present the data from benchmarking and validating the new methods within the developed simulation workflow. The simulation workflow introduced in this thesis is referred to as $\mathrm{wf}_{\mathrm{trac}}$, while the workflow presented in Ref. [9] is denoted as $\mathrm{wf}_{\mathrm{cut}}$.

### Validation of the simulation workflow

Table A.1: Comparison of the maximum dose values obtained using $\mathrm{wf}_{\mathrm{trac}}$ and $\mathrm{wf}_{\mathrm{cut}}$ for the ocular structures in the MC simulation of a $^{106}$Ru treatment with a COB eye applicator. The absolute deviation $\mathrm{dev}_{\mathrm{abs}}$ of the dose values is calculated with the formula $\mathrm{dev}_{\mathrm{abs}} = x_{\mathrm{trac}} - x_{\mathrm{cut}}$, where $x$ represents the maximum dose value for the respective structure. The relative deviation $\mathrm{dev}_{\mathrm{abs}}$ of the dose values is calculated with the formula $\mathrm{dev}_{\mathrm{rel}} = 100 \cdot \mathrm{dev}_{\mathrm{abs}}/x_{\mathrm{cut}}$. The associated uncertainties were calculated using Gaussian error propagation.

| structure | $\mathrm{wf}_{\mathrm{trac}}$ $\mathrm{dose}_{\mathrm{max}}$ / Gy | $\mathrm{wf}_{\mathrm{cut}}$ $\mathrm{dose}_{\mathrm{max}}$ / Gy | $\mathrm{dev}_{\mathrm{abs}}$ / Gy | $\mathrm{dev}_{\mathrm{rel}}$ / % |
|---|---|---|---|---|
| choroid | 1453.8 ± 3.5 | 1437.3 ± 2.8 | 16.5 ± 4.5 | 1.1 ± 0.3 |
| cornea | 0.5 ± 0.1 | 1.1 ± 1.2 | −0.6 ± 1.2 | −54.5 ± 50.5 |
| fovea | 1266.6 ± 4.2 | 1296.6 ± 9.9 | −30.0 ± 10.8 | −2.3 ± 0.8 |
| retina | 1493.2 ± 2.5 | 1416.1 ± 6.1 | 76.9 ± 6.6 | 5.4 ± 0.5 |
| lens | 0.9 | 1.8 ± 1.7 | −0.9 ± 1.7 | −50.0 ± 47.2 |
| papilla | 104.1 ± 0.6 | 96.7 ± 0.5 | 7.4 ± 0.8 | 7.7 ± 0.8 |
| sclera | 1601.3 ± 5.1 | 1602.8 ± 11.4 | −1.5 ± 12.5 | −0.1 ± 0.8 |
| optic nerve | 67.2 ± 0.6 | 98.9 ± 0.8 | −31.7 ± 1.0 | −32.1 ± 0.8 |
| tumour | 1374.9 ± 2.0 | 1305.8 ± 5.9 | 69.1 ± 6.2 | 5.3 ± 0.5 |

Table A.2: Comparison of the minimum dose values obtained using $\mathrm{wf_{trac}}$ and $\mathrm{wf_{cut}}$ for the ocular structures in the MC simulation of a $^{106}$Ru treatment with a COB eye applicator. The absolute deviation $\mathrm{dev_{abs}}$ of the dose values is calculated with the formula $\mathrm{dev_{abs}} = x_{\mathrm{trac}} - x_{\mathrm{cut}}$, where $x$ represents the minimum dose value for the respective structure. The relative deviation $\mathrm{dev_{abs}}$ of the dose values is calculated with the formula $\mathrm{dev_{rel}} = 100 \cdot \mathrm{dev_{abs}}/x_{\mathrm{cut}}$.The associated uncertainties were calculated using Gaussian error propagation.

| structure | $\mathrm{wf_{trac}}$ $\mathrm{dose_{min}}$ / Gy | $\mathrm{wf_{cut}}$ $\mathrm{dose_{min}}$ / Gy | $\mathrm{dev_{abs}}$ / Gy | $\mathrm{dev_{rel}}$ / % |
|---|---|---|---|---|
| choroid | 0 | 0 | – | – |
| cornea | 0 | 0 | – | – |
| fovea | 139.5 ± 5.2 | 190.9 ± 1.2 | −51.4 ± 5.3 | −26.9 ± 2.8 |
| retina | 0 | 0 | – | – |
| lens | 0 | 0 | – | – |
| papilla | 46.2 ± 0.9 | 53.2 ± 1.7 | −7.0 ± 1.9 | −13.2 ± 3.3 |
| sclera | 0 | 0 | – | – |
| optic nerve | 0 | 0 | – | – |
| tumour | 106.9 ± 0.9 | 0 | – | – |

Table A.3: Comparison of the mean dose values obtained using $\mathrm{wf_{trac}}$ and $\mathrm{wf_{cut}}$ for the ocular structures in the MC simulation of a $^{106}$Ru treatment with a COB eye applicator. The absolute deviation $\mathrm{dev_{abs}}$ of the dose values is calculated with the formula $\mathrm{dev_{abs}} = x_{\mathrm{trac}} - x_{\mathrm{cut}}$, where $x$ represents the mean dose value for the respective structure. The relative deviation $\mathrm{dev_{abs}}$ of the dose values is calculated with the formula $\mathrm{dev_{rel}} = 100 \cdot \mathrm{dev_{abs}}/x_{\mathrm{cut}}$.The associated uncertainties were calculated using Gaussian error propagation.

| structure | $\mathrm{wf_{trac}}$ $\mathrm{dose_{mean}}$ / Gy | $\mathrm{wf_{cut}}$ $\mathrm{dose_{mean}}$ / Gy | $\mathrm{dev_{abs}}$ / Gy | $\mathrm{dev_{rel}}$ / % |
|---|---|---|---|---|
| choroid | 178.2 ± 395.4 | 195.0 ± 418.9 | −16.8 ± 576.0 | −8.6 ± 282.2 |
| cornea | 0.2 ± 0.1 | 0.3 | −0.1 ± 0.1 | −33.3 ± 33.3 |
| fovea | 858.4 ± 334.2 | 883.1 ± 346.8 | −24.7 ± 481.6 | −2.8 ± 53.8 |
| retina | 154.8 ± 366.9 | 171.8 ± 392.6 | −17.0 ± 537.4 | −9.9 ± 296.6 |
| lens | 0.4 ± 0.1 | 0.4 ± 0.1 | 0 | 0 |
| papilla | 75.9 ± 16.3 | 76.2 ± 13.1 | −0.3 ± 20.9 | −0.39± 27.40 |
| sclera | 236.6 ± 477.6 | 249.1 ± 490.8 | −12.5 ± 684.8 | −5.0 ± 267.9 |
| optic nerve | 3.0 ± 8.7 | 3.5 ± 10.5 | −0.5 ± 13.6 | −14.3 ± 357.6 |
| tumour | 562.0 ± 322.9 | 570.0 ± 314.2 | −8.0 ± 450.5 | −1.4 ± 78.5 |

## Influence of STL mesh quality

Table A.4: Average simulation time $t$ and memory usage $RSS$ for the Monte Carlo simulation of the eye model in Geant4, evaluated at different STL export qualities and using the workflows $\mathrm{wf_{trac}}$ and $\mathrm{wf_{cut}}$. The data for $\mathrm{wf_{trac}}$ is published in Ref. [67].

| | $t$ / s | | $RSS$ / MiB | |
|---|---|---|---|---|
| quality | $\mathrm{wf_{trac}}$ | $\mathrm{wf_{cut}}$ | $\mathrm{wf_{trac}}$ | $\mathrm{wf_{cut}}$ |
| low | 5204.7 ± 21.4 | 24 395.5 ± 1215.7 | 1920.6 ± 15.3 | 5014.2 ± 7.5 |
| medium | 7928.7 ± 84.6 | 28 991.1 ± 1227.1 | 2841.8 ± 15.7 | 5070.7 ± 4.6 |
| high | 12 537.8 ± 169.2 | 32 753.8 ± 1936.0 | 6092.6 ± 14.8 | 8078.4 ± 4.9 |

## Impact of multi-threading on Monte Carlo simulation

Table A.5: Average simulation time $t$ and memory usage $RSS$ as a function of the number of threads in the MC simulation of the eye model in Geant4, using the workflows $\mathrm{wf}_{\mathrm{trac}}$ and $\mathrm{wf}_{\mathrm{cut}}$. The data for $\mathrm{wf}_{\mathrm{trac}}$ is published in Ref. [67].

| | $t$ / s | | $RSS$ / MiB | |
|---|---|---|---|---|
| threads | $\mathrm{wf}_{\mathrm{trac}}$ | $\mathrm{wf}_{\mathrm{cut}}$ | $\mathrm{wf}_{\mathrm{trac}}$ | $\mathrm{wf}_{\mathrm{cut}}$ |
| 1 | 5204.7 ± 21.4 | 24 395.5 ± 1215.7 | 1920.6 ± 15.3 | 5014.2 ± 7.5 |
| 2 | 2498.1 ± 32.6 | 14 472.9 ± 1127.3 | 2007.8 ± 11.2 | 5039.2 ± 8.1 |
| 3 | 1555.3 ± 70.0 | 9525.2 ± 807.6 | 2072.1 ± 24.4 | 5071.5 ± 7.7 |

## Volume analysis of the binning process with PyVista Boolean operation

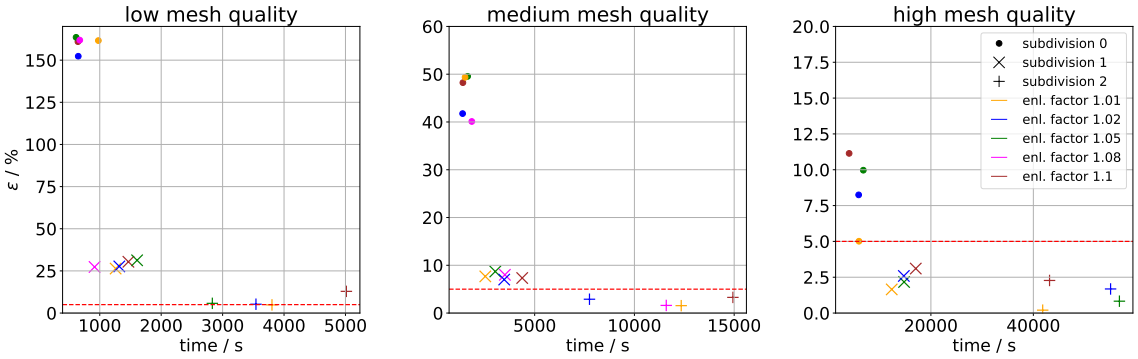


Figure A.1: Volume analysis for the choroid using the binning process with `PyVista` Boolean operation. Volume deviation $\epsilon$ in percentage represents the relative deviation between the volume obtained from the sum of the bin volumes and the calculated volume of the unbinned mesh. The mesh qualities correspond to the STL export qualities in Fusion.

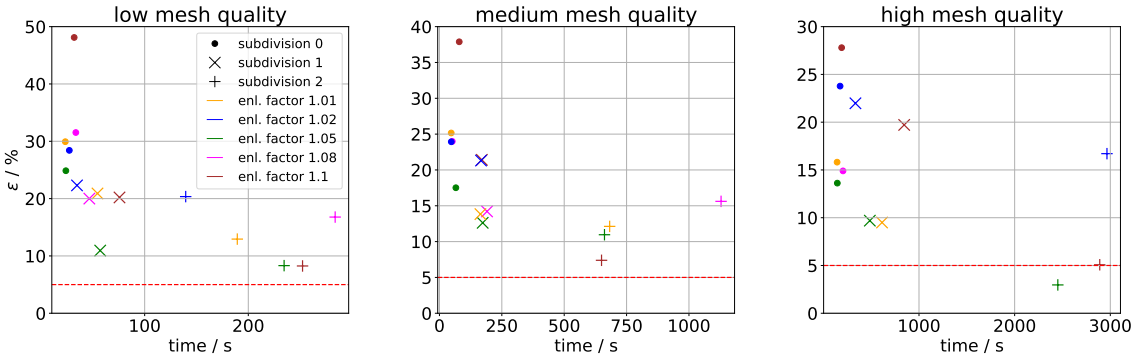


Figure A.2: Volume analysis for the cornea using the binning process with `PyVista` Boolean operation. Volume deviation $\epsilon$ in percentage represents the relative deviation between the volume obtained from the sum of the bin volumes and the calculated volume of the unbinned mesh. The mesh qualities correspond to the STL export qualities in Fusion.

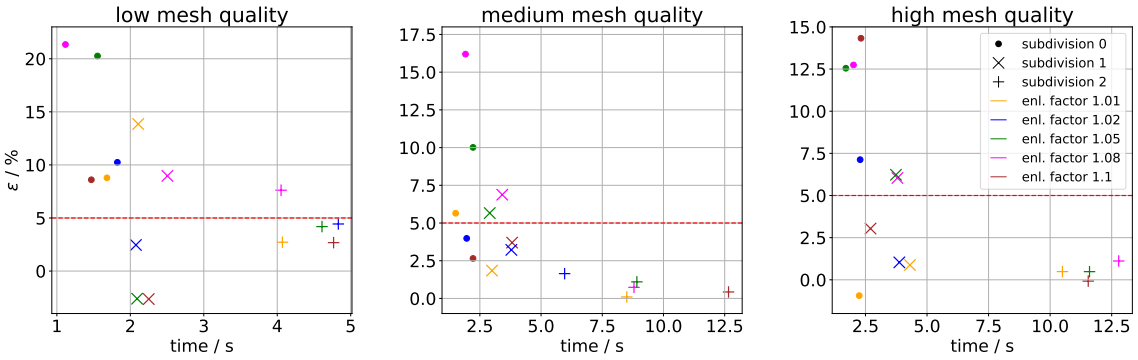


Figure A.3: Volume analysis for the fovea using the binning process with `PyVista` Boolean operation. Volume deviation $\epsilon$ in percentage represents the relative deviation between the volume obtained from the sum of the bin volumes and the calculated volume of the unbinned mesh. The mesh qualities correspond to the STL export qualities in Fusion.

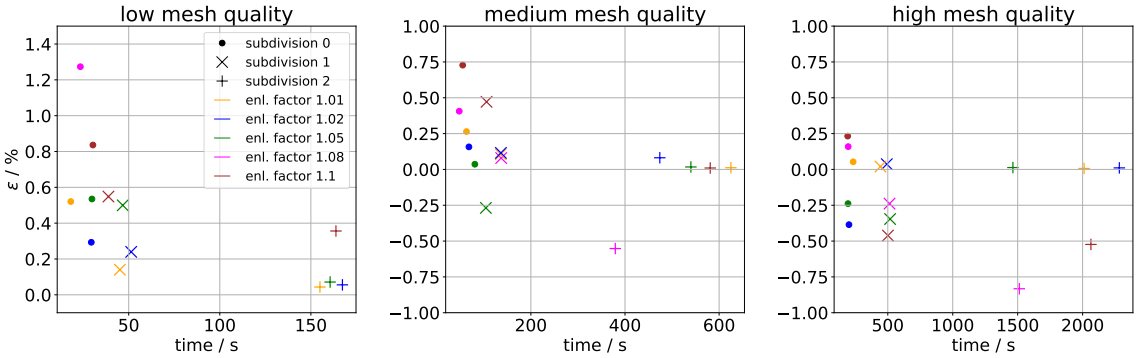


Figure A.4: Volume analysis for the lens using the binning process with `PyVista` Boolean operation. Volume deviation $\epsilon$ in percentage represents the relative deviation between the volume obtained from the sum of the bin volumes and the calculated volume of the unbinned mesh. The mesh qualities correspond to the STL export qualities in Fusion.

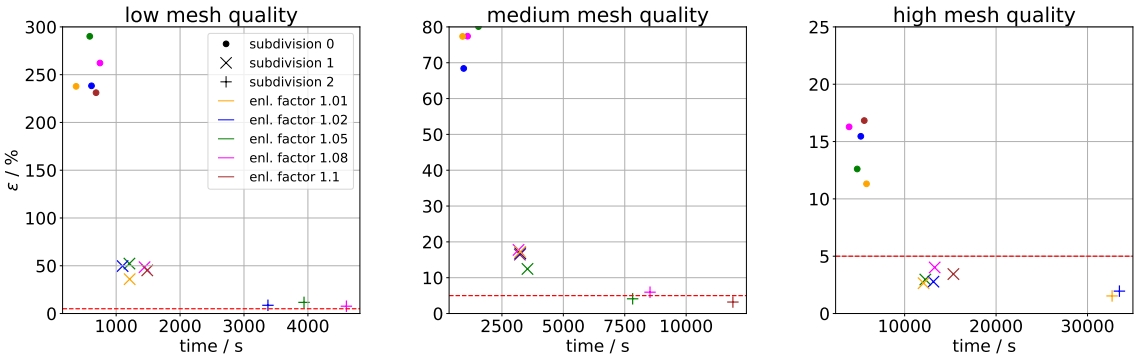


Figure A.5: Volume analysis for the retina using the binning process with `PyVista` Boolean operation. Volume deviation $\epsilon$ in percentage represents the relative deviation between the volume obtained from the sum of the bin volumes and the calculated volume of the unbinned mesh. The mesh qualities correspond to the STL export qualities in Fusion.

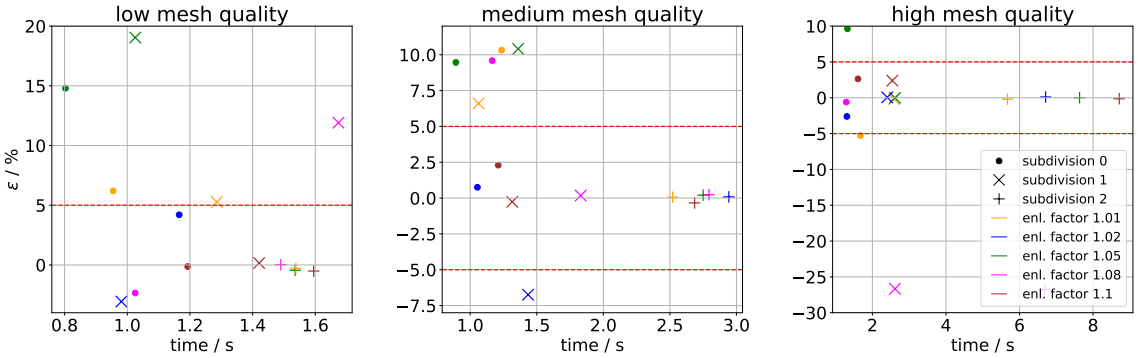


Figure A.6: Volume analysis for the papilla using the binning process with `PyVista` Boolean operation. Volume deviation $\epsilon$ in percentage represents the relative deviation between the volume obtained from the sum of the bin volumes and the calculated volume of the unbinned mesh. The mesh qualities correspond to the STL export qualities in Fusion.

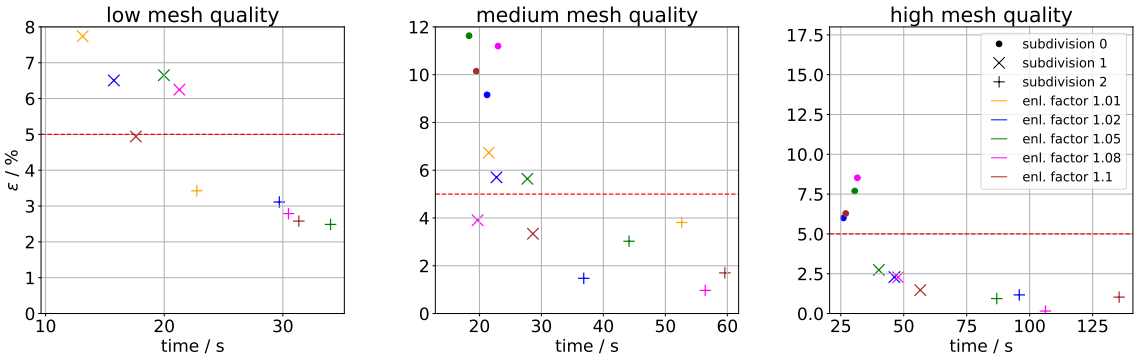


Figure A.7: Volume analysis for the optic nerve using the binning process with `PyVista` Boolean operation. Volume deviation $\epsilon$ in percentage represents the relative deviation between the volume obtained from the sum of the bin volumes and the calculated volume of the unbinned mesh. The mesh qualities correspond to the STL export qualities in Fusion.

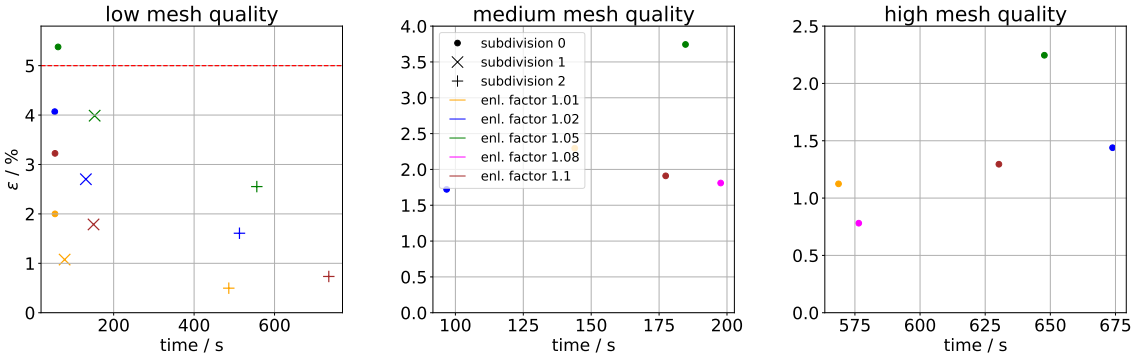


Figure A.8: Volume analysis for the tumour using the binning process with `PyVista` Boolean operation. Volume deviation $\epsilon$ in percentage represents the relative deviation between the volume obtained from the sum of the bin volumes and the calculated volume of the unbinned mesh. The mesh qualities correspond to the STL export qualities in Fusion.

### Validation of the binning process with MeshLib Boolean operation

Table A.6: Comparison of the maximum dose values obtained using `PyVista` (PV) and `MeshLib` (MH) for the ocular structures in the MC simulation of a $^{106}$Ru treatment with a COB eye applicator. The absolute deviation $\mathrm{dev}_{\mathrm{abs}}$ of the dose values is calculated with the formula $\mathrm{dev}_{\mathrm{abs}} = x_{\mathrm{PV}} - x_{\mathrm{MH}}$, where $x$ represents the maximum dose value for the respective structure. The relative deviation $\mathrm{dev}_{\mathrm{abs}}$ of the dose values is calculated with the formula $\mathrm{dev}_{\mathrm{rel}} = 100 \cdot \mathrm{dev}_{\mathrm{abs}}/x_{\mathrm{MH}}$. The associated uncertainties were calculated using Gaussian error propagation.

| structure | PV $\mathrm{dose}_{\mathrm{max}}$ / Gy | MH $\mathrm{dose}_{\mathrm{max}}$ / Gy | $\mathrm{dev}_{\mathrm{abs}}$ / Gy | $\mathrm{dev}_{\mathrm{rel}}$ / % |
|---|---|---|---|---|
| choroid | 1453.8 ± 3.5 | 1415.1 ± 2.1 | 38.7 ± 4.1 | 2.7 ± 0.3 |
| cornea | 0.5 ± 0.1 | 0.5 | 0.0 ± 0.1 | 0.0 |
| fovea | 1266.6 ± 4.2 | 1268.3 ± 4.4 | −1.7 ± 6.1 | −0.1 ± 0.5 |
| retina | 1493.2 ± 2.5 | 1390.7 ± 2.4 | 102.5 ± 3.5 | 7.4 ± 0.3 |
| lens | 0.9 | 0.9 | 0.0 | 0.0 |
| papilla | 104.1 ± 0.6 | 100.5 ± 0.5 | 3.6 ± 0.8 | 3.6 ± 0.8 |
| sclera | 1601.3 ± 5.1 | 1587.6 ± 3.1 | 13.7 ± 6.0 | 0.9 ± 0.4 |
| optic nerve | 67.2 ± 0.6 | 56.1 ± 1.0 | 11.1 ± 1.2 | 19.8 ± 2.4 |
| tumour | 1374.9 ± 2.0 | 1392.0 ± 6.4 | −17.1 ± 6.7 | −1.2 ± 0.5 |

Table A.7: Comparison of the minimum dose values obtained using `PyVista` (PV) and `MeshLib` (MH) for the ocular structures in the MC simulation of a $^{106}$Ru treatment with a COB eye applicator. The absolute deviation $\mathrm{dev}_{\mathrm{abs}}$ of the dose values is calculated with the formula $\mathrm{dev}_{\mathrm{abs}} = x_{\mathrm{PV}} - x_{\mathrm{MH}}$, where $x$ represents the minimum dose value for the respective structure. The relative deviation $\mathrm{dev}_{\mathrm{abs}}$ of the dose values is calculated with the formula $\mathrm{dev}_{\mathrm{rel}} = 100 \cdot \mathrm{dev}_{\mathrm{abs}}/x_{\mathrm{MH}}$. The associated uncertainties were calculated using Gaussian error propagation.

| structure | PV $\mathrm{dose}_{\mathrm{min}}$ / Gy | MH $\mathrm{dose}_{\mathrm{min}}$ / Gy | $\mathrm{dev}_{\mathrm{abs}}$ / Gy | $\mathrm{dev}_{\mathrm{rel}}$ / % |
|---|---|---|---|---|
| choroid | 0 | 0 | – | – |
| cornea | 0 | 0 | – | – |
| fovea | 139.5 ± 5.2 | 183.6 ± 1.1 | −44.1 ± 5.3 | −24.0 ± 2.9 |
| retina | 0 | 0 | – | – |
| lens | 0 | 0 | – | – |
| papilla | 46.2 ± 0.9 | 53.2 ± 1.7 | −7.0 ± 1.9 | −13.2 ± 3.3 |
| sclera | 0 | 0 | – | – |
| optic nerve | 0 | 0 | – | – |
| tumour | 106.9 ± 0.9 | 0 | – | – |

Table A.8: Comparison of the mean dose values obtained using `PyVista` (PV) and `MeshLib` (MH) for the ocular structures in the MC simulation of a $^{106}$Ru treatment with a COB eye applicator. The absolute deviation $\mathrm{dev}_{\mathrm{abs}}$ of the dose values is calculated with the formula $\mathrm{dev}_{\mathrm{abs}} = x_{\mathrm{PV}} - x_{\mathrm{MH}}$, where $x$ represents the mean dose value for the respective structure. The relative deviation $\mathrm{dev}_{\mathrm{abs}}$ of the dose values is calculated with the formula $\mathrm{dev}_{\mathrm{rel}} = 100 \cdot \mathrm{dev}_{\mathrm{abs}}/x_{\mathrm{MH}}$. The associated uncertainties were calculated using Gaussian error propagation.

| structure | PV $\mathrm{dose}_{\mathrm{mean}}$ / Gy | MH $\mathrm{dose}_{\mathrm{mean}}$ / Gy | $\mathrm{dev}_{\mathrm{abs}}$ / Gy | $\mathrm{dev}_{\mathrm{rel}}$ / % |
|---|---|---|---|---|
| choroid | 178.2 ± 395.4 | 183.1 ± 402.9 | −4.9 ± 564.5 | −2.7 ± 304.1 |
| cornea | 0.2 ± 0.1 | 0.3 | −0.1 ± 0.1 | −33.3 ± 33.3 |
| fovea | 858.4 ± 334.2 | 859.3 ± 337.4 | −0.9 ± 474.9 | −0.1 ± 55.2 |
| retina | 154.8 ± 366.9 | 155.6 ± 370.7 | −0.8 ± 521.6 | −0.5 ± 334.3 |
| lens | 0.4 ± 0.1 | 0.4 ± 0.1 | 0.0 | 0.0 |
| papilla | 75.9 ± 16.3 | 75.9 ± 15.5 | 0.0 ± 22.5 | 0.0 |
| sclera | 236.6 ± 477.6 | 240.9 ± 481.6 | −4.3 ± 678.3 | −1.8 ± 279.0 |
| optic nerve | 3.0 ± 8.7 | 2.6 ± 7.3 | 0.4 ± 11.4 | 15.4 ± 465.7 |
| tumour | 562.0 ± 322.9 | 570.1 ± 328.4 | −8.1 ± 460.6 | −1.4 ± 80.2 |

## Truncated mean filtering

Table A.9: Truncated mean analysis for the dose values of the retina. The maximum, mean and minimum dose values of the distribution are presented, with a cut-off value applied to the upper and the lower dose ranges. Additionally, the excluded volumes are listed as a proportion of the total structure volume [67].

| cut-off / % | $\mathrm{dose}_{\mathrm{max}}$ / Gy | $\mathrm{dose}_{\mathrm{mean}}$ / Gy | $\mathrm{dose}_{\mathrm{min}}$ / Gy | excl. vol. / % |
|---|---|---|---|---|
| 0 | 161 065.9 ± 22 626.9 | 167.8 ± 389.1 | 0 | 0.00 |
| 1 | 1455.9 ± 4.8 | 167.4 ± 388.3 | 0 | 0.04 |
| 2 | 1390.7 ± 2.4 | 155.6 ± 370.7 | 0 | 1.00 |
| 3 | 1372.5 ± 2.1 | 140.5 ± 346.3 | 0 | 3.00 |
| 4 | 1338.1 ± 2.8 | 126.4 ± 322.4 | 0.2 | 4.40 |
| 5 | 1315.7 ± 3.1 | 116.9 ± 304.8 | 0.2 | 5.60 |

Table A.10: Truncated mean analysis for the dose values of the choroid. The maximum, mean and minimum dose values of the distribution are presented, with a cut-off value applied to the upper and the lower dose ranges. Additionally, the excluded volumes are listed as a proportion of the total structure volume.

| cut-off / % | $\mathrm{dose}_{\mathrm{max}}$ / Gy | $\mathrm{dose}_{\mathrm{mean}}$ / Gy | $\mathrm{dose}_{\mathrm{min}}$ / Gy | excl. vol. / % |
|---|---|---|---|---|
| 0 | 1776.6 ± 334.5 | 194.9 ± 418.9 | 0 | 0.0 |
| 1 | 1460.3 ± 9.4 | 193.5 ± 417.0 | 0 | 0.1 |
| 2 | 1415.1 ± 2.1 | 183.1 ± 402.9 | 0 | 0.9 |
| 3 | 1385.9 ± 1.9 | 166.1 ± 378.8 | 0.1 ± 0.1 | 2.3 |
| 4 | 1358.0 ± 2.7 | 149.1 ± 352.5 | 0.2 | 4.5 |
| 5 | 1329.0 ± 2.5 | 135.1 ± 329.0 | 0.2 ± 0.1 | 6.4 |

Table A.11: Truncated mean analysis for the dose values of the cornea. The maximum, mean and minimum dose values of the distribution are presented, with a cut-off value applied to the upper and the lower dose ranges. Additionally, the excluded volumes are listed as a proportion of the total structure volume.

| cut-off / % | $dose_{max}$ / Gy | $dose_{mean}$ / Gy | $dose_{min}$ / Gy | excl. vol. / % |
|---|---|---|---|---|
| 0 | 1.5 ± 1.4 | 0.3 | 0 | 0.00 |
| 1 | 0.6 ± 0.5 | 0.3 | 0 | 0.01 |
| 2 | 0.5 | 0.3 | 0 | 0.04 |
| 3 | 0.4 | 0.3 | 0 | 0.46 |
| 4 | 0.4 | 0.3 | 0.1 ± 0.1 | 1.30 |
| 5 | 0.4 ± 0.1 | 0.3 | 0.1 ± 0.1 | 1.71 |

Table A.12: Truncated mean analysis for the dose values of the fovea. The maximum, mean and minimum dose values of the distribution are presented, with a cut-off value applied to the upper and the lower dose ranges. Additionally, the excluded volumes are listed as a proportion of the total structure volume. As the fovea is a small structure comprising only a few bins, the uppermost and lowermost 3 % of dose values cannot be represented by a single bin. Consequently, no volume can be excluded.

| cut-off / % | $dose_{max}$ / Gy | $dose_{mean}$ / Gy | $dose_{min}$ / Gy | excl. vol. / % |
|---|---|---|---|---|
| 0 | 1268.3 ± 4.4 | 859.3 ± 337.4 | 183.6 ± 1.1 | 0.0 |
| 1 | 1268.3 ± 4.4 | 859.3 ± 337.4 | 183.6 ± 1.1 | 0.0 |
| 2 | 1268.3 ± 4.4 | 859.3 ± 337.4 | 183.6 ± 1.1 | 0.0 |
| 3 | 1268.3 ± 4.4 | 859.3 ± 337.4 | 183.6 ± 1.1 | 0.0 |
| 4 | 1258.2 ± 9.2 | 875.0 ± 320.8 | 184.9 ± 3.3 | 1.0 |
| 5 | 1258.2 ± 9.2 | 875.0 ± 320.8 | 184.9 ± 3.3 | 1.0 |

Table A.13: Truncated mean analysis for the dose values of the lens. The maximum, mean and minimum dose values of the distribution are presented, with a cut-off value applied to the upper and the lower dose ranges. Additionally, the excluded volumes are listed as a proportion of the total structure volume.

| cut-off / % | $dose_{max}$ / Gy | $dose_{mean}$ / Gy | $dose_{min}$ / Gy | excl. vol. / % |
|---|---|---|---|---|
| 0 | 1.1 ± 0.1 | 0.4 ± 0.1 | 0 | 0.0 |
| 1 | 1.0 ± 0.5 | 0.4 ± 0.1 | 0 | 0.03 |
| 2 | 0.9 | 0.4 ± 0.1 | 0.1 ± 0.1 | 0.32 |
| 3 | 0.9 ± 0.1 | 0.4 ± 0.1 | 0.2 ± 0.1 | 0.69 |
| 4 | 0.9 | 0.4 ± 0.1 | 0.2 ± 0.1 | 0.85 |
| 5 | 0.8 | 0.4 ± 0.1 | 0.2 ± 0.1 | 2.0 |

Table A.14: Truncated mean analysis for the dose values of the papilla. The maximum, mean and minimum dose values of the distribution are presented, with a cut-off value applied to the upper and the lower dose ranges. Additionally, the excluded volumes are listed as a proportion of the total structure volume. As the papilla is a small structure comprising only a few bins, the uppermost and lowermost 5 % of dose values cannot be represented by a single bin. Consequently, no volume can be excluded.

| cut-off / % | $dose_{max}$ / Gy | $dose_{mean}$ / Gy | $dose_{min}$ / Gy | excl. vol. / % |
|---|---|---|---|---|
| 0 | 100.5 ± 0.5 | 75.9 ± 15.5 | 47.3 ± 1.8 | 0.0 |
| 1 | 100.5 ± 0.5 | 75.9 ± 15.5 | 47.3 ± 1.8 | 0.0 |
| 2 | 100.5 ± 0.5 | 75.9 ± 15.5 | 47.3 ± 1.8 | 0.0 |
| 3 | 100.5 ± 0.5 | 75.9 ± 15.5 | 47.3 ± 1.8 | 0.0 |
| 4 | 100.5 ± 0.5 | 75.9 ± 15.5 | 47.3 ± 1.8 | 0.0 |
| 5 | 100.5 ± 0.5 | 75.9 ± 15.5 | 47.3 ± 1.8 | 0.0 |

Table A.15: Truncated mean analysis for the dose values of the sclera. The maximum, mean and minimum dose values of the distribution are presented, with a cut-off value applied to the upper and the lower dose ranges. Additionally, the excluded volumes are listed as a proportion of the total structure volume.

| cut-off / % | $dose_{max}$ / Gy | $dose_{mean}$ / Gy | $dose_{min}$ / Gy | excl. vol. / % |
|---|---|---|---|---|
| 0 | 2100.3 ± 115.5 | 248.6 ± 491.2 | 0 | 0.0 |
| 1 | 1659.5 ± 7.8 | 247.0 ± 489.1 | 0 | 0.1 |
| 2 | 1587.6 ± 3.1 | 240.9 ± 481.6 | 0.1 ± 0.1 | 0.6 |
| 3 | 1544.8 ± 1.9 | 227.0 ± 464.4 | 0.2 | 1.7 |
| 4 | 1484.1 ± 1.8 | 211.2 ± 444.3 | 0.2 ± 0.1 | 3.2 |
| 5 | 1449.6 ± 1.7 | 188.8 ± 414.5 | 0.2 | 5.7 |

Table A.16: Truncated mean analysis for the dose values of the optic nerve. The maximum, mean and minimum dose values of the distribution are presented, with a cut-off value applied to the upper and the lower dose ranges. Additionally, the excluded volumes are listed as a proportion of the total structure volume.

| cut-off / % | $dose_{max}$ / Gy | $dose_{mean}$ / Gy | $dose_{min}$ / Gy | excl. vol. / % |
|---|---|---|---|---|
| 0 | 108.7 ± 0.9 | 3.5 ± 10.8 | 0.0 | 0.0 |
| 1 | 73.7 ± 0.4 | 3.2 ± 9.4 | 0.0 | 0.4 |
| 2 | 56.1 ± 1.0 | 2.6 ± 7.3 | 0.0 | 1.3 |
| 3 | 41.1 ± 0.5 | 2.3 ± 6.2 | 0.1 | 2.0 |
| 4 | 35.1 ± 0.3 | 1.9 ± 5.1 | 0.1 | 3.2 |
| 5 | 27.4 ± 0.2 | 1.6 ± 4.1 | 0.1 | 4.6 |

Table A.17: Truncated mean analysis for the dose values of the tumour. The maximum, mean and minimum dose values of the distribution are presented, with a cut-off value applied to the upper and the lower dose ranges. Additionally, the excluded volumes are listed as a proportion of the total structure volume.

| cut-off / % | $dose_{max}$ / Gy | $dose_{mean}$ / Gy | $dose_{min}$ / Gy | excl. vol. / % |
|---|---|---|---|---|
| 0 | 1438.9 ± 6.0 | 569.1 ± 330.1 | 89.0 ± 0.8 | 0.0 |
| 1 | 1420.7 ± 5.4 | 569.1 ± 329.7 | 100.1 ± 1.3 | 0.1 |
| 2 | 1392.0 ± 6.4 | 570.1 ± 328.4 | 112.5 ± 0.5 | 0.5 |
| 3 | 1365.5 ± 2.2 | 572.7 ± 325.5 | 124.6 ± 0.7 | 1.6 |
| 4 | 1317.1 ± 3.3 | 569.9 ± 321.2 | 131.3 ± 0.5 | 4.5 |
| 5 | 1302.1 ± 1.4 | 568.0 ± 316.4 | 138.7 ± 0.8 | 3.5 |

## A.2 $^{106}$Ru eye applicator sizes and measurement points

Table A.18: Diameter, spherical radius, inactive rim size, and measurement ring positions $\vartheta_{R1}$, $\vartheta_{R2}$, and $\vartheta_{R3}$ for the CCA, CCB, and COB applicator models [39, 123].

| model | diameter/ mm | spherical radius / mm | inactive rim / mm | $\vartheta_{R1}$ / ∘ | $\vartheta_{R2}$ / ∘ | $\vartheta_{R3}$ / ∘ |
|---|---|---|---|---|---|---|
| CCA | 15.3 | 12 | 0.8 | 11 | 22 | 33 |
| CCB | 20.2 | 12 | 0.8 | 16 | 32 | 47 |
| COB | 19.8 | 12 | 1.0 | 15 | 30 | 45 |

## A.3 Cylindrical detector positions

Table A.19: Positions and numbers of the cylindrical detectors serving as the basis for the phase space files for the CCA, CCB and COB applicator models. The sum $\sum$ indicates the total number of phase space files per angle $\vartheta$.

| model | $\vartheta$ | $\varphi$ | $\sum$ |
|---|---|---|---|
| CCA | 0 | 0 | 1 |
| | 11 | 0, 15, ..., 345 | 24 |
| | 22 | 0, 15, ..., 345 | 24 |
| | 33 | 0, 15, ..., 345 | 24 |
| CCB | 0 | 0 | 1 |
| | 8 | 0, 45, ..., 315 | 8 |
| | 16 | 0, 15, ..., 345 | 24 |
| | 24 | 0, 15, ..., 345 | 24 |
| | 32 | 0, 15, ..., 345 | 24 |
| | 40 | 0, 15, ..., 345 | 24 |
| | 47 | 0, 15, ..., 345 | 24 |
| COB | 0 | 0 | 1 |
| | 7 | 0, 45, ..., 315 | 8 |
| | 15 | 0, 30, ..., 330 | 12 |
| | 23 | 0, 15, ..., 345 | 24 |
| | 30 | 0, 15, ..., 345 | 24 |
| | 38 | 0, 15, ..., 345 | 24 |
| | 45 | 0, 15, ..., 345 | 24 |

## A.4 Transverse dose profile of a simulated phase space file

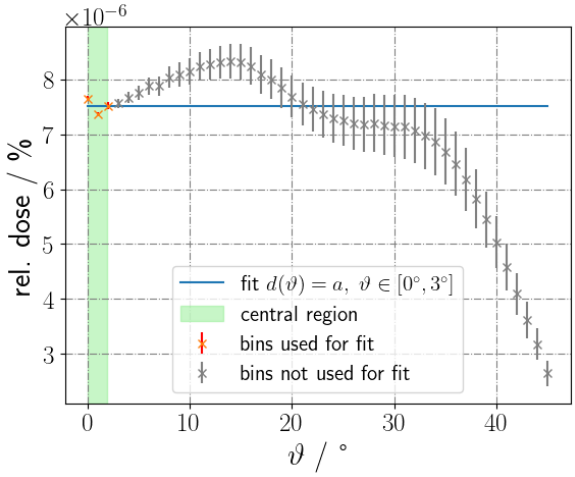


Figure A.9: Transverse dose profile corresponding to the distribution shown in Figure 4.6, recorded with the surface detector at a distance of 1 mm from the COB applicator. The profile represents the mean dose in the azimuthal direction, plotted as a function of the polar angle $\vartheta$ for the phase space file originating from the cylindrical detector at $\vartheta = 45°$ and $\varphi = 285°$. The dose values are normalised to 100 % in the central region ($\vartheta < 3°$), consistent with the measurement certificate convention. The normalisation factor is determined by averaging the azimuthal dose and fitting a constant function $d(\vartheta) = a, \vartheta \in [0°, 3°]$ to the central angular interval, with the resulting value used to scale the distribution.

## A.5 Overview of the measurement certificates

Table A.20: Certificate numbers and issue dates of the certificates used in subsection 4.7.2 to average the surface dose profile values for each applicator model. The certificates were kindly provided by the UME.

| model | certificate number | date of issue |
|---|---|---|
| CCA | 062323 | 04/09/2023 |
| | 078824 | 25/03/2024 |
| | 083424 | 11/06/2024 |
| | 087124 | 19/08/2024 |
| | 096024 | 13/12/2024 |
| CCB | 069723 | 04/12/2023 |
| | 062623 | 05/09/2023 |
| | 079024 | 25/03/2024 |
| | 087224 | 19/08/2024 |
| | 096124 | 13/12/2024 |
| COB | 58219 | 19/09/2013 |
| | 043622 | 05/12/2022 |
| | 057623 | 19/06/2023 |
| | 079124 | 25/03/2024 |
| | 096224 | 13/12/2024 |

## A.6 Comparison of simulated surface dose profiles with manufacturer certificates

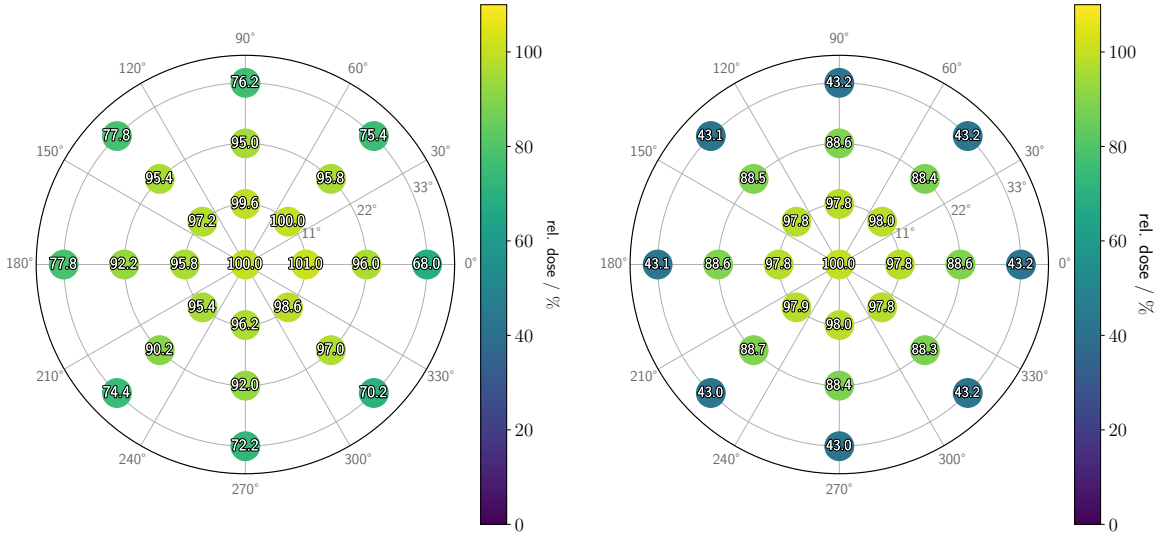


a) b)

Figure A.10: Surface dose values for the CCA applicator model. In a), the surface dose values averaged from five manufacturer certificates are depicted. In b), the homogeneous surface dose values from the MC simulation, recorded with the cylindrical detectors, are shown. The surface dose values of the simulation are normalised to 100 % at the centre, consistent with the certificates of the manufacturer.

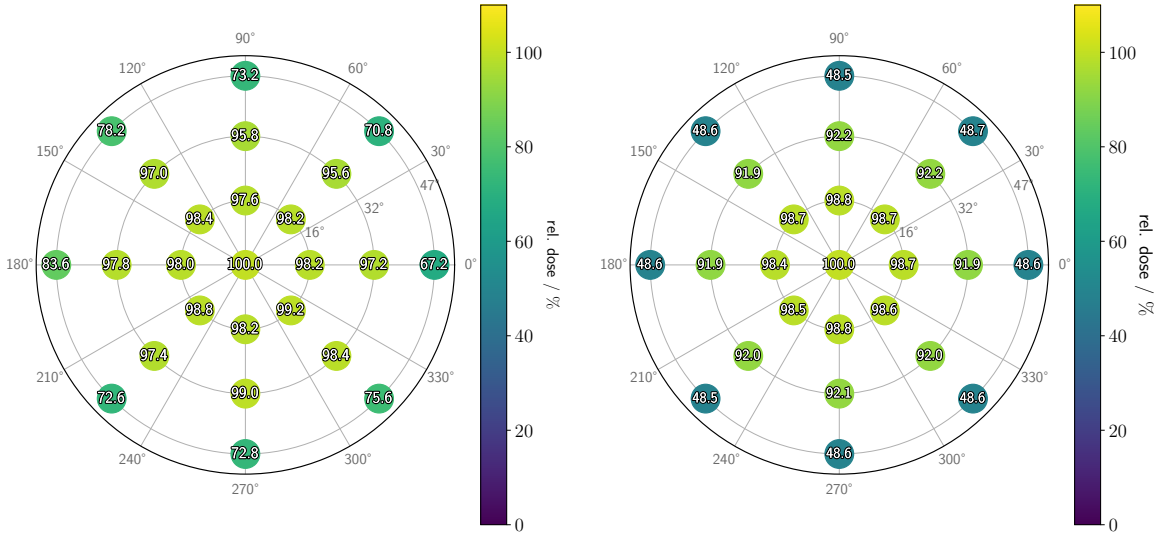


a) b)

Figure A.11: Surface dose values for the CCB applicator model. In a), the surface dose values averaged from five manufacturer certificates are depicted. In b), the homogeneous surface dose values from the MC simulation, recorded with the cylindrical detectors, are shown. The surface dose values of the simulation are normalised to 100 % at the centre, consistent with the certificates of the manufacturer.

## A.7 Validation of phase-space-based $^{106}$Ru applicator simulation

In this section, the three applicator models are compared using homogeneous surface dose distributions generated in two ways. The first employs the GPS, as described in chapter 3, while the second is based on phase space files using the PG, as outlined in chapter 4. In both simulations, the surface detector is used to record the dose values at a distance of 1 mm from the applicator.

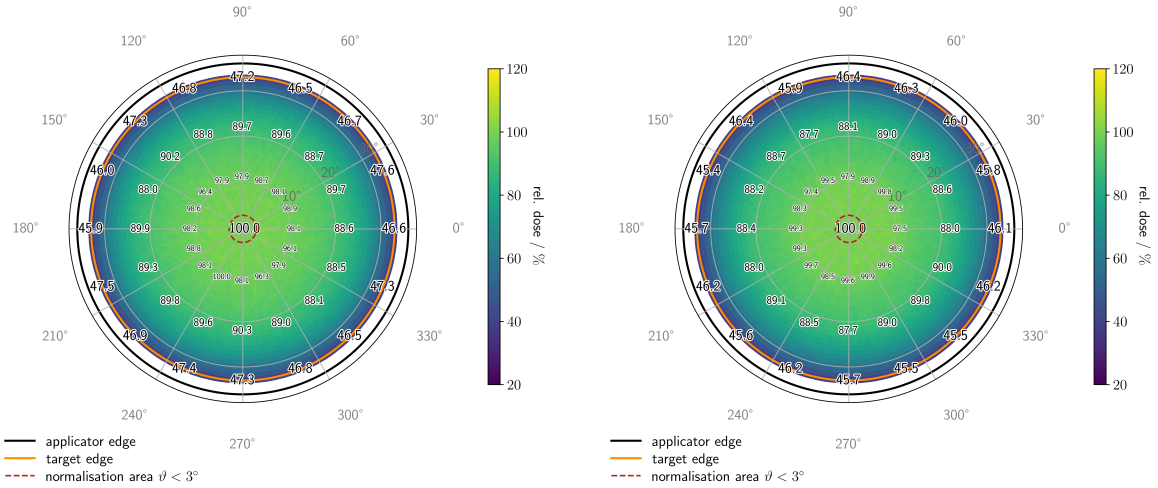


a) GPS-based surface dose profile

b) phase-space-based surface dose profile

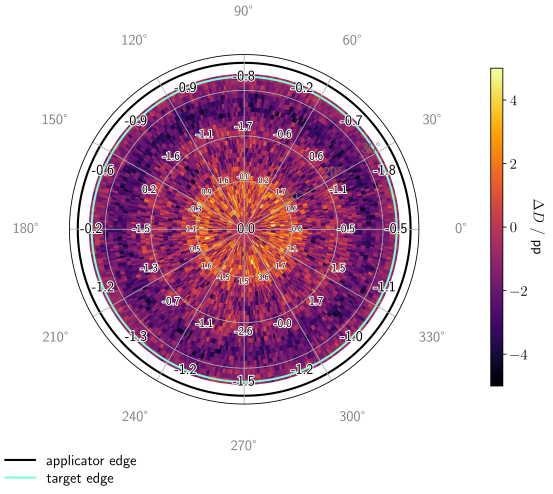


c) difference

Figure A.12: Surface dose profiles of the CCA applicator obtained using the different simulation methods. All surface dose values are normalised to 100 % at the centre, in accordance with the certificates of the manufacturer. The differences are calculated by subtracting the phase-space-based values obtained using the PG from those of the GPS-based simulation. For clarity, the statistical uncertainties ($< 2.2$ %) of the dose values are not shown.

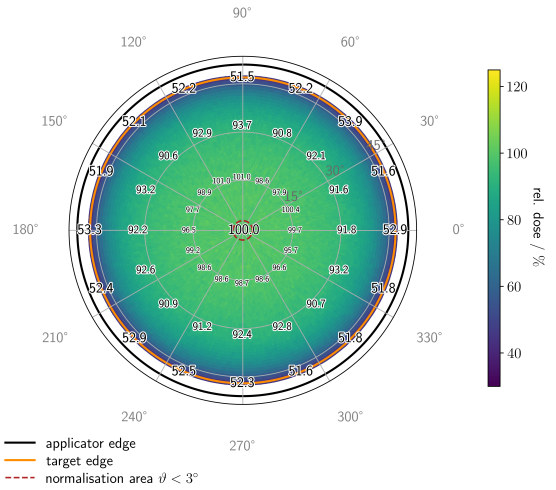


a) GPS-based surface dose profile

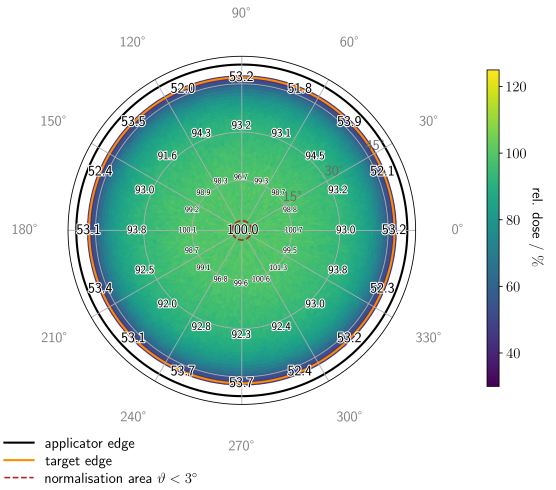


b) phase-space-based surface dose profile

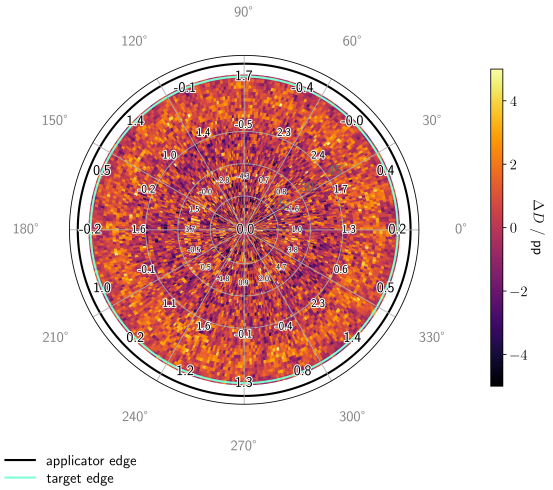


c) difference

Figure A.13: Surface dose profiles of the CCB applicator obtained using the different simulation methods. All surface dose values are normalised to 100 % at the centre, in accordance with the certificates of the manufacturer. The differences are calculated by subtracting the phase-space-based values obtained using the PG from those of the GPS-based simulation. For clarity, the statistical uncertainties ($< 3.0\,\%$) of the dose values are not shown.

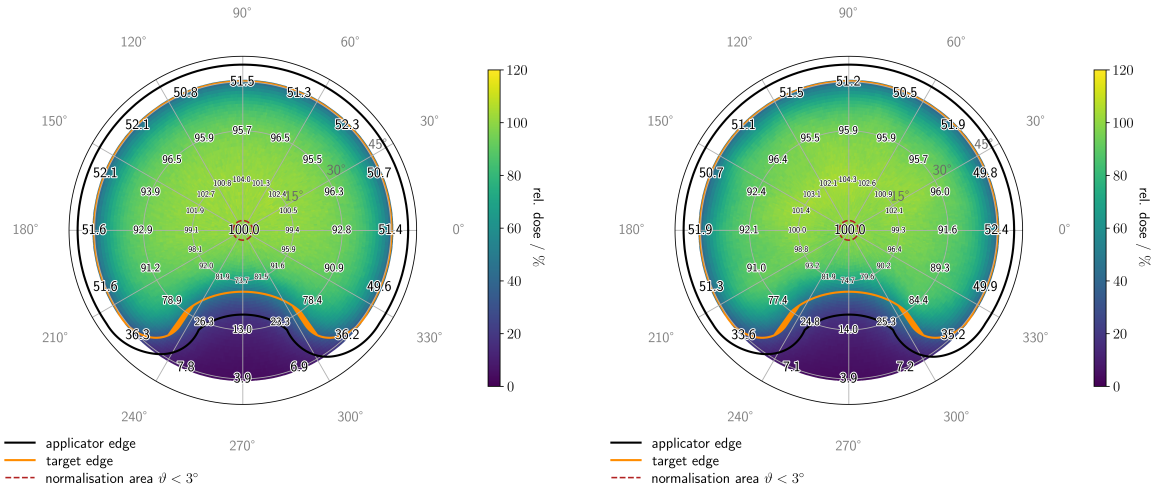


a) GPS-based surface dose profile

b) phase-space-based surface dose profile

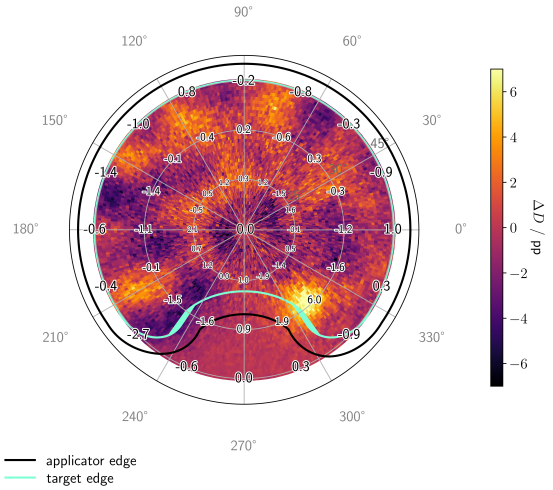


c) difference

Figure A.14: Surface dose profiles of the COB applicator obtained using the different simulation methods. All surface dose values are normalised to 100 % at the centre, in accordance with the certificates of the manufacturer. The differences are calculated by subtracting the phase-space-based values obtained using the PG from those of the GPS-based simulation. For clarity, the statistical uncertainties ($< 2.8\,\%$) of the dose values are not shown.

## A.8 Modelled inhomogeneities surface dose profiles

The following figures present the surface dose profiles of the various simulated inhomogeneity scenarios described in chapter 5 for the three applicator models. Here, HS denotes a hot spot scenario, CS a cold spot scenario, and HC a combined scenario. The scenarios that correspond to the limit values defined in section 4.1 for the QA are labelled 'QA', while those exceeding these limits are marked 'QA+'. For the mixed scenarios, a distinction is further made between worst-case (WC) and best-case (BC) configurations. $U_{\mathrm{AS}}$ and $U_{\mathrm{NU}}$ denote the source asymmetry and source non-uniformity, respectively, as introduced in section 4.1.
In all simulations, the surface detector described in chapter 4 is used to record the dose values at a distance of 1 mm from the applicator. All surface dose values are normalised to 100 % at the centre, in accordance with the certificates of the manufacturer certificates.
For clarity, the statistical uncertainties of the dose values ($< 2.5\,\%$ for all applicator models) are not shown.

### Hot spot scenarios

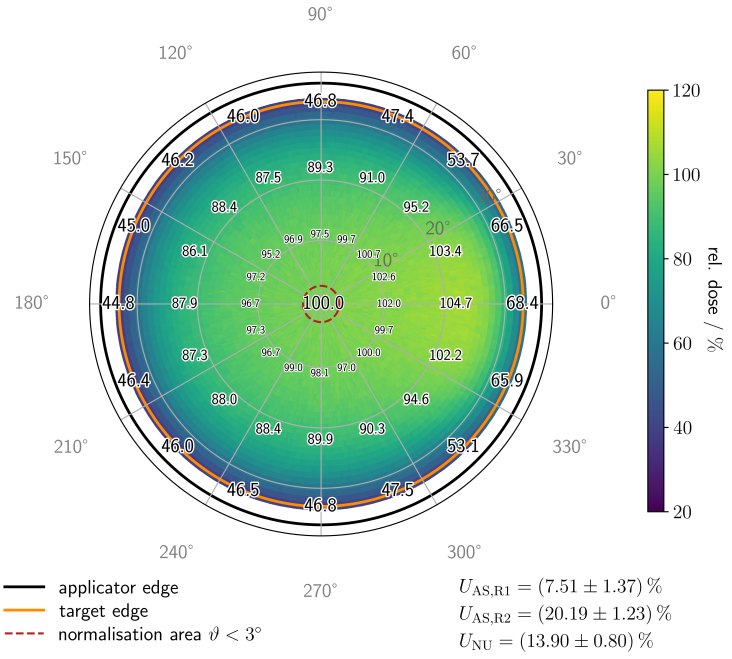


Figure A.15: Surface dose profile of the modelled hot spot scenario $\mathrm{HS}_{\mathrm{QA}}$ for the CCA applicator.

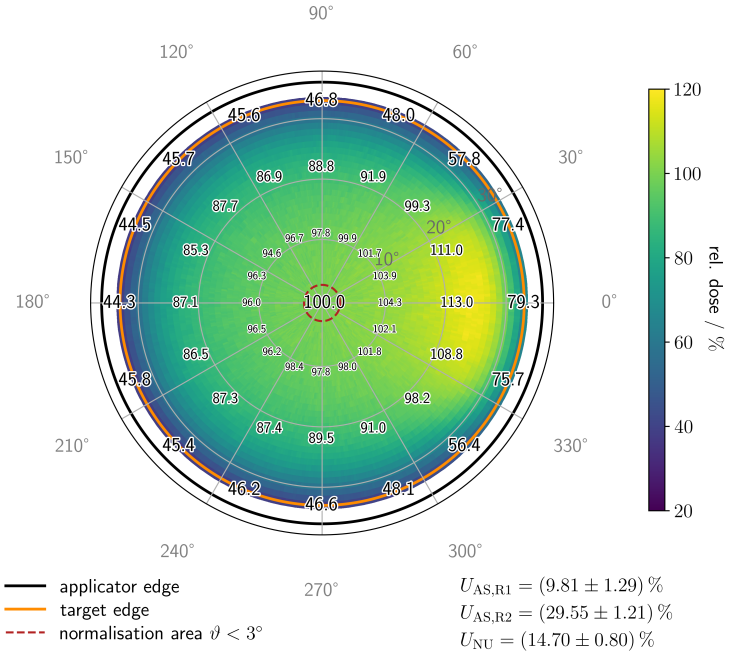


Figure A.16: Surface dose profile of the modelled hot spot scenario $\mathrm{HS_{QA+}}$ for the CCA applicator.

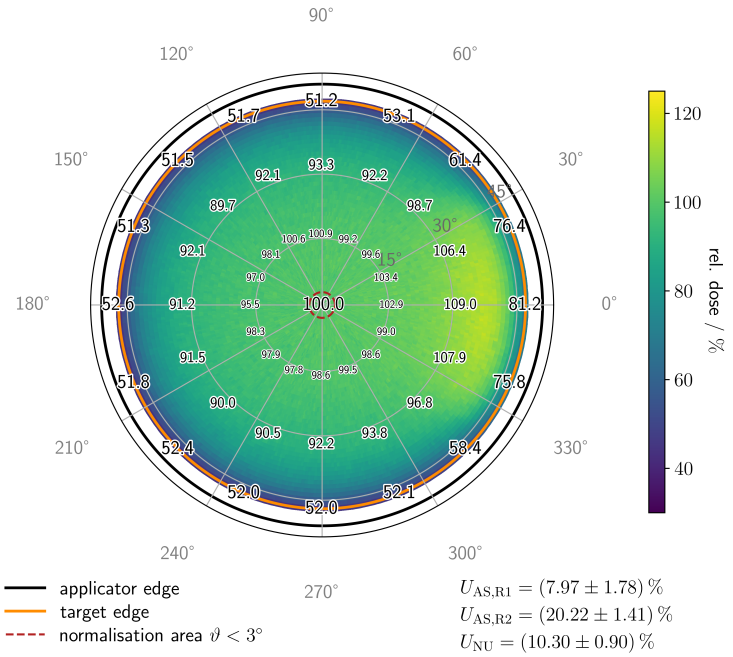


Figure A.17: Surface dose profile of the modelled hot spot scenario $\mathrm{HS_{QA}}$ for the CCB applicator.

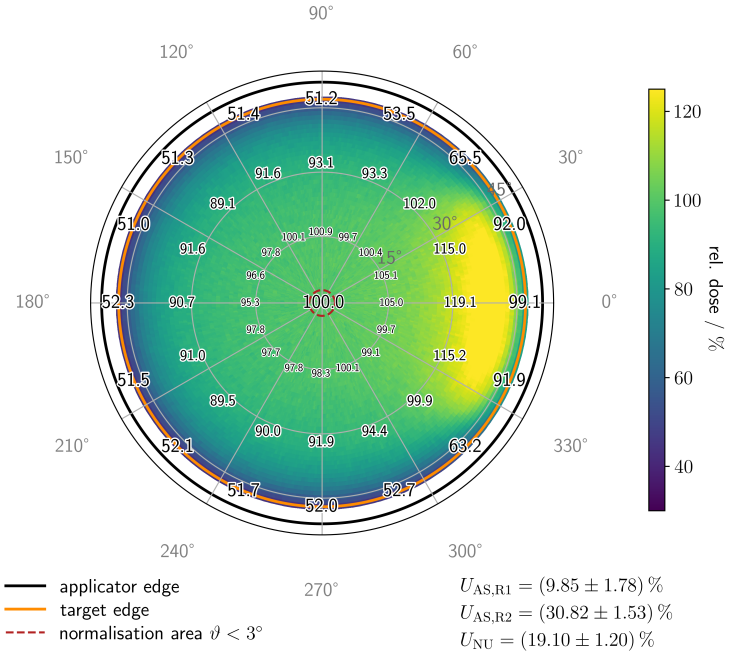


Figure A.18: Surface dose profile of the modelled hot spot scenario $\mathrm{HS_{QA+}}$ for the CCB applicator.

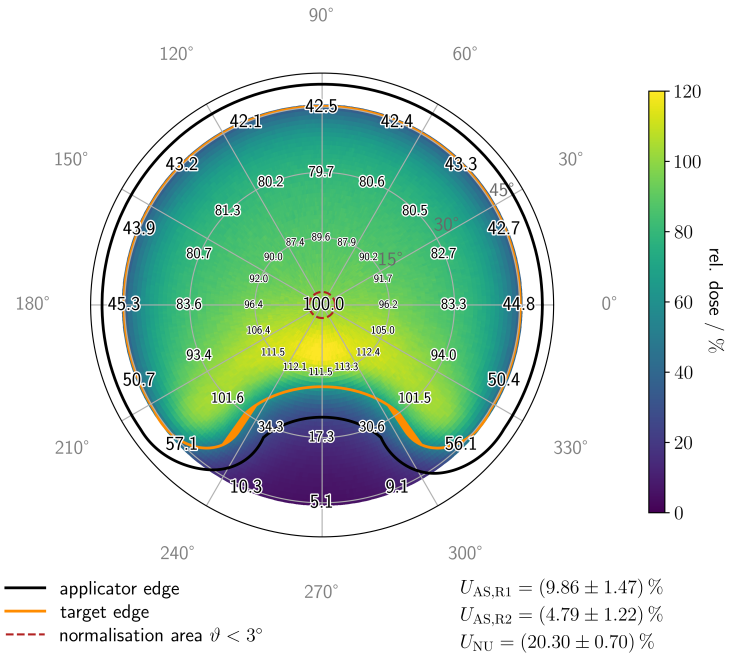


Figure A.19: Surface dose profile of the modelled hot spot scenario $\mathrm{HS_{QA}}$ for the COB applicator.

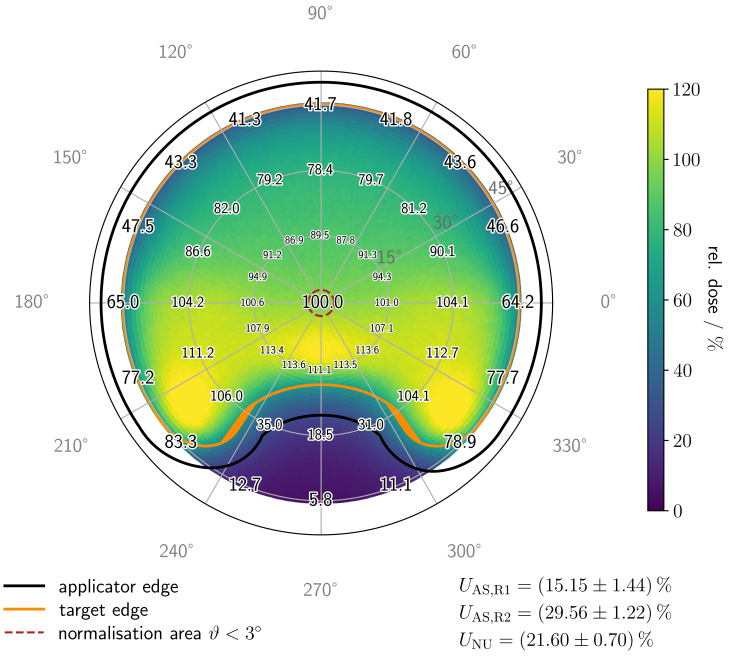


Figure A.20: Surface dose profile of the modelled hot spot scenario $\mathrm{HS_{QA+}}$ for the COB applicator.

## Cold spot scenarios

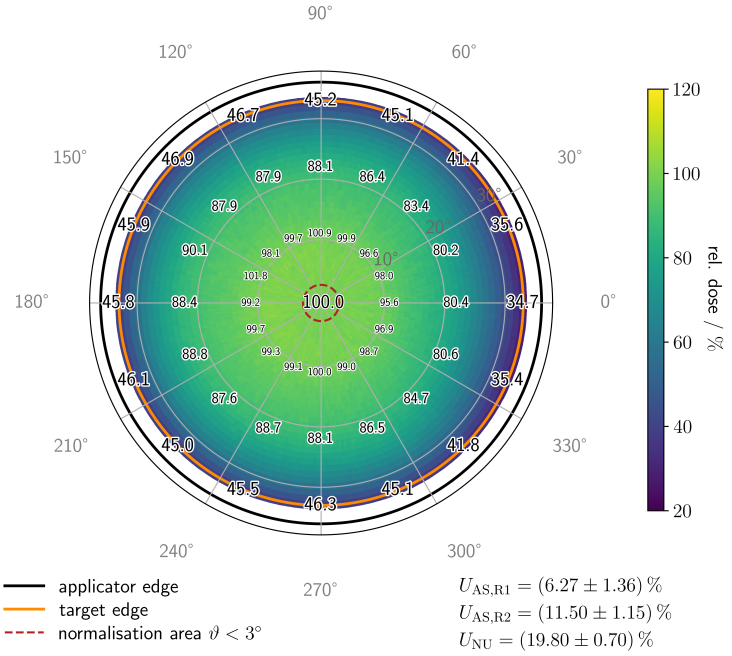


Figure A.21: Surface dose profile of the modelled cold spot scenario $\mathrm{CS_{QA}}$ for the CCA applicator.

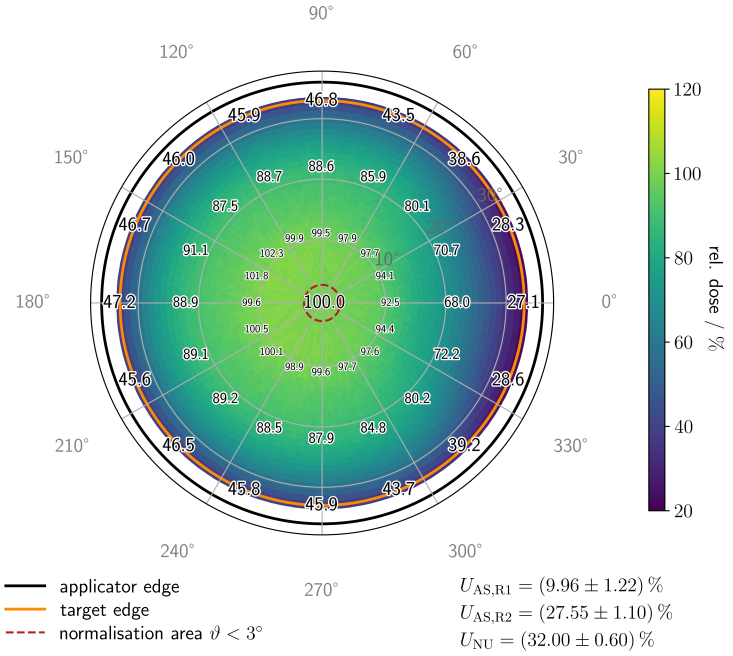


Figure A.22: Surface dose profile of the modelled cold spot scenario $\mathrm{CS_{QA+}}$ for the CCA applicator.

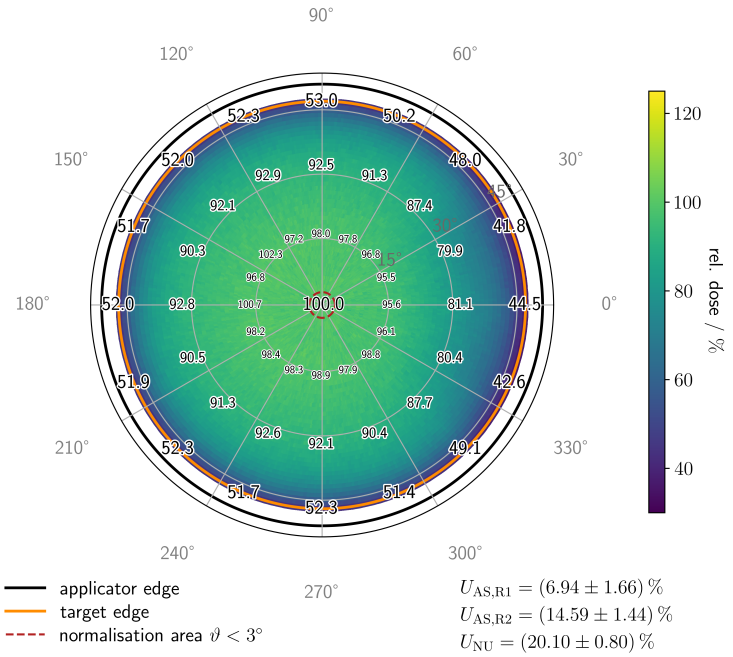


Figure A.23: Surface dose profile of the modelled cold spot scenario $\mathrm{CS_{QA}}$ for the CCB applicator.

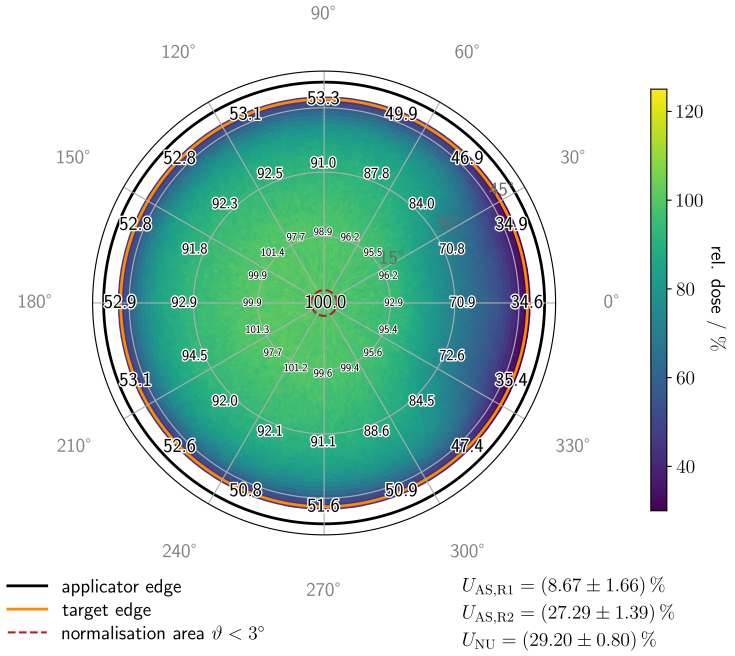


Figure A.24: Surface dose profile of the modelled cold spot scenario $CS_{QA+}$ for the CCB applicator.

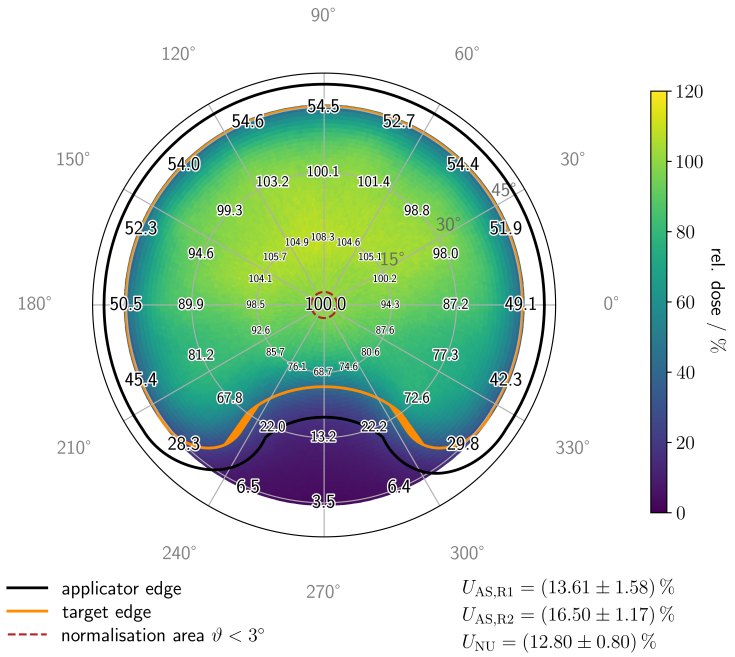


Figure A.25: Surface dose profile of the modelled cold spot scenario $CS_{QA}$ for the COB applicator.

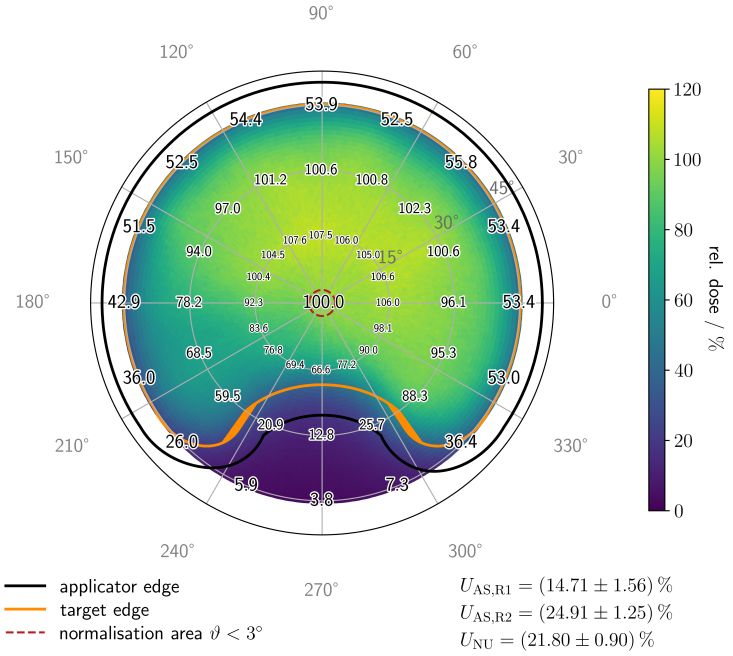


Figure A.26: Surface dose profile of the modelled cold spot scenario $\mathrm{CS}_{\mathrm{QA+}}$ for the COB applicator.

## Combined hot and cold spot scenarios

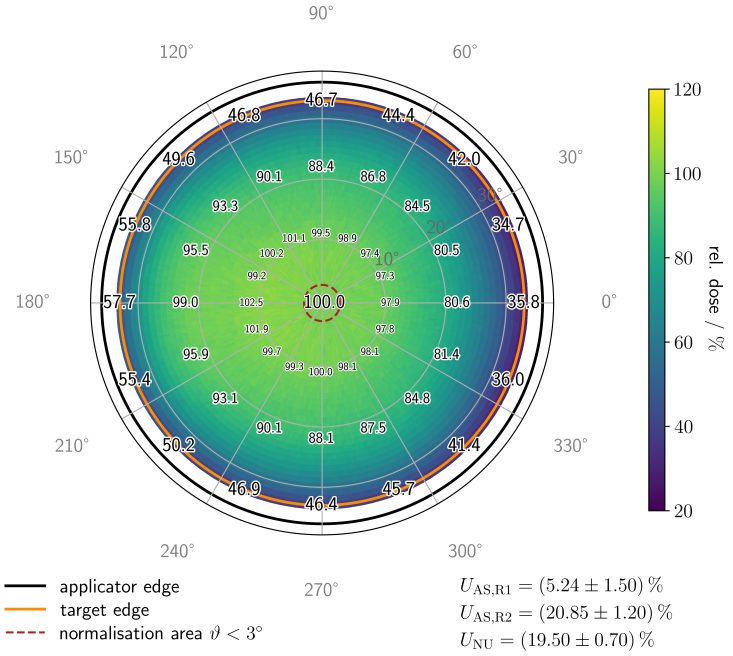


Figure A.27: Surface dose profile of the modelled combined scenario $\mathrm{HC}_{\mathrm{QA}}^{\mathrm{WC}}$ for the CCA applicator.

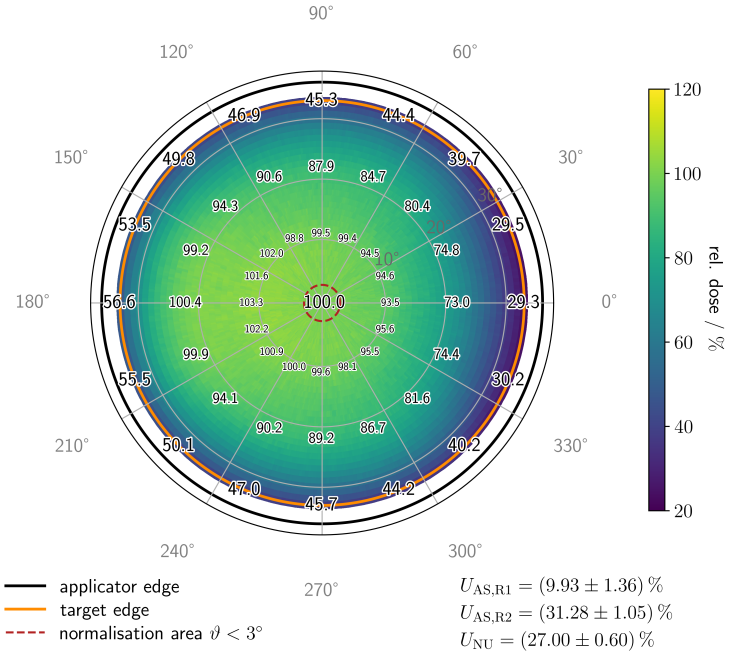


Figure A.28: Surface dose profile of the modelled combined scenario $\mathrm{HC}_{\mathrm{QA+}}^{\mathrm{WC}}$ for the CCA applicator.

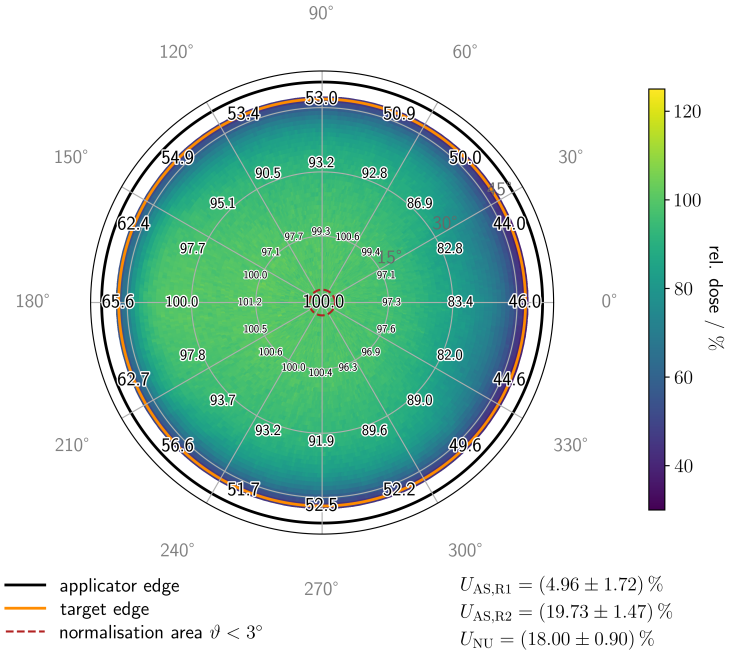


Figure A.29: Surface dose profile of the modelled combined scenario $\mathrm{HC}_{\mathrm{QA}}^{\mathrm{WC}}$ for the CCB applicator.

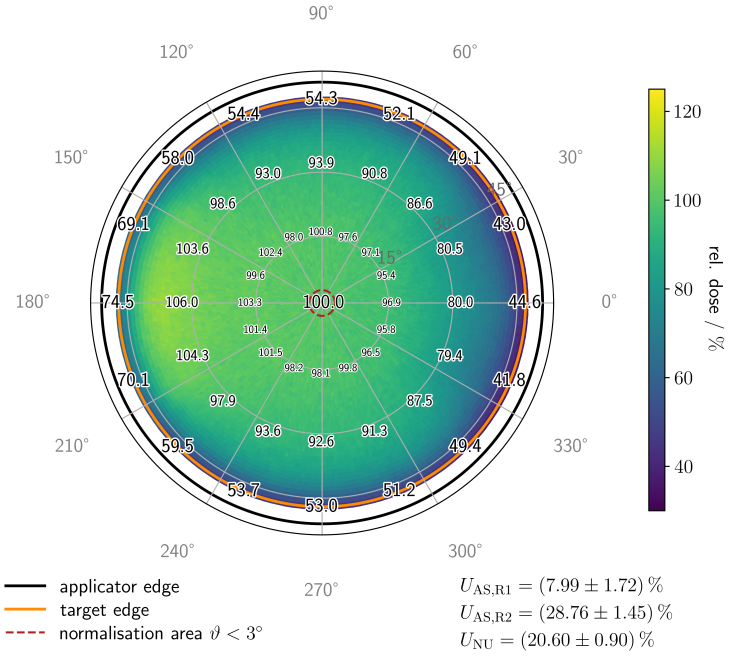


Figure A.30: Surface dose profile of the modelled combined scenario HC $^{\mathrm{WC}}_{\mathrm{QA+}}$ for the CCB applicator.

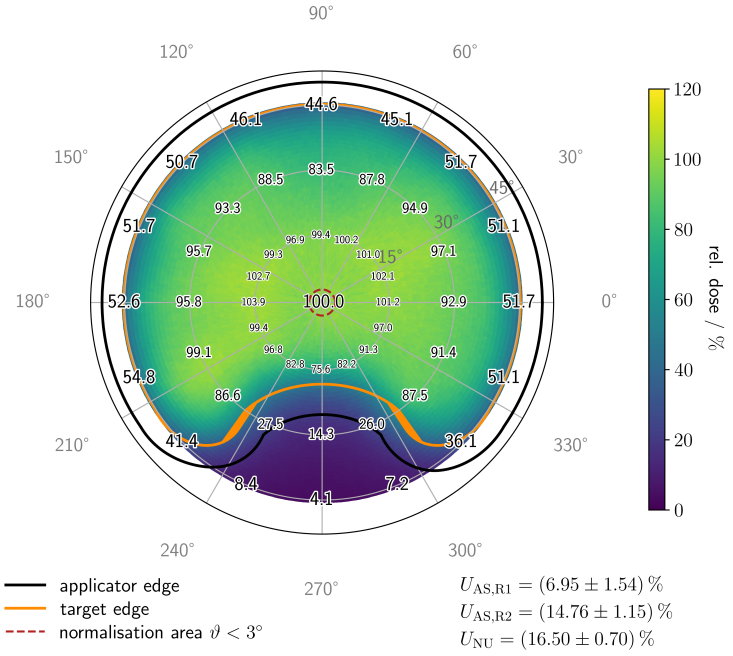


Figure A.31: Surface dose profile of the modelled combined scenario HC$^{\mathrm{WC}}_{\mathrm{QA}}$ for the COB applicator.

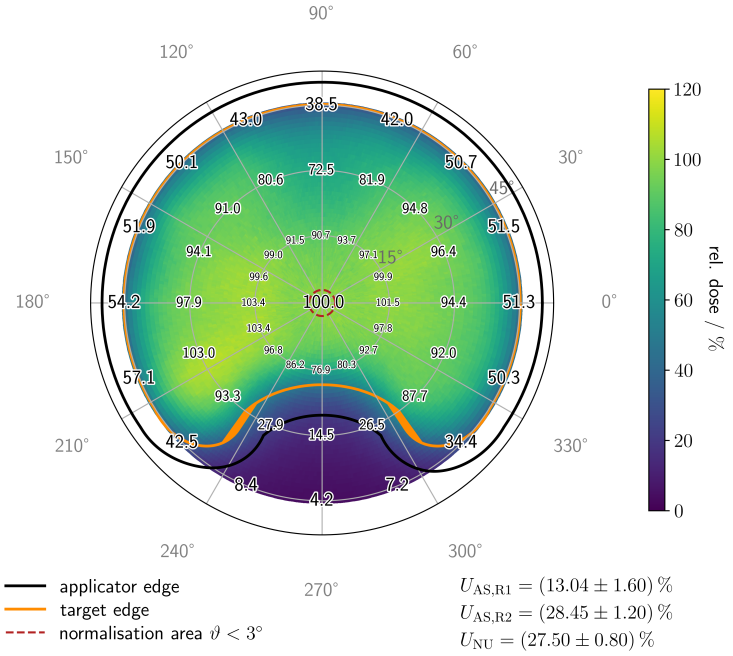


Figure A.32: Surface dose profile of the modelled combined scenario $\mathrm{HC}^{\mathrm{WC}}_{\mathrm{QA+}}$ for the COB applicator.

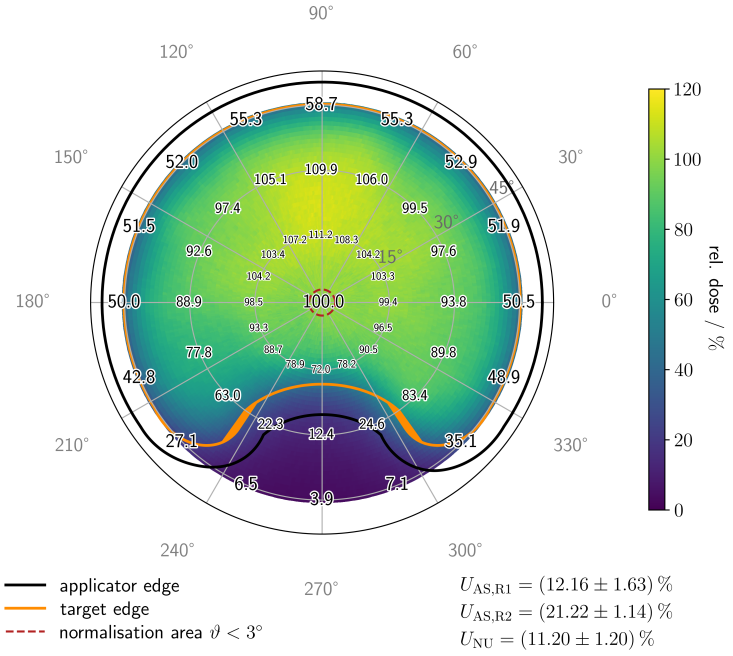


Figure A.33: Surface dose profile of the modelled combined scenario $\mathrm{HC}^{\mathrm{BC}}_{\mathrm{QA}}$ for the COB applicator.

## A.9 Parameter tuning studies

The following tables list the results of the evaluation parameters MAE and $\text{MAE}_{\text{DVH}}$ for the respective tuning studies presented in section 6.4. The reported results correspond to the mean across the entire test dataset, including the associated standard deviations.

### Dose tensor scaling

Table A.21: Evaluation parameters, including their standard deviations, for each anatomical structure across the entire test dataset, for the models trained on dose tensors scaled using the respective approaches.

| | factor: $2 \cdot 10^{13}$ | | factor: $9 \cdot 10^{12}$ | |
|---|---|---|---|---|
| structures | MAE / Gy | $\text{MAE}_{\text{DVH}}$ / pp | MAE / Gy | $\text{MAE}_{\text{DVH}}$ / pp |
| tumour | 69.2 ± 62.7 | 3.6 ± 2.4 | 71.5 ± 64.1 | 3.2 ± 2.3 |
| sclera | 51.6 ± 62.6 | 0.8 ± 0.5 | 52.6 ± 63.7 | 0.6 ± 0.4 |
| choroid | 50.5 ± 62.5 | 0.8 ± 0.4 | 51.4 ± 63.2 | 0.6 ± 0.4 |
| retina | 49.4 ± 62.3 | 0.8 ± 0.4 | 50.2 ± 62.9 | 0.6 ± 0.4 |
| papilla | 3.7 ± 3.4 | 6.0 ± 3.3 | 3.8 ± 3.7 | 10.3 ± 10.3 |
| o. nerve | 2.7 ± 3.0 | 3.4 ± 5.3 | 2.7 ± 3.1 | 3.0 ± 4.3 |
| fovea | 22.7 ± 48.3 | 3.0 ± 2.2 | 23.4 ± 50.3 | 2.6 ± 1.3 |
| lens | 0.9 ± 1.9 | 3.8 ± 2.6 | 0.9 ± 1.8 | 6.4 ± 6.5 |
| cornea | 0.4 ± 1.0 | 2.8 ± 2.5 | 0.5 ± 1.0 | 11.0 ± 13.5 |
| $\overline{x}_{\text{all}}$ | 27.9 ± 14.9 | 2.8 ± 0.9 | 28.5 ± 15.2 | 4.3 ± 2.1 |

Table A.22: Evaluation parameters, including their standard deviations, for each anatomical structure across the entire test dataset, for the models trained on dose tensors scaled using the respective approaches.

| | log | | mixed linear-log | |
|---|---|---|---|---|
| structures | MAE / Gy | $\text{MAE}_{\text{DVH}}$ / pp | MAE / Gy | $\text{MAE}_{\text{DVH}}$ / pp |
| tumour | 73.2 ± 66.4 | 3.2 ± 2.1 | 69.0 ± 62.8 | 3.1 ± 2.0 |
| sclera | 53.7 ± 65.8 | 0.7 ± 0.6 | 51.3 ± 62.1 | 0.9 ± 0.5 |
| choroid | 52.4 ± 65.8 | 0.7 ± 0.4 | 50.2 ± 62.0 | 0.8 ± 0.4 |
| retina | 51.2 ± 65.4 | 0.6 ± 0.4 | 49.0 ± 61.8 | 0.8 ± 0.4 |
| papilla | 3.8 ± 3.6 | 6.9 ± 4.4 | 3.5 ± 3.4 | 9.2 ± 7.7 |
| o. nerve | 2.8 ± 3.1 | 1.3 ± 0.9 | 2.6 ± 2.9 | 2.0 ± 2.3 |
| fovea | 24.5 ± 52.2 | 2.8 ± 1.5 | 22.6 ± 46.5 | 3.6 ± 1.8 |
| lens | 0.9 ± 2.1 | 1.5 ± 1.1 | 0.9 ± 1.9 | 2.0 ± 1.5 |
| cornea | 0.5 ± 1.1 | 1.7 ± 1.6 | 0.4 ± 1.0 | 1.6 ± 1.0 |
| $\overline{x}_{\text{all}}$ | 29.2 ± 15.7 | 2.2 ± 0.6 | 27.7 ± 14.8 | 2.7 ± 1.0 |

## Loss function

Table A.23: Evaluation parameters, including their standard deviations, for each anatomical structure across the entire test dataset, for the models trained with the different loss functions.

| | $\text{MSE}_{\text{masked}}$ | | $\text{Huber loss}_{\text{masked}}$ | |
|---|---|---|---|---|
| structures | MAE / Gy | $\text{MAE}_{\text{DVH}}$ / pp | MAE / Gy | $\text{MAE}_{\text{DVH}}$ / pp |
| tumour | 72.9 ± 60.6 | 4.3 ± 3.1 | 69.9 ± 62.8 | 3.1 ± 2.1 |
| sclera | 51.8 ± 60.1 | 1.0 ± 0.7 | 51.4 ± 61.6 | 0.7 ± 0.5 |
| choroid | 50.6 ± 59.7 | 1.0 ± 0.7 | 50.3 ± 61.1 | 0.8 ± 0.5 |
| retina | 49.4 ± 59.5 | 0.9 ± 0.7 | 49.2 ± 60.8 | 0.8 ± 0.6 |
| papilla | 3.9 ± 3.4 | 7.8 ± 5.2 | 3.7 ± 3.3 | 7.8 ± 7.7 |
| o. nerve | 2.9 ± 3.1 | 3.3 ± 3.6 | 2.7 ± 3.0 | 3.2 ± 4.5 |
| fovea | 25.8 ± 48.3 | 5.4 ± 4.9 | 23.4 ± 49.6 | 3.0 ± 2.3 |
| lens | 1.0 ± 1.8 | 6.6 ± 4.9 | 0.9 ± 1.9 | 5.5 ± 6.5 |
| cornea | 0.5 ± 1.0 | 4.8 ± 2.8 | 0.5 ± 1.0 | 5.5 ± 6.4 |
| $\overline{x}_{\text{all}}$ | 28.8 ± 14.4 | 3.9 ± 1.1 | 28.0 ± 14.8 | 3.4 ± 1.5 |

## Optimiser

Table A.24: Evaluation parameters, including their standard deviations, for each anatomical structure across the entire test dataset, for the models trained with the different optimiser.

| | $\texttt{AdamW}_{10^{-2}}$ | | $\texttt{AdamW}_{10^{-3}}$ | |
|---|---|---|---|---|
| structures | MAE / Gy | $\text{MAE}_{\text{DVH}}$ / pp | MAE / Gy | $\text{MAE}_{\text{DVH}}$ / pp |
| tumour | 75.3 ± 59.8 | 5.3 ± 4.7 | 70.1 ± 63.6 | 3.6 ± 3.0 |
| sclera | 51.6 ± 59.0 | 1.1 ± 0.9 | 51.9 ± 59.3 | 0.9 ± 0.8 |
| choroid | 50.4 ± 58.4 | 1.1 ± 1.0 | 50.3 ± 58.7 | 0.9 ± 0.9 |
| retina | 49.2 ± 57.9 | 1.1 ± 1.0 | 49.2 ± 58.2 | 0.9 ± 0.9 |
| papilla | 3.7 ± 3.5 | 7.1 ± 2.8 | 4.8 ± 4.3 | 12.8 ± 13.1 |
| o. nerve | 2.6 ± 3.0 | 1.9 ± 2.2 | 2.9 ± 3.0 | 4.4 ± 6.2 |
| fovea | 23.3 ± 50.4 | 2.6 ± 1.0 | 24.0 ± 50.8 | 3.1 ± 1.7 |
| lens | 0.9 ± 1.8 | 3.5 ± 1.8 | 1.0 ± 1.8 | 8.5 ± 10.2 |
| cornea | 0.4 ± 0.9 | 3.2 ± 2.9 | 0.5 ± 0.9 | 7.5 ± 9.1 |
| $\overline{x}_{\text{all}}$ | 28.6 ± 14.2 | 3.0 ± 0.8 | 28.3 ± 14.5 | 4.7 ± 2.3 |

Table A.25: Evaluation parameters, including their standard deviations, for each anatomical structure across the entire test dataset, for the models trained with the different optimiser.

| | $\texttt{AdamW}_{10^{-4}}$ | |
|---|---|---|
| structures | MAE / Gy | $\text{MAE}_{\text{DVH}}$ / pp |
| tumour | 73.0 ± 61.2 | 4.0 ± 3.5 |
| sclera | 51.6 ± 58.8 | 0.9 ± 1.0 |
| choroid | 50.4 ± 58.3 | 0.9 ± 1.0 |
| retina | 49.2 ± 57.8 | 0.9 ± 1.0 |
| papilla | 3.9 ± 3.7 | 6.3 ± 4.1 |
| o. nerve | 2.8 ± 3.1 | 2.2 ± 2.2 |
| fovea | 25.5 ± 52.4 | 3.6 ± 3.0 |
| lens | 0.8 ± 1.7 | 3.1 ± 2.6 |
| cornea | 0.4 ± 0.9 | 2.7 ± 3.8 |
| $\overline{x}_{\text{all}}$ | 28.6 ± 14.4 | 2.7 ± 0.9 |

## Data augmentation

Table A.26: Evaluation parameters, including their standard deviations, for each anatomical structure across the entire test dataset, for the models trained on the augmented dataset. The dataset is expanded by a factor of three by incorporating rotated and mirrored versions of the original dose tensors.

| | rotation ±90° | | rotation ±5° | |
|---|---|---|---|---|
| structures | MAE / Gy | $\text{MAE}_{\text{DVH}}$ / pp | MAE / Gy | $\text{MAE}_{\text{DVH}}$ / pp |
| tumour | 73.6 ± 60.7 | 3.6 ± 2.8 | 70.0 ± 63.4 | 3.0 ± 1.7 |
| sclera | 52.5 ± 61.8 | 0.8 ± 0.6 | 52.4 ± 63.7 | 0.7 ± 0.4 |
| choroid | 51.3 ± 61.4 | 0.8 ± 0.6 | 51.1 ± 63.3 | 0.6 ± 0.4 |
| retina | 50.1 ± 61.1 | 0.8 ± 0.6 | 50.0 ± 62.9 | 0.6 ± 0.3 |
| papilla | 4.1 ± 3.9 | 14.4 ± 17.6 | 4.0 ± 3.8 | 9.3 ± 9.0 |
| o. nerve | 2.7 ± 3.0 | 4.4 ± 6.6 | 2.7 ± 3.1 | 2.0 ± 2.3 |
| fovea | 24.9 ± 50.2 | 2.6 ± 1.8 | 23.9 ± 51.2 | 3.0 ± 2.5 |
| lens | 0.9 ± 1.8 | 11.2 ± 13.7 | 0.9 ± 1.9 | 2.4 ± 1.5 |
| cornea | 0.5 ± 1.0 | 13.4 ± 16.4 | 0.4 ± 1.0 | 1.9 ± 1.7 |
| $\overline{x}_{\text{all}}$ | 29.0 ± 14.7 | 5.8 ± 3.2 | 28.4 ± 15.2 | 2.6 ± 1.1 |

Table A.27: Evaluation parameters, including their standard deviations, for each anatomical structure across the entire test dataset, for the models trained on the augmented dataset. The dataset is expanded by a factor of three by incorporating rotated and mirrored versions of the original dose tensors.

| | rotation ±10° | |
|---|---|---|
| structures | MAE / Gy | $MAE_{DVH}$ / pp |
| tumour | 71.1 ± 64.5 | 3.2 ± 2.0 |
| sclera | 52.4 ± 64.7 | 0.6 ± 0.4 |
| choroid | 51.2 ± 64.4 | 0.6 ± 0.4 |
| retina | 50.1 ± 64.1 | 0.6 ± 0.4 |
| papilla | 3.6 ± 3.5 | 7.0 ± 7.1 |
| o. nerve | 2.7 ± 3.1 | 1.6 ± 1.6 |
| fovea | 22.8 ± 50.2 | 2.7 ± 1.8 |
| lens | 0.9 ± 1.9 | 2.5 ± 1.6 |
| cornea | 0.5 ± 1.0 | 2.3 ± 2.0 |
| $\overline{x}_{all}$ | 28.4 ± 15.4 | 2.4 ± 0.9 |

# Bibliography


[1] C. R. Harris et al., 'Array programming with NumPy', *Nature*, vol. 585, no. 7825, pp. 357–362, Sep. 2020. DOI: 10.1038/s41586-020-2649-2.

[2] The pandas development team. 'Pandas-dev/pandas: Pandas'. version 3.0.0rc1. (2025), [Online]. Available: https://doi.org/10.5281/zenodo.17992932.

[3] A. Paszke et al., 'Pytorch: An imperative style, high-performance deep learning library', *Advances in neural information processing systems*, vol. 32, 2019.

[4] W. Schroeder, K. Martin and B. Lorensen, 'The Visualization Toolkit (4th ed.)' Kitware, 2006, ISBN: 978-1-930934-19-1.

[5] N. Bornfeld et al., 'The interdisciplinary diagnosis andtTreatment of intraocular Tumors', *Deutsches Arzteblatt international*, vol. 115, no. 7, pp. 106–111, 16th Feb. 2018. DOI: 10.3238/arztebl.2018.0106.

[6] R. M. Thomson et al., 'AAPM recommendations on medical physics practices for ocular plaque brachytherapy: report of task group 221', *Medical physics*, vol. 47, no. 5, 2020.

[7] H. Manke et al., 'Measurements regarding a combined therapy concept for ophthalmic tumors consisting of brachytherapy and x-rays', *Biomedical Physics & Engineering Express*, vol. 10, no. 4, 2024. DOI: 10.1088/2057-1976/ad3bbb.

[8] A. Schüler and N. Bornfeld, 'Aktuelle Therapieaspekte intraokularer Tumoren', *Der Ophthalmologe*, vol. 97, no. 3, pp. 207–222, 2000. DOI: 10.1007/s003470050516.

[9] H. Manke, 'Brachytherapy meets X-rays, A novel concept to treat ophthalmic tumours', PhD thesis, TU Dortmund University, 2023. DOI: 10.17877/DE290R-24071.

[10] L. Tagliaferri et al., 'Uveal melanoma', *The GEC ESTRO handbook of brachytherapy*, 15th Apr. 2020.

[11] I. El Naqa and M. J. Murphy, 'Machine and deep learning in oncology, medical physics and radiology'. Springer, 2022. DOI: 10.1007/978-3-030-83047-2.

[12] N. Oldman, 'Simulation framework for modelling inhomogeneous dose distributions of $^{106}$Ru eye plaques', Supervised by Michelle Stroth, Master's thesis, TU Dortmund University, 2025.

[13] J. Wintz, 'Implementation and simulation of ruthenium-106 eye plaques', Supervised by Michelle Stroth, Master's thesis, TU Dortmund University, 2024.

[14] A. Bennemann, 'Neural network-based dose prediction for $^{106}$Ru brachytherapy of intraocular tumours', Supervised by Michelle Stroth, Master's thesis, TU Dortmund University, 2025.

[15] E. Marieb, P. Brady and J. Mallatt, 'Human Anatomy, Global Edition'. Pearson Deutschland, 2019, p. 896, ISBN: 9781292314471.

[16] S. Khan, C.-W. Do and E. A. Ho, 'Recent updates on drug delivery approaches for improved ocular delivery with an insight into nanostructured drug delivery carriers for anterior and posterior segment disorders', *Drug delivery and translational research*, pp. 1–49, 2024.

[17] I. D. Fabian and M. S. Sagoo, 'Surgical Ophthalmic Oncology: A Collaborative Open Access Reference'. Springer International Publishing, 2019, pp. 87–97. DOI: 10.1007/978-3-030-18757-6_8.

[18] M. Diener-West et al., 'Development of metastatic disease after enrollment in the COMS trials for treatment of choroidal melanoma: Collaborative Ocular Melanoma Study Group Report No. 26.' *Archives of ophthalmology (Chicago, Ill.: 1960)*, vol. 123, no. 12, pp. 1639–1643, 2005.

[19] F. Grehn, 'Augenheilkunde', 32nd ed. Springer-Verlag GmbH, 2019. DOI: 10.1007/978-3-662-59154-3.

[20] N. Bornfeld et al., 'Perspektiven der Ophthalmoonkologie', *Deutsches Ärzteblatt*, vol. 101, no. 38, pp. 2526–2535, 17th Sep. 2004.

[21] U. Kellner et al., 'Atlas des Augenhintergrundes'. Georg Thieme Verlag, 2020, ISBN: 978-3-13-146352-4.

[22] K. Irsch and D. L. Guyton, 'Encyclopedia of Biometrics'. Springer US, 2009. DOI: 10.1007/978-0-387-73003-5_253.

[23] M. Solnik et al., 'Imaging of uveal melanoma - current standard and methods in development', *Cancers*, vol. 14, no. 13, p. 3147, 2022.

[24] E. Stöckel, 'Das Sicherheitssaumkonzept in der okularen Brachytherapie mit Ruthenium-106 Applikatoren auf Basis von Dosisverteilungen und Unsicherheitsbetrachtungen', Master's thesis, TU Dortmund University, 2016.

[25] 'Radiology Key - Diagnostic Ophthalmic Ultrasound for Radiologists'. (2017), [Online]. Available: https://radiologykey.com/diagnostic-ophthalmic-ultrasound-for-radiologists/ (visited on 24th Feb. 2025).

[26] G. Stålhammar, S. Seregard and B. E. Damato, 'Uveal Melanoma: Brachytherapy'. Springer International Publishing, 2019, pp. 201–217. DOI: 10.1007/978-3-030-17879-6_12.

[27] S. S. Chaugule, S. G. Honavar and P. T. Finger, 'Surgical ophthalmic oncology: a collaborative open access reference'. Springer Nature, 2019. DOI: 10.1007/978-3-030-18757-6.

[28] A. W. Chan et al., 'Proton Therapy in Uveal Melanoma', *Cancers*, vol. 16, no. 20, p. 3497, 2024.

[29] M. W. Wilson and J. L. Hungerford, 'Comparison of episcleral plaque and proton beam radiation therapy for the treatment of choroidal melanoma', *Ophthalmology*, vol. 106, no. 8, pp. 1579–1587, 1999.

[30] K. Gündüz and N. E. Bechrakis, 'Exoresection and endoresection for uveal melanoma', *Middle East African journal of ophthalmology*, vol. 17, no. 3, pp. 210–216, 2010.

[31] S. Gulliford and K. Prise, 'Relative biological effect/linear energy transfer in proton beam therapy: a primer', *Clinical Oncology*, 2019.

[32] A. Kaiser et al., 'Proton therapy delivery and its clinical application in select solid tumor malignancies', *Journal of Visualized Experiments (JoVE)*, no. 144, 2019.

[33] J. Hrbacek et al., 'Practice patterns analysis of ocular proton therapy centers: the international OPTIC survey', *International Journal of Radiation Oncology· Biology· Physics*, vol. 95, no. 1, pp. 336–343, 2016.

[34] R. Slopsema et al., 'Dosimetric properties of a proton beamline dedicated to the treatment of ocular disease', *Medical physics*, vol. 41, no. 1, p. 011 707, 2014.

[35] W. Kilby et al., 'The CyberKnife® robotic radiosurgery system in 2010', *Technology in cancer research & treatment*, vol. 9, no. 5, pp. 433–452, 2010.

[36] K. Du and W. Luo, 'Efficacy and safety of robotic Cyberknife radiotherapy in uveal melanoma: a systematic review and meta-analysis', *Eye*, pp. 1–8, 2025.

[37] O. Semeniuk, E. Yu and M. J. Rivard, 'Current and emerging radiotherapy options for uveal melanoma', *Cancers*, vol. 16, no. 5, p. 1074, 2024.

[38] E. Van Limbergen et al., 'The GEC ESTRO handbook of brachytherapy', *Part II Clinical Practice Version*, pp. 1–30, 2019.

[39] Eckert & Ziegler BEBIG GmbH, 'Ru-106 Eye Applicators, Beta radiation for eye tumor treatment', P13D118/Rev.08, Jun. 2022. [Online]. Available: `https://medical.ezag.com/wp-content/uploads/2021/07/Fact-sheet-Ru-106-Eye-Applicators-Rev.08-English_WEB.pdf` (visited on 16th Dec. 2024).

[40] W. Sauerwein and H. Sack, 'Auge und Orbita', *Strahlentherapie: radiologische Onkologie*, pp. 425–452, 1996.

[41] H. Sommer et al., 'Monte Carlo simulation of ruthenium eye plaques with GEANT4: influence of multiple scattering algorithms, the spectrum and the geometry on depth dose profiles', *Physics in Medicine and Biology*, vol. 62, pp. 1848–1864, 8th Feb. 2017. DOI: `10.1088/1361-6560/aa5696`.

[42] Eckert & Ziegler BEBIG GmbH, 'Gebrauchsanweisung - Ru-106 Augenapplikatoren, Td04_000/rev.12', Mar. 2016.

[43] M.-M. Bé et al., 'Table of Radionuclides'. Bureau International des Poids et Mesures, 2016, vol. 8, ISBN: 978-92-822-2264-5.

[44] Dr. Daniela Frömberg, Physicist, Eckert & Ziegler Medical, Berlin, Germany, 'Personal communication', 25th Apr. 2025.

[45] Eckert & Ziegler BEBIG GmbH, *Certificate for sealed radioactive sources no. 54919 and protocol of mesurements*, 2019.

[46] M. Eichmann, D. Flühs and B. Spaan, 'Development of a high precision dosimetry system for the measurement of surface dose rate distribution for eye applicators',

*Medical Physics*, vol. 36, no. 10, pp. 4634–4643, 14th Sep. 2009. DOI: 10.1118/1.3218762.

[47] M. Eichmann, 'Entwicklung eines hochpräzisen Dosimetriesystems zur Messung der Oberflächendosisverteilung von Augenapplikatoren', PhD thesis, TU Dortmund University, 11th Nov. 2010. DOI: 10.17877/DE290R-8029.

[48] The American Brachytherapy Society (Ophthalmic Oncology Task Force) - E. Simpson et. al., 'The American Brachytherapy Society consensus guidelines for plaque brachytherapy of uveal melanoma and retinoblastoma', *Brachytherapy*, vol. 13, pp. 1–14, 2014. DOI: 10.1016/j.brachy.2013.11.008.

[49] E. Stöckel et al., 'Dose Distributions and Treatment Margins in Ocular Brachytherapy with $^{106}$ Eye Plaques', *Ocular Oncology and Pathology*, vol. 4, pp. 122–128, 16th Sep. 2017. DOI: 10.1159/000479558.

[50] D. Flühs, Medical physics expert, University Medicine Essen, Essen, Germany, 'Personal communication', Apr. 2025.

[51] D. J. Coleman et al., 'Computerized ultrasonic biometry and imaging of intraocular tumors for the monitoring of therapy', *Transactions of the American Ophthalmological Society*, vol. 85, p. 49, 1987.

[52] C. Haritoglou et al., 'Interobserver and intraobserver variability of measurements of uveal melanomas using standardised echography', *British journal of ophthalmology*, vol. 86, no. 12, pp. 1390–1394, 2002.

[53] D. Kook et al., 'Variability of standardized echographic ultrasound using 10 mHz and high-resolution 20 mHz B scan in measuring intraocular melanoma', *Clinical Ophthalmology*, pp. 477–482, 2011.

[54] S. Vurgese, S. Panda-Jonas and J. B. Jonas, 'Scleral thickness in human eyes', *PLOS One*, vol. 7, no. 1, 2012.

[55] J. W. Harbour et al., 'Intraoperative echographic localization of iodine 125 episcleral radioactive plaques for posterior uveal melanoma', *Retina*, vol. 16, no. 2, pp. 129–134, 1996.

[56] A. Almony et al., 'Tilting of radioactive plaques after initial accurate placement for treatment of uveal melanoma', *Archives of ophthalmology*, vol. 126, no. 1, pp. 65–70, 2008.

[57] W. Sauerwein and M. Zehetmayer, 'Strahlentherapie intraokularer Tumoren', *Der Onkologe*, vol. 5, no. 9, pp. 781–791, 1st Sep. 1999. DOI: 10.1007/s007610050439.

[58] N. Bornfeld et al., 'Metastatic Disease, Eye Retention and Visual Function in Conservative Treatment of Uveal Melanoma', *Radiotherapy of Ocular Disease*, vol. 30, pp. 97–110, 1997.

[59] I. D. Fabian et al., 'Secondary Enucleations for Uveal Melanoma: A 7-Year Retrospective Analysis', *American Journal of Ophthalmology*, vol. 160, no. 6, pp. 1104–1110, 2015. DOI: 10.1016/j.ajo.2015.08.034.

[60] G. Heilemann et al., 'Treatment plan optimization and robustness of $^{106}$Ru eye plaque brachytherapy using a novel software tool', *Radiotherapy and Oncology*, vol. 123, no. 1, pp. 119–124, 2017. DOI: 10.1016/j.radonc.2017.01.010.

[61] E. B. Podgorsak, 'Radiation Physics for Medical Physicists', 3rd. Springer, 2016. DOI: 10.1007/978-3-319-25383-3.

[62] H. Krieger, 'Grundlagen der Strahlungsphysik und des Strahlenschutzes'. Springer, 2019. DOI: 10.1007/978-3-662-60584-4.

[63] E. Richter and T. Feyerabend, 'Grundlagen der Strahlentherapie'. Springer-Verlag, 2013, pp. 34–41.

[64] R. Drzymala et al., 'Dose-volume histograms', *International Journal of Radiation Oncology · Biology · Physics*, vol. 21, no. 1, pp. 71–78, 1991.

[65] A. L. Fielding, 'Monte-Carlo techniques for radiotherapy applications I: Introduction and overview of the different Monte-Carlo codes', *Journal of Radiotherapy in Practice*, vol. 22, 2023.

[66] M. G. Jaarsma-Coes et al., 'Magnetic resonance imaging in the clinical care for uveal melanoma patients - a systematic review from an ophthalmic perspective', *Cancers*, vol. 15, no. 11, p. 2995, 2023.

[67] M. Stroth et al., 'Variable 3D resolution in complex detector geometries for Monte Carlo simulations', *Physics in Medicine and Biology*, vol. 70, no. 14, 2025. DOI: 10.1088/1361-6560/adeb3f.

[68] M. Stroth, 'Die Implementierung eines anatomisch approximierten Augenmodells und dessen Einfluss auf die simulierten Dosisverteilungen eines $^{106}$Ru-Applikators', Bachelor's thesis, TU Dortmund University, 2020. DOI: 10.17877/DE290R-23908.

[69] Autodesk Inc. 'Autodesk Fusion', [Online]. Available: https://www.autodesk.com/asean/products/fusion-360/ (visited on 12th Nov. 2024).

[70] P. Q. Ngo, 'Untersuchung von Unsicherheiten von Dosisverteilungen auf Grundlage von Monte-Carlo-Simulationen der Brachytherapie bei Augentumoren', Bachelor's thesis, TU Dortmund University, 2022.

[71] J. Seco and F. Verhaegen, 'Monte Carlo techniques in radiation therapy'. CRC press, 2016. DOI: 10.1201/b13961.

[72] J. Van Dyk et al., 'The modern technology of radiation oncology', *Madison, WI: Medical Physics Publishing*, pp. 437–479, 1999.

[73] D. Landau and K. Binder, 'A guide to Monte Carlo simulations in statistical physics'. Cambridge university press, 2021. DOI: 10.1017/9781108780346.

[74] S. Agostinelli et al., 'Geant4 – A simulation Toolkit', *Nuclear Instruments and Methods in Physics Research Section A: Accelerators, Spectrometers, Detectors and Associated Equipment*, vol. 506, pp. 250–303, 1st Jul. 2003. DOI: 10.1016/S0168-9002(03)01368-8.

[75] H. Lewis, 'Multiple Scattering in an Infinite Medium', *Phys. Rev.*, vol. 78, pp. 526–529, 5 1950. DOI: 10.1103/PhysRev.78.526.

[76] G. Molière, 'Theorie der Streuung schneller geladener Teilchen II Mehrfach-und Vielfachstreuung', *Zeitschrift für Naturforschung A*, vol. 3, no. 2, pp. 78–97, 1st Feb. 1948. DOI: 10.1515/zna-1948-0203.

[77] S. Goudsmit and J. Saunderson, 'Multiple Scattering of Electrons', *Physical Review*, vol. 57, no. 1, pp. 24–29, 1 Jan. 1940. DOI: 10.1103/PhysRev.57.24.

[78] C. M. Poole et al., 'A CAD interface for Geant4', *Australasian Physical & Engineering Science in Medicine*, vol. 35, no. 3, pp. 329–334, Sep. 2012. DOI: 10.1007/s13246-012-0159-8.

[79] Geant4 Collaboration, 'Geant4 - Book For Application Developers - Release 11.1', Geneva, 31st Jul. 2023. [Online]. Available: https://geant4-userdoc.web.cern.ch/UsersGuides/ForToolkitDeveloper/BackupVersions/V11.1b/fo/BookForToolkitDevelopers.pdf (visited on 14th Nov. 2024).

[80] R. Brun and F. Rademakers, 'Root - an object oriented data analysis framework', *Nuclear Instruments and Methods in Physics Research Section A: Accelerators, Spectrometers, Detectors and Associated Equipment*, vol. 389, pp. 81–86, Sep. 1997. DOI: 10.1016/S0168-9002(97)00048-X.

[81] Geant4 Collaboration, 'Geant4 - User's Guide for Toolkit Developers - Release 11.2', Geneva, 8th Dec. 2023. [Online]. Available: https://geant4-userdoc.web.cern.ch/UsersGuides/ForToolkitDeveloper/fo/BookForToolkitDevelopers.pdf (visited on 14th Nov. 2024).

[82] MeshLib SDK. 'Releases', [Online]. Available: https://github.com/MeshInspector/MeshLib/releases?page=6/ (visited on 20th Mar. 2025).

[83] C. Sullivan and A. Kaszynski, 'PyVista: 3D plotting and mesh analysis through a streamlined interface for the Visualization Toolkit (VTK)', *Journal of Open Source Software*, vol. 4, no. 37, p. 1450, 2019.

[84] Qingnan Zhou. 'Mesh Boolean', [Online]. Available: https://pymesh.readthedocs.io/en/latest/mesh_boolean.html (visited on 20th Mar. 2025).

[85] Python Software Foundation. 'concurrent.futures - Launching parallel tasks'. (2024), [Online]. Available: https://docs.python.org/3.11/library/concurrent.futures.html (visited on 12th Nov. 2024).

[86] MeshLib SDK. 'MeshLib SDK - Engineered to revolutionize', [Online]. Available: https://meshlib.io/ (visited on 20th Mar. 2025).

[87] MeshLib SDK. 'Example of boolean operation', [Online]. Available: https://meshlib.io/documentation/ExampleMeshBoolean.html (visited on 20th Mar. 2025).

[88] MeshLib SDK. 'VTK Alternatives: Comparing Visualization Libraries', [Online]. Available: https://meshlib.io/blog-post/vtk-alternative-comparison/ (visited on 20th Mar. 2025).

[89] B. Emami, 'Tolerance of normal tissue to therapeutic radiation', *Reports of radiotherapy and Oncology*, vol. 1, no. 1, pp. 123–7, 2013.

[90] C. Oare et al., 'Analysis of dose to the macula, optic disc, and lens in relation to vision toxicities–a retrospective study using coms eye plaques', *Physica Medica*, vol. 101, pp. 71–78, 2022.

[91] M. Guberina et al., 'Dose response relation for optic nerve atrophy at low-dose rate brachytherapy of uveal melanoma', *Radiotherapy and Oncology*, vol. 205, p. 110 775, 2025. DOI: https://doi.org/10.1016/j.radonc.2025.110775.

[92] J. Henk et al., 'Radiation dose to the lens and cataract formation', *International Journal of Radiation Oncology · Biology · Physics*, vol. 25, no. 5, pp. 815–820, 1993.

[93] J. Köster and S. Rahmann, 'Snakemake - A scalable bioinformatics workflow engine', *F1000Research*, vol. 10, no. 33, 2021. DOI: 10.12688/f1000research.29032.1.

[94] R. Kollaard et al., 'Quality control of sealed beta sources in brachytherapy', *Recommendations on Detectors, Measurement Procedures and Quality Control of Beta Sources. Report*, vol. 14, 2004.

[95] Dr. Daniela Frömberg, Physicist, Eckert & Ziegler Medical, Berlin, Germany, 'Personal communication', 11th Jul. 2025.

[96] W. L. Dunn, 'Inverse monte carlo analysis', *Journal of Computational Physics*, vol. 41, no. 1, pp. 154–166, 1981.

[97] M. F. Belosi et al., 'Monte carlo simulation of truebeam flattening-filter-free beams using varian phase-space files: Comparison with experimental data', *Medical physics*, vol. 41, no. 5, 2014.

[98] F. J. Güldenhaupt, 'Simulating a new setup for surface dose measurements of $^{106}$Ru eye plaques', Master's thesis, TU Dortmund University, 2025.

[99] The SciPy community. 'scipy.optimize. minimize', [Online]. Available: https://docs.scipy.org/doc/scipy/reference/generated/scipy.optimize.minimize.html#minimize.

[100] J. Wintz, In progress, PhD thesis, TU Dortmund University.

[101] V. Kearney et al., 'Dosenet: A volumetric dose prediction algorithm using 3d fully-convolutional neural networks', *Physics in Medicine & Biology*, vol. 63, no. 23, p. 235 022, 2018.

[102] S. Shiraishi and K. L. Moore, 'Knowledge-based prediction of three-dimensional dose distributions for external beam radiotherapy', *Medical physics*, vol. 43, no. 1, pp. 378–387, 2016.

[103] J. L. Uc Castillo et al., 'A systematic review of machine learning and deep learning approaches in mexico: Challenges and opportunities', *Frontiers in Artificial Intelligence*, vol. 7, 2025.

[104] N. Ketkar et al., 'Deep learning with Python: learn best practices of deep learning models with PyTorch'. Springer, 2021. DOI: https://doi.org/10.1007/978-1-4842-5364-9.

[105] T. Barua et al., 'Machine learning with python'. Walter de Gruyter GmbH & Co KG, 2024, ISBN: 978-3-11-069716-2.

[106] H. Abdi, D. Valentin and B. Edelman, 'Neural networks'. SAGE Publications, Inc., 1999.

[107] M. J. Neuer, 'Maschinelles Lernen für die Ingenieurwissenschaften'. Springer, 2024. DOI: https://doi.org/10.1007/978-3-662-68216-6.

[108] Y. Bengio, I. Goodfellow, A. Courville et al., 'Deep learning'. MIT press Cambridge, MA, USA, 2017, vol. 1.

[109] C. M. Bishop and H. Bishop, 'Deep learning: Foundations and concepts'. Springer Nature, 2023. DOI: https://doi.org/10.1007/978-3-031-45468-4.

[110] M. Vakalopoulou et al., 'Machine Learning for Brain Disorders'. Springer US, 2023, pp. 77–115. DOI: https://doi.org/10.1007/978-1-0716-3195-9_3.

[111] Ö. Çiçek et al., '3d u-net: Learning dense volumetric segmentation from sparse annotation', in *International conference on medical image computing and computer-assisted intervention*, Springer, 2016, pp. 424–432.

[112] PyTorch Contributors. 'PyTorch', [Online]. Available: https://github.com/pytorch/pytorch (visited on 26th Nov. 2025).

[113] O. Ronneberger, P. Fischer and T. Brox, 'U-net: Convolutional networks for biomedical image segmentation', in *International Conference on Medical image computing and computer-assisted intervention*, Springer, 2015, pp. 234–241.

[114] S. Gautam et al., 'Attention 3d unet for dose distribution prediction of high-dose-rate brachytherapy of cervical cancer: Intracavitary applicators', *Journal of Applied Clinical Medical Physics*, vol. 26, no. 2, 2025.

[115] S. Liu et al., 'A cascade 3d u-net for dose prediction in radiotherapy', *Medical physics*, vol. 48, no. 9, 2021.

[116] D. P. Kingma and J. Ba, 'Adam: A method for stochastic optimization', *arXiv preprint arXiv:1412.6980*, vol. 1412, no. 6, 2014.

[117] P. Veit-Haibach and K. Herrmann, 'Machine Learning in Nuclear Medicine and Hybrid Imaging'. Springer, 2022. DOI: 10.1007/978-3-031-00119-2.

[118] PyTorch Contributors. 'Huber Loss', [Online]. Available: https://docs.pytorch.org/docs/stable/generated/torch.nn.HuberLoss.html (visited on 10th Dec. 2025).

[119] I. Loshchilov and F. Hutter, 'Decoupled weight decay regularization', *arXiv preprint arXiv:1711.05101*, 2017.

[120] T. Akiba et al., 'Optuna: A next-generation hyperparameter optimization framework', in *The 25th ACM SIGKDD International Conference on Knowledge Discovery & Data Mining*, 2019, pp. 2623–2631.

[121] M. D. Evans et al., 'Computerized treatment planning systems for external photon beam radiotherapy', *International Atomic Energy Agency Publication*, pp. 387–406, 2005.

[122] Emscripten Contributors. 'Emscripten, Emscripten documentation', [Online]. Available: `https://emscripten.org/docs/index.html` (visited on 18th Dec. 2025).

[123] Eye Physics. 'BEBIG Spherical radius and surface dose rate measurement points', [Online]. Available: `https://eyephysics.com/PS/PS6/UserGuide/BEBIGPlaquesMenu.html` (visited on 27th Oct. 2025).

# Acknowledgments

Zuallererst möchte ich mich bei Prof. Johannes Albrecht bedanken, ohne dessen Aufgeschlossenheit diese Arbeit nicht möglich gewesen wäre. Seine Expertise liegt primär in der experimentellen Teilchenphysik, und dennoch hat er mir die Möglichkeit geboten, diese Arbeit in seiner Arbeitsgruppe zu schreiben. Ich danke dir, dass du mir ermöglicht hast, über mich hinauszuwachsen, über den Tellerrand zu schauen und die Vorteile interdisziplinären Arbeitens jeden Tag neu kennenzulernen. Dabei hatte ich das Gefühl, immer einen Ratschlag von dir zu bekommen, wenn ich ihn brauchte, sodass ich die Herausforderungen der Promotion meistern konnte.

Des Weiteren möchte ich mich bei Prof. Armin Lühr bedanken, der sich nicht nur bereit erklärt hat, Zweitgutachter dieser Arbeit zu sein, sondern mir auch während der Promotion bei medizinphysikalischen Fragen stets mit seiner Erfahrung zur Seite stand.

Ein sehr großer Dank gilt Dirk Flühs, dessen Expertise und Ideen die Basis des Projekts bilden, dessen Teil diese Promotion ist. Ich danke dir für deine Zeit und Mühe, mir nicht nur während der Bachelor- und Masterarbeit, sondern auch während der mehrjährigen Promotion jede Frage zu beantworten und jeden Vortrag, jedes Abstract sowie jedes Kapitel zu begutachten. Deine Begeisterung für das Thema hat mich von Beginn an angesteckt, und du hast in erheblichem Maße zu meiner wissenschaftlichen Ausbildung beigetragen.

Weiter möchte ich mich bei Carmen Schulz und Daniela Frömberg von der Firma Eckert & Ziegler Medical für die Kooperation, die Beantwortung meiner Fragen sowie das Bereitstellen von Informationen bedanken.

Der Deutschen Forschungsgemeinschaft (DFG) danke ich für die Finanzierung des Projektes 528648187, als dessen Teil diese Promotion entstanden ist.

Wissenschaft ist Teamarbeit, und ich bin sehr dankbar und stolz, ein so tolles Team an meiner Seite gehabt zu haben.
Ich danke Henning für den Input und den Austausch nicht nur zu dieser Arbeit, sondern auch zum Projektantrag, Karrieremöglichkeiten und eigentlich allem, was gerade so anstand. Ohne dich und deine Betreuung während meiner Bachelor- und Masterarbeit hätte ich eine Promotion vermutlich nicht in Betracht gezogen.
Ich danke den von mir betreuten Studierenden Annika, Nick und Johannes, die mit ihren Bachelor- und Masterarbeiten zum Fortschritt dieses Projektes beigetragen haben. Des Weiteren danke ich Annika und Nick für ihre Tätigkeit als studentische Hilfskräfte. Es hat mir unglaublich viel Spaß gemacht, mit euch zu arbeiten, zu brainstormen, Rad zu fahren, zu schwimmen und die manchmal nötige Ablenkung in eurem Büro zu finden.
Weiter danke ich den Teilnehmerinnen und Teilnehmern des Geant4-Meetings und des Joint Medical Physics Meetings für die interessanten Diskussionen und neuen Perspektiven.
Ein großer Dank gilt auch den Cluster-Admins unserer Arbeitsgruppe, ohne die die zahlreichen Simulationen und Studien auf separaten Maschinen nicht möglich gewesen wären.

Ich danke Dirk, Alex, Nick, Annika, Maik, Quentin, Noah und Henning für das Feedback und das Korrekturlesen dieser Arbeit.

Ich danke der Arbeitsgruppe für die gute Arbeitsatmosphäre, die spannenden Diskussionen und die spontanen Meetings im Türrahmen. Ich habe mich während der gesamten Zeit hier sehr wohlgefühlt! Besonders danken möchte ich meinen Bürokollegen Noah, Luca, Julian, Alex R., Henning und Fran,

die während der letzten Jahre jedes „Huhuu“ erwidert und mit ihrem Humor sowie ihren kreativen Whiteboard-Zeichnungen den Alltag immer wieder besonders gemacht haben.
Weiter möchte ich mich bei Alex S. und Jan Peter für die tolle Zusammenarbeit in der Organisation der Vorlesungen Experimentalphysik I und II bedanken, sowie bei Maik, der nicht nur mit seiner fröhlichen Art gute Laune im Büro verbreitet, sondern sich bei jedem Problem, sei es noch so klein, um eine Lösung bemüht.
Besonders bedanken möchte ich mich auch bei Nicole, Noah, Donata, Jan Peter, Jonas und Leandra für die fröhlichen Abende im Atlantico und die unterhaltsamen GIFs.

Jeder Tag ist schöner und jede Herausforderung leichter, wenn man Freundinnen und Freunde hat, die immer da sind, unterstützen, anfeuern, schöne Erinnerungen schaffen und dafür sorgen, dass Entfernung kein Hindernis ist. Sophia, Tilo, Lara, Marla, Ina, Lea, Kiki, Jule und Jessi, ich danke euch, dass ihr ein so fester Bestandteil meines Lebens seid und immer Verständnis hattet, wenn ich durch das Studium oder die Arbeit einmal weniger Zeit hatte.

Vom ersten bis zum letzten Tag der Promotion hatte ich das Glück, von meiner besten Freundin durch die guten und auch herausfordernden Zeiten begleitet zu werden, die ein so langes Projekt mit sich bringt. Nicole, ich bin so froh, dass ich dich im Master kennengelernt habe. Du bist aus meinem Leben nicht mehr wegzudenken. Danke für deine bunte, lebensfrohe Art und deinen Humor, der mich jeden Tag zum Lachen bringt. Du hast diese besondere Zeit in meinem Leben zu einer noch besondereren gemacht, und ich freue mich über jede gemeinsame Erinnerung, die wir gesammelt haben und noch sammeln werden.

Ich danke meinem Freund Alex für die bedingungslose Unterstützung, nicht nur mit Blick auf die Promotion, sondern in allen Bereichen meines Lebens. Danke, dass du jederzeit für eine Sporteinheit zu haben bist und mir hilfst, auch in anstrengenderen Zeiten Ruhe zu finden. Danke für deine Zeit und dein Durchhaltevermögen, die gesamte Thesis Korrektur zu lesen. Danke, dass du mit mir schwimmst, läufst, lachst und jeden Tag zu etwas ganz Besonderem machst. Ich freue mich darauf, weiter die Welt mit dir zu entdecken und allem, was das Leben noch für uns bereithält, mit einem Lächeln zu begegnen.

Seit ich mich erinnern kann, ist meine Familie mein größter Rückhalt. Ich wurde immer ermutigt, alles schaffen und alles sein zu können. Ich danke meiner Familie für die nie endende Unterstützung, durch mein ganzes Studium, über die Promotion hinweg und in meinem bisherigen Leben. Ich danke meiner Mutter, dass sie an mich glaubt und mich immer wieder ermutigt, auch wenn ich Zweifel habe. Ich danke meinem Vater, dass er mich immer daran erinnert, dass man einen Weg Schritt für Schritt geht und dass das die beste Strategie ist, um ans Ziel zu kommen. Ich danke meinem Bruder, dass er mich zum Lachen bringt, wenn ich es brauche, und mir das Gefühl gibt, nie allein zu sein. Es ist für mich das größte Glück, euch als Familie zu haben. Abschließend danke ich noch meinem Opa, der mich mein ganzes Leben begleitet hat und im letzten Jahr dieser Arbeit verstorben ist. Du fehlst mir.